2014-04-19

Enhancement of Mass Transfer and Electron Usage for Syngas Fermentation

James J. Orgill
Brigham Young University - Provo

Enhancement of Mass Transfer and Electron Usage for Syngas Fermentation

James J. Orgill

A dissertation submitted to the faculty of
Brigham Young University
in partial fulfillment of the requirements for the degree of

Doctor of Philosophy

Randy S. Lewis, Chair
William C. Hecker
William R. McCleary
Bradley C. Bundy
David O. Lignell

Department of Chemical Engineering

Brigham Young University

April 2014

ABSTRACT

Enhancement of Mass Transfer and Electron Usage for Syngas Fermentation

James J. Orgill
Department of Chemical Engineering, BYU
Doctor of Philosophy

Biofuel production via fermentation is produced primarily by fermentation of simple sugars. Besides the sugar fermentation route, there exists a promising alternative process that uses syngas (CO, H_2, CO_2) produced from biomass as building blocks for biofuels. Although syngas fermentation has many benefits, there are several challenges that still need to be addressed in order for syngas fermentation to become a viable process for producing biofuels on a large scale. One challenge is mass transfer limitations due to low solubilities of syngas species. The hollow fiber reactor (HFR) is one type of reactor that has the potential for achieving high mass transfer rates for biofuels production. However, a better understanding of mass transfer limitations in HFRs is still needed. In addition there have been relatively few studies performing actual fermentations in an HFR to assess whether high mass transfer rates equate to better fermentation results. Besides mass transfer, one other difficulty with syngas fermentation is understanding the role that CO and H_2 play as electron donors and how different CO and H_2 ratios effect syngas fermentation. In addition to electrons from CO and H_2, electrodes can also be used to augment the supply of electrons or provide the only source of electrons for syngas fermentation.

This work performed an in depth reactor comparison that compared mass transfer rates and fermentation abilities. The HFR achieved the highest oxygen mass transfer coefficient (1062 h^{-1}) compared to other reactors. In fermentations, the HFR showed very high production rates (5.3 mM_c/hr) and ethanol to acetic acid ratios (13) compared to other common reactors. This work also analyzed the use of electrons from H_2 and CO by *C. ragsdalei* and to study the effects of these two different electron sources on product formation and cell growth. This study showed that cell growth is not largely effected by CO composition although there must be at least some minimum amount of CO present (between 5-20%). Interestingly, H_2 composition has no effect on cell growth. Also, more electron equivalents will lead to higher product formation rates. Following Acetyl-CoA formation, H_2 is only used for product formation but not cell growth. In addition to these studies on electrons from H_2 and CO, this work also assessed the redox states of methyl viologen (MV) for use as an artificial electron carrier in applications such as syngas fermentation. A validated thermodynamic model was presented in order to illustrate the most likely redox state of MV depending on the system setup. Variable MV extinction coefficients and standard redox potentials reported in literature were assessed to provide recommended values for modeling and analysis. Model results showed that there are narrow potential ranges in which MV can change from one redox state to another, thus affecting the potential use as an artificial electron carrier.

Keywords: ethanol, bioelectric reactor, electron carrier, hollow fiber reactor, mass transfer, methyl viologen, redox potential, syngas fermentation, Wood-Ljungdahl pathway, thermodynamics.

ACKNOWLEDGMENTS

I am very grateful to have had the opportunity to study at Brigham Young University through my bachelors and now my PhD. I have received support from countless faculty and staff that have taught me how to learn.

I want to thank my advisor Dr. Randy Lewis for his support throughout my PhD studies. He taught me how to think through experiments intelligently and how to make my work have an impact in the field. He gave me the freedom to perform my own research with my own ideas, but still provided encouragement, support, and correction when needed. I also thank Dr. William Hecker, Dr. William McCleary, Dr. Brad Bundy, and Dr. David Lignell for their support, correction and ideas as I designed and worked through my research.

The shear amount of experiments and research performed in this research would not have been possible if not for the many undergraduate students that worked with me through the years, including: Spencer Bowen, Hannah Davis, Lee Jacobsen, Alex Foy, Chase Johnson, Jason Wheeler, Chad Schirmer, Chantelle Dolbin, Jordan Anderson, and Mike Abboud. They contributed many hours of sometimes tedious work, and many thoughtful ideas to aid me through me research. I also want to thank the graduate students for their research and ideas that helped build the foundation for my research: Chris Hoeger, Deshun Xu, Peng Hu, and Chang Chen.

Finally, I am especially grateful for my family who has supported me through all the years of my study. My wife, Joanna, has provided me with encouragement and support to gain the education that I have always desired. She has worked to support our family through the years as I pursued my education. I am eternally grateful for her love, support and sacrifice.

TABLE OF CONTENTS

LIST OF TABLES

LIST OF FIGURES

1 Introduction

1.1 The Push for Alternative Fuels

With growing concerns over fossil fuel shortages, there has been increased interest regarding alternative fuels. The government has pushed for more research and funding to increase alternative fuel usage. In 1992, "The Energy Policy Act of 1992" (EPAct 1992) was passed (1992). One aim of this act was to reduce US dependence on imported petroleum as well as discuss current aspects of energy supply and demand. In 2005, congress passed the "Energy Policy Act of 2005". This bill called for grant programs, testing initiatives, and tax incentives that promote the use of alternative fuels (2005). In 2007, the push for alternative fuels was furthered by the "Independence and Security Act of 2007" (EISA) (2007). EISA includes provisions to dramatically increase renewable alternative fuel sources by requiring transportation fuel sold in the United States to contain a minimum of 36 billion gallons of renewable fuels annually by 2022. These bills have created opportunities for much research to be performed in renewable alternative fuels. Alternative fuels can be a nebulous concept with differing opinions on what should be included on the list of alternative fuels. EPAct 1992 defined alternative fuels as: methanol, ethanol, and other alcohols; E85 blends or more of alcohol with gasoline; biodiesel (B100); fuels, besides alcohol, derived from biological materials; natural gas and liquid fuels produced from natural gas; propane; hydrogen; electricity; coal-derived liquid fuels; and P-Series fuels, the latter which were added in 1999. Many of these alternative fuels are already in use, and some are still in the research and development phase.

1.2 Biomass to Produce Alternative Fuels

Of these alternative sources, fuels produced from biomass have a promising future because of their renewable nature. Biomass is a broad term meaning any biological material derived from living, or recently living organisms (BEC 2011). Biomass has become increasingly important because it is the only renewable energy source that can be converted to liquid or gaseous products needed in the transportation industry (Alauddin, et al. 2010). Though many liquid products can be produced from biomass, one major product currently produced in large scales is ethanol. Fuel ethanol production in the U.S. has increased from 175 million gallons per year to 13 billion gallons per year in the last 30 years (RFA 2011). Besides being a renewable liquid energy source, ethanol also has benefits when used as a fuel. Ethanol gasoline blended fuels improve torque output and fuel consumption and dramatically decrease CO and HC emissions (Hsieh, et al. 2002). Ethanol is in many respects superior to gasoline for spark ignited engines because of its lower volumetric energy density and higher thermal efficiency in optimized engines (Lynd 1996). However, despite ethanol's growing popularity as a renewable liquid fuel, one major issue is its hygroscopic nature which makes it very susceptible to water contamination in transit (Whims 2002). This has caused a push for higher alcohols such as butanol to be produced from biomass.

1.3 Alcohols from Biomass

Alcohols from biomass can be produced by two different processes. The first process produces ethanol by fermentation of simple sugars. These sugars can be produced from sugar-based food crops by wet and dry milling (Lynd 1996). Besides sugar-based food crops, simple sugars can also be produced from lignocellulosic materials. To get simple sugar monomers from

lignocellulosic materials, the biomass is treated with acid, ammonia, steam, or alkaline chemicals in order to expose the cellulosic and hemi-cellulosic components to enzymes (Kadar, et al. 2004; Lynd 1996). These enzymes then degrade the cellulose and hemi-cellulose into their basic sugar monomers that can be used in fermentation. The sugar fermentation platform accounts for nearly 90% of the world bioethanol production (Abubackar, et al. 2011). Though sugar fermentation is by far the most widely used method, the production of ethanol from food sources has left some with serious concerns for food security (Srinivasan 2009).

The second process uses syngas (H_2, CO, and CO_2), produced from gasification. The syngas can then be used to produce ethanol either by fermentation or metal catalysis. The syngas produced from lignocellulosic gasification is advantageous because it does not necessarily require a food source and it can be produced from hard-to-handle softwoods (Dayton and Spath 2003). Another advantage is that gasification can more easily break cellulosic, hemi-cellulosic, and lignin bonds than the specialized enzymes used in sugar fermentation (McKendry 2002a). Thus, gasification can break down lignin rich fuels that cannot be hydrolyzed or enzymatically reduced to simple sugars (McKendry 2002a). Using metal catalysis, syngas can also be converted to ethanol by catalytic chemical processes like Fischer-Tropsch Synthesis. Though the focus of Fischer-Tropsch Synthesis is to make hydrocarbons, several industrial plants have been producing ethanol using Fischer-Tropsch Synthesis. In these processes, there are still limitations due to high temperatures and pressures, low selectivity and catalyst poisoning (Ragauskas, et al. 2006).

1.4 Syngas Fermentation Metabolic Pathway

For the syngas fermentation pathway, syngas is transported to a bioreactor where it is converted into ethanol/butanol, acetic acid, and other products via a microbial catalyst (Hurst and

Lewis 2010). The catalyst can be any number of the homoacetogenic bacteria (Abubackar, et al. 2011). The pathway usually followed by ethanol producing bacteria is the Wood-Ljungdahl pathway. The methyl branch of this pathway produces the methyl group of acetyl CoA through several reduction reactions. The carbonyl branch provides the carbonyl group in the acetyl CoA by reducing CO_2 to CO or by using CO directly. Acetyl CoA is then used to produce ethanol, acetic acid, and other products. The production of ethanol and acetic acid can be summarized in the following four reactions:

$$6CO + 3H_2O \rightarrow C_2H_5OH + 4CO_2 \quad \textbf{(1-1)}$$

$$6H_2 + 2CO_2 \rightarrow C_2H_5OH + 3H_2O \quad \textbf{(1-2)}$$

$$4CO + 2H_2O \rightarrow CH_3COOH + 2CO_2 \quad \textbf{(1-3)}$$

$$2CO_2 + 4H_2 \rightarrow CH_3COOH + 2H_2O \quad \textbf{(1-4)}$$

In these reactions, the most efficient carbon usage would be when H_2 is used as an electron donor in the reduction reactions instead of CO. However, this is generally not achievable because of the thermodynamic favorability of electron donation of CO as opposed to H_2 (Hu 2011).

1.5 Shift of Focus to Butanol Production in Bacterial Fermentation

Though the current focus of most studies has been ethanol conversion, it is likely that in the future, bacterial fermentation will be utilized to focus on other alcohols, such as butanol, and even non-alcohol fuels. Butanol is a better liquid fuel than ethanol because it has a lower toleration for water contamination and is less corrosive (DuPont 2011). Recent research has focused on genetic engineering of bacteria in order to produce

more butanol by reducing butanol toxicity to the fermenting organisms. One study has shown that genetic engineering leads to reduction in butanol toxicity to the fermenting microorganism, improved substrate utilization, and improved bioreactor performance (Ezeji, et al. 2007). Most of the research in genetic engineering has been done on organisms used in the fermentation of sugar monomers. However, with the more recent use of syngas fermenting microbes, genetic engineering of these microbes to produce more ethanol or butanol would greatly enhance the field. Even though the focus of future research may be on butanol as opposed to ethanol, the current research performed on ethanol production can easily be applied to butanol production.

1.6 Challenges in Syngas Fermentation

The syngas-fermentation platform has a promising future for ethanol and other biofuels (e.g. butanol). However, more research needs to be performed in order to improve the current process. One major issue is mass transfer limitations of syngas in the bacterial media. Future research needs to be performed in order to increase mass transfer rates while still keeping production costs feasible. This includes reactor design and modeling endeavors. In addition to reactor performance, another issue that needs to be addressed is ethanol tolerability of fermenting microbes (Abubackar, et al. 2011). Increasing tolerability would enable the microbes to produce more ethanol per volume. Still another issue besides ethanol tolerability and reactor design is electron usage. Current calculations show that the use of CO is more thermodynamically favorable than H_2 for supplying electrons (Hu 2011). This leads to low carbon conversion and an overall low efficiency for the process since CO used for electrons reduces the CO available for product. Future research needs to focus on improving syngas fermentation efficiency by understanding and collecting more data on H_2 and CO as electron sources so that methods can be developed to provide greater carbon conversion to ethanol. If these problems can be addressed,

the syngas fermentation platform can potentially become even more valuable in the quest for alternative energy sources. This work will aim to address some of the issues related to mass transfer and electron usage in order to make syngas fermentation a more viable option for renewable fuel production.

1.7 Research Objectives

1.7.1 Objective 1: Mass Transfer

The first objective of this study was to assess the hypothesis that a hollow fiber reactor (HFR) has much better mass transfer characteristics than other common bioreactors and, as a result, will enhance the syngas fermentation process by increasing production rates, cell concentrations and cell retention. This first objective was divided into two tasks. The first task (Task 1) was to perform an in depth reactor comparison that compared mass transfer rates and fermentation abilities. The reactors that were compared were a trickle bed reactor (TBR), HFR, and continuous stirred tank reactor (STR). This work was done in collaboration with Oklahoma State University, a land-grant university performing similar research. The TBR and CSTR work was performed by students at Oklahoma State University. The HFR work was performed at Brigham Young University. The two schools shared data and collaborated in order to establish conditions necessary for reactor comparison. This work compared reactors first in the absence of cells, based on simple mass transfer of oxygen, and then a complete comparison involving cell growth and product formation. The second task (Task 2) was to devise a method to measure the mass transfer coefficients of H_2, and CO in one of the HFRs studied in Task 1 and compare the measurements to the a mass transfer model based on mass transfer theory.

1.7.2 Objective 2: Electron Usage

Besides mass transfer, one other difficulty with syngas fermentation is understanding the role that CO and H_2 play as electron donors and how different CO and H_2 ratios affect syngas fermentation. In addition to electrons from CO and H_2, electrodes can also be used to augment the supply of electrons or provide the only source of electrons for syngas fermentation. Thus, the second objective was to assess the hypotheses that gas composition ratios affect electron usage and that the concentrations of methyl viologen (MV) in its three redox states can be predicted based on thermodynamics. In order to do this, the objective was split into two tasks. The first task of the second objective (Task 3) was to analyze the use of electrons from H_2 and CO by *C. ragsdalei* and to study the effects of these two different electron sources on product formation and cell growth. The second task of the second objective (Task 4) was to measure MV^+ versus potential and compare to a thermodynamic model that includes the effect of Cl^- and other relevant MV species. Assessing the state of MV can help provide additional insights into the role of MV as a potential electron carrier in syngas fermentation.

2 Literature Review

The purpose of this dissertation is to aid future researchers in designing more efficient syngas fermentation systems for the production of biofuels. The following literature review will outline the current state of syngas fermentation and the key aspects of syngas fermentation that remain a challenge in production of biofuels.

2.1 Gasification

Syngas fermentation relies heavily on the current state of gasification methods. The technology leading to current gasification methods has been developing since its early inception in the late seventeenth century (Hamper 2006). Though the industry declined due to natural gas and electrical transmission lines, it has survived, and is now a successful industry (GTC 2011). Gasification is a process that converts carbon-containing feedstock to a synthesis gas (syngas) that can then be used for any number of purposes, one of them being syngas fermentation.

The chemical conversion attained in the gasification process can be summarized into three main reactions: partial oxidation, complete oxidation, and the water gas reaction, shown in Equations 2-1 through 2-3 (McKendry 2002b).

Furthermore, carbon monoxide (CO), hydrogen (H_2) and water (H_2O) can undergo further reactions shown in Equations 2-4 and 2-5 so that the product gas contains a mixture of CO, carbon dioxide (CO_2), methane (CH_4), H_2, and H_2O. The composition of this mixture varies depending on the type of gasifying agent and the feedstock. Different gasifying agents include air, steam, steam/air, oxygen/steam, oxygen/air, oxygen/air/steam and hydrogen.

Partial oxidation	$C + \frac{1}{2}O_2 \leftrightarrow CO$	**(2-1)**
Complete oxidation	$C + O_2 \leftrightarrow CO_2$	**(2-2)**
Water gas reaction	$C + H_2O \leftrightarrow CO + H_2$	**(2-3)**
Water gas shift reaction	$CO + H_2O \leftrightarrow CO_2 + H_2$	**(2-4)**
Methane formation	$CO + 3H_2 \leftrightarrow CH_4 + H_2O$	**(2-5)**

There are two main types of gasifiers; fixed bed and fluidized bed. Fixed bed reactors have a simple design in which the gasifying agent is blown over a fixed bed of combustible material. However, fixed bed reactors generally produce producer gas with a lower calorific value and high tar content (McKendry 2002b).

The terms, producer gas, synthesis gas, and syngas are generally used interchangeably. This work uses the term, syngas; referring to both the gas produced from gasification of carbonaceous material and synthetic gas mixtures containing H_2, CO and CO_2. Fluidized bed reactors have overcome some of the shortcomings of the fixed bed reactor. In the fluidized bed gasifier, a fine-grained feed is introduced to the gasifying agent producing a fluid like mixture. Fluidized bed reactors are the gasifier of choice for lignocellulosic biomass because of its low

gasification temperatures and the uniform temperature distribution (Alauddin, et al. 2010; McKendry 2002b). There are many types of fluidized bed reactors, but the two chief types are the bubbling fluidized bed (BFB) and the circulating fluidized bed (CFB).

Because of the great variety of feedstocks, gasifying agents, and gasifiers, synthesis gas can vary greatly in composition. Table 2-1 lists several different feedstocks and the resulting syngas compositions using BFBs and CFBs.

Table 2-1. Syngas compositions of various biomass types and reactors. [1](Cao, et al. 2006), [2](Turn, et al. 1998), [3](Pan, et al. 2000), [4](Weerachanchai, et al. 2009), [5](Rapagna, et al. 2000), [6](Mansaray, et al. 1999), [7](Miccio, et al. 2009), [8](Bingyan X. 1994), [9](Li, et al. 2004).

Reference	1	2	3	4	5	6	7	8	9
Fluidized bed type	Bubbling	Bubbling	Bubbling	Bubbling	Bubbling	Bubbling	Bubbling	Circulating	Circulating
Biomass type	Wood Sawdust	Cedar Wood	Pine Chips / Coal	Larch Wood	Almond Shell	Rice Husk	Spruce Wood Pellet	Wood Powder	Sawdust
Gas yield (m^3 gas/kg biomass)	2.99	1.90	2.46	1.55	1.10	1.05	1.20	1.93	2.35
Syngas composition									
vol% CO	9	16	17	8	33	20	18	17	18
vol% CO_2	13	16	8	29	12	14	14	16	16
vol% Cn compounds	6	6	2	7	12	5	1	0	3
vol% H_2	9	11	13	56	44	4	30	16	7
vol% N_2 + other	62	51	59	0	0	57	0	43	55

Table 2-1 shows the varying compositions of syngas produced from gasification of different biomasses. During gasification, about 10 percent of the original carbon mass can be lost to tars. Also, the CO_2 percentage varies depending on the method and feedstock. CO_2 is not as readily used in fermentation and is essentially lost carbon unless H_2 is efficiently utilized. In order for higher carbon conversion, gasification still needs to be enhanced in order to reduce carbon losses to tar and CO_2 as much as possible. This has been one of the goals of gasification

since its inception; however, there is still much research that needs to be performed in order to optimize the gasification process.

2.2 Syngas Impurities

Thus far, syngas has only been discussed in terms of its major components, H_2, CO and CO_2. However, raw syngas straight from the gasifier will include a greater number of components. The gaseous species are mainly CO, CO_2, H_2, H_2O, and CH_4 (Higman and Burgt 2003). Besides these there are also a number of other constituents: carbon-containing species like methane, acetylene, ethylene, ethane, benzene; sulfur-containing species like hydrogen sulfide, sulfur dioxide, and carbonyl sulfide; nitrogen-containing species like ammonia, nitrogen, hydrogen cyanide; chlorine compounds; tars; ash. In his dissertation, Xu reported the highest impurity values measured in syngas generated from biomass, coal, and co-feeding of biomass and coal (Xu 2011). Methane impurities can be as high as 7% and 15% for coal and biomass gasification respectively (Babu 2005; McIlveen-Wright, et al. 2006). Ethylene can be as high as 5% for biomass and coal gasification. C_2 to C_{10} carbons can also be in the range of 0.02% to 2% (Xu 2011). Besides carbon species, NH_3, H_2S, SO_2, and NO_x, can be as high as 0.28%, 1.0E-4%, 0.06%, and 0.1% respectively. Many of these impurities are known inhibitors of enzymes found in the Wood-Ljugdahl pathway. For example, NH_3 inhibits the alcohol dehydrogenase enzyme (Xu 2011).

Besides the known effects on individual enzymes, the effects of two of these soluble components—ammonia and benzene—on one acetogenic bacteria, *Clostridium ragsdalei*, have been studied. Ammonia, when dissolved in water, very quickly becomes NH_4^+. In order to measure the effects of NH_4^+ on *C. ragsdalei*, one study measured cell density with varying levels of NH_4^+ (Xu 2011). This study showed that at very low [NH_4^+] (0-50 mM), cell growth was not

adversely affected. Cell growth inhibition increased slightly when [NH_4^+] was varied from 100-200 mM, but when [NH_4^+] reached 250 mM, cell growth was significantly inhibited. The inhibitory effects of the ammonium ion were shown to be due to the osmolarity of the solution increasing as opposed to a direct effect of the ammonium ion. In another study on *C. ragsdalei* using benzene as the contaminant, cell growth and ethanol production were greatly inhibited with increasing concentrations of benzene (Xu 2011).

2.3 Syngas Fermentation Reactors

Many different reactors can be used for syngas fermentation. These include, but are not limited to, stirred tank reactor (STR), bubble column reactor (BCR), gas spargers, membrane bioreactor (MBR), and trickling bed reactor (TBR) (Abubackar, et al. 2011). Of the membrane bioreactors there are also several subclasses including; hollow fiber reactor (HFR), stacked array bioreactor (SAB), modular membrane supported bioreactor (MMSB), and horizontal array bioreactor (HAB) (Abubackar, et al. 2011). There are advantages and disadvantages to all of the reactors. In order to optimize biofuel production from syngas fermentation the optimal reactor must be chosen. For ethanol production, there have been several studies of bioreactors using different organisms. In a review regarding biological conversion of CO, the authors provided a comparison between several of these biological reactors with different organisms and studies (Abubackar, et al. 2011). In this review, the highest concentration of ethanol was achieved by *C. ragsdalei* in the modular membrane supported bioreactor. Using this same microbe in a stirred tank bioreactor, the process took 59 days to reach 25 g/L of ethanol, whereas *C. ljungdahlii* took only 1 day in the same reactor to reach half of this level of ethanol. However, it should be noted that product formation is a strong function of cell concentration. This review provides a good comparison between different fermentation studies; however, it cannot be used to compare

ethanol production between the reactors. The reason for this is because there are too many confounding variables. For example, it is evident that the organism used for fermentation has a large effect on ethanol production. The differences between these organisms and their metabolism make it difficult to see the effects of the different reactors.

Also, in the experiments that compare the same organism, the media is not necessarily held as a constant. For example, in two studies that use *C. ragsdalei* as the fermenting organism and a membrane bioreactor there is a slightly different media composition between the studies. Tsai et al. used 30 ml of mineral solution and 5 ml reducing agent per liter of media in their membrane bioreactor (Tsai, et al. 2009d). Hickey et al. used 25 ml of mineral solution and 2.5 ml reducing agent per liter of media in their moving bed membrane bioreactor (Hickey 2009). These slight changes in media composition can have large effects on ethanol production and cell concentration. Another confounding factor is the gas retention time, flow rates, pressure, composition, and culture elapsed time. A more efficient comparison that has yet to be done is a multi-bioreactor study that uses the same organism, media composition, syngas composition and flow rate per liquid volume.

2.4 Syngas Fermentation Mass Transfer

In order for the syngas to be utilized by the fermenting bacteria, it must be present in the fermenting media. For sparingly soluble gases like CO and H_2, mass transfer can become a limiting factor in syngas fermentation unless high mass transfer rates are achieved in the fermentation reactor. Apparent mass transfer coefficients (which assumes the liquid concentration of CO/H_2 is zero) for several different reactors were gathered by Munasinghe et al. (Munasinghe and Khanal 2010b). A summary of these results are shown in Table 2-2. Of the reactors shown here, the trickle bed reactor and the stirred tank reactors have the highest

apparent mass transfer coefficients. Though stirred tank reactors can achieve relatively high mass transfer rates, they are more difficult to scale up because of power considerations required for the agitators.

Table 2-2. Mass transfer coefficients for different reactors.

Reactor configurations	Agitation Speed	Gaseous substrates	Apparent mass transfer coefficient (h^{-1})
Trickle bed	n/a	Syngas	22
STR	n/a	Syngas	38
STR	200	CO	14.2
STR	300	Syngas	31 for CO, 75 for H_2
STR	300	Syngas	35 for CO
STR	300	Syngas	28.1 for CO
STR	450	Syngas	101 for CO
Stirred tank	200	CO	90.6
Stirred tank	300	Syngas	104 for CO, 190 for H2
Packed bubble column	n/a	Syngas	2.1
Trickle bed	n/a	Syngas	55.5
Trickle bed	n/a	Syngas	121 for CO, 335 for H2
Trickle bed	n/a	Syngas	137 for CO
Batch stirred tank	n/a	CO	7.15
STR	300	CO	14.9
STR	400	CO	21.5
STR	500	CO	22.8

Table 2-2 Continued.

STR	600	CO	23.8
STR	700	CO	35.5
Bubble column	n/a	CO	72
STR	400	CO	10.8 to 155
STR	500	Syngas	71.8
Column diffuser	n/a	CO	2.5 to 40.0
20-lm bulb diffuser	n/a	CO	31.7 to 78.8
Sparger only	n/a	CO	29.5 to 50.4
Sparger with mechanical mixing	150	CO	33.5 to 53.3
Sparger with mechanical mixing	300	CO	34.9 to 55.8
Submerged CHFM module	n/a	CO	0.4 to 1.1
Air-lift combined with a 20-lm bulb diffuser	n/a	CO	49.0 to 91.1
Air-lift reactor combined with a single point gas entry	n/a	CO	16.6 to 45.0

Fermentation systems can become mass transfer limited if mass transfer rates are not high enough to support the kinetics of the cell. Depending on cell density and cellular activity, syngas usage can vary, but typical reported values are in the range of 0.5 mol/g_{cell}/day for CO and 0.4 mol/g_{cell}/day for H_2 (Frankman 2009). Using these rates, the highest mass transfer coefficient in Table 2-1 for CO which is 137 h^{-1} and the mass transfer equation from Chapter 4 (Equation 4-16)

the system becomes mass transfer limited at a cell concentration of about 1 gram per liter. This is a relatively low concentration for an economical syngas fermentation system. In order to achieve the best carbon utilization, mass transfer should be enhanced so that the only remaining limits are the thermodynamics and kinetics in the cell. One reactor not shown here is the HFR. Though literature does not list mass transfer coefficients for a flow-through HFR with CO and H_2, there are many reported values for CO_2 and O_2. Comparing these values with other reactors, the HFR may be the reactor of choice for high mass transfer. However, there has been relatively little research performed in using a HFR for syngas fermentation. There may be other aspects of the HFR that are not optimal for syngas fermentation.

2.5 Hollow Fiber as a Bioreactor and Mass Transfer Calculations

In syngas fermentation, mass transfer is important because of the use of sparingly soluble gases like CO and H_2. One reactor that has specifically high mass transfer rates is the HFR. The mass transfer resistance through the hollow fiber module can be split into a sum of three resistances through the gas boundary layer, membrane boundary layer, and liquid boundary layer. However, when considering mass transfer limitations in a hollow fiber system, only the membrane and liquid boundary layer significantly contribute to the overall mass transfer resistance. The mass transfer rates for HFRs are usually high because of the large surface area to volume ratio of these reactors and the high mass transfer coefficients of the membranes. Some HFRs that can be commercially purchased include membrane permeability for various species. If the value has not been measured by the manufacturer for a specific HFR, then it must be measured experimentally. Kim et al. provide a statistically robust method for calculating membrane mass transfer coefficients from an overall mass transfer coefficient (Kim, et al. 2008). This study uses a Wilson-plot method with a resistance in series model to calculate membrane

resistance. Besides the membrane mass transfer coefficient, the mass transfer coefficient through the liquid boundary layer must also be determined experimentally; this is a function of the Reynolds number of the liquid being used. Thus, if an overall mass transfer coefficient is desired, it ultimately has to be measured experimentally.

Because of the use of HFRs in waste management, there is a considerable amount of data on CO_2 mass transfer rates for various different membranes and reactors. One such study calculates the overall mass transfer coefficient of CO_2 for several microporous hydrophobic membranes (Korikov and Sirkar 2005). Values are reported for PTMSP, Celgard 2400 bar, Saint-Gobain, and Modified Celgard 2400. Another study models CO_2 absorption for a gas-liquid membrane contacting process by a multistage cascade reactor (Atchariyawut, et al. 2008). This data and other reported data is valuable for the CO_2 in syngas fermentation, especially since CO_2 is much more soluble in liquid as compared to CO and H_2. However, there is a lack of data available for H_2 and CO in HFRs. Thus, there is a need for further mass transfer analysis to be performed with syngas on common HFRs in order to be able to do an initial comparison of reactors based solely on mass transfer.

Besides high mass transfer rates, there are specific advantages to a membrane system. One such advantage is the ability for cells to be immobilized. *C. ragsdalei* can efficiently be immobilized in membrane systems. Hickey et al. has shown that a biolayer of *C. ragsdalei* grew on the exterior surface of the hollow fibers in their system (Hickey, et al. 2010). In order to achieve this, the cells were initially circulated on the shell side and then the shell side was pressurized, forcing the liquid into the lumen side thus forcing the cells onto the fibers. Afterwards, the syngas flowed through the shell side to expose the cells to the syngas directly, while liquid media circulated on the lumen side. The system was initially operated in batch mode

for three days and then switched to continuous operation for 406 hours. The fibers were then viewed under an electron-scanning microscope revealing a biolayer 30-40 μm thick. A biolayer was efficiently immobilized onto the fibers, however, ethanol production decreased to 0.4 g/L at 193 hours and eventually 0 g/L after 406 hours. From this experiment we can see that the experimental setup necessary for the formation of a biolayer resulted in very low ethanol production. This could be a result of the biolayer being separated by a porous membrane form the liquid media.

In another experiment by Hickey et al., media with active *C. ragsdalei* was continuously circulated on the shell side while syngas flowed through the lumen side (Hickey, et al. 2010). The media was replenished at a rate of 15 ml/hr. After 480 hours the withdrawn fermentation liquid contained 10 g/L of ethanol. In this experiment the authors do not mention biofilm formation on the exterior surface of the fibers as with the first experiment.

In another experiment by Tsai et al., a polysulfone hollow fiber unit was inoculated with an active culture of *Clostridium carboxidivorans* (Tsai, et al. 2009d). The media was continuously circulated for 480 hours along with intermittent "purging" of biomass build up on the fibers. The authors also do not mention the formation of a biolayer on the fibers. Based on the studies by Hickey et al. and Tsai et al. there is a lack of evidence of biolayer formation when the cells are exposed to circulating liquid media. Based on these studies, further experiments need to be conducted that show the conditions necessary for biolayer formation in syngas fermentation. This information is necessary because ethanol production predictions rely on accurate cell density approximations. Also, if an accurate model is to be designed for hollow fiber syngas fermentation, the biolayer must be described in full.

As mentioned previously, HFRs have also been used heavily in the waste management industry to remove toxins (Yun, et al. 1993) and to produce fuel gasses from waste using microbes immobilized on the membranes (Gassanova, et al. 2006). When HFRs are used with immobilized microbes, the dynamics of the system change dramatically. This type of a system has been successfully modeled. In a 2003 publication, Zheng at al. compared the several different mass transfer models in parallel flow HFRs (Zheng, et al. 2003). This study compared literature correlations with real hollow fiber data to conclude which model is best. This study however was not concerned with relating HFRs to traditional bioreactors.

Another study by Kleinstreuer et al. presented an economical computer simulation model for HFRs (Kleinstreuer and Agarwal 1986). In this study the authors successfully compared their model with two laboratory case studies. The model developed in this study is a general model. The authors mentioned that future work will include simulation of specific bioreactors for different systems. A later study was performed that reviews the development of several different mathematical models for axial-flow non-mammalian bioreactors (Brotherton 1996). The models reviewed in this literature can be applied to syngas fermentation. A model has yet to be devised that accurately models gas usage for syngas fermentation in a HFR. A model of this proportion would aid in optimizing fuel production from syngas fermentation.

Based on this review of the HFR as a bioreactor, it is unclear whether or not acetogenic bacteria form a true biofilm in syngas fermentation in an HFR. It is also evident that in order to predict the mass transfer capabilities of the HFR as a syngas fermentation reactor, there needs to be more research into predicting the mass transfer coefficients for syngas species such as H_2 and CO in an HFR gas liquid-contact system. Also, a mass transfer model aimed at predicting the

mass transfer capabilities of the HFR in syngas fermentation would aid future researchers in choosing an appropriate reactor.

2.6 Electron Usage in Syngas Fermentation

Gasification, impurities, and mass transfer all represent large bottlenecks in syngas fermentation that must continue to be explored. In addition to these challenges, there is another issue in syngas fermentation related to electron usage. In order to reduce the CO and CO_2 to ethanol and butanol, electrons must be provided by either H_2 or CO. The most carbon efficient electron usage would be for all electrons to come from H_2 so that all carbon can be converted into product. In order to evaluate whether or not this is possible, a literature review was done relating specifically to electron usage in syngas fermentation and other means to provide electrons besides the traditional H_2 and CO routes.

2.6.1 Electrons from CO and H_2

Acetogenic bacteria produce ethanol and acetic acid via the Wood Ljungdahl pathway, as shown in Figure 2-1. The methyl branch of this pathway produces the methyl group of acetyl CoA through several reduction reactions. The carbonyl branch provides the carbonyl group in the acetyl CoA by reducing CO_2 to CO or by using CO directly. Acetyl CoA is then used to produce ethanol, acetic acid, and other products (Wood, et al. 1986). In the methyl branch of the Wood-Ljungdahl pathway, six electrons and one ATP are used to convert CO_2 into a methyl moiety that combines with CO from the carbonyl branch and coenzyme A to form acetyl-CoA. In the carbonyl branch, CO can either be provided from a gas source or can be produced by CO_2 reduction via two electrons. The electrons in the methyl and carbonyl branch can be provided by H_2 or CO via electron carriers that have been reduced.

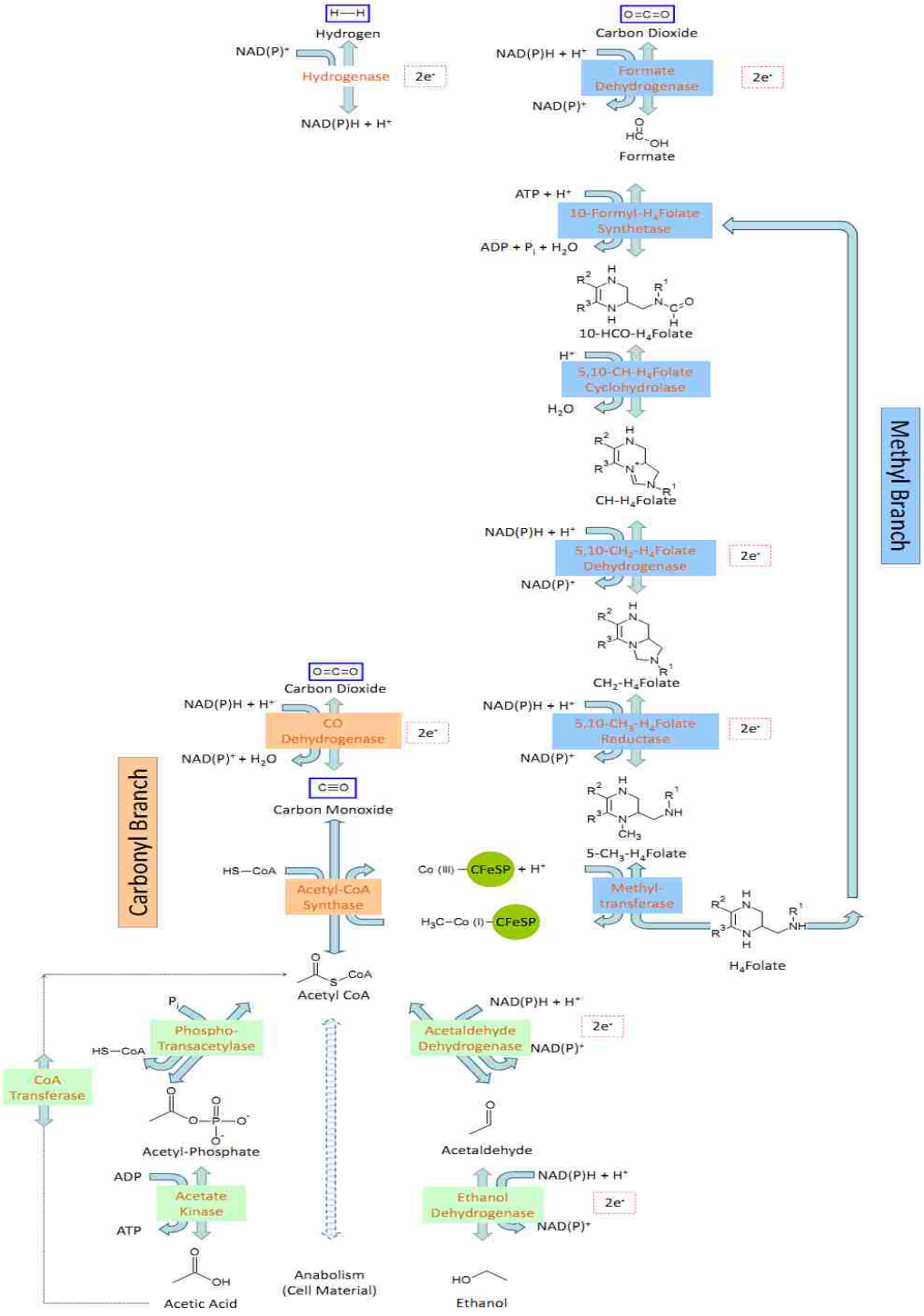

Figure 2-1. The Wood-Ljungdahl pathway (Hurst and Lewis 2010; Ljungdahl 1986).

In his dissertation, Peng Hu performed an in-depth thermodynamic analysis in order to address the question of electron production between CO and H_2 during typical syngas fermentation conditions (Hu 2011). In this analysis transformed Gibbs free energies were used to compare CO and H_2 as electron donors. It was shown that depending on reactor conditions, H_2 can become more thermodynamically favored to provide electrons. However, CO always has a lower Gibbs free energy than H_2, indicating that it will always be the preferred species for electron donation.

Other studies have confirmed the thermodynamic favorability for CO, as opposed to H_2, for providing electrons. In one study *C. ljungdahlii* was used to ferment syngas while measuring CO, H_2 and CO_2 consumption rates (Younesi, et al. 2005). The conclusion was that H_2 was either not used at all, or only used after CO was completely depleted, depending on reaction pressures. Another study using *C. carboxidivorans* to ferment biomass generated syngas, showed that both CO and H_2 were used during the growth phase of the cells (Datar, et al. 2004). The reason for this discrepancy could be the differences in reactor conditions changing the thermodynamic favorability of H_2 reduction. In any case, there is a lack of data to confirm the rates at which CO and H_2 are consumed, specifically in a controlled environment.

In another study performed by Hurst et al., it was shown that the greater the partial pressure of CO (between .35 and 2 atm) the larger the overall growth and the larger the potential for growth for *C. carboxidivorans* (Hurst and Lewis 2010).The study went on to show that when the partial pressure of CO was between .35 and .70 atm the amount of acetic acid produced at similar cell concentrations was higher than when the partial pressure was between 1.05 and 2 atm. When ethanol production was compared, it was observed that as the partial pressure of CO increased the production of ethanol began early and was higher overall. It is interesting to note

that at partial pressures of 1.35 and 2 atm the acetic acid production decreased and the ethanol production increased. The authors explain this by the fact that CO can be used as an electron donor. The amount of electrons donated would affect the metabolic pathway and cause the change in product formation that was seen because the excess electrons from CO would be used to convert acetic acid to ethanol once the cells were grown. This effect of increased electron equivalents is also shown in Chapter 6 of this work. Although the study was not able to determine the reason behind the increased growth potential of the cells at high partial pressures it was determined that CO was not a toxin to the cells.

In another study performed on *C. ragsdalei* it was shown that cells grown on H_2, CO_2, and N_2 grew more slowly than cells grown with standard syngas (30% H_2, 30% CO_2, 40% CO). Yet the cells grown with 30% H_2, 30% CO_2, and 40% N_2 yielded more ethanol and acetic acid per cell concentration (Hoeger 2012). It was concluded that the energetically unfavorable conditions associated with the absence of CO, in the metabolic pathway, would explain the decrease that occurred in cell growth. It was also concluded that decrease in growth meant that the reduction of CO_2 was a rate limiting step which could be explained by the high amount of energy required for reduction. This study also acknowledged the fact that CO is a known hydrogenase inhibitor and it was hypothesized that the lack of CO would in fact allow more product formation due to the performance of hydrogenase. In essence it was established that cells could be grown, and products produced, using only H_2 and CO_2.

Based on the above studies there is not yet a full understanding as to the effects of H_2 and CO on growth and product formation, especially when both gasses are used together. It would be beneficial to analyze the effects of these gasses when they are both present and available to the cell to obtain a greater understanding as to the electron usage by these gases.

2.6.2 Electrons from Electrodes and Mediators

In addition to providing electrons from CO and H_2, electrodes can also be used to augment the supply of electrons or provide the only source of electrons (Aulenta, et al. 2007; Lymar and Hurst 1994; Marshall and May 2009; Park and Zeikus 1999; Wang, et al. 2011). While some cells can directly accept electrons from an electrode, most cannot (Nevin, et al. 2010; Nevin, et al. 2011b). Therefore, in order to transfer electrons to the cells, external electron mediators must be used. Some electron mediators that have been used in the past include methyl viologen (MV) (Lymar and Hurst 1994), neutral red (Park and Zeikus 1999), AQDS (Bond, et al. 2002), resazurin (Sund, et al. 2007), and phenosafranin (Strehlitz, et al. 1994). Though electron mediators can provide electrons, in some cases they may be toxic to the cells (Panneerselvam, et al. 2010), become inactive (Damian 2007) and have low energy efficiencies (Schroder 2007).

Bioelectric reactors (BERs) may be of great use for syngas fermentation. The ultimate goal of using BERs in syngas fermentation is to provide electrons to the cells via an electrode as opposed to providing electrons via H_2 or CO. This additional supply of electrons could potentially increase the carbon conversion efficiency through reducing the amount of electrons provided by CO and/or enabling unused CO_2 to be further converted to product through the Wood-Ljungdahl pathway (Figure 2-1). However, in order for this to be accomplished much more work needs to be performed with BERs and electron mediators.

2.6.3 Methyl Viologen as a Mediator

MV is an effective electron mediator that is frequently used in biological systems and has been shown to increase ethanol and butanol yields when added to cell fermentations (Aulenta, et al. 2007; Erbes and Burris 1978; Kim, et al. 1999; Lymar and Hurst 1994; Rao 1986; Tashiro, et

al. 2007). MV has also been studied extensively for bioelectrical reactor purposes (Cheng, et al. 2003; Kundiyana, et al. 2010; Park, et al. 1995). These studies include kinetic analyses, thermodynamic analyses, and diffusional analyses in water. However, one drawback to MV is that it has been reported to be toxic to cells and inactivate enzymes (Kim and Yun 2004; Panneerselvam, et al. 2010). However, there are many other studies that report no toxicity. Thus, the conclusion that all extracellular MV species are toxic to cells may not be valid. The reason for this discrepancy may be that the redox state (MV^{2+}, MV^{+}, MV^{0}) of MV used in the studies is not always clearly stated. When MV is sold commercially it is most often sold as $MVCl_2$. $MVCl_2$ dissociates into MV^{2+} and Cl^{-} (Monk and Hodgkinson 1998). MV^{2+} can also react with NADH inside the cells forming MV^{+} and MV^{0} (Kim and Yun 2004). Thus, although $MVCl_2$ may have been the only species added to the system, all three redox states of MV could be present in the solution due to the redox reactions in the cell and reactions with an electrode when one is present.

As mentioned above, MV is purchased in the form of $MVCl_2$. When dissolved in water the following equilibrium is established, $MVCl_2 \leftrightarrow MV^{2+} + 2Cl^{-}$. Thus, depending on the amount of surface sites on the electrode, the amount of MV^{2+} may be limiting the kinetics of the electron transfer capabilities of the system. Using a thermodynamic model established for predicting the amount of MV^{+} present in a BER using MV as an electron carrier, Chen makes predictions about the relation of electrode potential to MV species (Chen 2012). Predictions like Chen's are important for reactor designs using electrodes so that redox states of MV can be controlled experimentally. Controlled redox states of MV provide an opportunity to assess toxic effects of MV on cellular systems when seeking to use MV to augment electron availability via electrodes.

Based on this electron usage review, the effects of H_2 and CO as electron donors on cells is still unclear. Further studies on the effects of H_2/CO ratios in a syngas fermentation system would aid in analysis of the effects of electron equivalents from different sources on cells. Also, if electron carriers such as MV are going to be used in conjunction with electrode systems, the actual state of MV is very important. Chen provided groundwork for modeling the state of MV in electrode systems. However, her work did not take into account the most accurate $MVCl_2$ equilibrium values and did not include other species of MV besides the three redox states. Thus, there needs to be further work done to provide a more accurate analysis of MV to be used in syngas fermentation electrode systems.

2.7 Conclusions

Syngas fermentation relies on the technology of gasification. This is a process that has been developed over the centuries but still has room for improvement for syngas fermentation purposes. Syngas impurities are one issue that can be considered a bottleneck in the process. Another bottleneck is the mass transfer limitations that can be present in syngas fermentation reactors. One possible reactor that may be useful in overcoming these limitations is the HFR. In other applications, mass transfer analyses have been performed on HFRs. Mass transfer models for a HFR can provide guidance in overcoming mass transfer limitations in syngas fermentation by providing the ability to predict when a system may become mass transfer limited. Additionally, low mass transfer rates may limit the amount of electron equivalents that are available to cells in syngas fermentation. In order to further aid in mass transfer predictions, this work aimed to analyze the mass transfer in several HFRs and compared them to other reactors. Also, the mass transfer coefficients for H_2 and CO were measured and validated by mass transfer models. It is clear that H_2/CO ratios effect the cells based on thermodynamic availability of

electrons, thus this work performed an in depth analysis on varying H_2 and CO ratios to further decipher the effect of H_2/CO ratio on cells and product formation. One other way to deliver electron equivalents is in a bioelectric reactor that provides equivalents either directly via an electrode or by the use of electron mediators such as MV. MV is used frequently in biological systems, but it has not been well studied in order to accurately predict its electron transfer capabilities in a syngas fermentation system. This work derived a thermodynamic model for MV as an electron carrier, taking into account all relevant species of MV and appropriate equilibrium values. This model was validated by experimental data.

3 Hollow Fiber Reactor Comparison

3.1 Introduction

The dominant biofuel in the U.S. is ethanol made via yeast-based fermentation of corn. In, fact, sugar and starch based feedstocks account for nearly 90% of the world bioethanol production (Abubackar, et al. 2011; Aulenta, et al. 2007). However, due to limitations in corn supply, potential interference with the food chain, and the low energy efficiency of the process, "second generation" biofuel processes using biomass feedstocks are being developed. These feedstocks include agricultural residues, wood, municipal solid waste and dedicated energy crops such as switchgrass. These second generation biofuel processes can be divided into three different platforms. The first platform is a biochemical process that produces biofuels, such as ethanol, by fermentation of simple sugars produced from lignocellulosic biomass. The sugars are produced after pretreatment of the biomass using methods such as acid, ammonia, steam, or alkaline chemicals in order to expose the hemicellulosic and cellulosic components to enzymes (Lynd 1996; Park and Zeikus 1999). This is followed by hydrolysis of the hemicellulose and cellulose using cellulases into C5 and C6 sugars. Common yeast strains convert only C6 sugars into ethanol. However, genetically modified yeast and bacterial strains capable of metabolizing both sugars have been developed (Pessani, et al. 2011).

The second platform first converts the biomass into syngas (primarily H_2, CO, and CO_2) via gasification. The syngas is then converted to biofuels by a metal catalytic process such as Fischer-Tropsch Synthesis.

Though several industrial plants have been producing biofuels using Fischer-Tropsch Synthesis, there are still limitations due to high temperatures and pressures, low selectivity and catalyst poisoning (Abubackar, et al. 2011).

The third platform is a hybrid thermochemical-biochemical conversion of biomass into biofuels. The biomass is first converted to syngas via gasification. The syngas is then fermented to biofuels using acetogenic microorganisms (Liu, et al. 2011; Ukpong, et al. 2012b; Wilkins and Atiyeh 2011). Syngas produced from gasification of biomass is advantageous because it does not necessarily require a food source and it can be produced from hard-to-handle softwoods (Spath and Dayton 2003). One advantage of syngas fermentation over the saccharification-fermentation process (i.e. first platform noted above) is that the syngas utilizes all lignocellulosic components (cellulose, lignin and hemicellulose) in the biomass, leading to a greater potential for ethanol production from the same quantity of biomass. The lignin, which accounts for 15% to 30% of the biomass composition is not utilized in traditional sugar/starch fermentations (Sierra, et al. 2008). In addition, syngas fermentation can utilize biomass from various sources since the chemical composition differences between feedstocks are mostly eliminated in the gasification process. Predictions for syngas derived ethanol range from 70 to 105 gallons of ethanol per ton of dry biomass, and 55 gallons of ethanol per ton of municipal waste (Coskata 2012; Spath and Dayton 2003).

Although there are several positive aspects for syngas fermentation to biofuels, there are several bottlenecks that must be addressed to improve biofuel productivity and syngas conversion efficiency. These include gas-liquid mass transfer limitations (related to low solubility of CO and H_2 components of the syngas in the fermentation broth), low cell density, and enzyme inhibition by syngas components (Bredwell, et al. 1999). The gas-liquid mass

transfer is reported to be a limiting factor in syngas fermentation especially when the cell concentration is high (Abubackar, et al. 2011; Meyer, et al. 1985).

Several types of reactors can be utilized for syngas fermentation although particular attention on how the reactor affects mass transfer and the associated gas utilization and biofuel productivity should be an important consideration in reactor selection. Reports on various bioreactor configurations used in syngas fermentation have been summarized (Bredwell, et al. 1999; Munasinghe and Khanal 2010c; Ungerman and Heindel 2007). It was reported that a trickle-bed reactor (TBR) achieved higher CO conversion compared to both a stirred tank reactor (STR) and a packed bubble column reactor in biological production of methane from syngas (Meyer, et al. 1985). The TBR can minimize the liquid resistance to mass transfer because a very thin liquid film is in contact with the gas. In addition, the volumetric mass transfer coefficient of the STR was 14-fold higher than in the packed bubble column reactor. STRs, especially continuous STRs (CSTR), are often used in industrial fermentations because of their good mixing capability and high mass transfer rate although power requirement for scale-up can be an issue. A common approach to enhance the mass transfer in STRs is to increase the impeller speed which breaks up large bubbles into smaller ones, thus increasing the interfacial area for mass transfer. However, the increase in the impeller speed increases the power to volume ratio, which is not economically feasible for large reactors due to high power cost (Bredwell, et al. 1999). To offset the power cost associated with scale-up, micro-bubbles can be employed to improve the mass transfer (Abubackar, et al. 2011). Mass transfer can also be improved by using hollow fiber reactors (HFRs) (Atchariyawut, et al. 2008; Ebrahimi, et al. 2005; Monk, et al. 1999; Nerenberg and Rittmann 2004; Rao and Mutharasan 1986). HFRs can greatly improve mass transfer rates because of their large surface area to volume ratios.

Previous reports have presented mass transfer coefficients for different reactors (Monk, et al. 1999; Munasinghe and Khanal 2010a; Munasinghe and Khanal 2010c). To our knowledge, only one other study acquires and compares mass transfer coefficients of syngas fermentation reactors in the same study (Munasinghe and Khanal 2010c). However, in this study, no liquid flow analysis is performed on the reactors. Also, there is some ambiguity in the mass transfer capabilities of the HFR. In one report, a submerged HFR is reported to have the lowest mass transfer coefficient and in another it is reported to be much higher than a TBR or STR (Monk, et al. 1999; Munasinghe and Khanal 2010c). Also, in these studies and others, it is unclear as to what volume is being used (i.e. the volume of the reactor or the volume of the system) in the volumetric mass transfer coefficient. This volume is crucial in comparing a reactor's mass transfer capabilities.

3.2 Research Objective

The objective of this study was to measure and compare the mass transfer coefficients of trickle-bed reactors (TBR), various types of hollow fiber reactors (HFR), and stirred tank reactors (STR) for syngas fermentation applications. Unlike previous studies, this study performed a mass transfer analysis on different reactors that included a liquid flow analysis. Also, the volumes used in the volumetric mass transfer coefficient were clearly specified and discussed. This work also aimed to clear up confusion as to why the HFR would seem to outperform other reactors in terms of mass transfer characteristics in one study, and not in another. For this study, the analysis was performed using O_2 as the gaseous mass transfer agent. Though the diffusivities of CO, CO_2, and H_2 in water at 37 ºC are 107%, 90%, and 212%, respectively, as compared to O_2 (Tamimi, et al. 1994a; Verhallen, et al. 1984b; Wise and

Houghton 1968), the comparison is still valuable in providing the relative mass transfer capabilities of each reactor at various operating conditions.

3.3 Materials and Methods

3.3.1 Trickle Bed Reactor and Stirred Tank Reactor

The TBR and STR studies were performed by students at Oklahoma State University. The setup and schematic for the TBR and STR is described by Orgill et al (Orgill, et al. 2013). The overall mass transfer coefficient of O_2 ($K_{tot}A/V_L$) in the TBR and STR was calculated according to Equation 3-1.

$$\frac{K_{tot}A}{V_L} = \frac{\ln\left(1 - \frac{C_L}{C_S}\right)}{t} \cdot \frac{V_S}{V_L} \tag{3-1}$$

where, K_{tot} is the total mass transfer coefficient (m/h), A is the mass transfer area (m^2), V_L is the volume of liquid within the TBR (m^3), V_S is the total volume of the system including sump and circulation loop (m^3), C_L is the bulk DO concentration in the liquid (mol/m^3), C_S is the saturated DO concentration (mol/m^3), and t is the time (h). Since C_L/C_S is a ratio, % DO in the bulk liquid was used in place of C_L and saturated % DO was used in place of C_S. The temperatures used in this study were 37 °C for the TBR and STR and 25 °C for the HFR. Preliminary studies with the TBR at 20 ºC showed that there was no statistical difference between the mass transfer coefficients at 37 °C and 20 °C (Orgill, et al. 2013). This is consistent with the theory in which the binary diffusion coefficient is proportional to temperature to the 3/2 power (Incropera, et al. 2006). Thus, the diffusion coefficient, which is the most influential

component of the variables in mass transfer, only increases by 6% when the temperature is raised from 25 °C to 37 °C. Therefore, results from all three reactors are compared in this study.

3.3.2 Hollow Fiber Reactor

The schematic of the HFR system is shown in Figure 3-1. The specifications of the five HFR modules tested are given in Table 3-1.

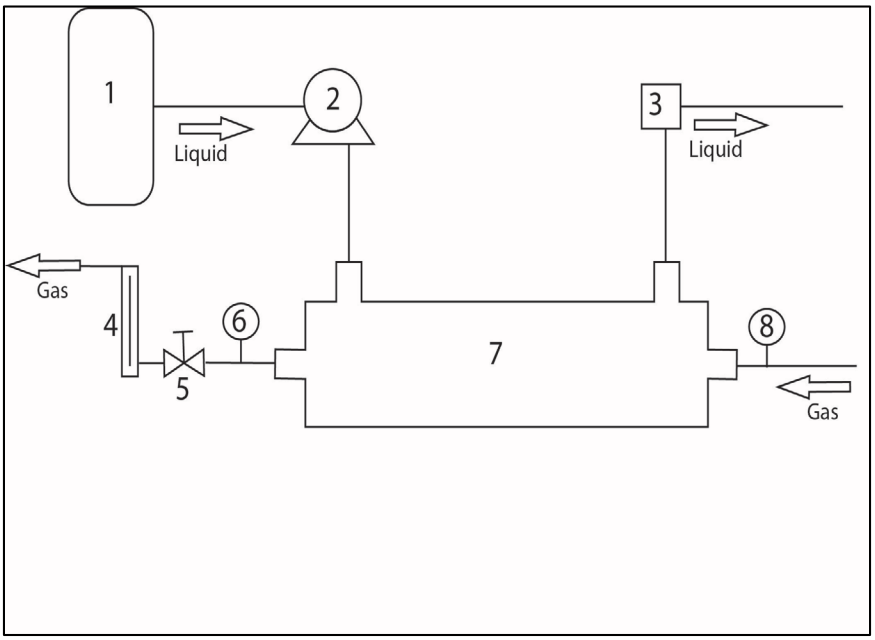

Figure 3-1. HFR mass transfer experimental setup. (1) water holding tank, (2) peristaltic pump, (3) DO probe, (4) rotameter, (5) gas outlet pressure control valve, (6) air outlet pressure transducer, (7) hollow fiber reactor, and (8) air inlet pressure transducer

Four of the hollow fibers were porous and one was non-porous. The porous modules ranged from hydrophilic to hydrophobic membranes to represent a wide variety of hollow fiber materials. A DO probe (alpha DO 500, Eutech, Aachen, Germany) was used to measure the outlet dissolved O_2 concentrations in DI water after one pass through the HFR. DI water in a 5 liter tank was purged with nitrogen until it reached 0% DO. The water was then pumped through the *shell* side of the hollow fiber reactor using a peristaltic pump (Model #7523-90, Masterflex, Vernon Hills, IL, USA). Compressed air (Airgas, Salt Lake City, UT, USA) containing 20.9 ± 0.1

% O_2 was passed through the fiber lumen of the HFR at a flow rate of 1 to 2 standard liters per minute (SLPM). The high gas flow rate was chosen to ensure a constant gas partial pressure across the fiber length so that variable gas compositional effects could be excluded in the analysis. However, as noted later, the gas flow rate does not significantly affect the mass transfer coefficient. Pressure in the lumen was regulated by a valve at the lumen outlet. Pressure transducers were placed at the inlet and outlet of the HFR lumen. A rotameter measured the outlet gas flow rate.

Table 3-1. Specifications of HFR modules used in the mass transfer experiments. [a]PS: polystyrene; PES: polyethersulfone; PP: polypropylene; PDMS: polydimethylsiloxane; FPS: Fresenius polysulfone. [b] Spectrum Laboratories, Inc. (Rancho Dominguez, CA, USA). [c] MedArray (Ann Arbor, MI, USA). [d] Fresenius (Ogden, UT, USA)

Module #	**1**	**2**	**3**	**4**	**5**
Model number	M1-500S-260-01N[b]	M12E-261-01N[b]	34101552[b]	PDMS-XA PermSelect 2500[c]	Optiflux F160NR[d]
Material[a]	PS	PES	PP	PDMS	FPS
Type	Hydrophilic/ Porous	Hydrophilic/ porous	Hydrophobic/ porous	Hydrophobic/ Non-porous	Hydrophilic/ porous
Fiber OD (μm)	660	1300	630	300	280
Fiber Thickness (μm)	80	150	75	50	40
Shell Priming Volume (V_L) (mL)	18.6	16.6	9.7	25.0	237.0
Fiber OD Surface Area divided by V_L (A/V_L) (m^{-1})	4366	2271	4361	10,000	9,198

Porous hydrophilic fibers absorb water into the pores in a process called wetting. In order to ensure that the porous hydrophilic HFRs were wetted to the same degree in each experiment, the porous hydrophilic HFRs were first wetted using a 50% (v/v) isopropyl alcohol/water mixture. To properly wet the fiber, 1 L of the alcohol solution was pumped through the fibers between 50-80 ml/min. To remove the alcohol solution, the alcohol was first drained from the HFR and then 200 mL of DI water was passed through the shell side and 200 mL through the fibers. This wetting procedure removed all air bubbles from the pores before the beginning of the mass transfer experiment. Though wetting the fibers lowers the mass transfer coefficient, it more properly replicates a gas-liquid contact system with a hydrophilic membrane.

The hollow fiber modules were tested at 25 °C at liquid flow rates ranging from 20 to 80 mL/min. Module 4 was tested with flow rates up to 400 mL/min because it has the highest A/V_L ratio. The liquid on the shell side was at atmospheric pressure. The gas inlet pressure was between 0.7 and 4.8 kPa above atmospheric pressure depending upon the pressure required for gas flow. Oxygen from the gas diffused through the pores and into the bulk liquid. The %DO in the liquid outlet was recorded by a DO probe. Data collection began after the system reached a quasi-steady state in the liquid, which was determined to be when the %DO did not change in a 5 min period. The time required for quasi-steady state at the liquid flow rates used was 40 min (for 20-30 mL/min), 30 min (for 30-80 mL/min), 20 min (for 80-140 mL/min), and 10 min (for >140 mL/min). After the system reached quasi-steady state, the % DO values were manually recorded every 30 sec for 5 min and the average was used. Runs were performed in triplicate for all modules.

For the HFR, a steady state mass transfer analysis was developed to calculate the overall mass transfer coefficient of O_2 ($K_{tot}A/V_L$). The mass balance equation used for calculation of the mass transfer coefficient in the HFR is shown in Equation 3-2.

$$\frac{K_{tot}A}{V_L} = \frac{C_{Lout} \cdot Q}{V_L \Delta C_{lm}} \tag{3-2}$$

where K_{tot} is the total mass transfer coefficient (m/h), A is the mass transfer area (m^2) based on the total fiber outer surface area for non-porous HFRs and the total outer pore area for the porous HFRs, V_L is the volume of liquid in the shell of the HFR (m^3), C_{Lout} is the quasi-steady state concentration of O_2 in the liquid outlet (mol/m^3), Q is the liquid volumetric flow rate (m^3/h), and ΔC_{lm} is the log mean O_2 concentration difference between saturated water at the partial pressure of the gas inlet and outlet and the dissolved O_2 concentrations in the liquid inlet and outlet (mol/m^3). For the HFR, K_{tot} includes the intrinsic mass transfer coefficient of the module membrane. Dissolved oxygen concentrations in mol/m^3 were determined by multiplying the % DO reading by the ambient pressure and the molar density of water and then dividing by the Henry's law constant. The value used for the Henry's law constant for oxygen was 4.57×10^6 kPa at 300 K (Incropera, et al. 2006).

3.4 Results and Discussion

3.4.1 Trickle Bed Reactor

The effects of bead size and various liquid and gas flow rates on the mass transfer coefficients ($K_{tot}A/V_L$) in the TBR for 3 mm and 6 mm beads are shown in Figure 3-2 and 3-3 with permission from Mamatha Devarapalli who performed this TBR study. The $K_{tot}A/V_L$ increased with an increase in the gas flow rate from 5.5 sccm to 130.9 sccm. However, $K_{tot}A/V_L$ values decreased with an increased liquid flow rate for a given gas flow rate. This is due to an

increase in the liquid holdup with increasing liquid flow rate. The gas flow rate had no effect on the liquid holdup in the TBR. However, increasing the liquid flow rate will displace the gas phase thus increasing the liquid hold up (Ranade, et al. 2011). For the range of liquid flow rates from 50 mL/min to 1000 mL/min used in this study, the liquid holdup within the 3 mm beads was 30% to 60% higher than with the 6 mm beads. The specific surface area, defined as the surface area of the particle divided by its volume, is 50% higher for the 3 mm beads as compared to the 6 mm beads. This results in an increase of the liquid retention time and holdup. Thus, the $K_{tot}A/V_L$ value in the TBR with 3 mm beads (Figure 3-2) was lower by the same percentage compared to 6 mm beads (Figure 3-3). The highest $K_{tot}A/V_L$ values in the TBR with 3 mm and 6 mm beads were 178 h^{-1} and 421 h^{-1}, respectively.

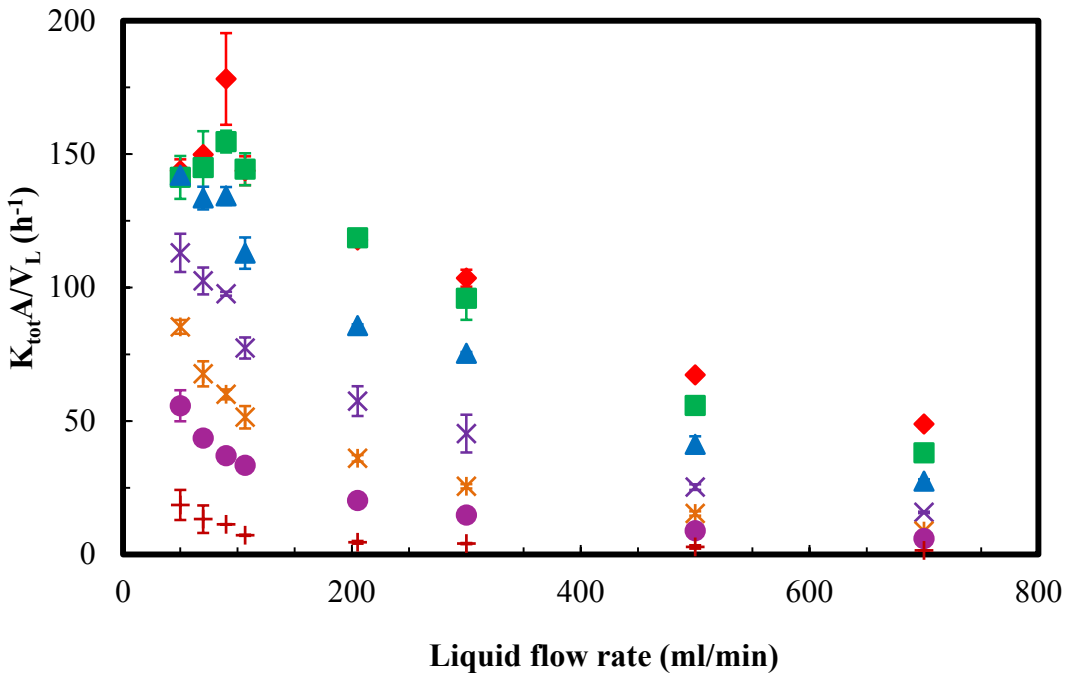

Figure 3-2. $K_{tot}A/V_L$ values at various liquid flow rates in a TBR with 3 mm beads at air flow rates (+) 5.5, (●) 18.2, (*) 28.2, (×) 46.4, (▲) 72.8, (■) 106.4, (♦) 130.9 sccm. Error bars represent ± 1 standard deviation. Reproduced with permission from Mamatha Devarapalli who performed this TBR study.

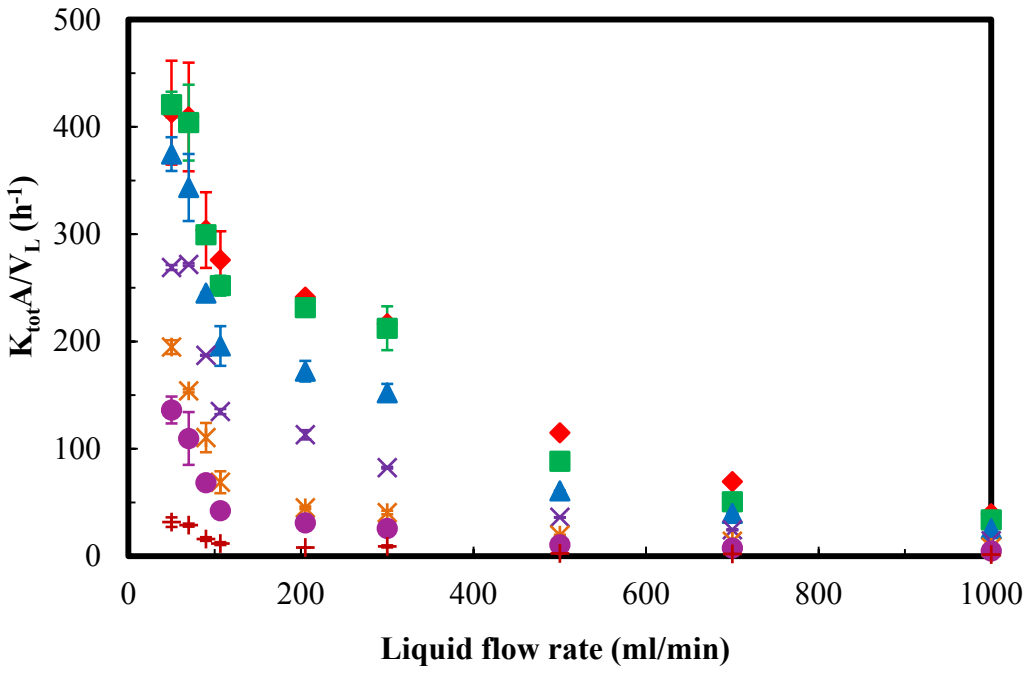

Figure 3-3. $K_{tot}A/V_L$ values at various liquid flow rates in a TBR with 6 mm beads at air flow rates (+) 5.5, (●) 18.2, (*) 28.2, (×) 46.4, (▲) 72.8, (■) 106.4, (♦) 130.9 sccm. Error bars represent ± 1 standard deviation. Reproduced with permission from Mamatha Devarapalli who performed this TBR study.

3.4.2 Hollow Fiber Reactor

The mass transfer coefficients ($K_{tot}A/V_L$) for five different hollow fiber modules were analyzed. Because the diffusivity of O_2 is about four orders of magnitude larger in air than in water (Incropera, et al. 2006), it was assumed that the gas flow rate had a negligible effect on the mass transfer coefficient. The V_L used in the analysis of the $K_{tot}A/V_L$ value was the shell priming volume of each HFR module as given in Table 3-1.

3.4.2.1 Module 1-PS: M1-500S-20-01N

A total of 20 tests were performed using the M1-500S-20-01N module. The liquid flow rates ranged from 10 to 160 mL/min. The results of these tests are shown in Figure 3-4.

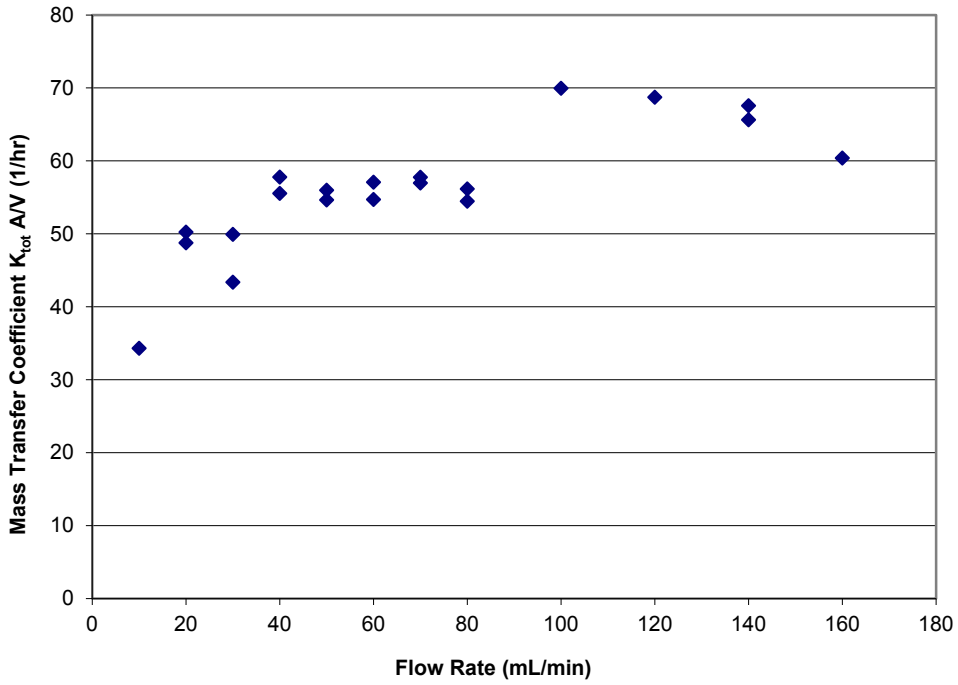

Figure 3-4. Porous PS data (Module M1-500S-260-01N)

In Figure 3-4 a large jump can be seen in the mass transfer coefficient between 80 and 100 mL/min. In order to pump 100 mL/min, a separate pump of the same model was used with larger tubing. This jump could be due to error introduced from larger tubing and a separate pump. Another possibility is that at these higher flow rates the DO probe is again at the lower end of its calibration.

3.4.2.2 Module 2-PES: M12E-261-01N

The first 19 tests using the M12E-261-01N module were performed at liquid flow rates of 70 and 40 mL/min. 16 tests at 40 mL/min and 3 tests at 70 mL/min. These initial tests were trial runs in order to check repeatability of the experiments. The next 16 experiments were performed

with liquid flow rates ranging from 5 to 80 mL/min using properly wetted fibers. The results of all of these tests are shown in Figure 3-5.

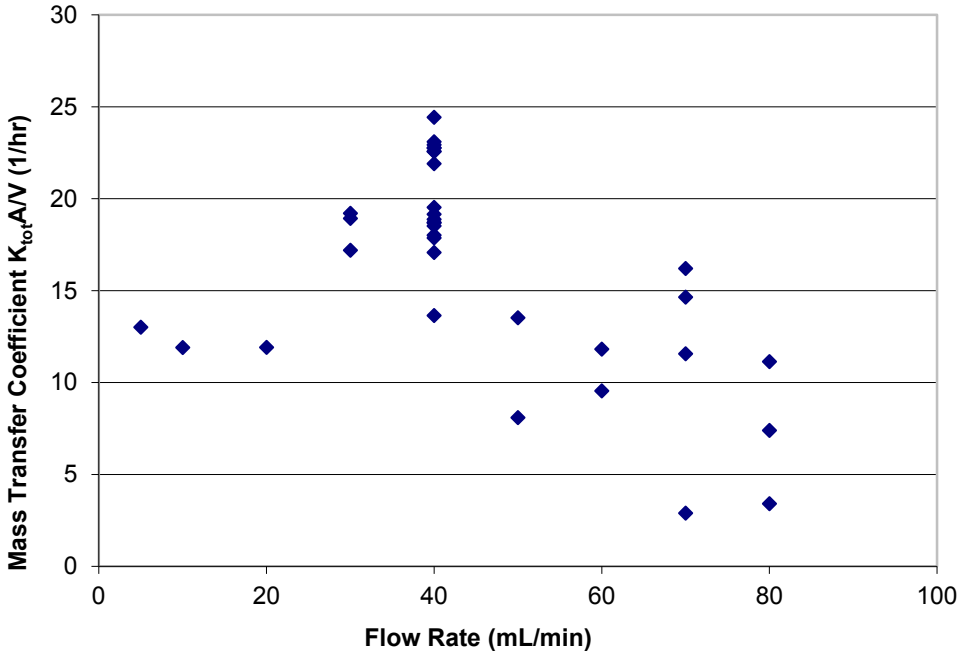

Figure 3-5. Porous PES results with air (Module M12E-261-01N)

As can be seen from Figure 3-5, the results from the M12E-261-01N module had large variability. The results also did not follow the expected trend for mass transfer. According to mass transfer theory, the mass transfer coefficient should increase with flow rate and asymptotically level off at some value. However, these data show a decreasing trend with increasing flow rate. One hypothesis for this trend was that the readings on the DO meter were too low in order to be representative of the actual oxygen content in the water. For example, at 80 mL/min the reading on the probe ranged from 0.01 to 0.05 %. In order to correct for this, a higher partial pressure was needed. This could be achieved by raising the gas pressure or by raising the mole percentage of oxygen in the gas. In order to keep results between HFRs

comparable, pure oxygen was used instead of higher pressures. When pure oxygen was used, the variability between experiments was greatly reduced and the data followed the expected trend. The 14 tests performed with pure oxygen are shown in Figure 3-6.

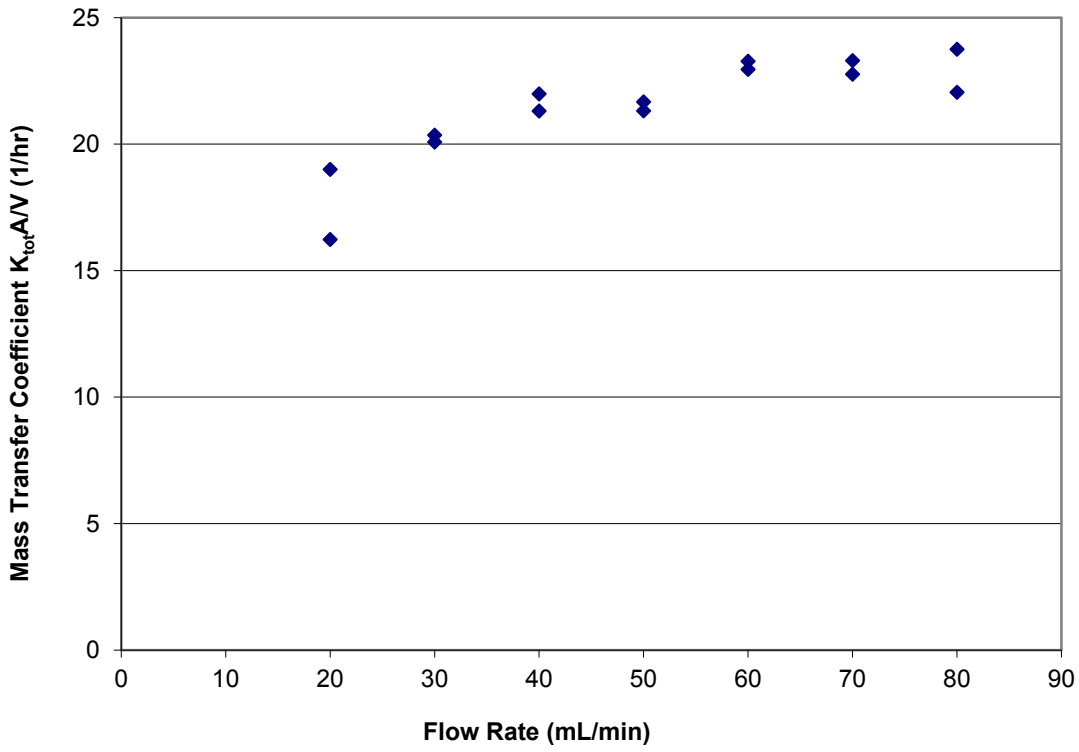

Figure 3-6. Porous PES results with oxygen (Module M12E-261-01N)

3.4.2.3 Module 3-PP: Spectrum (400-007)

A total of 21 tests were performed using the Spectrum (400-007) module. The results are shown in Figure 3-7.

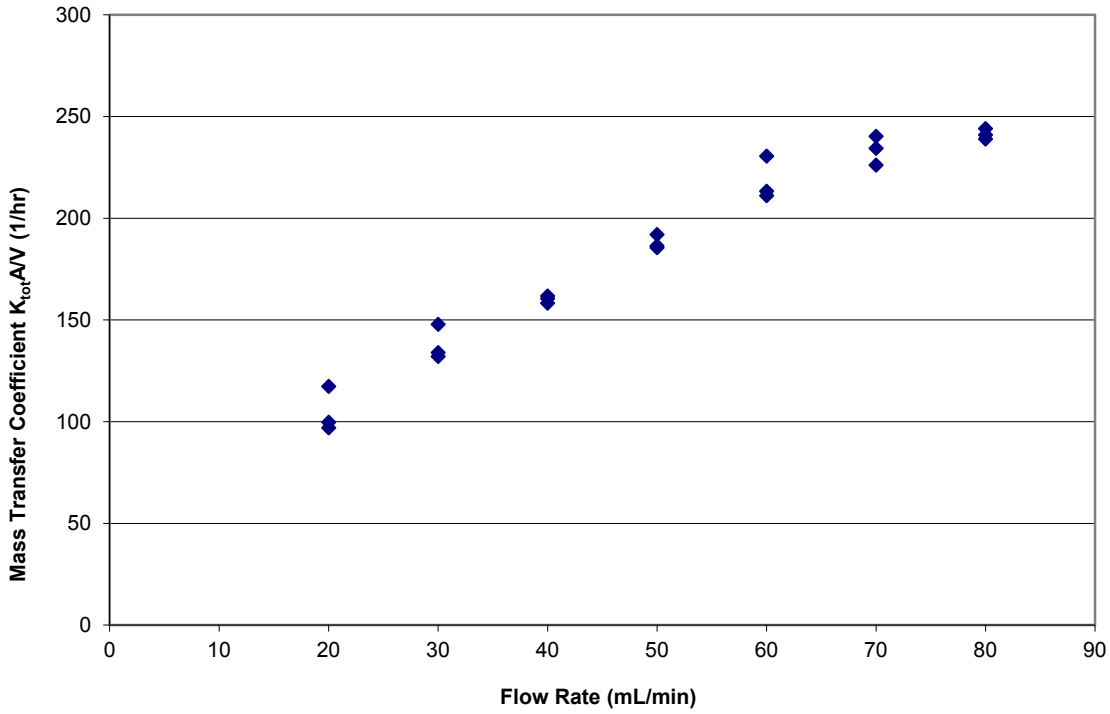

Figure 3-7. Porous PP data (Module 34101552)

3.4.2.4 Module 4-PDMS: PDMS-XA PermSelect-2500

A total of 32 tests were performed using the PDMS-XA PermSelect-2500 module. This module had a different flow pattern than the other modules. The main flow component was a crossflow pattern. The results for this experiment are shown in Figure 3-8. Because of the high mass transfer rates in this module, it was tested at much higher flow rates than the other modules. The higher flow rates were achieved by combining two peristaltic pumps in parallel and combining the outlet. The flow rates were checked periodically to ensure that this did not change the calibrated flow rates of each pump.

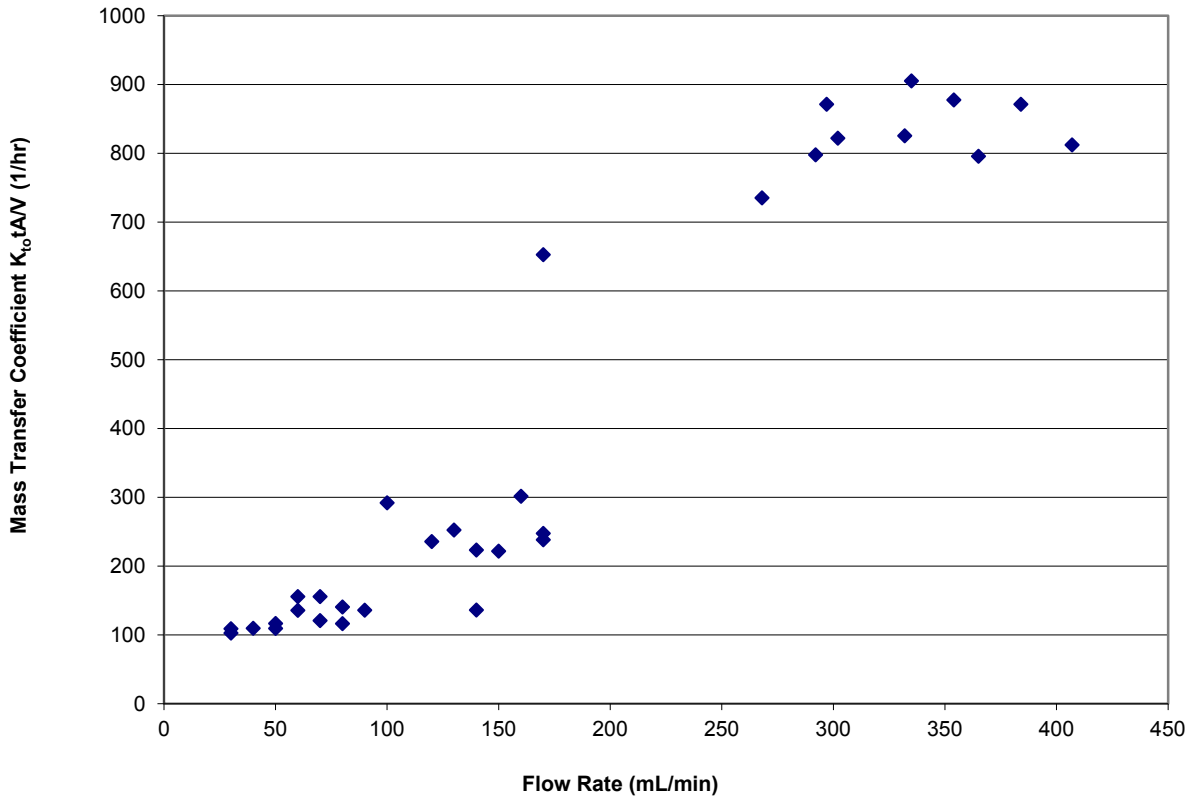

Figure 3-8. Non-porous PDMS data (Module PDMS-XA-2500)

The data shown in Figure 3-8 had large variability and poor repeatability. Because of the crossflow patterns across the banks of hollow fibers it was hypothesized that the variability resulted from different flow patterns arising in the banks of tubes. This hypothesis came about because after higher liquid flow rates were flown through the HFR the mass transfer results seemed to be different and more repeatable. To test this hypothesis another PDMS-XA PermSelect-2500 module was purchased. This time, initially a flow rate of 200 ml/min was flowed through the HFR for 30 minutes. The mass transfer experiments were then repeated. The results are shown in Figure 3-9.

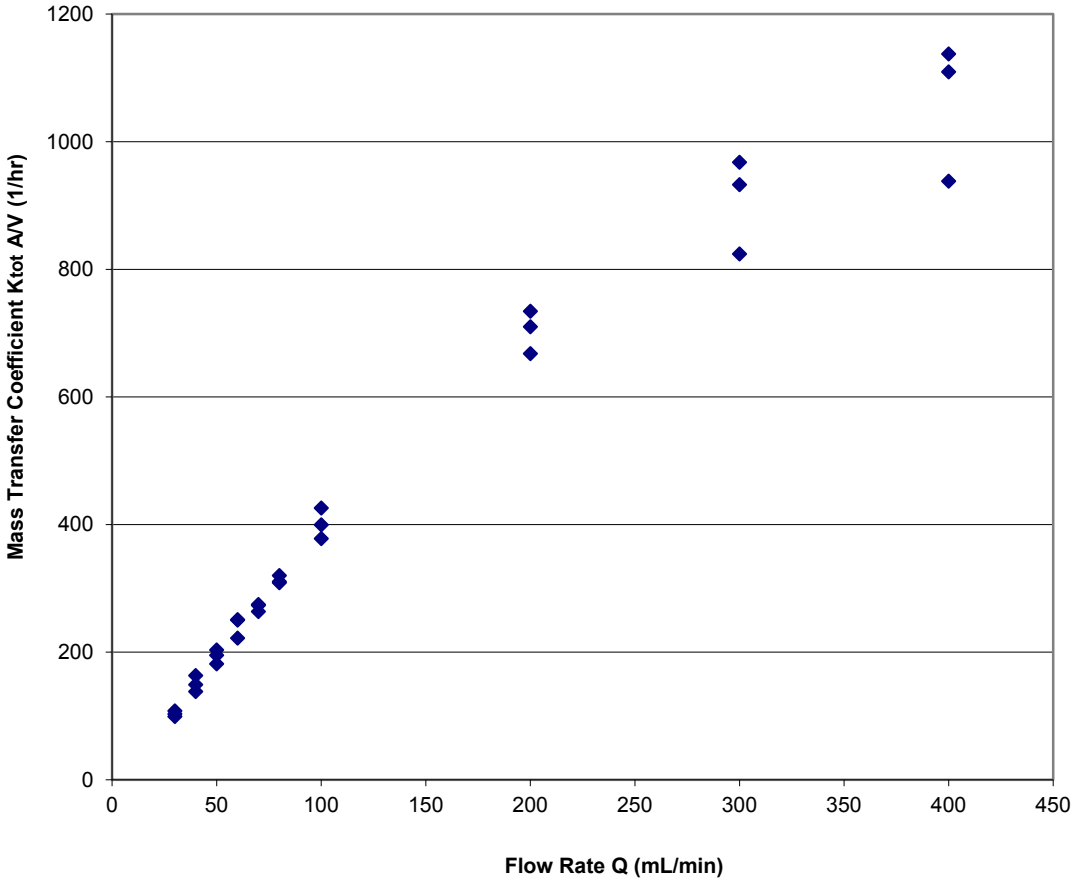

Figure 3-9. Non-porous PDMS data (Module PDMS-XA-2500) with initial treatment of high flow rates

Figure 3-9 shows that the repeatability was greatly improved by first flowing a higher flow rate though the HFR.

3.4.2.5 Module 5-FPS: Optiflux F160 NR

A total of 19 tests were performed using the Optiflux F160 NR module. The results are shown in Figure 3-10.

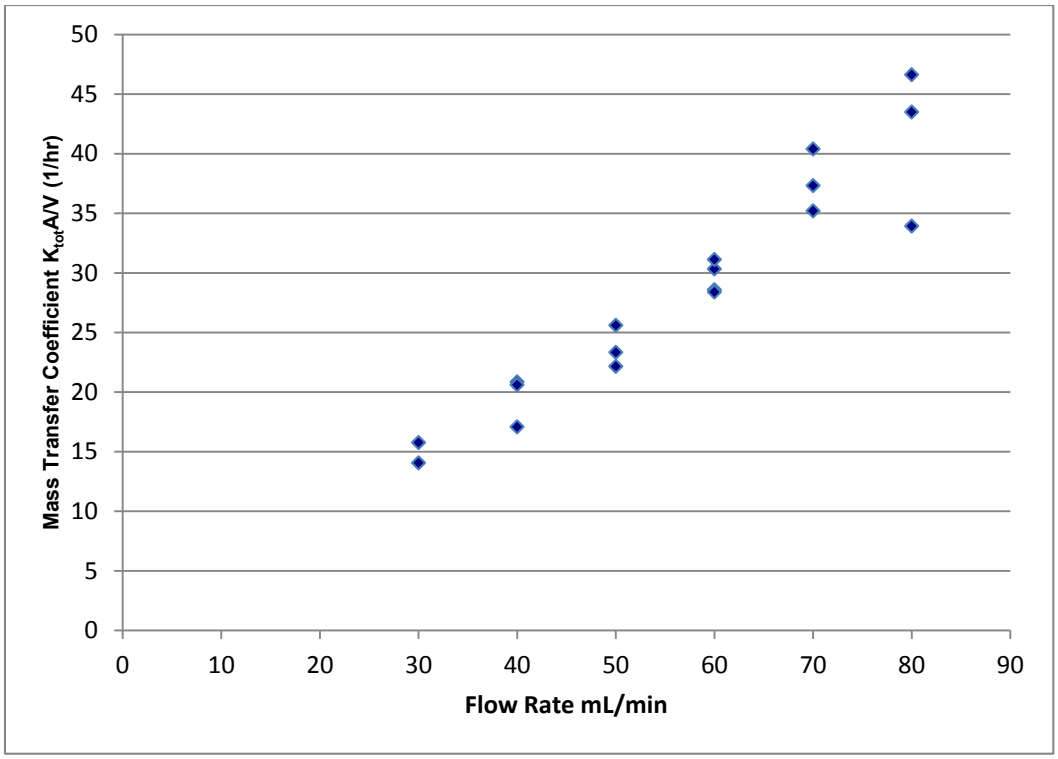

Figure 3-10. Porous FP (Optiflux F160 NR).

3.4.2.6 HFR Results Summary

Figure 3-11 shows the effect of Reynolds Number (*Re*) on $K_{tot}A/V_L$ for all five different HFR modules. *Re* was calculated based on the hydraulic diameter and the maximum liquid velocity. For all of the modules except Module 4, the flow was parallel to the fibers. For Module 4, the flow was perpendicular to the fibers. As *Re* approaches ∞, $K_{tot}A/V_L$ reaches an asymptote in which the mass transfer is purely limited by the membrane resistance. Thus, the asymptote value is the maximum $K_{tot}A/V_L$ that can be obtained. For all HFRs shown in Figure 3-11, the largest *Re* reported for each HFR is equivalent to a liquid flow rate of 80 mL/min (the insert plot in Figure 3-11 shows Module 4 extended to Re = 7.4, which is equivalent to flow rates of 400 mL/min). For example, *Re* = 27 for Module 2 is equivalent to 80 mL/min. Since *Re* is

proportional to the flow rate, *Re* = 27/2=13.5 for Module 2 is equivalent to 40 mL/min. This analysis is similar for the other modules. As shown in Figure 3-11, each HFR module has a unique dependence on *Re* based on the module's flow dynamics.

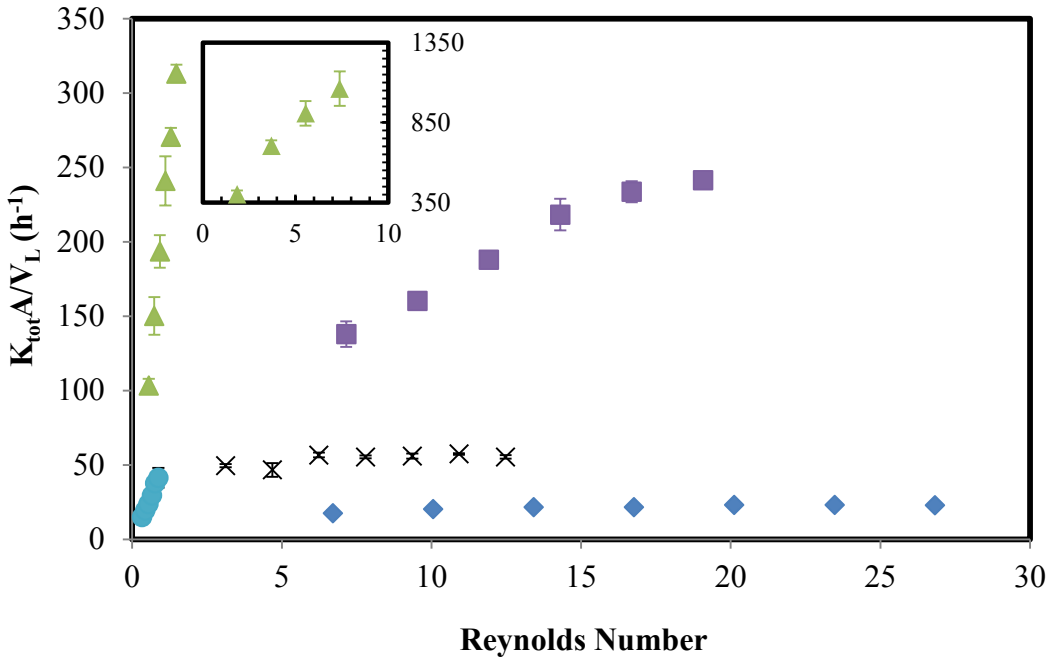

Figure 3-11. ***$K_{tot}A/V_L$*** **values in HFR at various Reynolds number for (×) Module 1-PS, (♦) Module 2-PES, (■) Module 3-PP, (▲) Module 4-PDMS, (●) Module 5-FPS as in Table 3-1. Insert graph is a continuation for Module 4-PDMS. Error bars represent ± 1 standard deviation.**

The highest $K_{tot}A/V_L$ values for 80 mL/min liquid flow rate were obtained in Module 3 (porous polypropylene) and Module 4 (non-porous PDMS). The reason for the high $K_{tot}A/V_L$ values for Module 3 is because of its hydrophobicity. This allows for most diffusion through the membrane material from the lumen side to the shell side of the HFR to be gaseous diffusion through the pores as opposed to mostly liquid diffusion through the pores in a porous hydrophilic HFR. The reason for the high $K_{tot}A/V_L$ values for Module 4 is because of a combination of the effects of thinner fiber membranes, smaller fiber diameters, and especially the large A/V_L ratio compared to other modules (Table 3-1).

Figure 3-11 clearly shows that Modules 1 and 2 have approached their asymptotes such that they are limited by the membrane resistance. The membrane limitations are depicted by the small change in mass transfer (less than 5 h^{-1}) with a large change in *Re* (around 10). Module 3 started to show signs of membrane limitations at a *Re* around 20. However, Modules 4 and 5 show a large increase in mass transfer coefficient with increasing *Re*, indicating that most of the resistance is from diffusion through the liquid boundary layer. Thus, with increasing *Re*, $K_{tot}A/V_L$ is expected to increase for Modules 4 and 5 until the membrane resistance dominates. To test this, studies conducted at up to *Re*=7.4 (400 mL/min) for Module 4 showed that $K_{tot}A/V_L$ continued to rise even at these higher flow rates, with a maximum $K_{tot}A/V_L$ of 1062 h^{-1}. However, it appears the module 4 may be approaching an asymptote indicating it is starting to become limited by the membrane resistance.

For mass transfer applications, the optimal HFR will provide the highest $K_{tot}A/V_L$ at a desired *Re*. With increasing *Re*, Module 4 shows that very high mass transfer rates can be achieved (Figure 3-11). For Module 4 at *Re*=7.4, the shear rate for flow over a cylinder, in this case the fibers, was only 100 s^{-1} (Incropera, et al. 2006). This relatively low shear rate is beneficial to cellular systems because shear rates higher than 300 s^{-1} can potentially retard cell growth and cause cell death (Nejadnik, et al. 2008; Rickard, et al. 2004).

3.4.3 Stirred Tank Reactor

For the STR, $K_{tot}A/V_L$ is dependent on the geometry of the vessel and impellers, agitation speed, and volumetric gas flow rate. The $K_{tot}A/V_L$ is also affected by the gas and liquid properties and the interfacial area per liquid volume. In the air/water mass transfer system used, the interfacial area increases with the increase in the gas flow rate and agitation speed that breaks the gas into smaller bubbles. Higher liquid turbulence around each gas bubble in the STR from

increased agitation speed reduces the stagnant film of water that resists diffusion of O_2 into the bulk liquid, thus increasing the $K_{tot}A/V_L$. Figure 3-12 shows a near linear increase in $K_{tot}A/V_L$ with increasing agitation. Another trend that is observed is the increase in $K_{tot}A/V_L$ with increased gas flow. This can be attributed mostly to the increased surface area as a result of more bubbles. Figure 3-12 also shows a 60-70% increase in $K_{tot}A/V_L$ when the gas flow rate was doubled.

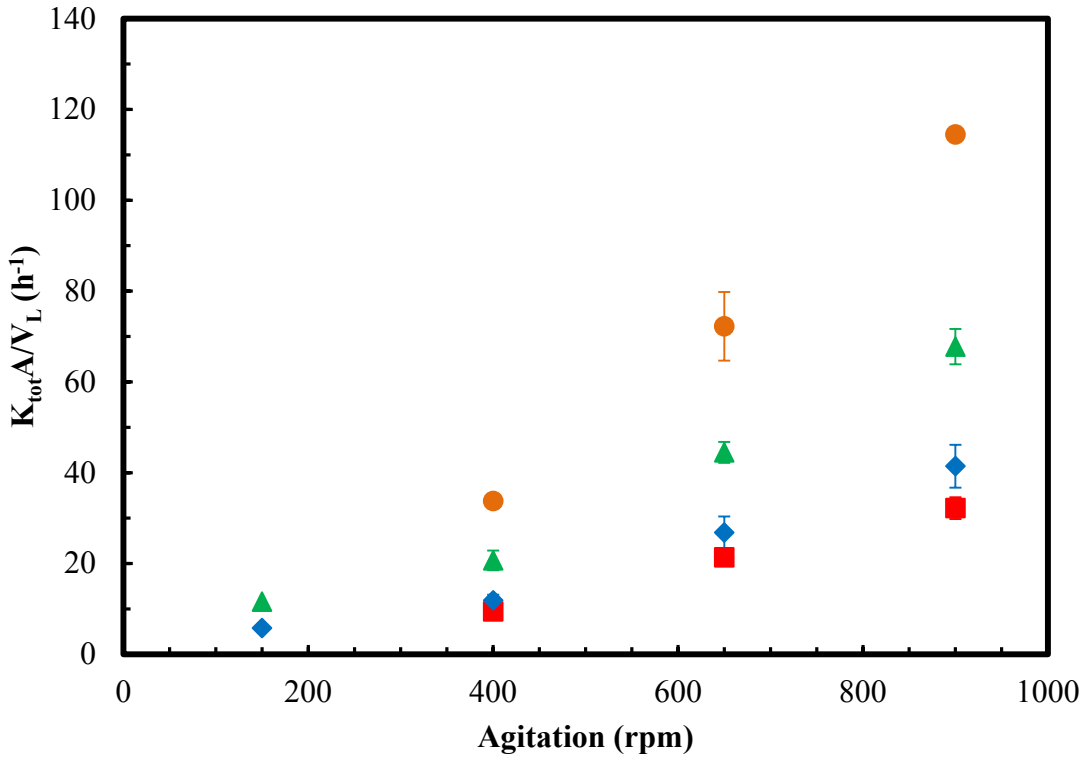

Figure 3-12. $K_{tot}A/V_L$ values in STR at various air flow rates (■) 60, (♦) 100, (▲) 200 and (●) 400 sccm. Error bars represent ± 1 standard deviation. Reprinted with permission from Randy Phillips who performed the work.

3.4.4 Discussion

Figure 3-13 shows a comparison of the highest $K_{tot}A/V_L$ for the STR, TBR, and HFR at each different experimental condition for each reactor.

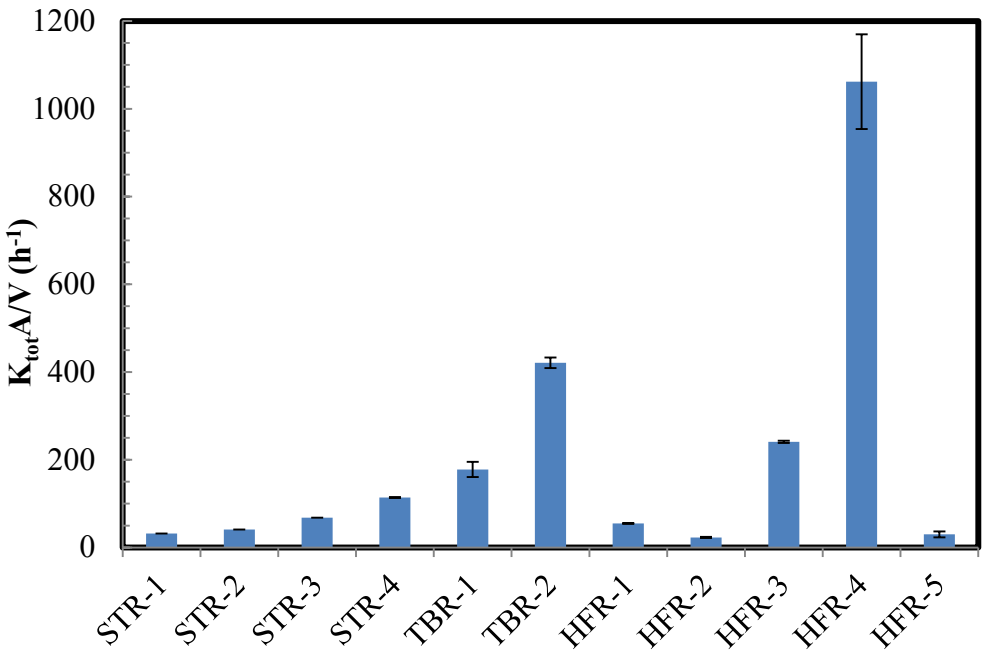

Figure 3-13. Maximum $K_{tot}A/V_L$ for STR, TBR and HFR at various conditions. STR-1 (60 sccm, 900 rpm), STR-2 (100 sccm, 900 rpm), STR-3 (200 sccm, 900 rpm), and STR-4 (400 sccm, 900 rpm), TBR-1 (131 sccm, 3 mm beads), TBR-2 (106 sccm, 6 mm beads), HFR-1 (Module 1, membrane limited Re), HFR-2 (Module 2, membrane limited Re), HFR-3 (Module 3, membrane limited Re), HFR-4 (Module 4, membrane and boundary layer limited Re), HFR-5 (Module 5, boundary layer limited Re). Error bars represent ± 1 standard deviation.

As shown, the highest $K_{tot}A/V_L$ was achieved with HFR-4. This is due to the high surface area to volume ratio in HFRs. For application purposes in syngas fermentation, it is necessary to scale up these reactors. HFRs can be scaled up to production volumes by increasing the shell size and number of fibers. HFRs have no moving parts in the reactor, but require constant liquid recirculation by an external pump. Under the conditions studied, the highest HFR mass transfer coefficient achieved was 1062 h^{-1}. However, the HFR performance is largely dependent on the liquid flow regime and the type and size of fibers. In some cases shown in Figure 3-13 depending on the flow regime and module, the HFR does not have a higher $K_{tot}A/V_L$ than the TBR or STR.

The TBR had the next best $K_{tot}A/V_L$ of 421 h^{-1}. TBR scale up can be done by maintaining either the same superficial velocities or the space velocity across the different scales. However,

scale up of a TBR can be difficult because of the complex fluid dynamics of trickle bed reactors (Ranade, et al. 2011). From the mass transfer studies in the TBR, it is evident that the gas flow rate is the major factor affecting the $K_{tot}A/V_L$. In syngas fermentation, use of high gas flow rates to achieve high $K_{tot}A/V_L$ can result in poor gas conversions.

The STR had the lowest maximum reported $K_{tot}A/V_L$ of 114 h^{-1}. In addition, STR scale up requires at least some change in the physical environment of the fermentation system such as flow pattern, mass transfer rate, shear rate and mixing times (Shuler and Kargi 2002b). The power required for a STR is proportional to the cube of the impeller speed. Since the mass transfer coefficient of a STR increases almost linearly with impeller speed, a linear increase in mass transfer results in a cubic increase in the power requirement. The STR and TBR $K_{tot}A/V_L$ are both largely dependent on the gas flow rate (Figures 5 and 14). However, the gas flow rates of the HFR can be low, without affecting the $K_{tot}A/V_L$. For syngas fermentation in general, high gas flow rates are to be avoided in order to achieve high gas utilization. However, to obtain high $K_{tot}A/V_L$ in the TBR and STR, higher gas flow rates and agitation speeds must be used, resulting in lower gas conversion efficiencies and product yields.

Although $K_{tot}A/V_L$ values were obtained for the three reactor configurations, it is important to note that mass transfer comparisons among reactors should also be related to the total liquid associated with the reactor system (V_S). For instance, if a STR has a recycle loop, then V_S would represent the sum of V_L and the excess volume (V_E) of liquid in the recycle loop. For any reactor system in which V_S is well-mixed, a mass balance for any gas without any reaction would as shown in Equation 3-3, where V_{Ltot} (m^3) is the total volume of liquid in the reactors (i.e. $V_{Ltot} = 3 \cdot V_L$ if three reactors of equal volumes were used), V_S is the total liquid volume of the reactor system (m^3) which includes the recycle loop, sump and other sampling

ports, *dn/dt* is the change in moles of dissolved gas in the liquid with time, C_S is the saturated concentration of the gas at the reactor partial pressure, and C_L is the concentration of the gas in the total liquid.

$$\frac{1}{V_S} \cdot \frac{dn}{dt} = \frac{dC_L}{dt} = \frac{K_{tot}A}{V_L} \cdot \left(\frac{V_{Ltot}}{V_S}\right) \cdot (C_S - C_L) \quad (3\text{-}1)$$

Thus, the important parameter to compare is the product of $K_{tot}A/V_L$ and V_{Ltot}/V_S where the latter is the ratio of liquid in the reactor to total liquid in the system. Therefore, when high mass transfer rates are desired in a fermentation system, it is important to have a system with a large ($K_{tot}A/V_L$) and a large (V_{Ltot}/V_S). V_{Ltot}/V_S is often unity but will be less than unity with recycle loops and other peripheral liquid volumes (liquid sampling system in a recycle loop). For the TBR and HFR, multiple reactors may be used in order to increase V_{Ltot}/V_S. Thus, direct comparisons of $K_{tot}A/V_L$ should be done with caution since a system with a higher $K_{tot}A/V_L$ and a lower V_{Ltot}/V_S as compared to another system could actually have less mass transfer per unit of total volume. If the well-mixed assumption is not valid, such that Equation 3-3 is not valid for comparison, a more comprehensive model is needed to determine the best method for comparison. In summary, $K_{tot}A/V_L$ can provide a comparison at a general level but should not be used for absolute comparisons. On another note, care should be taken as to the value of V_L used in the mass transfer calculations since some studies may use V_s in place of V_L.

In a recent study, the mass transfer capabilities of CO for a TBR, CSTR, stirred tank with microbubble sparger, packed bubble column, batch-stirred tank, and bubble column were reviewed (Munasinghe and Khanal 2010a). In this review, it was reported that the highest $K_{tot}A/V$ occurred in the TBR with a value of 137 h^{-1}, whereas the highest $K_{tot}A/V$ reported for a STR was 101 h^{-1}. This review did not report any values for a HFR. In another study, a maximum $K_{tot}A/V$

for CO was reported for a HFR to be 947 h^{-1} (Monk, et al. 1999). Although it was not reported in the second study, these results are consistent with the findings of this work that a HFR has better mass transfer capabilities as compared to a STR and TBR. However, one difficulty of the above noted studies is that it is unclear as to the volume used for the mass transfer calculations. Also, many of the mass transfer coefficients cited in Munasinghe and Khanal (2010a), were calculated with active cell cultures where the partial pressure of the gas in the liquid was assumed rather than measured.

Another study compared the mass transfer capabilities of CO for several different reactor configurations without cells (Munasinghe and Khanal 2010c). In this study, the reactor configurations were a column diffuser, a 20-µm bulb diffuser, gas sparger, gas sparger with mechanical mixing, submerged composite hollow fiber membrane (CHFM) module, air-lift combined with a 20-µm bulb diffuser, and an air-lift combined with a single gas entry point. The study reported the $K_{tot}A/V$ ranging from 3 to 91 h^{-1} for CO for different reactor configurations with varying CO flow rates. Though this study is valuable for understanding mass transfer capabilities with different gas flow rates, the effects of liquid flow rates were not addressed. Since the main resistance in mass transfer comes from liquid boundary layers, it is important to analyze the effects of liquid flow rates in addition to gas flow rates. For example, the CHFM used with CO in Munasinghe and Khanal (2010c) study had no liquid flow, and thus the CHFM had the lowest reported $K_{tot}A/V$. A conclusion from this study would be that a CHFM would not be a good reactor choice when in actuality, the mass transfer would most likely have been much higher with liquid flow.

It is clear from the studies above and the results reported in the present study that reactor conditions (e.g. flow rates, agitation speed, etc.) are critical for noting when comparing reactors.

For example, if HFR-2 (module 2) is compared to STR-1,2,3, or 4 in Figure 3-13, then it appears that the STR would be a better reactor based solely on mass transfer capabilities. However if HFR-4 (module 4) is chosen, then the conclusion would be that the HFR significantly outperforms the STR and TBR. Thus, the individual operating parameters must be carefully considered when comparing the mass transfer capabilities of different reactors. The appropriate reactor for syngas fermentation is not as clear cut as choosing the reactor with the highest $K_{tot}A/V_L$. Obviously economics and scale-up issues must play a pivotal role in reactor selection.

Several key points can be noted from the study of this work to support that a HFR has the highest potential mass transfer benefits for syngas fermentation. First, the highest reported $K_{tot}A/V_L$ values in the present work and in literature were reported for a HFR. Second, though not shown in this study, the gas flow rate does not play a critical role in $K_{tot}A/V_L$ for a HFR such that lower gas flow rates that may be required for efficient gas utilization would be more beneficial for a HFR. Third, the HFR may have fewer limitations for implementation. For example, the TBR mass transfer coefficient eventually decreases with increasing liquid flow rate. Thus, higher gas flow rates are needed to increase mass transfer rates, but high flow rates result in lower gas utilization. For the STR, the mass transfer coefficient can be increased by increasing gas flow rate, which again decreases gas utilization, or by increased agitation, which raises the power requirements significantly. Once an appropriate HFR is chosen with a large area to volume ratio and good mass transfer capabilities, the mass transfer coefficient can be increased simply by increasing the liquid flow rate. However, as stated previously, every reactor must be carefully considered for the application and strict comparisons between mass transfer coefficients should be done with caution.

There are many parameters that will cause one reactor to outperform another in terms of mass transfer capabilities. The STR has been the traditional bioreactor of choice for syngas fermentation because the process design and scale up are well understood. However, based on the results of this study, alternative bioreactors like the HFR and TBR should be strongly considered when mass transfer limitations are expected. Since mass transfer coefficients of CO, CO_2, and H_2 can have some differences (based on solubility in membranes and water) compared to coefficients observed for O_2 or CO alone further studies should be performed to look at mass transfer comparisons of actual syngas constituents and how the composition can affect the individually observed coefficients.

3.5 Conclusion

The non-porous polydimethylsiloxane (PDMS) HFR provided the highest mass transfer coefficient, $K_{tot}A/V_L$, of 1062 h^{-1}, followed by the TBR with 6 mm beads (421 h^{-1}), and then the STR (114 h^{-1}). The HFR and TBR can transfer O_2, a sparingly soluble gas similar to the fermentation substrates CO and H_2, into water at rates much higher than achieved in the STR. Higher mass transfer in the HFR and TBR suggest a more efficient process design might be attained for syngas fermentation. However, caution should be used when simply comparing the $K_{tot}A/V_L$ values between reactors. When measuring mass transfer coefficients in a HFR, specific precautions must be taken for maximum accuracy. For example, in order to accurately measure the mass transfer coefficients for HFR Module-2, pure oxygen needed to be used because of the lower mass transfer rates. For HFR Module-4 a higher flow rate of 200 ml/min needed to be employed initially in order to achieve repeatable results.

4 H_2 and CO Mass Transfer Coefficients in a Hollow Fiber Reactor

4.1 Introduction

Though there are advantages to syngas fermentation, one bottleneck that needs to be addressed is mass transfer limitations. In syngas fermentation, mass transfer is important because of the use of sparingly soluble gases like CO and H_2. One reactor that has specifically high mass transfer rates is the HFR (Atchariyawut, et al. 2008; Ebrahimi, et al. 2005; Lee, et al. 2012). HFRs have been used extensively in waste management, therefore, there is a considerable amount of data on CO_2 mass transfer rates for various different membranes and reactors (Atchariyawut, et al. 2008; Korikov and Sirkar 2005). There have also been several studies performed measuring CO mass transfer in HFRs (Lee, et al. 2012; Munasinghe and Khanal 2010b). However, most of these studies only predict an apparent mass transfer coefficient (assumes the dissolved CO concentration is zero) which is not an accurate assumption in many situations. In the studies that measure the true mass transfer coefficient, there is little mass transfer modeling or theory used to make predictions for other species.

Though oxygen is not involved in the syngas fermentation process, it can be helpful for predicting mass transfer of other gasses based on liquid boundary layer theory. Because of this fact, there have been studies performed on oxygen mass transfer for comparing reactors for syngas fermentation (Orgill, et al. 2013). However, in HFRs, since the membrane resistance has to be taken into account, there must be a more rigorous approach to relating oxygen mass

transfer coefficients to syngas component mass transfer coefficients. This is especially important since mass transfer rates of syngas constituents can differ among each other. The diffusivities of CO, CO_2 and H_2 in water at 37 °C are 107%, 90%, and 212%, respectively, as compared to O_2 (Tamimi, et al. 1994b; Verhallen, et al. 1984a; Wise and Houghton 1968). Based solely on the differences in these diffusivities, the H_2 mass transfer should be significantly greater than either CO or CO_2. To our knowledge only one other study has attempted to measure H_2 mass transfer in a HFR and this was for the H_2 dissolution into groundwater (Fang, et al. 2002).

Important mass transfer rates in syngas fermentation are for the two electron donors H_2 and CO. This work determines the mass transfer coefficients for CO and H_2 in a HFR using a novel measurement technique. The technique was validated by measuring mass transfer of O_2 using a dissolved oxygen probe and the new technique in order to compare results. A mass transfer model is also presented that allows for accurate mass transfer predictions of H_2 and CO in a HFR based solely on oxygen mass transfer characteristics. This is important because it allows researchers to predict the mass transfer capabilities of a specific HFR syngas fermentation system before any cellular work is performed.

4.2 Materials and Methods

4.2.1 Experimental Materials and Setup

The experimental setup is shown in Figure 4-1. Deionized water was pumped through the shell side of the hollow fiber module using a calibrated peristaltic pump (Masterflex; Model #7523-90). Masterflex Norprene tubing was used for both the gas and liquid tubing to ensure minimal gas transfer through the tubing and into the surroundings. Gas was flowed through the tube side of the hollow fiber module. The inlet gas flow rate was controlled by a calibrated mass

flow controller (Parker Porter; Model 201). The outlet gas was sampled by opening a valve and inserting a needle connected to a 5 ml gas tight syringe through a septum. The gas sample was analyzed using a Shimadzu 2014 Gas Chromatograph (Shimadzu Scientific Instruments, Columbia, Maryland) with a thermal conductivity detector and a Carboxen 1010 PLOT capillary GC column (Sigma-Aldrich, Switzerland). The outlet gas flowed through a bubble flow meter for outlet gas flow rate measurements. The outlet liquid flowed through a glass holder with a calibrated dissolved oxygen probe (Eutech; alpha DO 500). The hollow fiber reactor used in this work was a non-porous module with polydimethylsiloxane fibers (PDMS-XA PermSelect-2500, MedArray Inc., Ann Arbor, MI). This module was chosen because it portrayed the highest mass transfer capabilities based on the studies performed in Chapter 3. The module had 3200 fibers with an inner diameter of 0.2 mm and an outer diameter of 0.3 mm. The module had a shell priming volume of 25 ml and a surface area of 2500 cm^2 based on the fiber outer diameter. The shell priming volume was measured experimentally by filling the shell (including shell ports) with pure water and measuring the input volume. The effective length of the fibers was 8.4 cm.

4.2.2 Experimental Procedure

Oxygen mass transfer was measured by pumping de-ionized water through the shell side of the hollow fiber module at liquid flow rates ranging from 50 ml/min to 200 ml/min. The experiments were performed in random order. The inlet water was initially purged with pure argon to attain a 0-10% dissolved oxygen solution. This inlet DO concentration value was not critical because the actual measured value was used in the mass transfer calculations. The DO of the inlet water was measured with a separate DO probe. The water purging was done in a well-sealed 5 liter bioreactor. A 20/80 oxygen/argon gas mixture flowed through the lumen side of the hollow fiber module at an inlet flow rate of 4.6 sccm. The gas flow rate was chosen to be low

enough to allow for discernable concentration and flow rate changes between the inlet and outlet gas lines. Data collection began after the system reached a quasi-steady state, where the average O_2 concentration did not change by more than 1% in a 5 minute time period. This was determined to be after 40 minutes for flow rates between 20 and 30 mL/min, 30 minutes for flow rates between 30 and 80 mL/min, 20 minutes for flow rates between 80 and 140 mL/min, and 10 minutes for flow rates between above 140 mL/min. Oxygen mass transfer was measured using two different techniques. The first technique (dissolved gas method) measured the amount of oxygen dissolved in the outlet water. For this technique, after the system reached steady state, the outlet DO was collected by manually recording the dissolved oxygen reading on the DO transmitter. The reading was recorded every 30 seconds for 5 minutes and the average was taken to be the DO value at that specific flow rate.

The second technique (GC method) measured the change in gas flow rates and O_2 concentration between the inlet and outlet gas. For this method, the system was allowed to reach steady state and a gas sample was taken from the outlet gas sampling port. The port was opened and a 5 ml syringe was inserted, the syringe was pumped three times and allowed to sit for 2 minutes while still inserted. The syringe was then pumped three more times and then finally a gas sample was taken. This slow sampling allowed any atmospheric gas contamination to be dissipated. The gas sample was injected into the GC in order to attain an oxygen concentration from a GC area graph. GC areas were converted to concentrations using an oxygen calibration performed with known O_2 concentrations from 0-20% O_2, made by mixing known volumes of argon and O_2. Argon was also used as a carrier gas in the GC so that argon in the sample did not show on the GC output. The outlet gas flow from the HFR was measured using a 50 ml bubble

flow meter. The volumetric flow rate was calculated by dividing the volume of the bubble flow meter (50 ml) by the time it took a thin soap film to travel the distance of the flow meter.

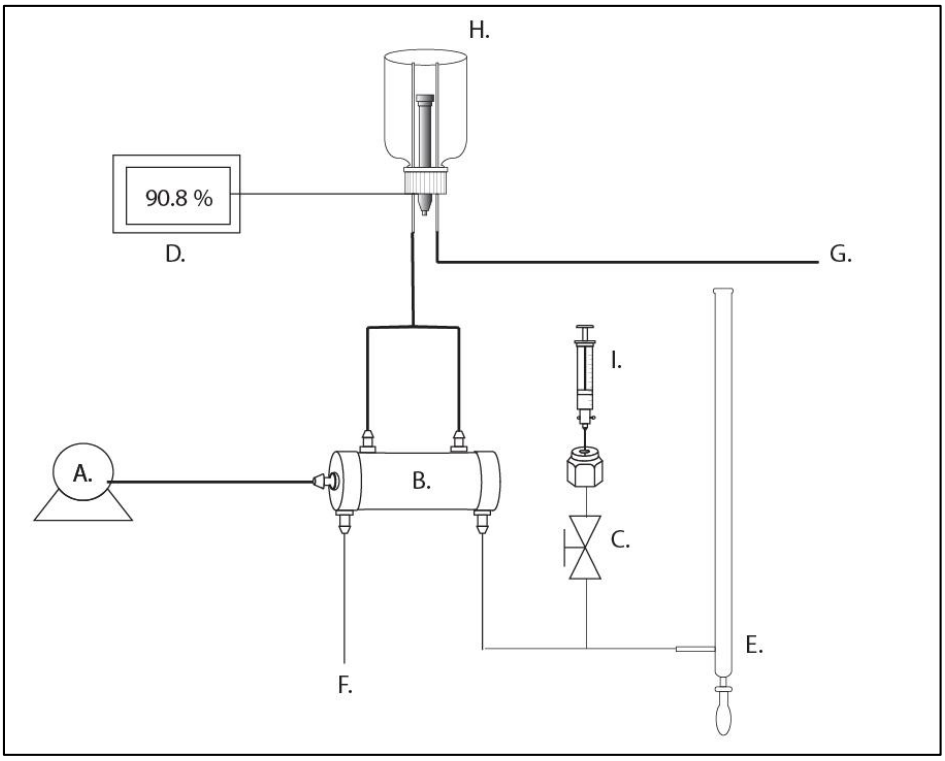

Figure 4-1. HFR mass transfer experimental setup: (A) peristaltic pump, (B) hollow fiber reactor, (C) gas sampling port (valve and septum), (D) DO transmitter, (E) bubble flow meter, (F) gas inlet flow line, (G) liquid outlet flow line, (H) glass holder with calibrated dissolved oxygen probe, and (I) gas tight syringe.

CO mass transfer was measured by pumping DI water through the shell side of the hollow fiber module at liquid flow rates of 46, 93, 135, and 184 ml/min. The inlet DI water was contained 0% dissolved CO. 99.99% pure CO was flowed through the lumen side of the hollow fiber module at an inlet flow rate of 5 sccm. The experiments were done in triplicates and performed in random order. Data collection began after the system reached a quasi-steady state as described above. Only the second technique was used to measure CO mass transfer. The same GC sampling and gas flow techniques were used for CO.

H_2 mass transfer was measured by pumping DI water through the shell side of the hollow fiber module at liquid flow rates ranging from 45 ml/min to 180 ml/min. The inlet DI water was contained 0% dissolved CO. 99.99% pure H_2 was flowed through the lumen side of the hollow fiber module at an inlet flow rate of 5 sccm. The experiments were done in triplicates and performed in random order. Data collection began after the system reached a quasi-steady state as described above. Only the second technique was used to measure H_2 mass transfer. The same GC sampling and gas flow techniques were used for H_2. Extra tubing had to be added to the top of the bubble flow meter for H_2 in order to ensure that no H_2 transferred through the bubble in the bubble flow meter. H_2 diffusion through the bubble occurred when air from the atmosphere was present on one side of the bubble and H_2 was on the other, thus creating a diffusion gradient for H_2 through the bubble. This would lead to a lower measured gas flow rate. Adding the extra tubing to the end of the bubble flow meter allowed for similar concentrations of H_2 on either side of the bubble, and thus, no diffusion gradient.

4.2.3 Experimental Mass Transfer Coefficient Calculation

The mass transfer coefficient was calculated by defining a mass transfer coefficient as a proportionality factor, K_{tot}, that relates the mass transfer rate (N) to a characteristic area (A) and a characteristic concentration difference (ΔC_{lm}) (Bird, et al. 2007). This relationship is

$$N = K_{tot} A \cdot \Delta C_{lm} \qquad \textbf{(4-1)}$$

The characteristic area in this definition for a hollow fiber reactor is the outer surface area of the fibers that is active in mass transfer. The characteristic concentration difference used for determination of the mass transfer coefficient depends on the flow pattern in the hollow fiber. The reactor used in this work had a liquid cross flow pattern. The log mean concentration

difference used in this work is equivalent to the log mean concentration used under the assumption of counter flow conditions multiplied by a correction factor *F* (Incropera, et al. 2011). This relationship is

$$\Delta C_{lm} = F \cdot \Delta C_{lm,CF} = F \cdot \frac{\left(C_{sat_{in}} - C_{liquid_{out}}\right) - \left(C_{sat_{out}} - C_{liquid_{in}}\right)}{ln\left(\frac{\left(C_{sat_{in}} - C_{liquid_{out}}\right)}{\left(C_{sat_{out}} - C_{liquid_{in}}\right)}\right)} \quad \textbf{(4-2)}$$

$$C_{sat} = H \cdot P_x \cdot C_w \quad \textbf{(4-3)}$$

In these equations, $\Delta C_{lm,CF}$ is the log mean concentration difference under the assumption of counter flow. $C_{liquid_{in}}$ and $C_{liquid_{out}}$ are the inlet and outlet liquid concentrations. $C_{sat_{in}}$ and $C_{sat_{out}}$ are the inlet and outlet saturated concentrations at the inlet and outlet partial pressures and were calculated according to Equation 4-3, where *H* is the henry's law constant for the gas in water at 300 K. P_x is the partial pressure of the gas, and C_w is the total molar concentration of the liquid, in this case it is assumed to be equal to the concentration of water. The correction factor, *F*, is a function of reactor type, flow rates, and concentrations in the system. Incropera et al. give *F* for several reactor conditions in supplemental material (Incropera, et al. 2011). F approaches unity as the concentration change from inlet to outlet for each gas approaches zero. In this work, the concentration change from inlet to outlet for each gas was less than 10% so that *F* was assumed to be unity.

With these definitions in place, the overall volumetric mass transfer coefficient ($K_{tot}A/V_L$) for each gas was calculated according to Equation 4-4. V_L is the liquid volume of the HFR, in this case 25 ml. *N* is the molar mass transfer rate of O_2, CO, or H_2 into the liquid. Using the dissolved gas method for O_2, this is found by multiplying the liquid outlet concentration of O_2 by the liquid volumetric flow rate and subtracting the inlet concentration of O_2 multiplied by the liquid flow rate since the molar amount of O_2 transferred into the liquid is equivalent to the

molar amount of O_2 leaving in the gas. In this method $C_{liquid_{in}}$, $C_{liquid_{out}}$ and $C_{sat_{in}}$ were known. $C_{sat_{out}}$was calculated to assess ΔC_{lm} based on the amount of moles transferred, calculated from the difference of $C_{liquid_{in}}$ and $C_{liquid_{out}}$. Using the GC method, *N* is found by multiplying the gas inlet concentration of O_2 by the inlet gas outlet volumetric flow rate. In this method $C_{liquid_{in}}$, $C_{sat_{in}}$ and $C_{sat_{out}}$ were known. $C_{liquid_{out}}$was calculated to assess ΔC_{lm} based on the amount of moles transferred, calculated from the difference of $C_{sat_{in}}$ and $C_{sat_{out}}$.

$$\frac{K_{tot}A}{V_L} = \frac{N}{\Delta C_{lm} \cdot V_L} \quad \textbf{(4-4)}$$

4.2.4 Mass Transfer Coefficient Model

Figure 4-2 shows a pictorial representation of the different mass transfer regions in a HFR. In Figure 4-2, C^{BG} represents the bulk concentration in the gas, C^{Gi} represents the concentration in the gas at the inner surface of the fiber (the lumen side), C^{f1} represents the concentration in the fiber at the gas interface, C^{f2} represents the concentration in the fiber at the liquid interface, C^{Li} represents the concentration in the liquid at the outer surface of the fiber (shell side), and C^{BL} represents the bulk concentration in the liquid. Equation 4-1 can be used to define the mass transfer rate (N) in mol/s through the gas boundary layer (GBL), the fiber (F), and the liquid boundary layer (LBL) as shown in Equations 4-5 through 4-7 where *L* is the length of the fibers, n_{fibers} is the total number of fibers, $D_{g,f}$ is the diffusivity of the gas in the fiber material, *OD* and *ID* are the inner and outer fiber diameters, A_{r1} and A_{r2} are the total fiber areas based on the inner and outer radii, K_{GBL} and K_{LBL} are the mass transfer coefficients of the gas and liquid boundary layers.

At steady state, the mass transfer rate through each region must be equal, as shown in Equation 4-8.

$$N_{GBL} = K_{GBL}A_{r1} \cdot (C^{BG} - C^{Gi}) \quad \textbf{(4-5)}$$

$$N_F = \frac{2\pi L \cdot n_{fibers} \cdot D_{g,f}}{\ln\left(\frac{OD}{ID}\right)} \cdot (C^{f1} - C^{f2}) \quad \textbf{(4-6)}$$

$$N_{LBL} = K_{LBL}A_{r2} \cdot (C^{Li} - C^{BL}) \quad \textbf{(4-7)}$$

$$N_{GBL} = N_F = N_{LBL} \quad \textbf{(4-8)}$$

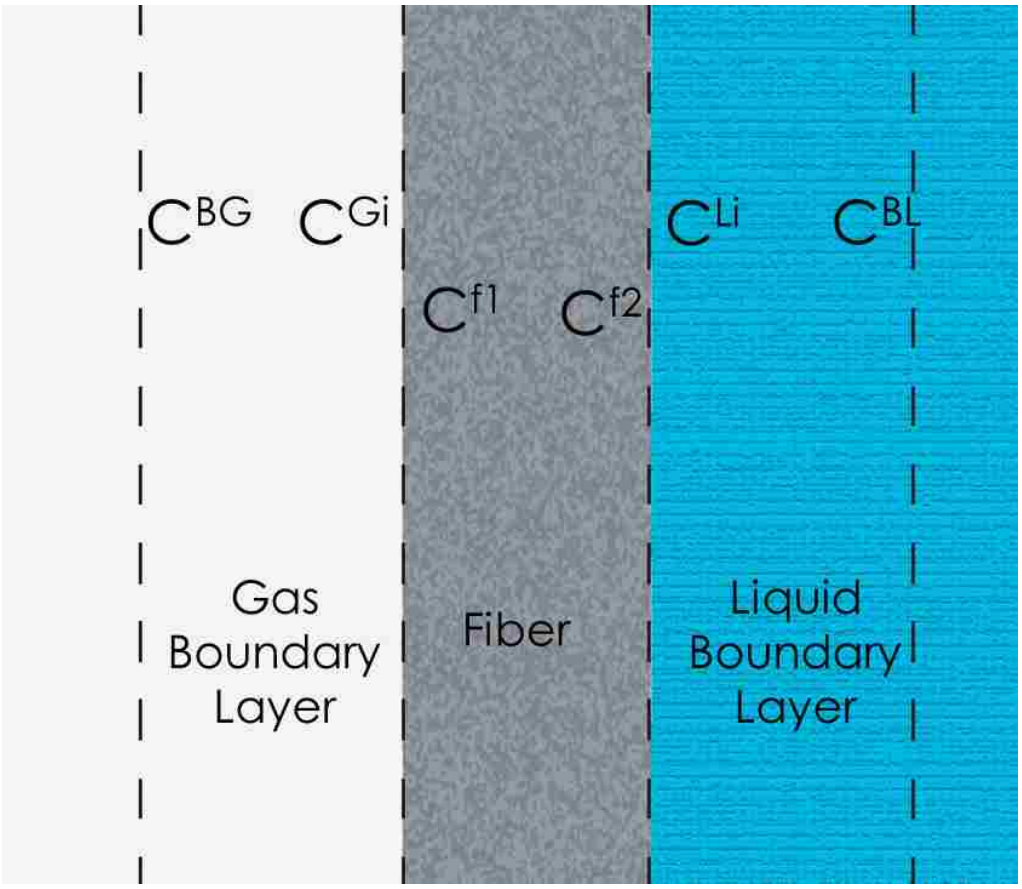

Figure 4-2. Mass transfer across hollow fiber boundary layers.

Assuming ideal gas conditions (P=CRT) and Henry's law, the concentrations at each boundary are related to each other as shown in Equations 4-9 and 4-10.

$$C^{f1} = S \cdot P_i^{Gi} = S \cdot R \cdot T \cdot C^{Gi} \quad \textbf{(4-9)}$$

$$C^{f2} = \frac{S \cdot P_i^{Li}}{H} = \frac{S \cdot R \cdot T}{H} \cdot C^{Li} \quad \textbf{(4-10)}$$

Here, R is the gas constant, T is the temperature, S is the gas solubility in the fiber material, H is the dimensionless Henry's law constant for the gas. Combining Equations 4-5 through 4-10, the mass transfer resistance through the hollow fiber module can be split into a sum of resistances through the gas boundary layer, membrane and liquid boundary layer as shown in Equation 4-11.

$$R_{tot} = R_{GBL}{}^{*} + R_F + R_{LBL} \quad \textbf{(4-11)}$$

where R_{tot} represents the total mass transfer resistance, R_{GBL} represents the resistance through the gas boundary layer, R_F represents the resistance through the fiber, and R_{LBL} represents the resistance through the liquid boundary layer. Because gas diffusivities are four orders of magnitude larger than gas-liquid diffusion, the resistance through the gas boundary layer (R_{GBL}) is very small in comparison with the fiber and liquid resistances and is considered negligible for this work.

Based on the above definitions, the overall resistance and resistances for each region are shown in Equations 4-12 through 4-14. In these equations, A is the active surface area which for a non-porous membrane is simply the fiber outer surface area. *OD* and *ID* represent the membrane outer and inner diameter. γ and δ are parameters specific to the HFR, but are independent of gas species. *Perm* represents the PDMS HFR gas permeability. Permeability is equal to the membrane gas diffusivity ($D_{g,f}$) times gas solubility (S) in the membrane. In this

work the permeability values used were 600, 340, 650, 3800×10^{-10} cm^3 (STP)· cm /(cm^2 · s · cm-Hg) for O_2, CO, H_2 and CO_2 respectively (MedArray 2011). *H* is the dimensionless Henry's law constant for the gas. The dimensionless values used in this work were 0.03, 0.03, and 0.021, and 1.22 for O_2, CO, H_2, and CO_2 respectively (Incropera, et al. 2011; Lide 1995; Smith and Harvey 2007). $D_{x,water}$ is the gas diffusivity in water. The values used in this work were 2.4×10^{-9}, 2.2×10^{-9}, 6.3×10^{-9}, and 2.0×10^{-9} m^2/s for O_2, CO, H_2, and CO_2 respectively (Incropera, et al. 2011; Wise and Houghton 1968).

$$R_{tot} = \frac{1}{K_{tot}\mathrm{A}} \quad \textbf{(4-12)}$$

$$R_F = \frac{H}{\frac{2\pi L \cdot n_{fibers}}{\ln\left(\frac{OD}{ID}\right)} \cdot Perm \cdot R \cdot T} \quad \textbf{(4-13)}$$

$$R_{LBL} = \frac{1}{\gamma \cdot Re^{\delta} \cdot Sc^{1/3} \cdot \frac{D_{x,water}}{OD} \cdot A} \quad \textbf{(4-14)}$$

The liquid boundary layer uses a model for flow across a bank of tubes because this is similar to the flow pattern in the HFR (Incropera, et al. 2011). The characteristic length used for the Reynolds number is the fiber outer diameter. The characteristic velocity is the maximum velocity found by assuming an aligned tube bank. Combining Equations 4-12 through 4-14 and dividing by the reactor volume, V_L, yields the overall volumetric mass transfer coefficient shown in Equation 4-15.

The values for γ and δ were attained by fitting the oxygen data to Equation 4-15 and minimizing the square error between the model and the data.

The 95 % confidence regions for the parameters were then calculated using the nonlinear statistics package *nlstools* in the software R (http://www.r-project.org/).

$$\frac{K_{tot}\mathrm{A}}{V_L} = \frac{1}{\left(\frac{1 \cdot V_L}{\gamma \cdot Re^{\delta} \cdot Sc^{1/3} \cdot \frac{D_{x,water}}{OD} \cdot A}\right) + \left(\frac{H \cdot V_L}{\frac{2\pi L \cdot n_{fibers}}{\ln\left(\frac{OD}{ID}\right)} \cdot Perm \cdot R \cdot T}\right)} \quad \textbf{(4-15)}$$

4.3 Results and Discussion

4.3.1 Experimental Technique Comparison and Modeling

Figure 4-3 shows $K_{tot}A/V_L$ for oxygen versus Reynolds number. The graph shows the results for the two measurement techniques described in Section 4.2.2. Two different techniques were used with oxygen mass transfer measurements in order to validate the new GC analysis technique. Figure 4-3 shows that there is no statistical difference between the two techniques. Therefore the GC analysis technique is considered to be a valid measurement tool for H_2 and CO mass transfer. The maximum average $K_{tot}A/V_L$ of 484 h^{-1} was achieved at the highest flow rate of 200 ml/min. Figure 4-3 shows that as flow rate increases, $K_{tot}A/V_L$ increases, but begins to asymptote and approach a constant. This is consistent with Equation 4-15 which shows that as the Reynolds number increases, the liquid boundary layer term becomes smaller and smaller, so that R_{LBL} approaches zero and $K_{tot}A/V_L$ is just associated with R_F which is independent of Re. The maximum mass transfer coefficient can be achieved when there is no liquid boundary layer and the only resistance is the fiber resistance. Similarly, as the flow rate decreases the mass transfer coefficient approaches zero as the liquid boundary layer becomes infinitely large. Because there is a large increase in $K_{tot}A/V_L$ with increasing Reynolds number seen in Figure 4-3, this shows

that the liquid boundary layer is the dominant resistance in this flow range. This is because of the relatively high permeability of the gasses used in this work through a PDMS HFR.

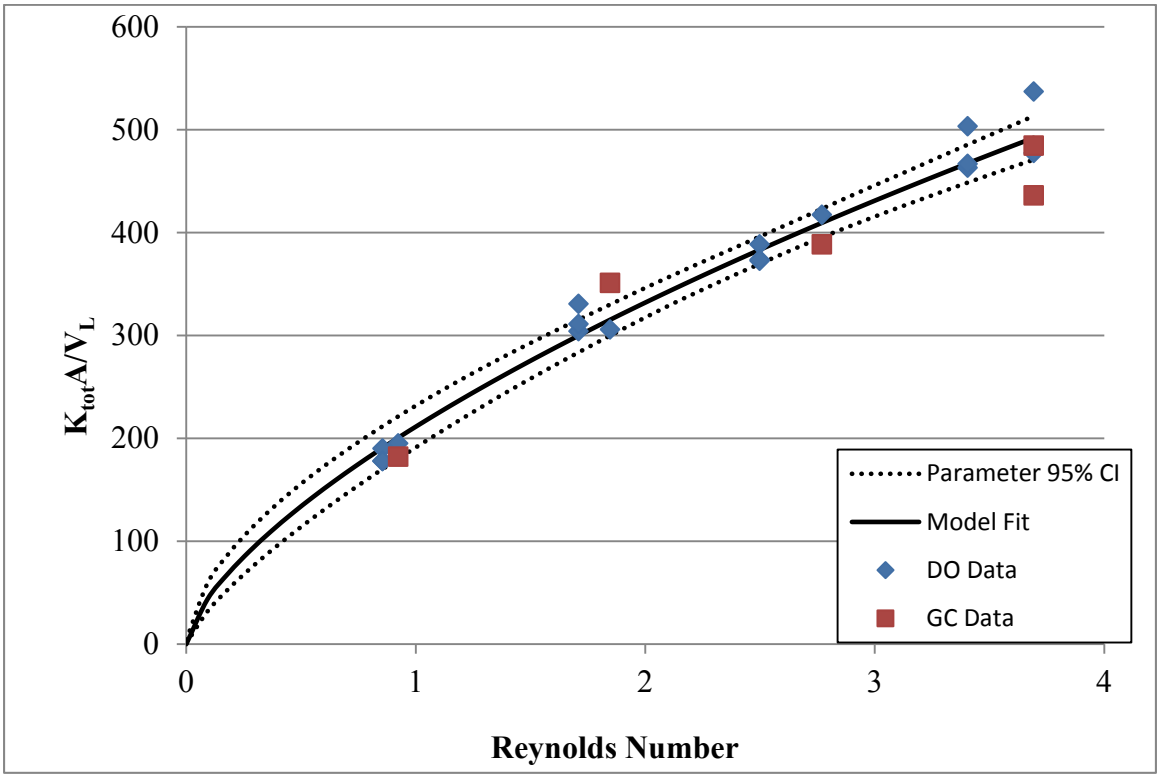

Figure 4-3. *KtotA/VL* for oxygen at different Reynolds numbers using both measurement techniques with 95% confidence interval shown.

Equation 4-15 was fit to all of the oxygen data (both measurement techniques) shown in Figure 4-3 in order to attain values for γ and δ. The fitting method is described in Section 4.2.4. The values attained for γ and δ were 0.103 ±0.004 and 0.670 ±0.035 respectively. Literature values for these parameters are typically in the range of 0.063-0.357 for γ and 0.592-0.752 for δ (Incropera, et al. 2011). Thus, the values attained in this work fall within previously attained experimental values for cross flow conditions. The model with the best fit parameters is also shown in Figure 4-15 along with the model with the parameters' 95% confidence intervals.

4.3.2 CO and H_2 Experimental Mass Transfer Coefficients

Figure 4-4 shows measured $K_{tot}A/V_L$ for CO and H_2 versus Reynolds number. The data for H_2 and CO follow the same trend as the oxygen data. The maximum average $K_{tot}A/V_L$ of 420 h^{-1} was achieved at the highest flow rate of 184 ml/min for CO. The maximum average $K_{tot}A/V_L$ of 840 h^{-1} was achieved at the highest flow rate of 181 ml/min for H_2. As flow rate increases, $K_{tot}A/V_L$ increases but begins to asymptote and approach a constant which is again consistent with Equation 4-15 which shows that as the Reynolds number increases, R_{LBL} approaches zero and $K_{tot}A/V_L$ is just associated with R_F. Also, as the flow rate decreases the mass transfer coefficient approaches zero as the liquid boundary layer becomes infinitely large. However, the magnitude of $K_{tot}A/V_L$ for H_2 is about twice that of CO or O_2. The main reason for the magnitude differences in $K_{tot}A/V_L$ is the differences in diffusivities of the gasses in water. The diffusivities of CO and H_2 in water at these experimental conditions are 93%, and 263%, respectively, as compared to O_2 (Incropera, et al. 2011; Wise and Houghton 1968). Since $K_{tot}A/V_L$ is not directly proportional to diffusivity in Equation 4-15, the differences in $K_{tot}A/V_L$ are not exactly what would be expected based solely on diffusivity differences. Since the liquid boundary layer is the dominating resistance, the differences in permeability through PDMS do not have a large effect at these flow rates.

In addition to the experimental $K_{tot}A/V_L$ values for CO and H_2 versus Reynolds number, Figure 4-4 also shows the *a priori* predicted values for CO, H_2, and CO_2 using the model shown in Equation 4-15 and the species-independent fitted parameters obtained from the oxygen data. The experimental data for CO matches the predicted values for CO very nicely and fall within the parameter uncertainty. For H_2 the experimental data matches the predicted values within the parameter uncertainty with the exception of the lowest flow rate data. The error bars for the H_2

data are noticeably higher than for the CO data. This is due to the fact that H_2 is much harder to perform experiments with than CO because of the high diffusivity of H_2 through tubing and other materials compared to other gasses. However, despite the difficulty in measuring accurate gas flow rates and concentrations, the data follow the model predictions quite well. This again confirms that the experimental technique used to measure H_2 and CO mass transfer coefficients gives accurate results. This also validates the model shown in Equation 4-15 and the parameters attained in Section 4.3.1. Because the model is assumed to be valid for any gas in which the appropriate variables are known, CO_2 is also shown in Figure 4-4 even though no experimental data was taken for CO_2 in this work. This figure shows that the $K_{tot}A/V_L$ values for H_2 are about twice that of CO or CO_2 at the same flow rate.

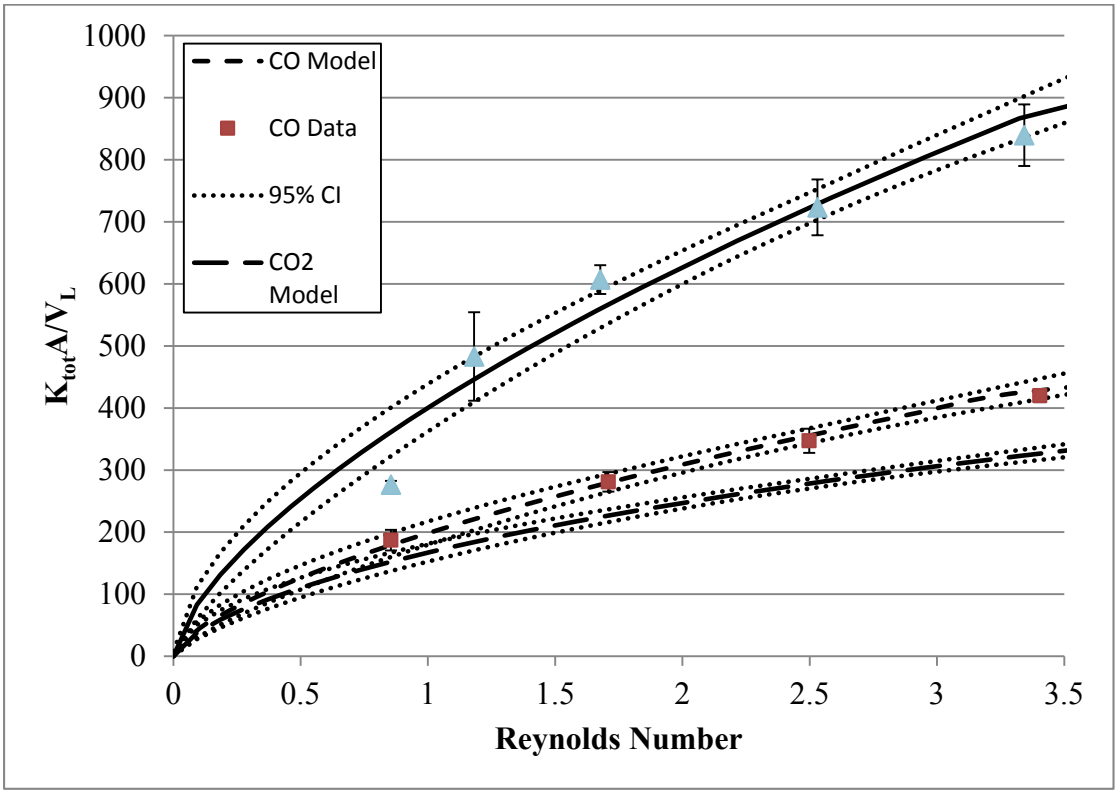

Figure 4-4. *KtotA/VL* for CO and H_2 at different Reynolds numbers with model prediction. Model prediction curve for CO_2 also shown.

4.3.3 Mass Transfer Application

One purpose of mass transfer coefficient calculations is to provide guidance on mass transfer limitations for a specific system. Figure 4-5 shows a hypothetical fermentation with one or several HFRs in series.

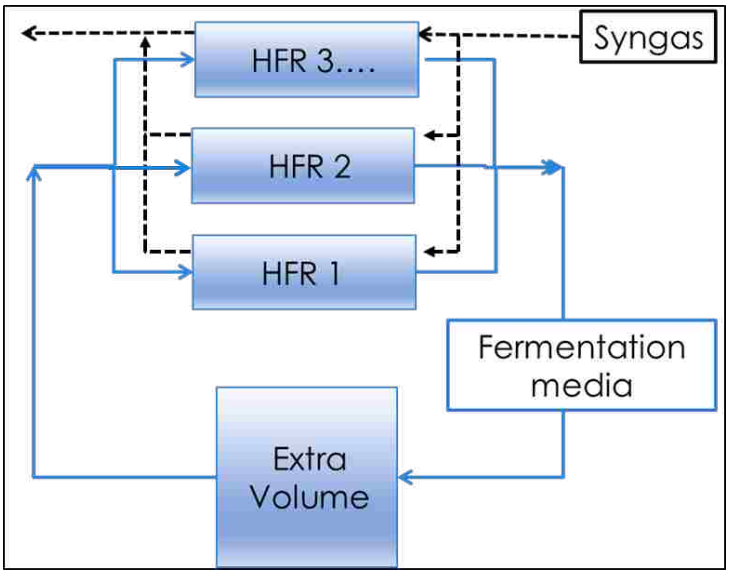

Figure 4-5. Hypothetical fermentation scheme with several HFRs in series.

The rate of gas used in a fermentation system is shown in Equation 4-16

$$R_{G,i} = R_{cells,i} \cdot X_{cells} \quad \textbf{(4-1)}$$

where $R_{G,i}$ is the volumetric gas usage of gas i, $R_{cells,i}$ is the rate of gas i used per gram of cells used for growing cells and making products, and X_{cells} is the grams of cells per total liquid volume. Assuming a well-mixed reactor, the rate of gas transferred for a HFR is shown in Equation 4-17.

$$R_{T,i} = \frac{K_{tot}A_T}{V_L}_{i} \cdot \left(\frac{V_{L_{tot}}}{V_S}\right) \cdot \left(C_{sat,i} - C_{Liquid,i}\right) \quad \textbf{(4-2)}$$

where $R_{T,i}$ is the volumetric gas usage of gas i, $C_{sat,i}$ is the well-mixed saturated concentration of gas i in the system, and $C_{Liquid,i}$ is the well-mixed concentration of gas i in the liquid, and

$K_{tot}A/V_{L,i}$ is the mass transfer coefficient of gas i. This equation assumes that the hollow fiber inlet and outlet concentration changes are small, and thus, ΔC_{lm} approaches (C_{sat}-C_{liquid}). In a real HFR fermentation system there needs to be circulating liquid and ports for removing product etc., thus, there is also an additional term that accounts for liquid that is not in the HFRs by multiplying by a V_{Ltot}/V_s ratio. V_s is the total liquid volume in the whole system, V_{Ltot} is the total liquid volume in one or more HFRs. At steady state conditions, $R_{G,i}$ and $R_{T,i}$ are equal.

$K_{tot}A/V_L$ alone does not necessarily reflect the mass transfer rates under similar conditions since the mass transfer rate is a product of the coefficient and the driving force. For example, at 200 ml/min, the $K_{tot}A/V_L$ values for CO, H_2 and CO_2 are 453, 926, and 340 h^{-1}. However, if C_{Liquid} for each gas is assumed to be zero, using Equation 4-17, the mass transfer rates for pure inlet gasses of CO, H_2 and CO_2 are 7.3, 8.2 and 240 mmol/hr, respectively. When mass transfer rates are compared, CO and H_2 are very similar, despite the mass transfer coefficient of H_2 being twice as great as CO. Also, the mass transfer rate of CO_2 is an order of magnitude greater than that of CO or H_2 despite it having the lowest mass transfer coefficient. This is due to the differences in solubility of the gasses in water. Thus, if mass transfer limitation studies are to be performed with syngas components it is important to evaluate mass transfer rates in addition to the mass transfer coefficients.

Inlet syngas partial pressures can vary depending on the source of syngas. The partial pressure depends on types of biomass gasified and type of fluidized bed reactor. Based on literature values, the average CO, H_2 and CO_2 volume percent for inlet syngas are 17%, 21%, and 15% respectively (Bingyan X. 1994; Cao, et al. 2006; Li, et al. 2004; Mansaray, et al. 1999; Miccio, et al. 2009; Pan, et al. 2000; Rapagna, et al. 2000; Turn, et al. 1998; Weerachanchai, et al. 2009). If the above calculation is repeated with the inlet liquid concentration of each gas again

assumed to be zero, the liquid flow rate is 200 ml/min and the volume percent for the inlet syngas is 17% CO, 21% H_2 and 15% CO_2, then $K_{tot}A/V_L$ values for CO, H_2 and CO_2 are again 453, 926, and 340 h^{-1}. However, the mass transfer rates for CO, H_2 and CO_2 are now 1.2, 1.7 and 36 mmol/hr respectively.

When C_{Liquid} is set to zero in Equation 4-17, this is the maximum driving force possible in a system, thus providing an upper limit to mass transfer rates. Figure 4-6 shows a plot of X_{cell} versus V_{Ltot}/V_s with different $K_{tot}A/V_L$ values obtained by equating Equations 4-16 and 4-17.

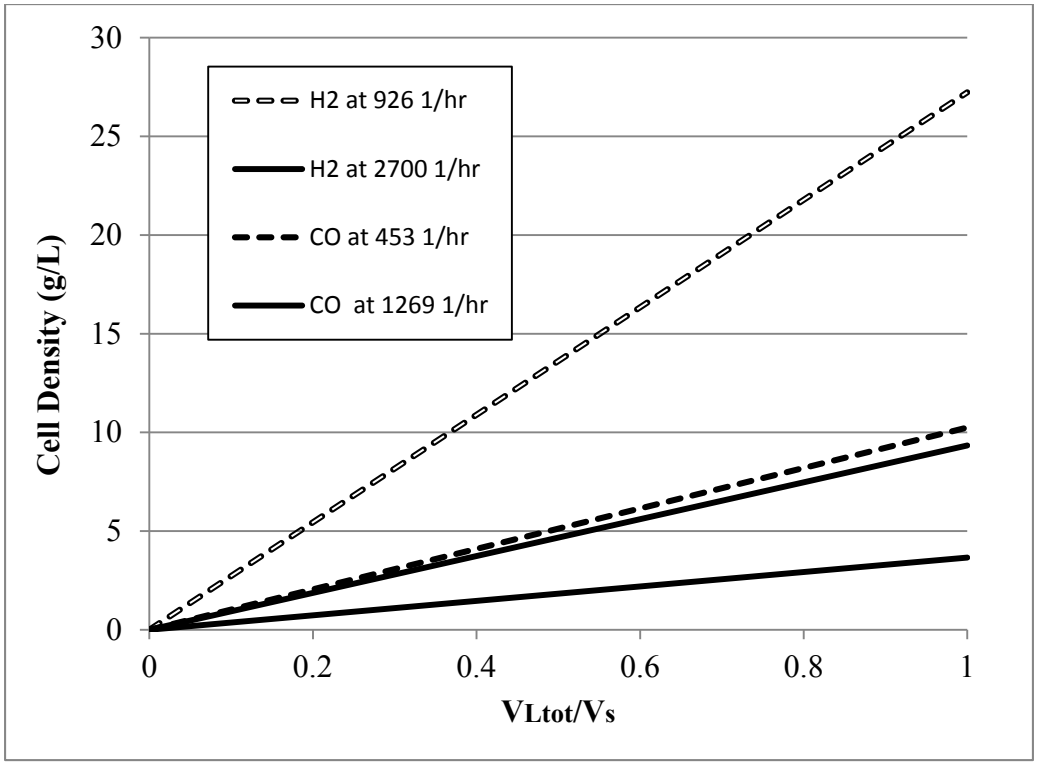

Figure 4-6. Maximum cell density of a system before becoming mass transfer limited at different volume ratios.

The data shown in Figure 4-6 assumes an inlet syngas volume percentage of 17% CO, 21% H_2 and 15% CO_2 with a balance of inert nitrogen used to calculate $C_{sat,i}$ at total pressure of 1 atm according to Equation 4-3. The $R_{cells,i}$ assumed was 0.5 and 0.4 mole/g_{cell}/day for CO and H_2 respectively. These rates are the maximum gas usage rates attained by Frankman in 50 mL

experimental bottle studies (Frankman 2009). The lines in Figure 4-6 show the maximum cell density that could possibly be supported at the given V_{Ltot}/V_s, with the aforementioned assumptions and Equation 4-16. The two lines for H_2 and CO mass transfer limitations are based on the highest mass transfer rate achievable in this type of HFR based on maximum allowable shear rates on cells, and the maximum measured mass transfer coefficients in this work. The maximum shear rate was considered to be 300 s^{-1} because literature shows that higher rates than this can potentially retard cell growth and cause cell death (Nejadnik, et al. 2008; Rickard, et al. 2004). This corresponds to a Reynolds number of 23 and a liquid flow rate of 1.2 L/min for this HFR module. The highest reported free floating cell density for syngas fermentation in a stirred tank reactor is 7.1 g/L (Abubackar, et al. 2011). However, Figure 4-6 shows that the cell concentration could reach well beyond this value especially in membrane reactors where cell immobilization can occur. According to Figure 4-6, the maximum cell density that could be supported is 10.2 g/L, for CO and 27.2 g/L for H_2. Syngas fermentation typically relies on H_2 and CO, such that the cells will become mass transfer limited on CO before H_2. Though Figure 4-6 makes several assumptions, it does provide an estimated upper limit of cell concentration with the given consumption rates. This can provide guidance in initial reactor choice to avoid mass transfer limitations.

Syngas fermentation relies on mass transfer of H_2, CO and CO_2. However, the mass transfer rates of CO and H_2 are the critical components as CO_2 is considered a waste product. H_2 has the highest mass transfer coefficients in the HFR followed by CO and CO_2. However, mass transfer rates for H_2 and CO are similar, while mass transfer rates for CO_2 are much higher, depending on reactor driving forces. When considering mass transfer limitations in a hollow fiber system there are two resistances that significantly contribute to the overall mass transfer resistance. The first is

the fiber resistance. However, if the appropriate material is chosen, then this resistance can be considered negligible, even at higher flow rates. The second resistance is the liquid boundary layer. As the flow rate increases, the liquid boundary layer decreases. However, caution should be used with high liquid flow rates in cellular systems because shear rates higher than 300 s^{-1} can potentially retard cell growth and cause cell death (Nejadnik, et al. 2008; Rickard, et al. 2004).

4.4 Conclusion

In this study a new technique was developed to measure the mass transfer coefficients for H_2 and CO using GC and gas flow rate measurements. The technique was validated by comparing O_2 data to an established traditional technique using a dissolved oxygen probe. The two techniques were found to be statistically the same ($\alpha = 0.05$). A mass transfer coefficient model was presented for mass transfer through a non-porous HFR. The model parameters were determined using oxygen data. These model parameters were independent of the gas species. These parameters were then used with the model in order to predict H_2, CO and CO_2 mass transfer coefficients for the non-porous HFR. The model was found to be in very good agreement with the experimental data for CO and H_2. The strong agreement between the mass transfer theoretical model and the experimental data again validated the method for measuring the mass transfer coefficient for H_2 and CO. This is the only study to measure both H_2 and CO mass transfer coefficients in the same study, thus directly comparing the two species. This is very important for syngas fermentation purposes because of the electron donor capabilities of both H_2 and CO. Also, to our knowledge there has only been one other study that directly measured the mass transfer coefficient of H_2 in a membrane system. Thus, this study adds to the sparse data on H_2 mass transfer coefficients in membrane systems. The mass transfer coefficient for H_2 was about twice that of CO and CO_2. However, it should be noted that the actual mass transfer rates

will depend on the driving force in the actual fermentation system. Based on the predictions made in this study and the mass transfer coefficients measured, HFRs can support high cell densities without mass transfer limitations if the proper experimental configuration is achieved. Thus, the HFR may be a reactor of choice for syngas fermentation based solely on the mass transfer capabilities.

5 Hollow Fiber Membrane Fermentation

5.1 Introduction

Typical reactors that have been used in the past for syngas fermentation are the stirred tank reactor (STR) and the trickle bed reactor (TBR). The hollow fiber membrane reactor (HFR) has recently gained attention for use in syngas fermentation because of its high mass transfer rates and surface area to volume ratios (Atchariyawut, et al. 2008; Ebrahimi, et al. 2005; Monk, et al. 1999; Nerenberg and Rittmann 2004; Rao and Mutharasan 1986). Though membranes have been used extensively with microorganisms in the past, the application to syngas fermentation is a newer technique that is currently being investigated (Hickey, et al. 2010; Hickey, et al. 2009; Tsai, et al. 2009a; Tsai, et al. 2009b; Tsai, et al. 2009c; Tsai, et al. 2009d).

The microorganisms used in syngas fermentation generate little metabolic energy from the process and, as a result, grow very slowly and produce the most biofuel during the non-growth phase of their life cycle (Tsai, et al. 2009d). Because of this fact, cell retention is particularly important in order to achieve high cell concentrations and thus high yields. Membrane reactors such as the HFR can prove useful for cell retention because of the possibility for biofilm formation on the membrane. Hickey et al. showed that a biolayer of *C. ragsdalei* grew on the exterior surface of the hollow fibers membranes in their system (Hickey, et al. 2010). In this system, the cells were exposed to syngas directly, while liquid media circulated on the lumen side. The system operated for a total of 406 hours. In order to confirm the presence of a biolayer, the fibers were viewed under an electron scanning microscope revealing a biolayer

30-40 μm thick. Though a biolayer was efficiently immobilized onto the fibers, ethanol production decreased to 0.4 g/L at 193 hours and eventually 0 g/L after 406 hours. The low ethanol could have been a result of the biolayer being separated by a membrane from the liquid media. In another experiment by Hickey et al., media with active *C. ragsdalei* was continuously circulated on the shell side while syngas flowed through the lumen side (Hickey, et al. 2010). After 480 hours the fermentation liquid contained 10 g/L of ethanol. In this case there is no mention of biofilm formation. In another experiment by Tsai et al., a polysulfone hollow fiber unit was inoculated with an active culture of *Clostridium carboxidivorans* (Tsai, et al. 2009d). These studies show that in some cases a biolayer can form on the membranes in a HFR. However, the formation of a biolayer when the cells are in the circulating media is not clear. Further experiments need to be conducted that show the conditions necessary for biolayer formation in syngas fermentation.

In a review of biological conversion of CO, the authors provide a comparison between several different biological reactors including membrane reactors (Abubackar, et al. 2011). In this review, the highest concentration of ethanol (30 g/L) is achieved by *C. ragsdalei* in a modular membrane supported bioreactor after 30 days. Using this same microbe, in a stirred tank bioreactor, the process took 59 days to reach 25 g/L of ethanol, whereas *C. ljungdahlii* took only 1 day in the same reactor to reach half of this level of ethanol. Based on this review, membrane reactors have the potential to outperform traditional reactors, possibly because of the high mass transfer rates and cell retention capabilities.

However in these experiments there are many factors that could also greatly affect the system besides the type of reactor. For example, in two membrane bioreactor studies that use *C. ragsdalei* as the fermenting organism, there is a slightly different media composition between the

studies. Tsai et al. used 30 ml of mineral solution and 5 ml reducing agent per liter of media in their membrane bioreactor (Tsai, et al. 2009d). Hickey et al. used 25 ml of mineral solution and 2.5 ml reducing agent per liter of media in their moving bed membrane bioreactor (Hickey 2009). These slight changes in media composition can have large effects on ethanol production and cell concentration. Other confounding factors are the gas retention time, liquid circulation rates, pressure, composition, and culture elapsed time. The objective in this work was to analyze whether the higher mass transfer capabilities of HFRs result in better product formation rates in HFR fermentation studies compared to other common bioreactors. This work analyzed biofilm formation along with the effects of HFR volume to total liquid volume ratios and other effects such as liquid circulation rates, culture elapsed time, and media replacements.

5.2 Materials and Methods

5.2.1 HFR Media and Cells

The media in the HFR studies was made by adding 10 ml metals stock solution, 30 ml mineral stock solution, 10 ml vitamin stock solution, 1 g yeast extract, and 10 g MES buffer to 950 ml distilled water. The trace metals stock solution contained (per liter) 0.2 g cobalt chloride, 0.02 g cupric chloride, 0.8 g ferrous ammonium sulfate, 1 g manganese sulfate, 0.2 g nickel chloride, 2 g nitrilotriacetic acid, 0.02 g sodium molybdate, 0.1 g sodium selenate, 0.2 g sodium tungstate, and 1 g zinc sulfate. The mineral stock solution contained (per liter) 4 g calcium chloride, 20 g hydrated magnesium sulfate, 10 g potassium chloride, 10 g potassium phosphate monobasic, and 80 g sodium chloride. The vitamin stock solution contained (per liter) 0.005 g aminobenzoic acid, 0.002 g d-Biotin, 0.005 g pantothenic acid, 0.002 g folic acid, 0.01 g MESNA, 0.005 g nicotinic acid, 0.01 g pyridoxin, 0.005 g riboflavin, 0.005 g thiamine, 0.005 g

thioctic acid, and 0.005 g vitamin B12 (Rajagopalan, et al. 2002). After preparing media from stock solutions, the media was titrated to pH 6.0 using 5N KOH (EMD Chemicals, Gibbstown, New Jersey). After titration, the solution was made anaerobic by boiling and purging with nitrogen. Then, 1% vol/vol of a Na_2S solution, containing 4 g of $Na_2S{\cdot}9H_20$ (EMD Chemicals, Gibbstown, New Jersey) in 100 mL water and 4 g of L-cysteine (Sigma-Aldrich, St. Louis, Missouri) in 100 mL water, was added to act as an oxygen scavenger.

The bacterium used in this study was *Clostridium ragsdalei* denoted as P11. P11 was kindly provided by Ralph Tanner from the University of Oklahoma. The source was originally isolated from the sediment of an agricultural settling lagoon. Before addition to the experimental system, P11 was passaged three times in the media noted above with an additional 1% vol/vol cysteine-sulfide solution. The inoculums for experiments conducted in this work were chosen when cells were in the exponential growth phase during the third passage.

5.2.2 Hollow Fiber Reactor Setup

A schematic of the HFR fermentation is shown in Figure 5-1. The liquid was circulated from the HFR shell side through the sump and back into the HFR. The syngas flowed countercurrent to the liquid through the HFR into the sump and then out the sump outlet and vented. The hollow fiber module used in this work was the Optiflux F160 NR module (Fresenius, Ogden, UT, USA). This HFR was chosen based on the results of the O_2 mass transfer studies performed in Chapter 3. This HFR was chosen to represent an HFR that has average mass transfer capabilities and would be a typical porous HFR used in syngas fermentation. The membrane was made of Fresenius polysulfone denoted as FPS. The membrane was porous and slightly hydrophilic. The outer diameter of the fibers was 280 μm and the fibers were 40 μm thick. The shell priming volume was measured to be 237 mL by adding water to the shell side of the reactor until filled.

The area to volume ratio of the reactor was 9,198 m^{-1} calculated by dividing the outer diameter surface area by the priming volume. The media was circulated by a calibrated peristaltic pump (Masterflex; Model #7523-90). Masterflex Norprene tubing was used for both the gas and liquid tubing to ensure minimal O_2 transfer through the tubing. The inlet gas flow rate was controlled by a calibrated mass flow controller (Parker Porter; Model 201). In order to take redox and pH measurements, and provide a pressure equilibrium area between the lumen and shell side of the reactor, a liquid sump was used. The sump was a 3 liter BioFlo 110 Benchtop Fermentor (New Brunswick Scientific, Brunswick, New Jersey). A bioreactor was used as the sump because it provided air-tight seals for the redox and pH probes and also for the inlet and outlet lines for the liquid and gas. The volume in the sump was kept to a minimum (0.3-0.6 liters) and the gas was not bubbled through the media so that most of the gas usage occurred in the HFR. pH and redox potential were continuously measured using pH and ORP probes (Cole Parmer, Vernon Hills, Illinois) inserted into the sump.

Liquid and gas sample ports were placed on the liquid and gas outlets of the HFR and on the gas outlet of the sump. The sample ports were constructed by using a t-valve connected in-line. After the valve, a septum was inserted into a Swagelock connector that was then screwed on to the valve outlet. This provided a valve that could remain closed until a liquid or gas sample was taken. The gas samples were taken by opening the valve and inserting a needle connected to a 5 ml gas tight syringe through the septum. The gas sample was analyzed using a Shimadzu 2014 Gas Chromatograph (Shimadzu Scientific Instruments, Columbia, Maryland) with a thermal conductivity detector and a Carboxen 1010 PLOT capillary GC column (Sigma-Aldrich, Switzerland). The liquid sample was taken by opening the valve and inserting a needle through the septum in the same manner as the gas. Optical density was measured at 660 nm with a UV-

spectrophotometer (1700 UV-spectrophotometer, Shimadzu, Columbia, MD). The liquid sample was centrifuged and the cell-free supernatant was analyzed for ethanol and acetic acid using a Shimadzu 2014 Gas Chromatograph (Shimadzu Scientific Instruments, Columbia, Maryland) with a flame ionization detector and a Restek Porapak QS 80/100 Shimadzu 14A column (Bellefont, Pennsylvania).

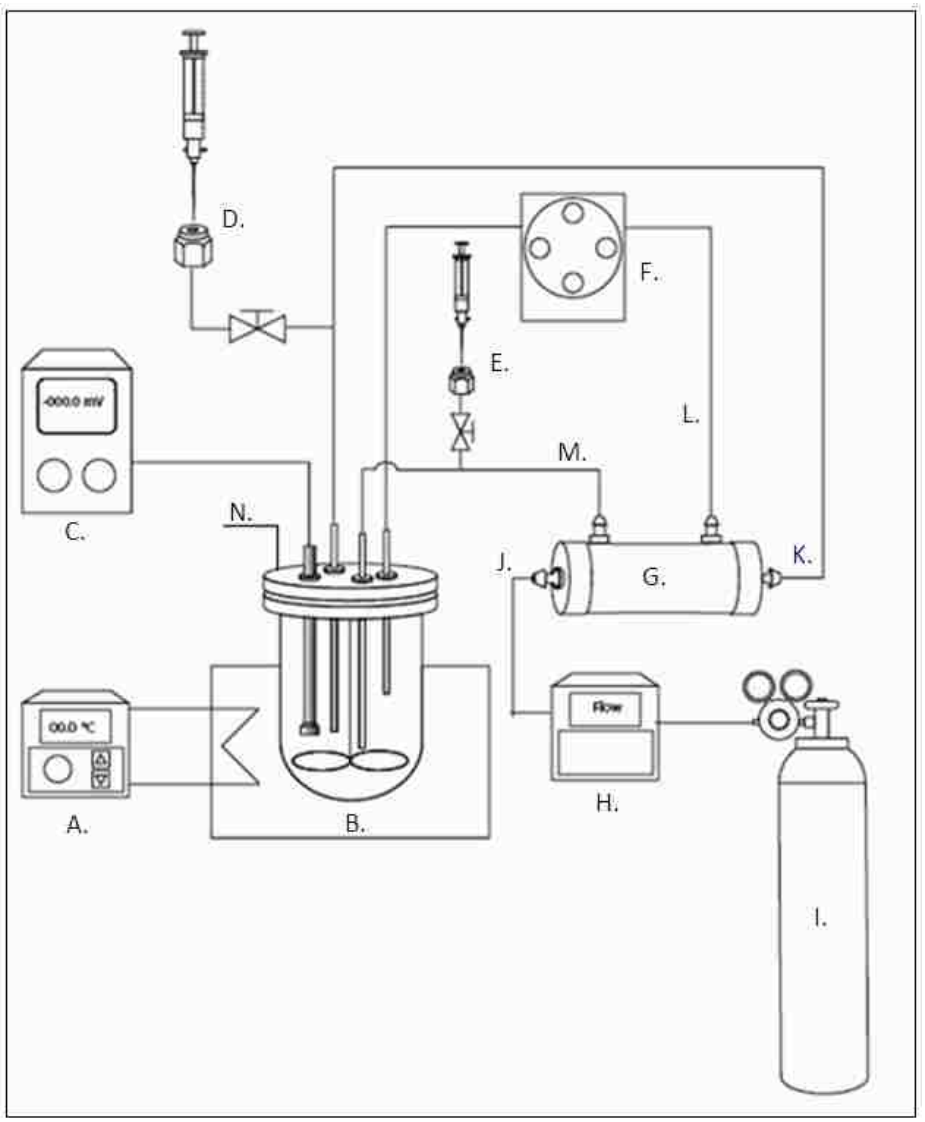

Figure 5-1. Hollow fiber fermentation experimental setup showing (A) temperature controller, (B) heated sump, (C) redox transmitter, (D) gas sample port, (E) liquid sample port, (F) peristaltic pump, (G) hollow fiber reactor, (H) syngas flow rate controller, (I) syngas cylinder, (J) gas line into HFR, (K) gas line out of HFR, (L) liquid line into HFR, (M) liquid line out of HFR, and (N) gas line out of sump

5.2.3 Hollow Fiber Reactor Fermentations

After media preparation, the media was put in serum bottles and autoclaved at 121 °C for 15 minutes and then purged with N_2 at ~1500 sccm for two minutes. Bottles were then pressurized with N_2 at 20 psig. The HFR reactor as described above was autoclaved at 121 °C for 15 minutes and then purged with syngas (30% H_2, 30% CO_2 and 40% CO) for at least 2 hours at 220 sccm. Once purged, media was added into the reactor through the liquid port by inserting a needle attached to an autoclaved tube with a syringe on both ends into the liquid port and the bottled media. Media was usually prepared in 50 mL aliquots, so several bottles were used until the appropriate amount of media was added to the reactor. After the media was added to the reactor, inoculum was added in the same manner. A 20-50% inoculum was used throughout these experiments. The total media in the reactor ranged from 600 mL to 1250 mL depending on the experiment being performed. Syngas containing N_2 (5% N_2, 28.5% CO_2, 28.5% H_2, 38% CO) then flowed through the reactor at 7.9 sccm. N_2 was used as an inert species in order to assess gas usage by the use of a mass balance and outlet gas concentrations obtained by GC analysis. The liquid flow rate was set to the pump maximum of 170 mL/min for all experiments except one. The high liquid flow rate provided a higher mass transfer rate (see Chapter 3). The reactor was pressurized slightly above atmospheric pressure (1.2 psig) to avoid any oxygen contamination.

The HFR fermentations were run in a semi-batch manner according to the following method. After inoculation, the HFR was run until the outlet CO concentration was 80-90% of the inlet CO concentration. At this point, media was removed from the HFR leaving only 20-50% of the original media containing cells. Fresh media was then added according to the method described

above to obtain the original volume. The total volume remained constant from one media replacement to the next.

5.3 Results and Discussion

5.3.1 Biofilm Formation

Based on the literature discussed in Section 5.2, it is unclear whether or not a biolayer is formed in an HFR when cells are circulated in the liquid media on the shell side with syngas flowing through the lumen side of the fibers. A true biofilm contains bacteria enclosed in a protective extracellular polymeric matrix (Hall-Stoodley, et al. 2004). Thus, this biofilm study was to assess whether or not a true biofilm was formed, whether or not the cells were loosely attached to the fibers, or if there was any cellular affinity to the fibers. A preliminary biofilm experiment was performed by altering cell growth in a bottle to incorporate hollow fibers. This initial experiment used a 150 ml bottle of media with a syngas inlet and outlet going through the stopper at the top. The syngas flowed through a bundle of about 20 PDMS hollow fibers that were immersed in the media. The fibers had an outer diameter of 300 μm and were 50 μm thick. This setup is shown in Figure 5-2.

The bottle was regassed daily with syngas to a pressure of about 15 psig. After 6 days the bottle had reached an optical density (OD) of 0.37. The fibers were then removed and examined under a light microscope. Figure 5-3 shows a picture from a fiber that was not rinsed after removal from the experiment. Figure 5-4 shows a fiber that was rinsed by squirting DI water on the fiber. Though there is no apparent biofilm in Figure 5-3, individual bacterium can be seen on the fiber. However, when the fibers were rinsed, no bacteria can be seen on the fibers.

This preliminary experiment showed evidence of loosely attached cells as opposed to a biofilm formation. However, in order to confirm these results another experiment was performed that more closely mimicked how an actual HFR would be used in syngas fermentation. In this next study the experiment was setup according to Section 5.3 with the Optiflux HFR. The conditions used in this experiment were set to allow for maximum biofilm formation by using a lower liquid flow rate and a higher gas flow rate than were used in later experiments. The liquid circulation rate was set to 40 ml/min with a gas flow rate of 66 sccm. The experiment was inoculated with a 16% vol/vol inoculum. A liquid sample was taken every 24 hours in order to monitor cell growth and product formation. After 12 days the experiment was terminated and the HFR unit was carefully cut open in order to remove the bundle of fibers. The OD and product formation are shown in Figures 5-5 and 5-6.

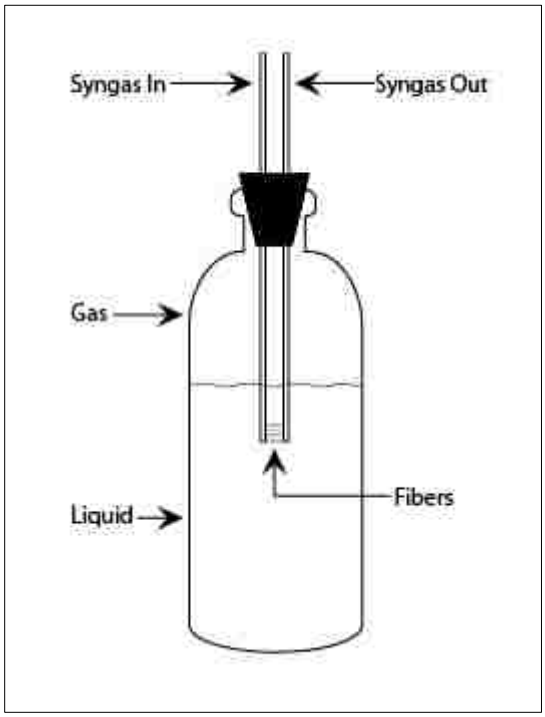

Figure 5-2. Bottle fiber biofilm study experimental setup.

Figure 5-3. Image of PDMS hollow fiber under a light microscope before rinsing. No apparent biofilm is present, but loosely attached individual bacterium can be seen.

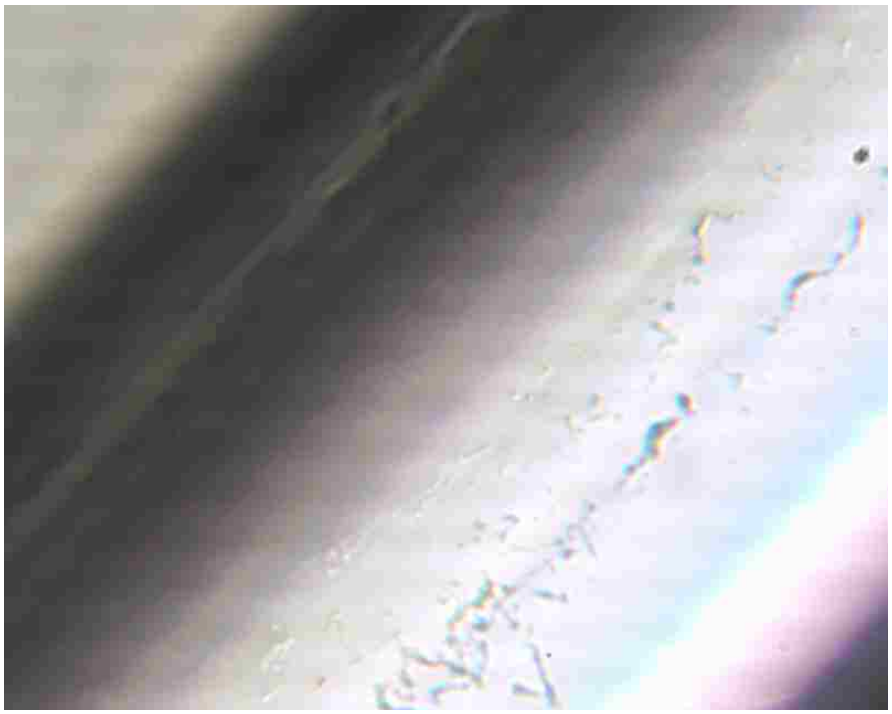

Figure 5-4. Image of PDMS hollow fiber under a light microscope after rinsing. No bacteria are present.

This preliminary experiment showed evidence of loosely attached cells as opposed to a biofilm formation. However, in order to confirm these results another experiment was performed that more closely mimicked how an actual HFR would be used in syngas fermentation. In this next study the experiment was setup according to Section 5.3 with the Optiflux HFR. The conditions used in this experiment were set to allow for maximum biofilm formation by using a lower liquid flow rate and a higher gas flow rate than were used in later experiments. The liquid circulation rate was set to 40 ml/min with a gas flow rate of 66 sccm. The experiment was inoculated with a 16% vol/vol inoculum. A liquid sample was taken every 24 hours in order to monitor cell growth and product formation. After 12 days the experiment was terminated and the HFR unit was carefully cut open in order to remove the bundle of fibers. The OD and product formation are shown in Figures 5-5 and 5-6.

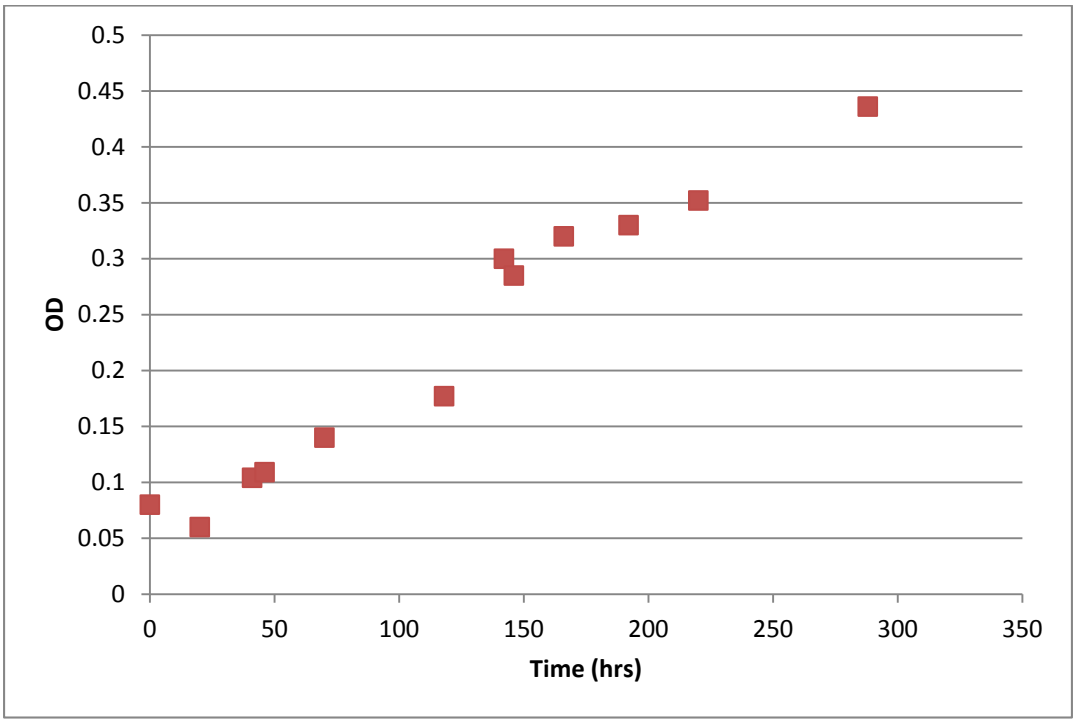

Figure 5-5. Cell growth during HFR fermentation for fiber microscopy study.

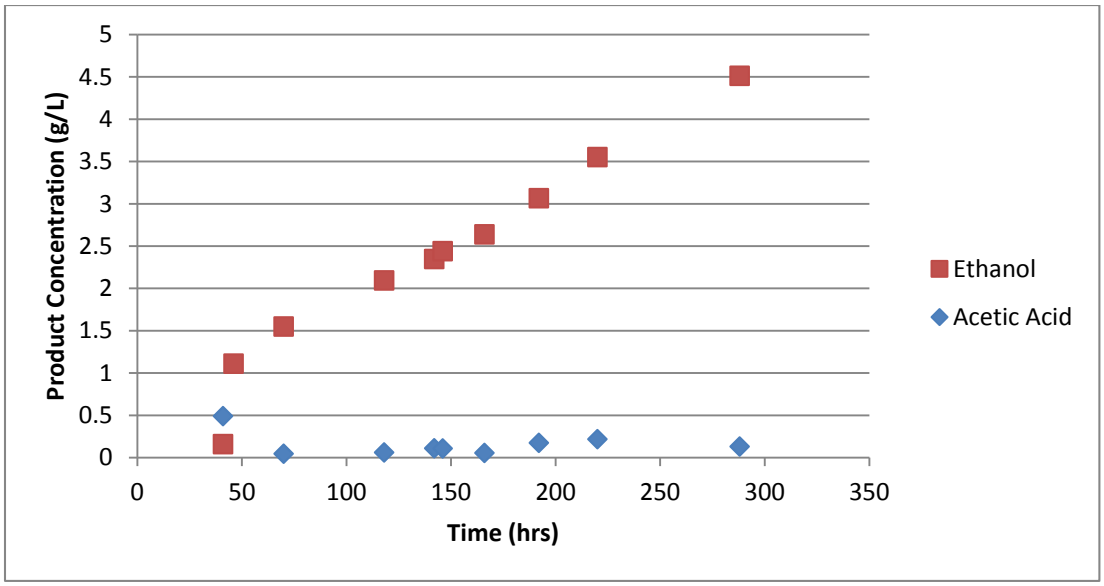

Figure 5-6. Product formation showing active cell culture for HFR fermentation for fiber microscopy study.

The fibers examined were chosen from the center and outer parts of the fiber bundle in order to represent all locations in the bundle. Instead of a light microscope, a scanning electron microscope (SEM) was used in order to determine biofilm formation. The SEM was chosen in order to give a more precise view of the cells on the fibers and also because the Optiflux fibers were not optically transparent and thus could not be used with a light microscope. Three different treatment methods were used in order to see the level of cell attachment. The first method was to not rinse or treat the fibers with any chemical but metallic sputter coating with palladium was used. The metal coating is needed in the SEM to disperse the charge caused by the beam of electrons, thus obtaining a clear image. The second method was to fix cells that might have been attached on the fibers by soaking the fibers in 2.5% glutaraldehyde for one hour. Glutaraldehdye fixes cells by crosslinking the cell's proteins together into a matrix. The samples were sputter coated with palladium. The third method did not treat the fibers in any way, not even with the metallic sputter coating. The result of not using sputter coating was that images were not as clear

as the sputter treated results. Figures 5-7 through 5-11 show scanning electron micrographs of fibers using the three methods. Figure 5-7shows fibers treated using method 1 showing a view where some bacteria can be seen on top of the fibers. Figure 5-8 shows a side view of one fiber treated with method 2 showing that there is no extra biofilm thickness on the outer layer of the fiber. The porosity of the fibers can clearly be seen in this SEM. Figures 5-9 through 5-11 show fibers with method 3. These images are not nearly as clear as the metal coated samples because of charge buildup in the microscope. However, in Figure 5-9 material can be seen on top of the fiber. It is likely that this is a mixture of cells and crystalline minerals from the media. Figure 5-10 shows a close up of the material showing some boundaries that could be dehydrated cells in the crystals and Figure 5-11 shows a view of the material indicating sharp crystalline-like boundaries. It is likely that this material is not a polymer matrix because it is not apparent in the samples treated with methods 1 and 2. All of these figures demonstrate that the cells were only loosely attached, likely dislodged in the glutaraldehyde solution, or came off during the sputtering treatment.

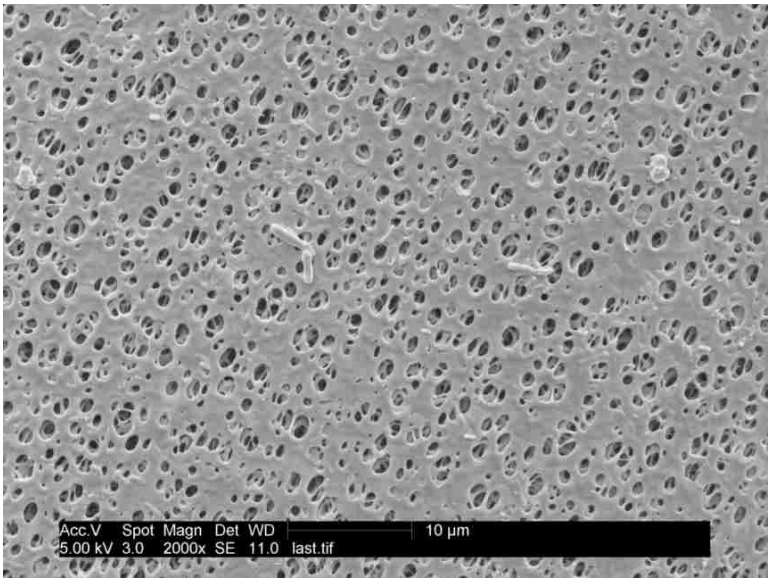

Figure 5-7. Top-view SEM of a fiber treated by method 1. Individual bacterium can be seen.

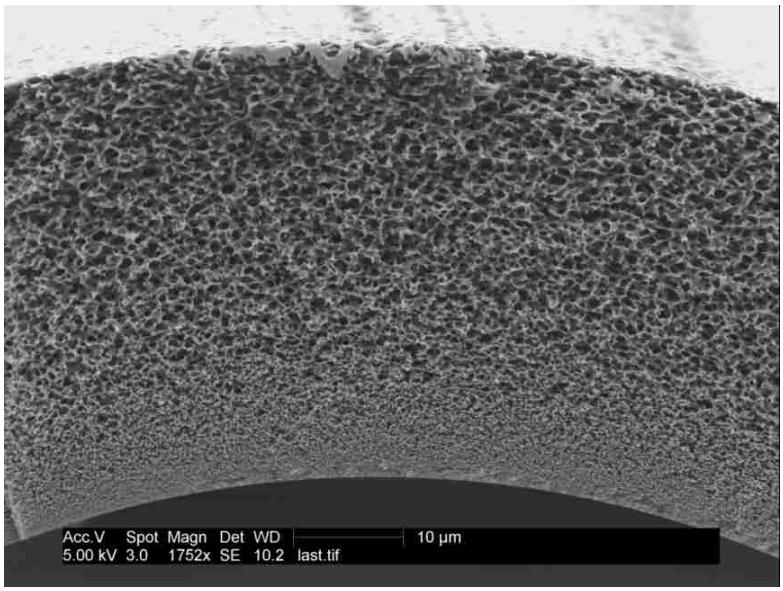

Figure 5-8. Side-view SEM of one fiber treated by method 2. No extra biofilm thickness can be seen on the outer layer of the fiber.

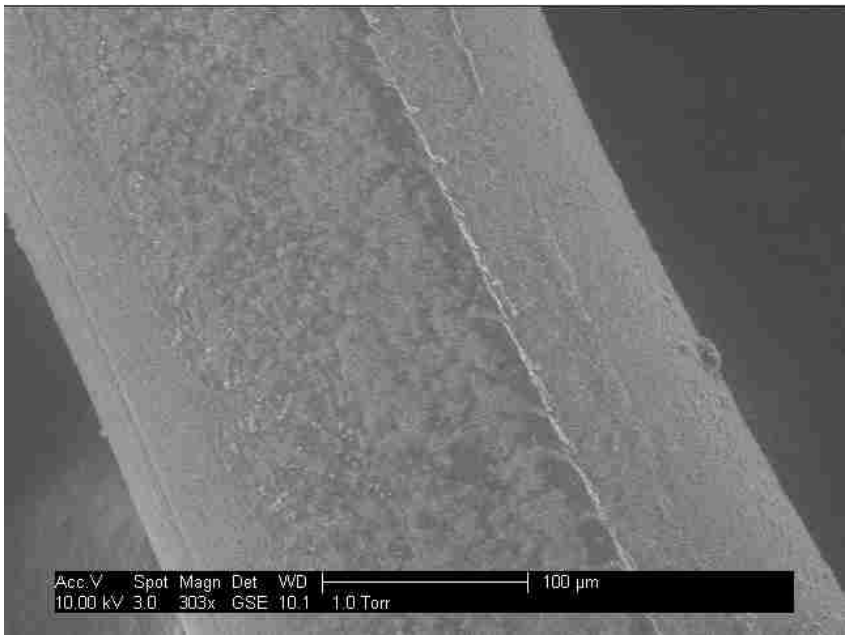

Figure 5-9. Top-view SEM of a fiber not treated (method 3) showing what is likely a mixture of cells and crystalline minerals from the media.

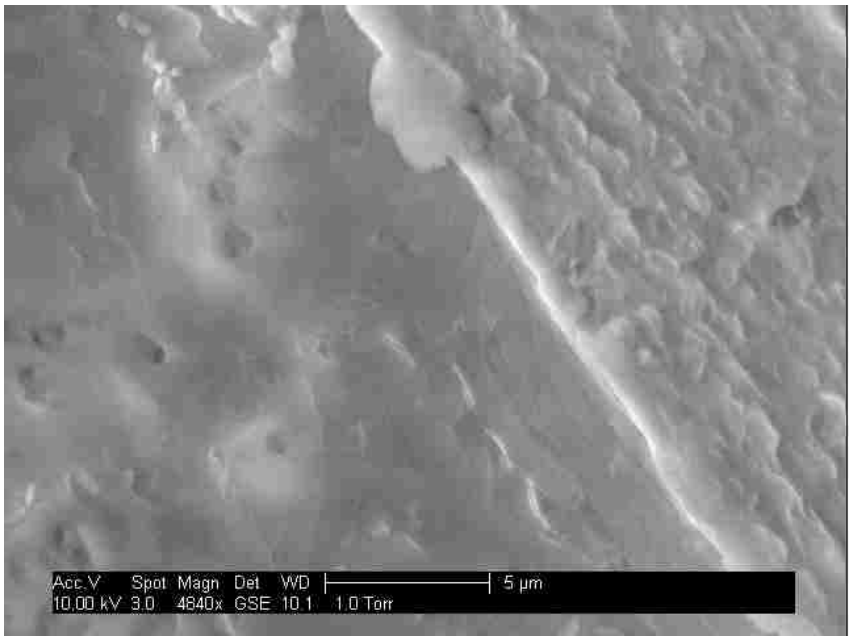

Figure 5-10. Magnified SEM of the material seen in Figure 5-9. Possible cell outlines can be seen.

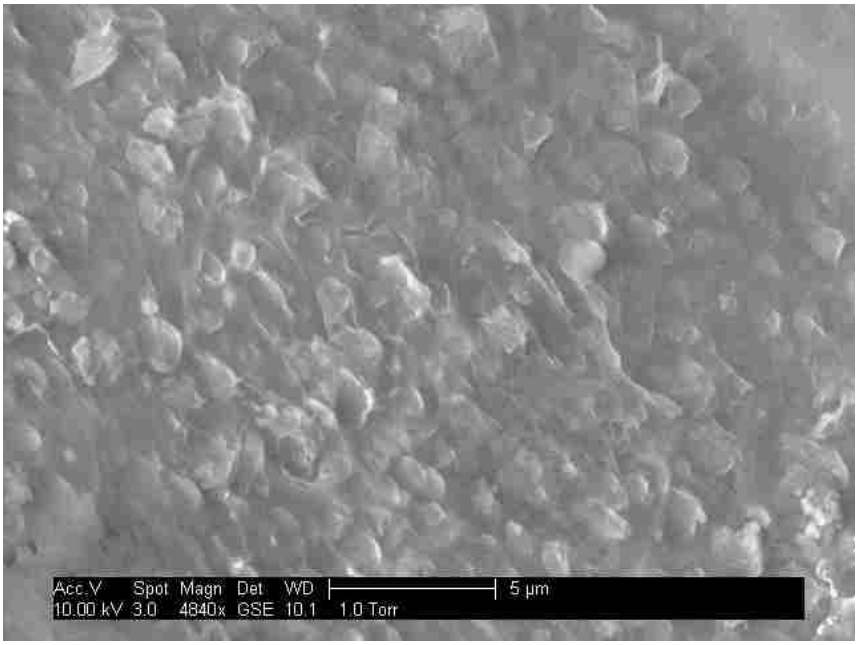

Figure 5-11. Magnified SEM of the material seen in Figure 5-9. Crystalline structures can be seen.

These figures show that there is no obvious biofilm formation, but they do give indications of loosely attached cell formations on the fiber surface. In order to confirm that there were indeed

loosely attached cells, another experiment was performed that measured the amount of loosely attached cells. This experiment used the hollow fiber reactor from the HFR1 experiment discussed in the next section. In this experiment, there was 833 mL total liquid with a circulation rate of 170 ml/min and a syngas flow rate of 7.9 sccm. After two media replacements and a total of 30 days run time, the liquid OD was 0.1 which is equivalent to 0.04 g of cells. The HFR was then emptied of the previous liquid and refilled with DI water several times. A preliminary experiment showed that over a short testing period, DI water does not affect the measured cell concentration. After each refill, the HFR liquid was emptied into a beaker. After several refills the liquid became clear. At that point the total liquid volume was measured and then OD of the liquid was taken. The total volume was 720 ml with a 0.827 OD. Using the conversion of 0.5155 g/L times OD to give cell density (g_{cell}/L) and the total volume, it was calculated that there were about 0.3 grams of cells loosely attached on the fibers. Thus, there were 0.3 grams associated with the fibers and 0.04 grams in the bulk solution showing that a majority of the cells were located in the fiber unit. The cell amount associated with the fibers is equivalent to about 3×10^{11} cells assuming 10^{-12} g/cell (wet) (Davis B. 1973). With a projected surface area of 5 μm^2 per cell, the cells could cover a surface area of approximately 1.5 m^2 with a monolayer of cells. This compares to the HFR surface area which was also1.5 m^2. Thus, it appears that cells could have covered the full surface area of the fibers in a monolayer even though this was not observed in the microscopes. Since the cells were only seen sporadically in the electron micrographs, then they must have been washed off in the preparation procedure. Thus, we can conclude that there can be a large amount of cells loosely attached to the fibers that can be easily washed off and dislodged. Or the cells could have been largely in the interstitial spaces of the fibers and not spread evenly across the full fiber area.

5.3.2 HFR Fermentation Results

5.3.2.1 HFR1 Results

The first experiment denoted as HFR1, used a total liquid volume (*Vs*) of 833 mL. There were 4 media replacements performed in this experiment, including the initial inoculation, as shown in Figure 5-12. All fermentation studies are labeled as HFRx-y, where x represents the experiment number and y represents the media replacement cycle within the experiment. The optical density for the free floating cells with time is shown in Figure 5-12 and the liquid product concentrations with time are shown in Figure 5-13 through 5-14. The redox potential is shown in Figure 5-15 and the pH with time is shown in Figure 5-16.

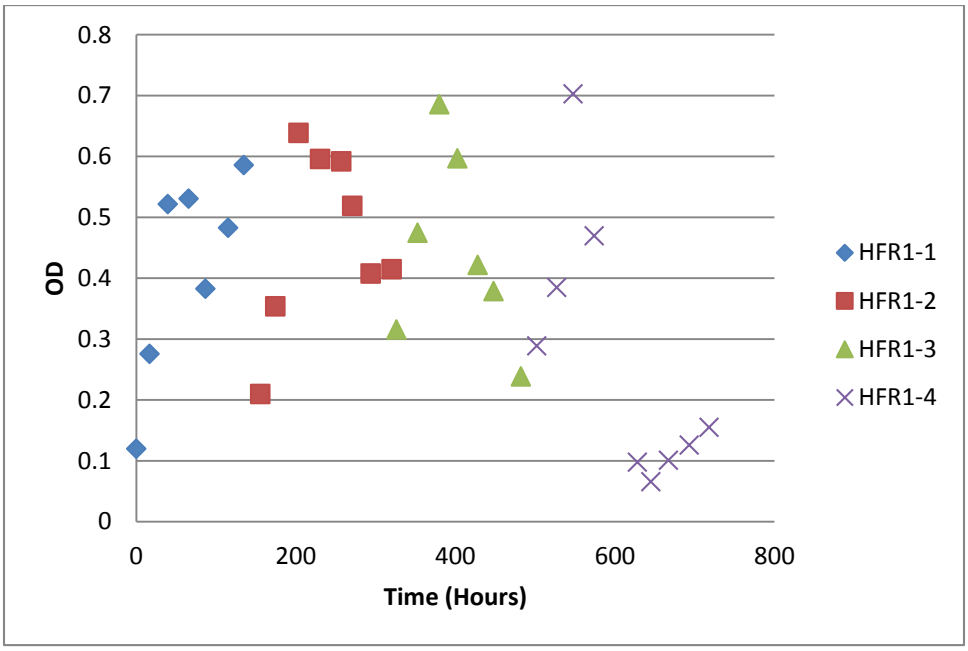

Figure 5-12. Optical density for the free floating cells over time for HFR1. Each media replacement data set is labeled as HFR1-1, 2, 3, and 4 respectively.

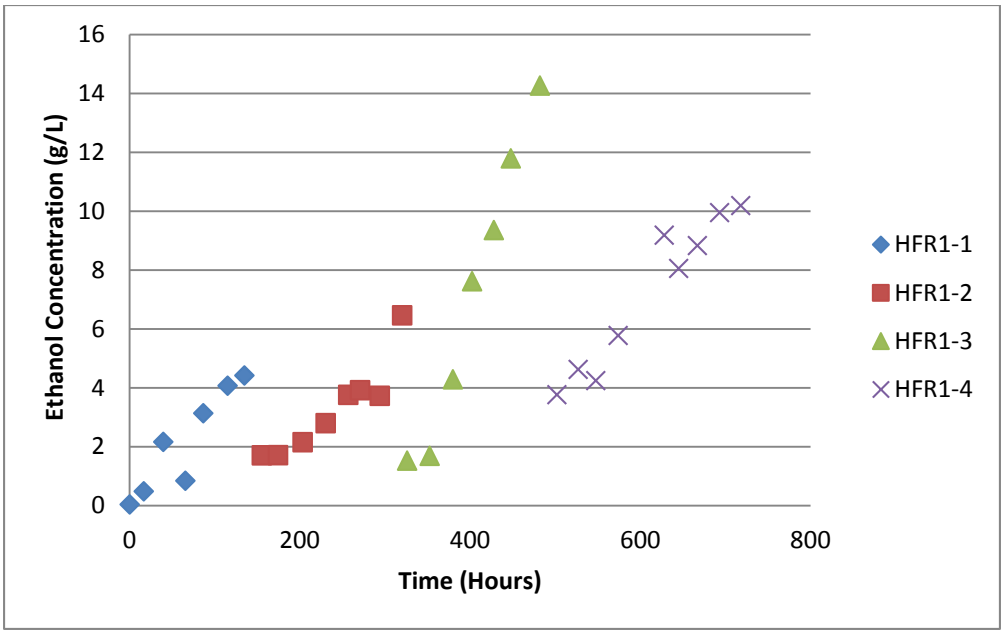

Figure 5-13. Liquid ethanol concentration over time for HFR1. Each media replacement data set is labeled as HFR1-1, 2, 3, and 4 respectively.

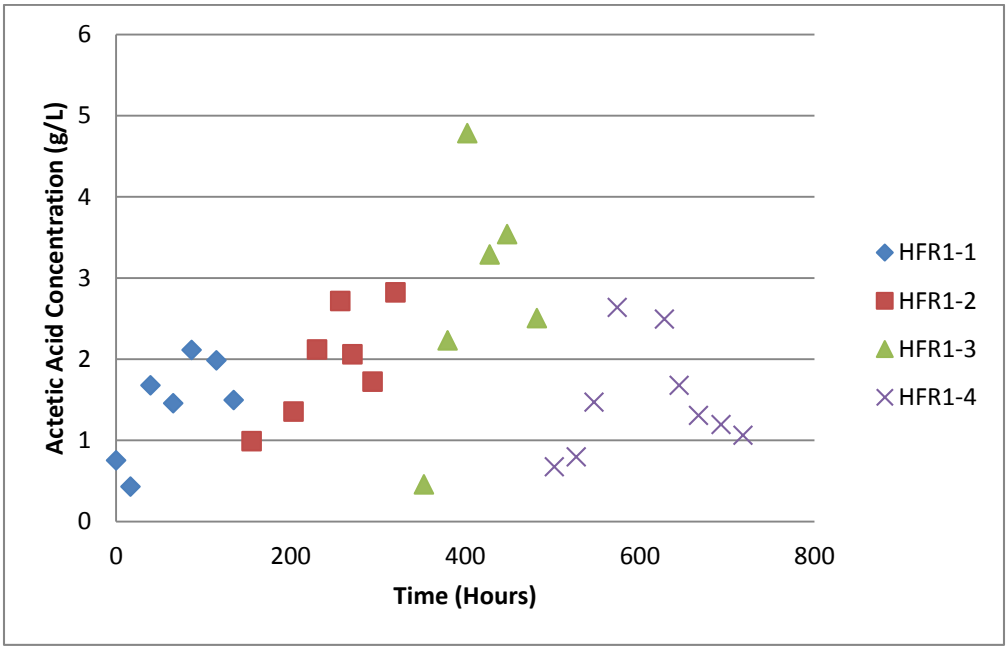

Figure 5-14. Liquid acetic acid concentration over time for HFR1. Each media replacement data set is labeled as HFR1-1, 2, 3, and 4 respectively.

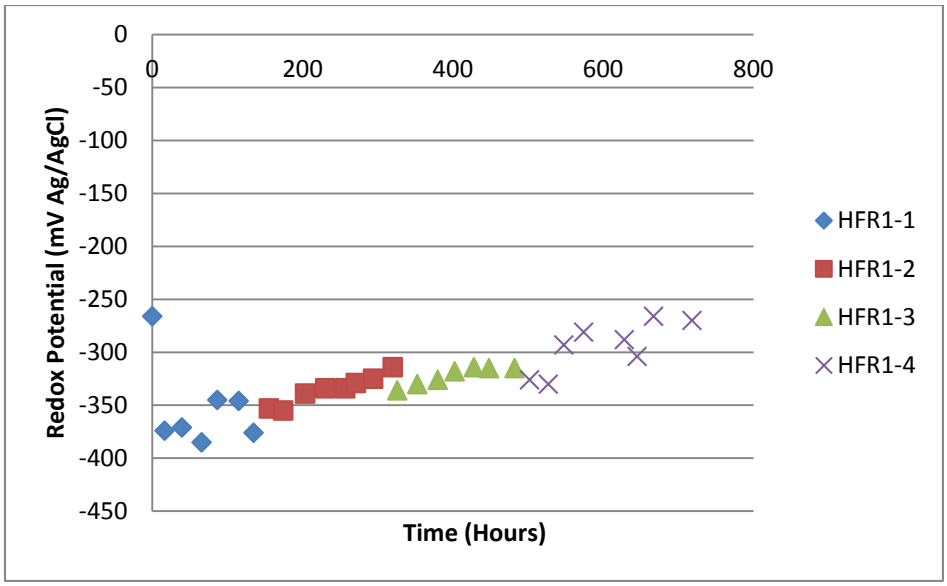

Figure 5-15. Redox potential for HFR1. Each media replacement data set is labeled as HFR1-1, 2, 3, and 4 respectively.

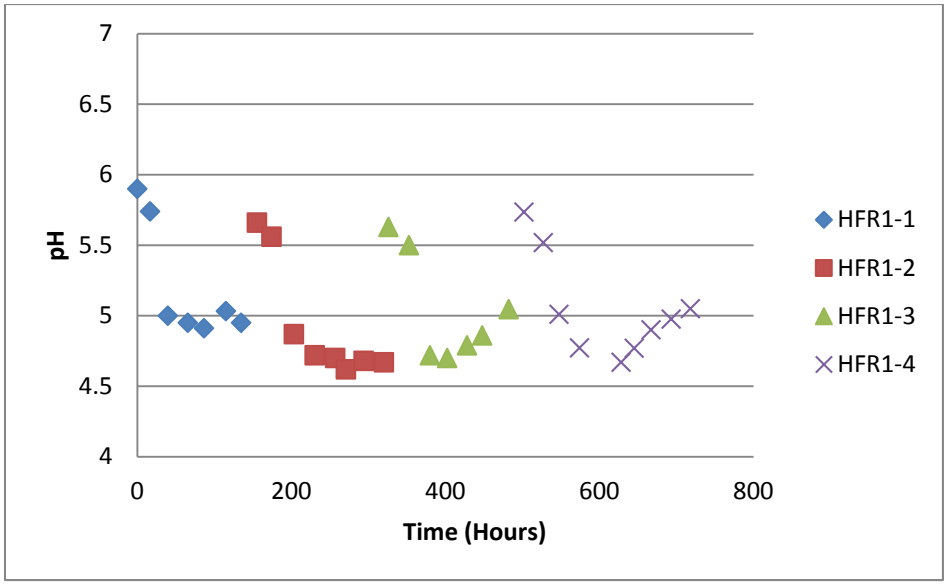

Figure 5-16. pH with time for HFR1.

These data show that for each media replacement, the OD increases to a maximum and then decreases. The growth of the cells shows a typical cell growth curve with a short lag phase followed by an exponential phase, then a stationary stage and finally a decline phase. Since

ethanol is still being produced in Figure 5-13 when the OD is decreasing, it is evident that the decline in OD does not correlate with cell death but more with cells attaching to the fibers or interstitial spaces. Thus, it is clear that the OD for the free floating cells does not represent the total amount of cells in the system. This can be deduced by looking at the dilution of ethanol compared to the OD following each media replacement. For the second media replacement at 320 hours, the ethanol was reduced by 78% which was expected when the dilution rate was 75%. However, the OD was only reduced by 24%. If all of the cells were free floating, then the OD should follow the same dilution as the ethanol. This is not surprising because, as shown in the previous section, the cells can be loosely attached to the hollow fiber bundles and there is a possibility they became dissociated from the bundles and went into solution during the media replacement.

The ethanol production rates shown are nearly linear. These rates and acetic acid rates are discussed in detail in Section 5.3.2.6. The acetic acid concentration for each media replacement increased to a maximum and then decreased. This decrease can be caused by the CoA Transferase enzyme which converts acetic acid back into acetyl CoA, the acetyl CoA can then be converted into ethanol or cell mass, or by the acetaldehyde dehydrogenase enzyme which converts acetate into acetaldehyde which can then be converted to ethanol (see Figure 2-1). The conversion of acetic acid to ethanol is dependent on the pH and the ratio NAD_{red}/NAD_{ox}. With a lower pH and/or higher NAD_{red}/NAD_{ox}, the Gibbs free energy for conversion of acetic acid to ethanol increases (Hu 2011). Thus, as the pH reaches a minimum in Figure 5-16, the conversion of acetic acid to ethanol begins to occur. As the acetic acid level decreases, the pH begins to rise as a result of less acid in the system. The redox potential shown in Figure 5-15 began around

-380 mV and steadily increased to around -280 mV by around 700 hours. This increase is not due the presence of ethanol or acetic acid (Frankman 2009). It was shown that increases in ethanol and acetic acid concentrations had minimal effects on liquid redox potential. Typically cells decrease in redox potential during growth phases, and begin to level out or increase in the non-growth phase. Thus, the redox increase suggests that the cells were generally in a non-growth phase. Also, lower redox potentials have been associated with a switch from acetogenesis (acetic acid production) to solventogenesis (ethanol formation) (Frankman 2009). However, in the Frankman studies, the ratio of ethanol to acetic acid did not increase with these increasing redox potentials whereas in this study the ratio did increase. Thus, it is clear that the causes and effects of redox potential in syngas fermentation are still not very well understood.

Figure 5-17 shows the total cumulative carbon concentration as liquid product with time. These data include just the carbon from acetic acid and ethanol. The slope of a linear regression on these data gives the rate of formation of mmoles of carbon in the liquid carbon-containing products (ethanol and acetic acid) per total liquid volume, R_{Lc} (units of mM_{Lc}/hr).These rates and the fits are discussed in detail in Section 5.3.2.6. The shading below the data shows the amount of carbon from ethanol and the amount of carbon from acetic acid. HFR1-3 showed the largest R_{Lc} of 4.6 mM_{Lc}/hr. There is nothing in the cell growth or the redox data that would indicate that this run is any different than the others, however R_{Lc} is about 2.5 times that of the other runs. This could be indicative of an internal trigger that is discussed in Section 5.3.2.6. It is interesting to note that for all runs, ethanol continues to increase with time while acetic acid stays fairly constant. This results in high ethanol to acetic acid ratios, which is a desired trait for a fermentation system. Clark et. al. suggests that it is unlikely that acetogenesis and solventogenesis operate simultaneously in the same cell, thus when simultaneous production

occurs, there are some cells that are in the acetogenesis state and some in the solventogenesis state. Because the levels of acetic acid stay relatively constant compared to the increasing levels of ethanol, this could mean that after an initial growth in the acetogenesis state, cells begin to shift to the solventogenesis state leaving relatively few in the acetogenesis state, and thus production of acetic acid is minimal and even decreases because of conversion to ethanol as discussed above.

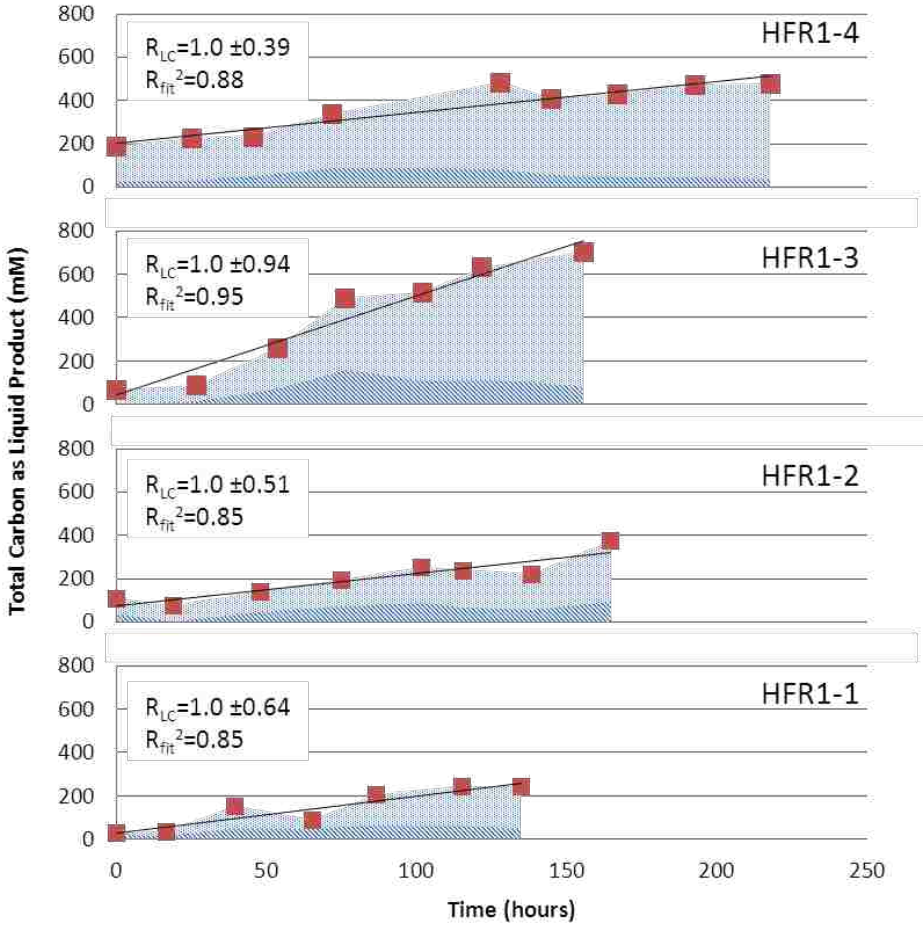

Figure 5-17. Cumulative carbon concentration as liquid product with time for HFR1. The slope of a linear regression on these data gives the rate of formation of moles of carbon in the liquid products (ethanol and acetic acid) per total liquid volume, R_{Lc} (mM_{Lc}/hr). The lighter hashed area ( ) area represents the amount of carbon from ethanol and the darker area ( ) represents the amount of carbon from acetic acid with the total amount equal to the square data points.

5.3.2.2 HFR2 Results

HFR2 used a total liquid volume (V_S) of 1125 mL and two HFRs in series in order to increase the total volume of liquid in the HFR (V_{Ltot}). There were 2 media replacements performed in this experiment, including the initial inoculation. The optical density for the free floating cells with time is shown in Figure 5-18 and the liquid product concentrations with time are shown in Figure 5-19 through 5-20 for HFR2. The redox potential is shown in Figure 5-21 and Figure 5-22 shows the pH with time.

These data also show that for each media replacement, the OD increased to a maximum and then decreased. The total concentration of ethanol in this run did not increase with successive media replacements. Again, based on these data, it is clear that the OD for the free floating cells does not represent the total amount of cells in the system. This can be deduced by looking at the dilution of ethanol compared to the OD for each media replacement. For the second media replacement at 220 hours, the ethanol is reduced by 64%, however the OD actually increased from 0.38 to 0.4 indicating that cells were likely released from the hollow fibers and re-suspended in the media. The acetic acid concentration for HFR2-1 increased to a maximum and then decreased as in HFR1. For HFR2-2, the pH never dropped low enough to trigger conversion of acetic acid to ethanol.

The redox potential shown in Figure 5-21 decreased to around -330 mV and reached a minimum of -371 mV and then increased to -276 mV. Other than one jump to a lower redox at 318 hours, the redox again has a general trend to a more positive potential over time as with HFR1. This suggests that most cells are in the non-growth phase.

Figure 5-23 shows the total cumulative carbon concentration as liquid product with time. The shading below the data shows the amount of carbon from ethanol and the amount of carbon

from acetic acid. HFR2-1 showed the largest R_{Lc} of 1.2 mM_{Lc}/hr. Again, for HFR2 ethanol continues to increase with time while acetic acid stays fairly constant. HFR2-1 shows that the rate is initially non-linear, or at least a different linear slope, but then at around 120 hours, the rate changes to a much lower slope. A possible reason for this as discussed in Section 5.3.2.6 is that the cells are most likely intrinsically limited. These intrinsic limitations are subject to change depending on the cellular activity and thus allows for discontinuous jumps when enzymes or other factors are up-regulated. It should be noted that the error in the GC liquid concentrations of ethanol and acetic acid were calculated to be about ± 3% of the total.

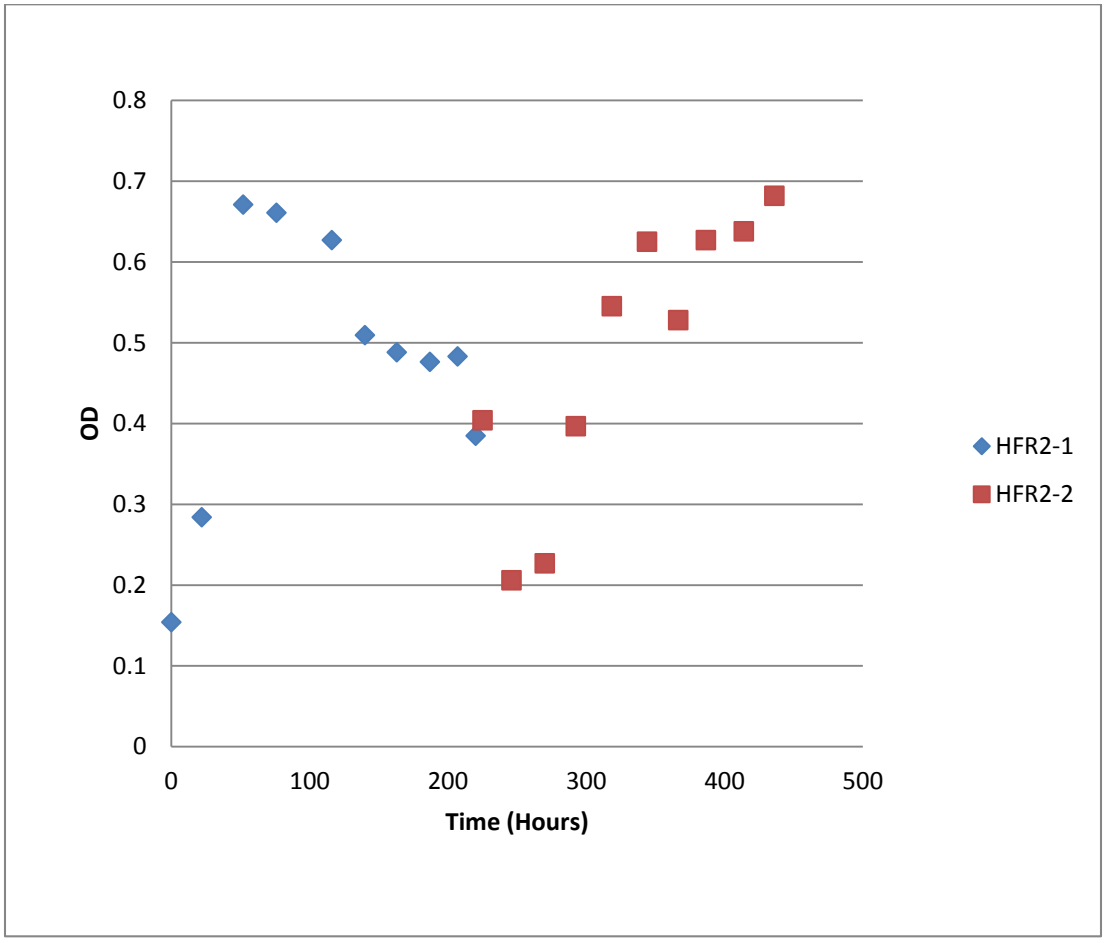

Figure 5-18. Optical density for the free floating cells over time for HFR2. Each media replacement data set is labeled as HFR2-1 and HFR2-2 respectively.

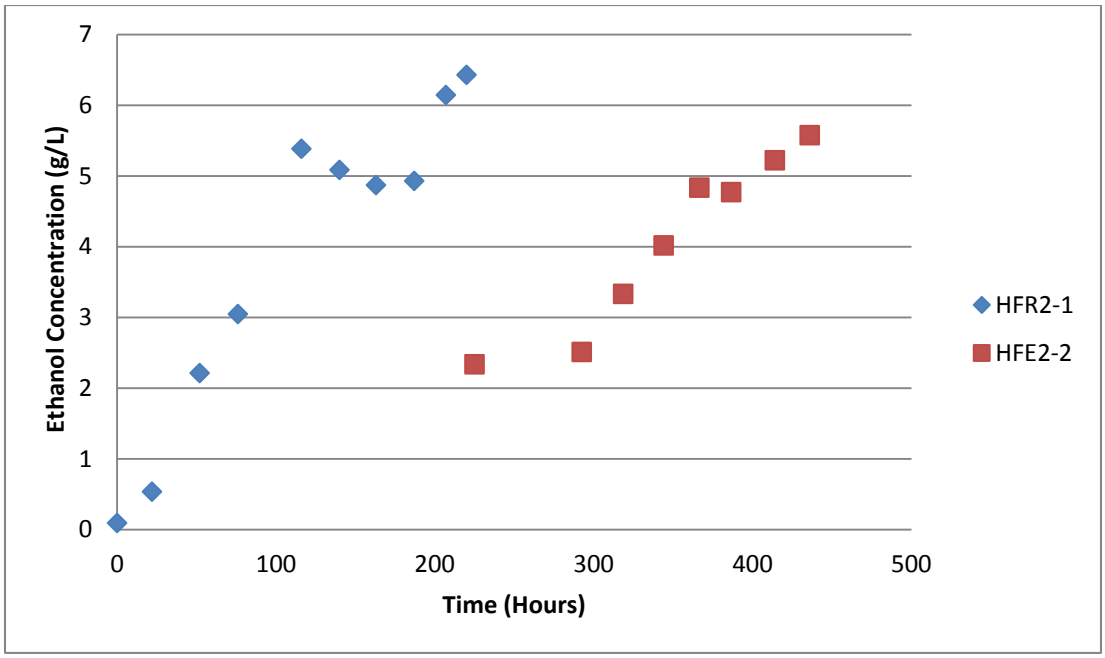

Figure 5-19. Liquid ethanol concentration over time for HFR2. Each media replacement data set is labeled as HFR2-1 and HFR2-2 respectively.

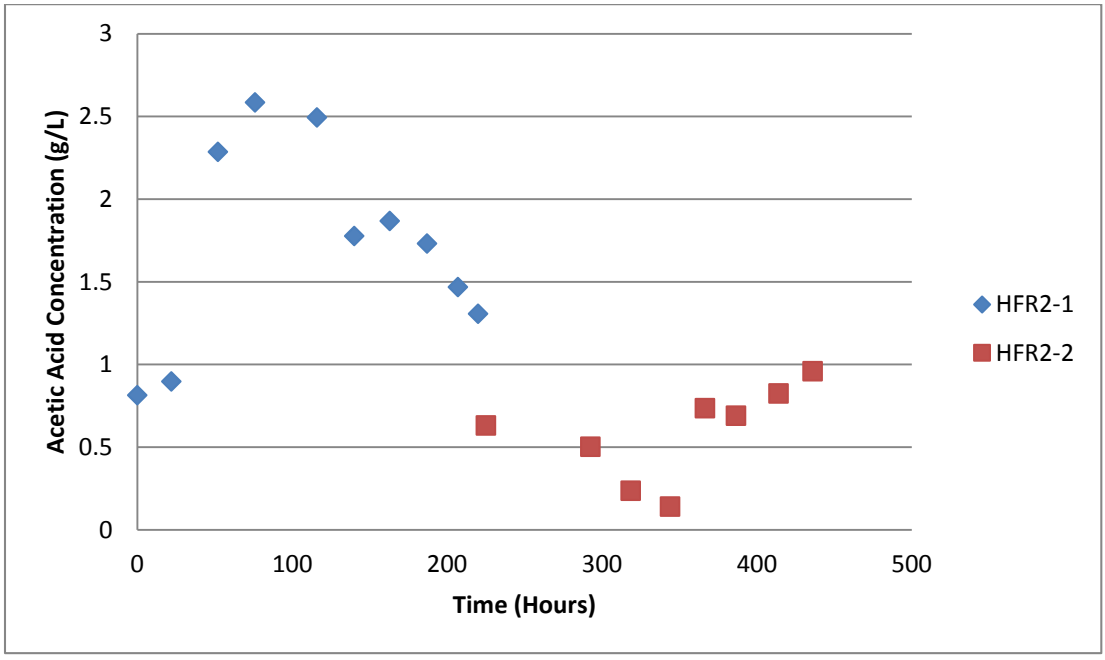

Figure 5-20. Liquid acetic acid concentration over time for HFR2. Each media replacement data set is labeled as HFR2-1 and HFR2-2 respectively.

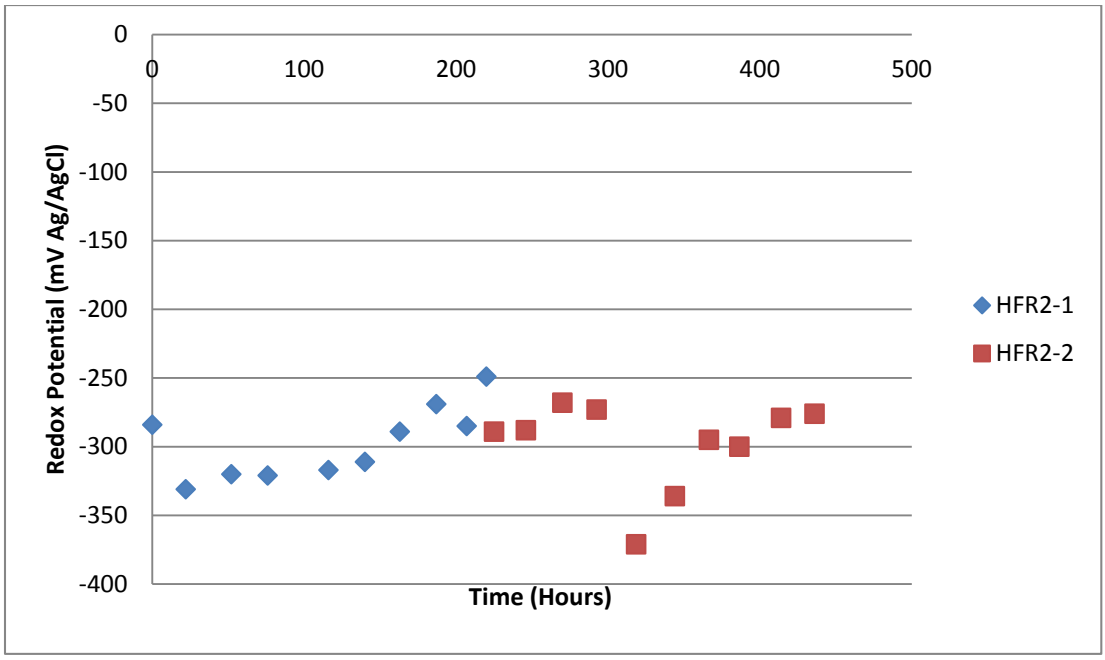

Figure 5-21. Redox potential for HFR2. Each media replacement data set is labeled as HFR2-1 and HFR2-2 respectively.

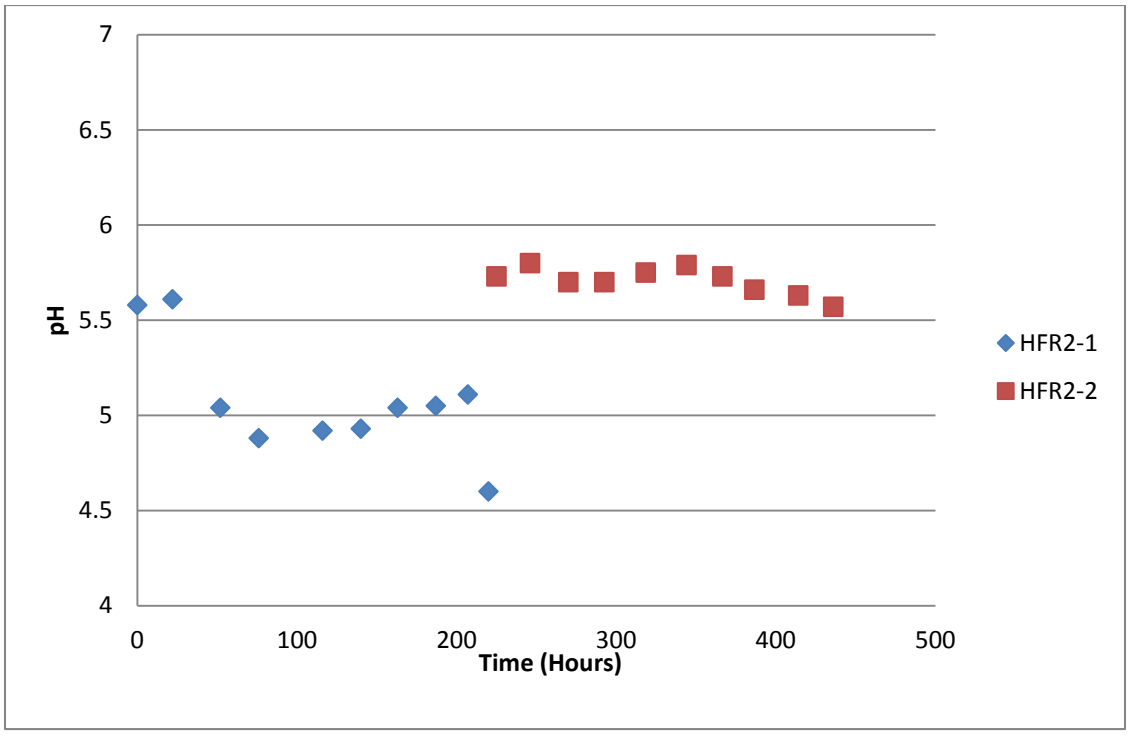

Figure 5-22. pH with time for HFR2.

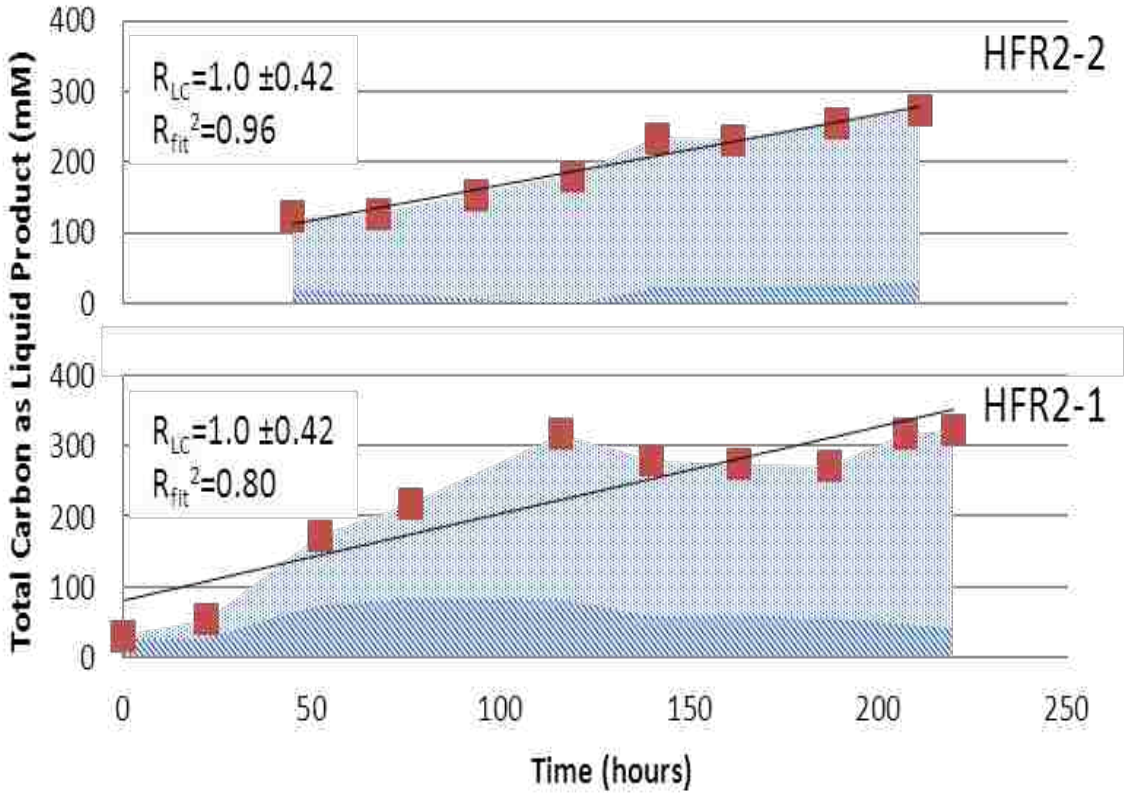

Figure 5-23. Cumulative carbon concentration as liquid product with time for HFR2. The slope of a linear regression on these data gives the rate of moles of carbon in the liquid products (ethanol and acetic acid) per total liquid volume, R_{Lc} (mM_{Lc}/hr). The lighter hashed area ( ) area represents the amount of carbon from ethanol and the darker area ( ) represents the amount of carbon from acetic acid with the total amount equal to the square data points.

5.3.2.3 HFR3 Results

HFR3 used a total liquid volume (V_S) of 600 mL. There were 2 media replacements performed in this experiment, including the initial inoculation. The optical density for the free floating cells with time is shown in Figure 5-24 and the liquid product concentrations with time is shown in Figure 5-25 through 5-26 for HFR3. The redox potential is shown in Figure 5-27 and the pH with time is shown in Figure 5-28.

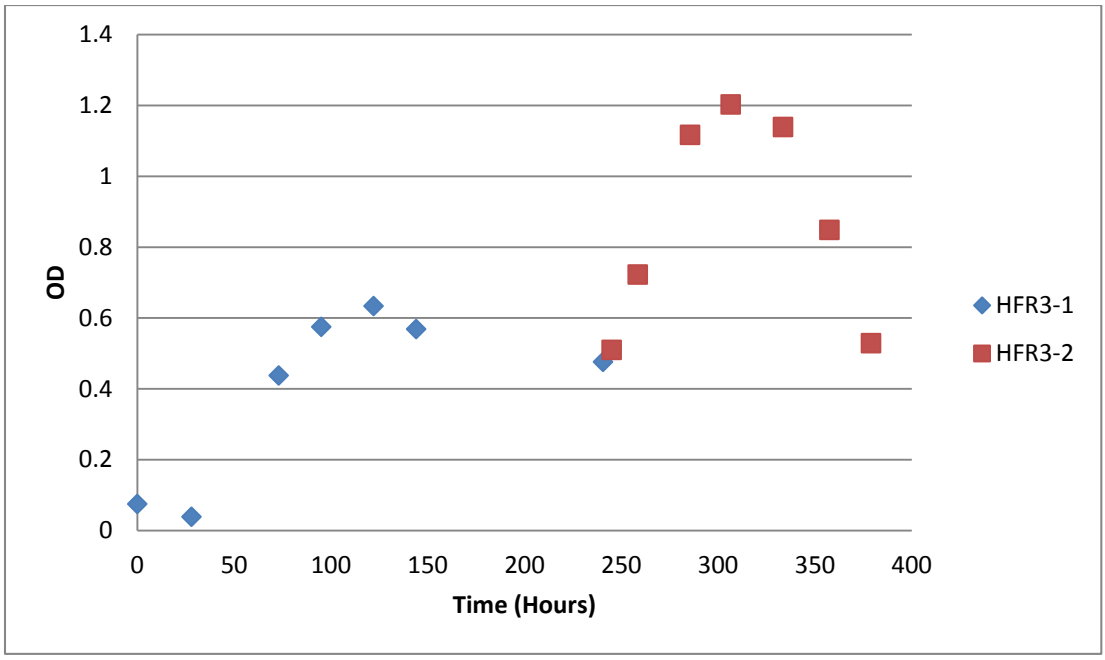

Figure 5-24. Optical density for the free floating cells over time for HFR3. Each media replacement data set is labeled as HFR3-1 and HFR3-2 respectively.

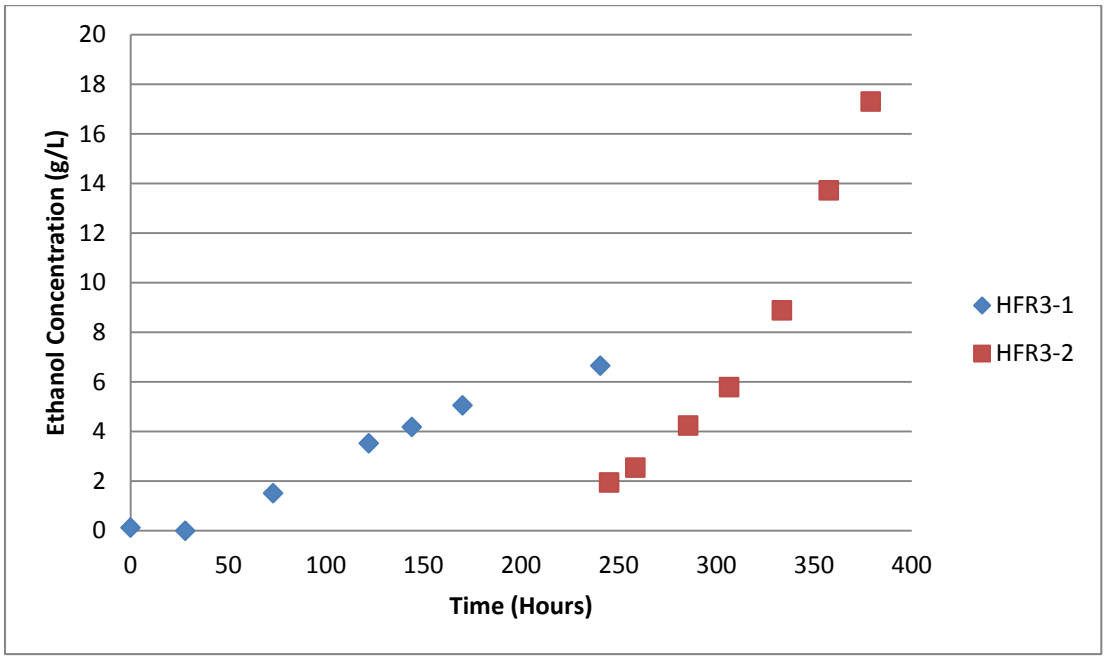

Figure 5-25. Liquid ethanol concentration over time for HFR3. Each media replacement data set is labeled as HFR3-1 and HFR3-2 respectively.

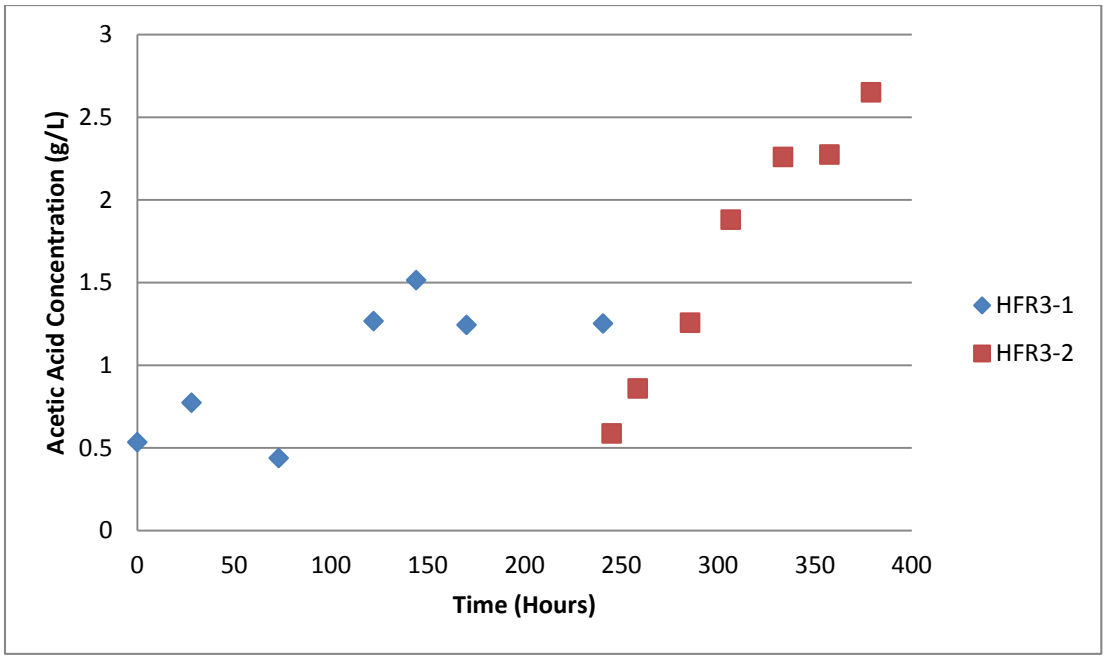

Figure 5-26. Liquid acetic acid concentration over time for HFR3. Each media replacement data set is labeled as HFR3-1 and HFR3-2 respectively.

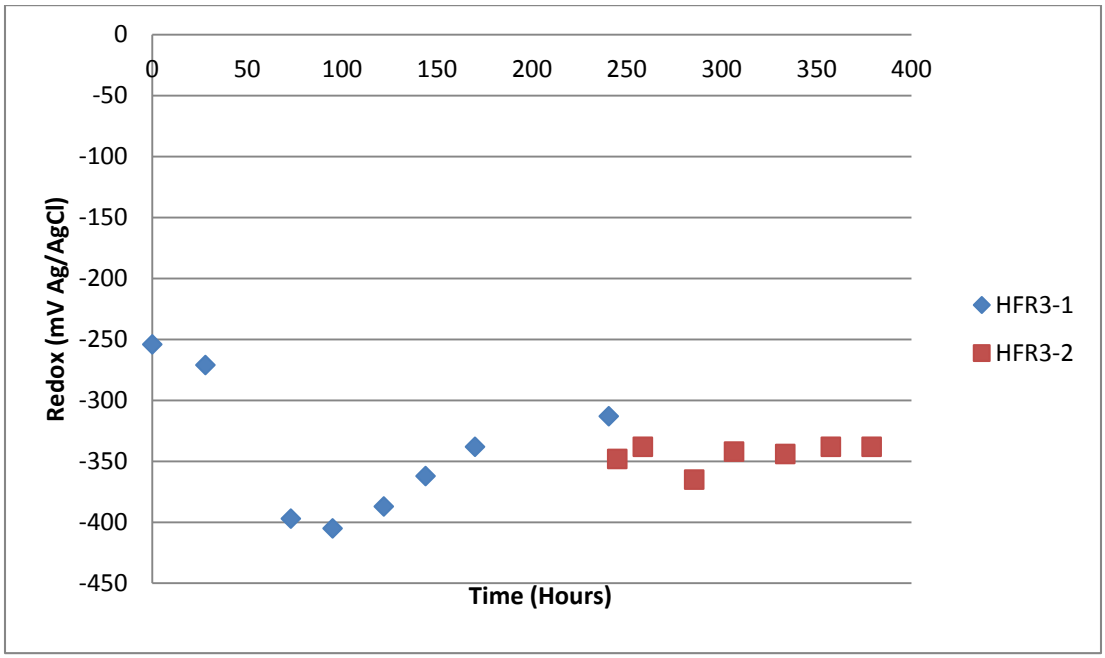

Figure 5-27. Redox potential over time for HFR3. Each media replacement data set is labeled as HFR3-1 and HFR3-2 respectively.

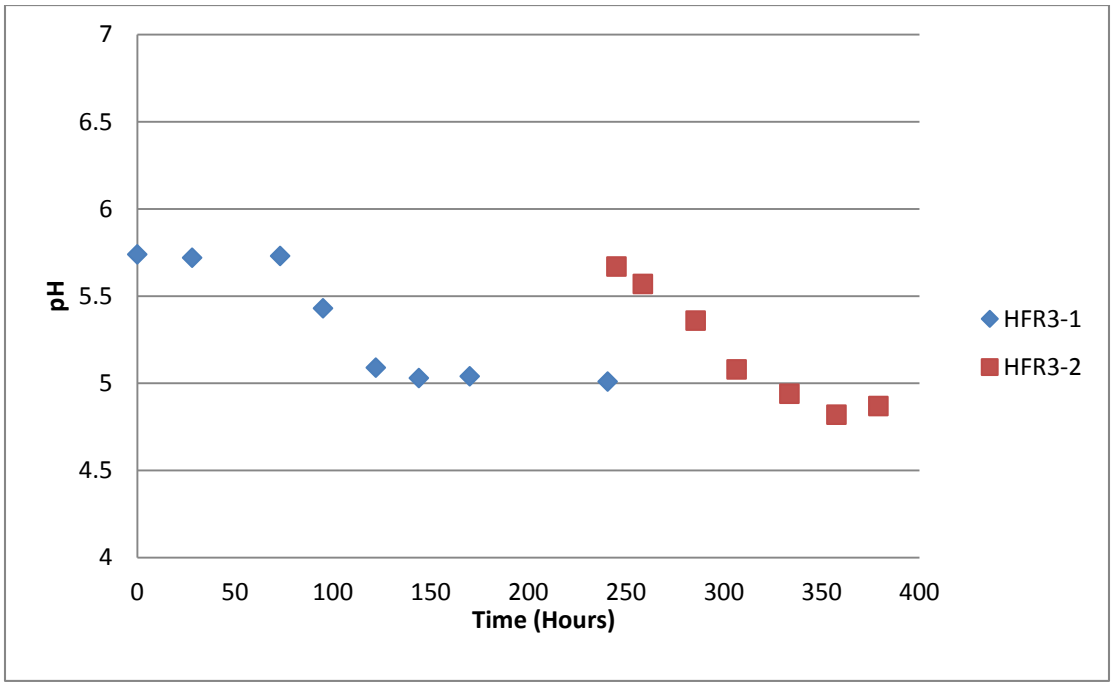

Figure 5-28. pH with time for HFR3.

Similar to HFR1 and HFR2, these data also show that for each media replacement, the OD increased to a maximum and then decreased to almost the same initial OD. This dip in OD could be due to cell death, but it is more likely that the cells begin to attach to the fibers, thus decreasing the free floating cell OD. The highest OD (1.2) of all HFR experiments was achieved in this run. Similarly this high OD corresponds to the largest R_{Lc} achieved in this work shown in Figure 5-29. However, the high production rates cannot be solely attributed to high OD because a similar rate achieved in HFR1-3 showed no increase in OD compared to other runs. In this experiment the acetic acid did not follow the general trend of increasing and then decreasing as seen in HFR1 and HFR2. This means that there was little conversion of acetic acid to ethanol even though the pH was as low as the previous experiments where conversion occurred. This implies that the NAD_{red}/NAD_{ox} ratio in the cell was probably lower than in the previous experiments. The redox potential shown in Figure 5-27 is similar to HFR1 and HFR2 in that

there is a general trend upwards over time, again suggesting a strong non-growth phase. Figure 5-29 shows the total cumulative carbon concentration as liquid product with time. The shading below the data shows the amount of carbon from ethanol and the amount of carbon from acetic acid. HFR3-2 showed the largest R_{Lc} of 5.3 mM_{Lc}/hr. For HFR3 ethanol also increases with time more than acetic acid, resulting in large ethanol to acetic acid ratios. HFR3-2 also shows that the rate of product formation is not very linear. Though the R^2 value shows a good fit, an exponential model might fit this curve more accurately. This shows that the rate of product formation can be approximated as linear in most of the fermentation studies in this work, but there can also be periods where another rate model would be more appropriate. This aspect is discussed further in Section 5.3.2.6.

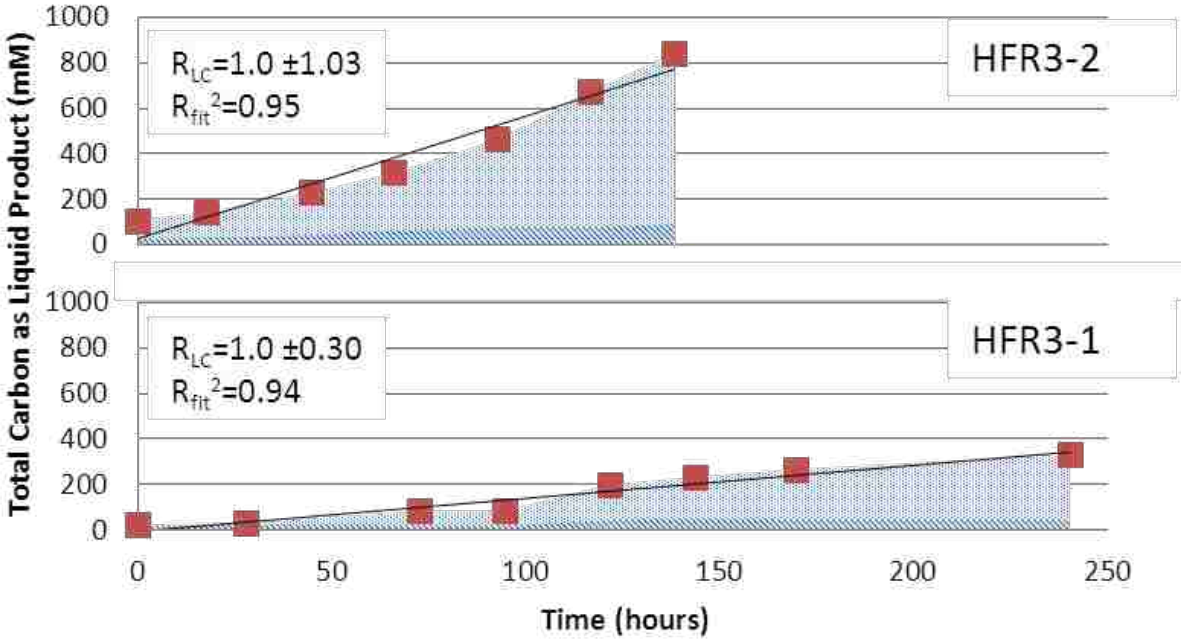

Figure 5-29. Cumulative carbon concentration as liquid product with time for HFR3. The slope of a linear regression on these data gives the rate of formation of moles of carbon in the liquid products (ethanol and acetic acid) per total liquid volume, R_{Lc} (mM_{Lc}/hr). The lighter hashed area ( ) area represents the amount of carbon from ethanol and the darker area ( ) represents the amount of carbon from acetic acid with the total amount equal to the square data points.

5.3.2.4 HFR4 Results

HFR4 again used a total liquid volume (*Vs*) of 600 mL. There were 5 media replacements performed in this experiment, including the initial inoculation. This experiment was the longest fermentation with a total of 2578 hours run time. The optical density for the free floating cells with time is shown in Figure 5-30 and the liquid product concentrations with time are shown in Figure 5-31 through Figure 5-32 for HFR4. The redox potential is shown in Figure 5-33 and the pH is shown in Figure 5-34.

The OD in this run did not follow the typical pattern as in HFR1-HFR3. With HFR1-4 the OD continued to increase with each media replacement and then decreased in HFR4-5. This increase could have been due to cell growth, or cells becoming dislodged from the HFR.

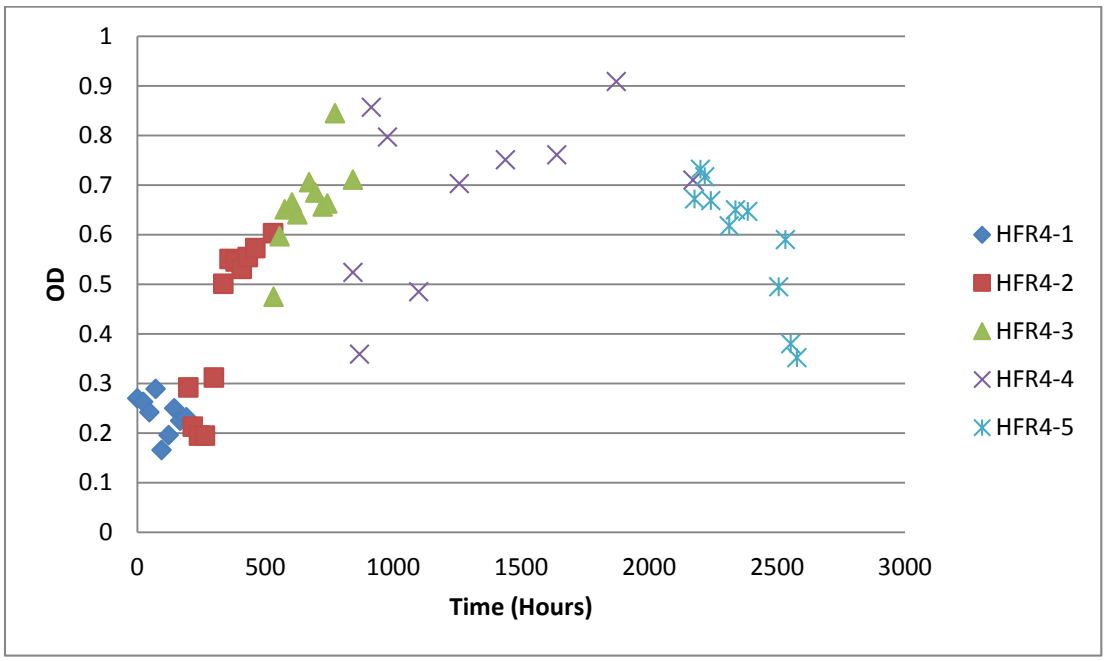

Figure 5-30. Optical density for the free floating cells over time for HFR4. Each media replacement data set is labeled as HFR4-1, 2, 3, 4 and 5 respectively.

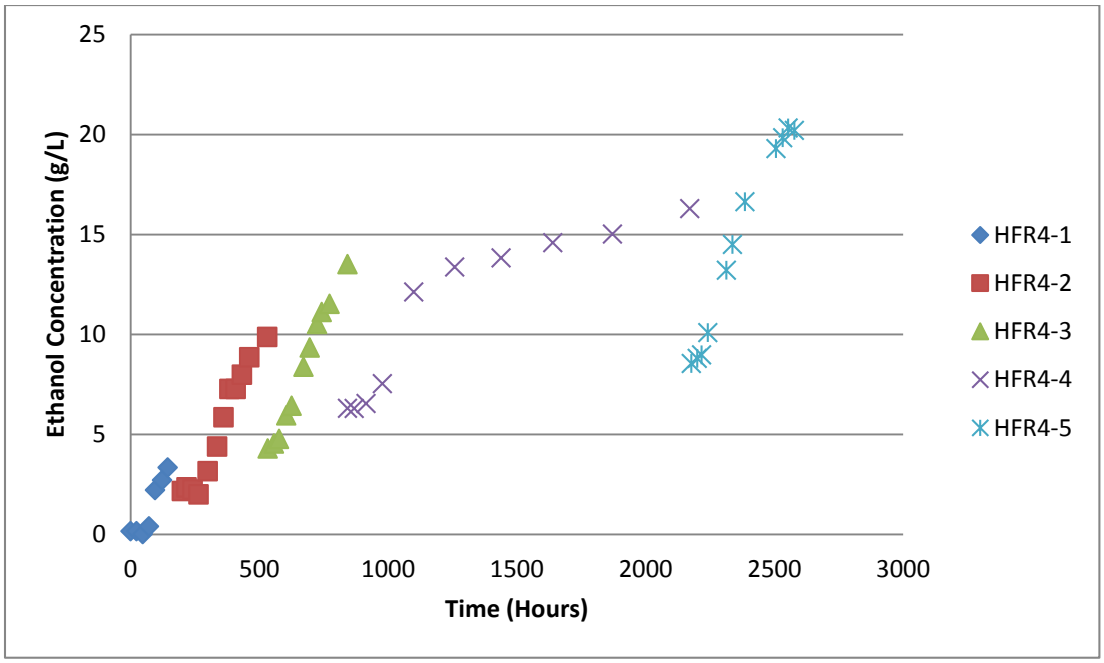

Figure 5-31. Liquid ethanol concentration over time for HFR4. Each media replacement data set is labeled as HFR4-1, 2, 3, 4 and 5 respectively.

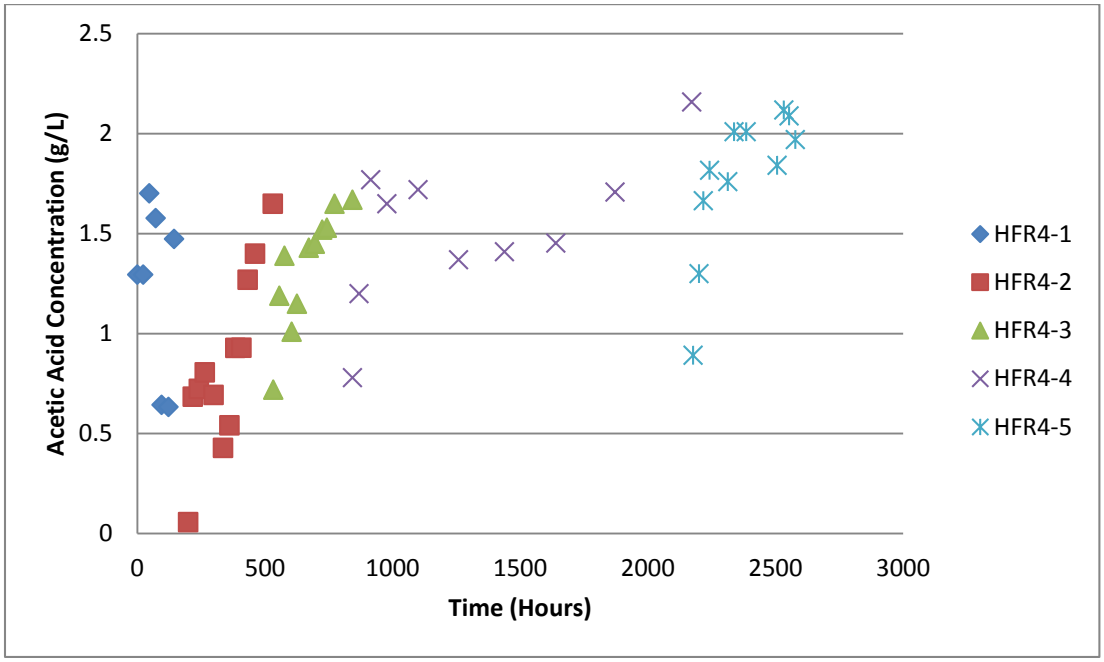

Figure 5-32. Liquid acetic acid concentration over time for HFR4. Each media replacement data set is labeled as HFR4-1, 2, 3, 4 and 5 respectively.

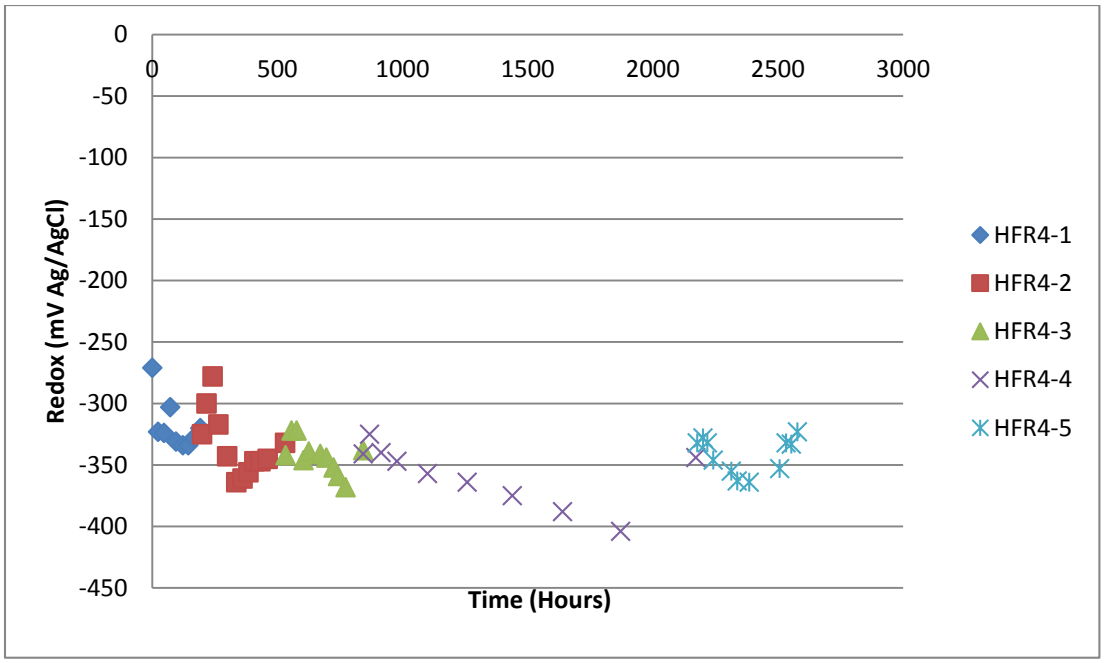

Figure 5-33. Redox potential over time for HFR4. Each media replacement data set is labeled as HFR4-1, 2, 3, 4 and 5 respectively.

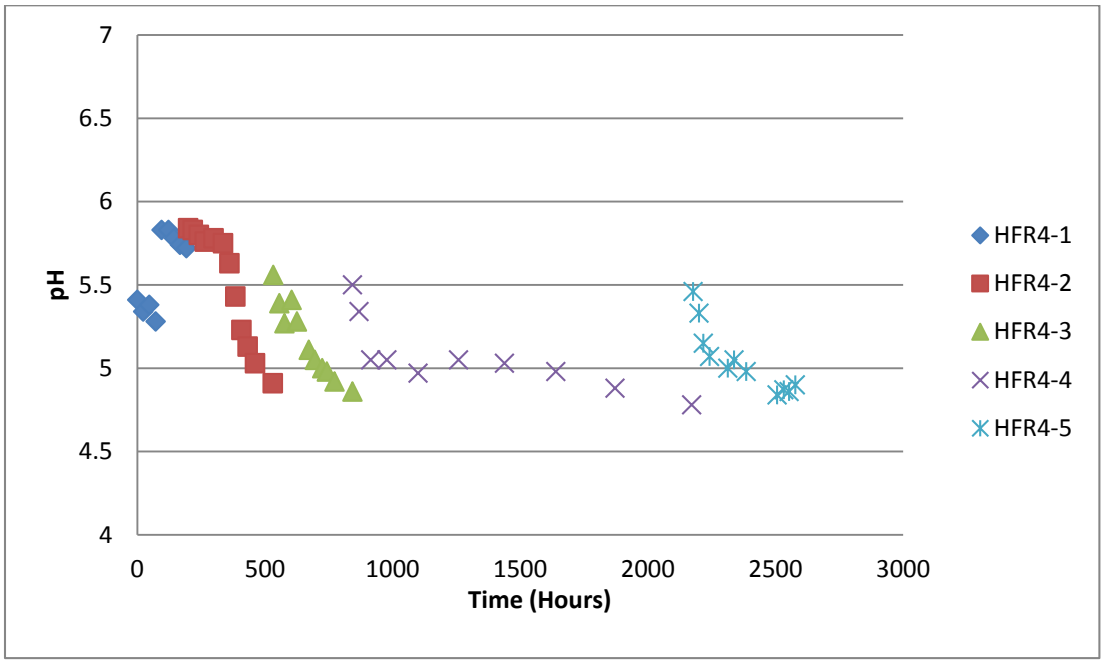

Figure 5-34. pH with time for HFR4.

The redox for HFR4 followed somewhat of a different pattern than HFR1-HFR3. In this run the redox generally decreased most of the time—suggesting cell growth rather than non-cell growth. Interestingly, the ethanol production was very high compared to acetic acid production so it is not completely clear as to the state of the cells. The increase in redox potential occurring in part of the runs did not correspond with an increase in any other data i.e. OD, pH.

Figure 5-35 shows the total cumulative carbon concentration as liquid product with time. The slope of a linear regression on these data gives the rate of formation of liquid carbon-containing products (ethanol and acetic acid), R_{Lc} (mM_{Lc}/hr). The shading below the data shows the amount of carbon from ethanol and the amount of carbon from acetic acid. HFR4-2 showed the largest R_{Lc} of 1.7 mM_{Lc}/hr. HFR4 had the same settings as HFR3, however, as shown in Figure 5-31, the production rates of ethanol were much less than HFR3. Though this run achieved the highest ethanol concentration (20.2 g/L) of all runs, this can be attributed to the longer run time. One potential cause for the lower production rates could be due to the fact that the cell OD continually increased with each media replacement indicating that many cells were being detached from the hollow fibers. Since there were fewer cells in the HFR, the cells were not exposed to as high of liquid concentrations as they would have been near the HFR membrane. From 840 to 1871 hours the cell concentration was highly unstable indicating an unstable aggregation of cells on the fibers in which cells were continually detaching and reattaching. This experiment also reached the lowest redox potential of -404 mV. This run exposes the unknowns that still exist with HFR fermentation. For example, it seems that the amount of cells that are actually loosely attached to the membrane compared to the free floating cells may greatly affect production rates. HFR4 showed large ethanol to acetic acid ratios as with the other runs.

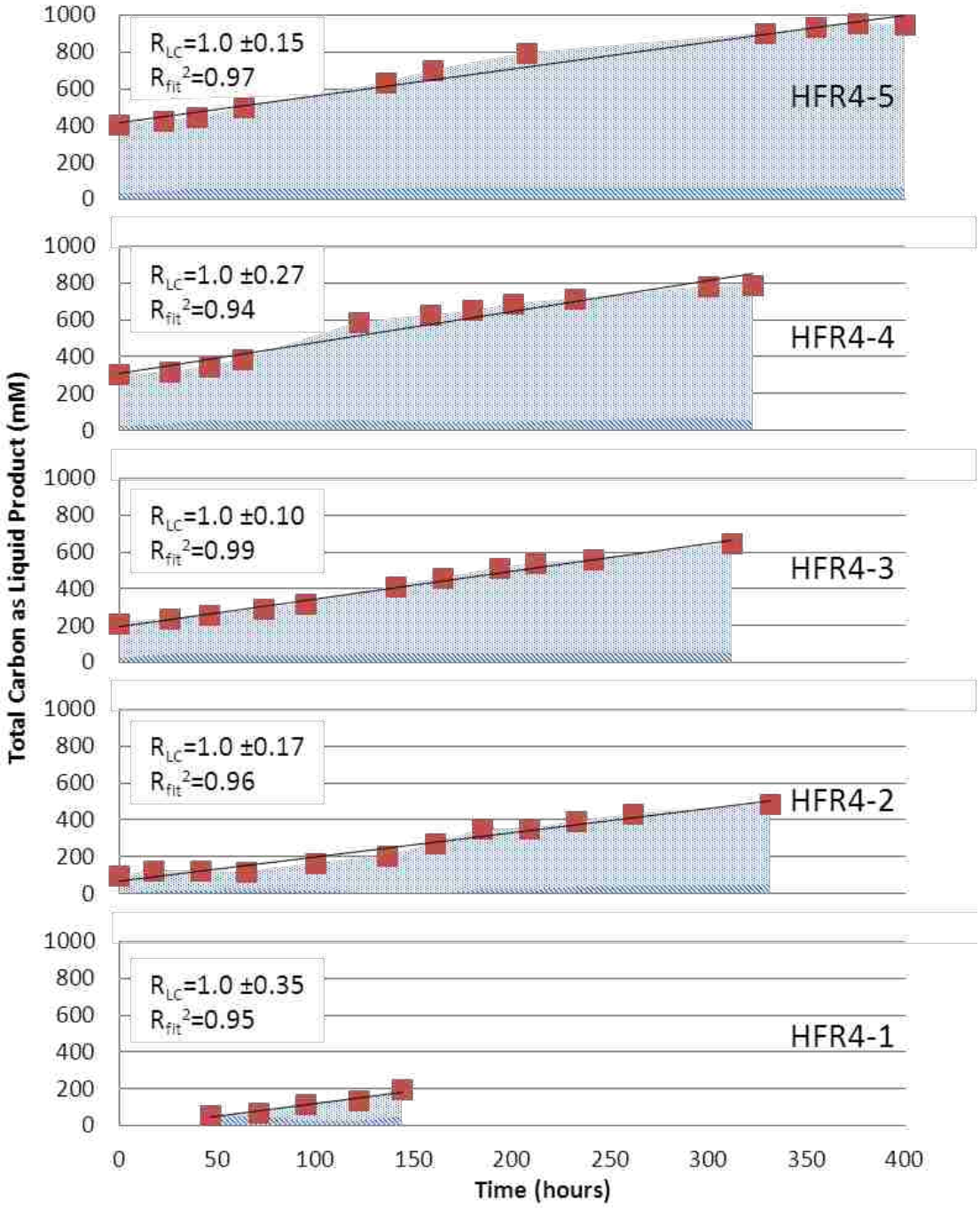

Figure 5-35. Cumulative carbon concentration as liquid product with time for HFR4. The slope of a linear regression on these data gives the rate of formation of moles of carbon in the liquid products (ethanol and acetic acid) per total liquid volume, R_{Lc} (mM_{Lc}/hr). The lighter hashed area ( ) area represents the amount of carbon from ethanol and the darker area ( ) represents the amount of carbon from acetic acid with the total amount equal to the square data points.

5.3.2.5 HFR5 Results

HFR5 again used a total liquid volume (V_S) of 600 mL. However, in this experiment, the liquid flow rates were changed to affect the mass transfer coefficient. The initial (HFR5-1) liquid flow rate was 170 ml/min. After the second media replacement (HFR5-2), the liquid flow rate was then changed to 85 ml/min. There were 3 media replacements performed in this experiment, including the initial inoculation. The optical density for the free floating cells with time is shown in Figure 5-36 and the liquid product concentrations with time are shown in Figure 5-37 through 5-38 for HFR5. The redox potential is shown in Figure 5-39 and the pH with time is shown in Figure 5-40.

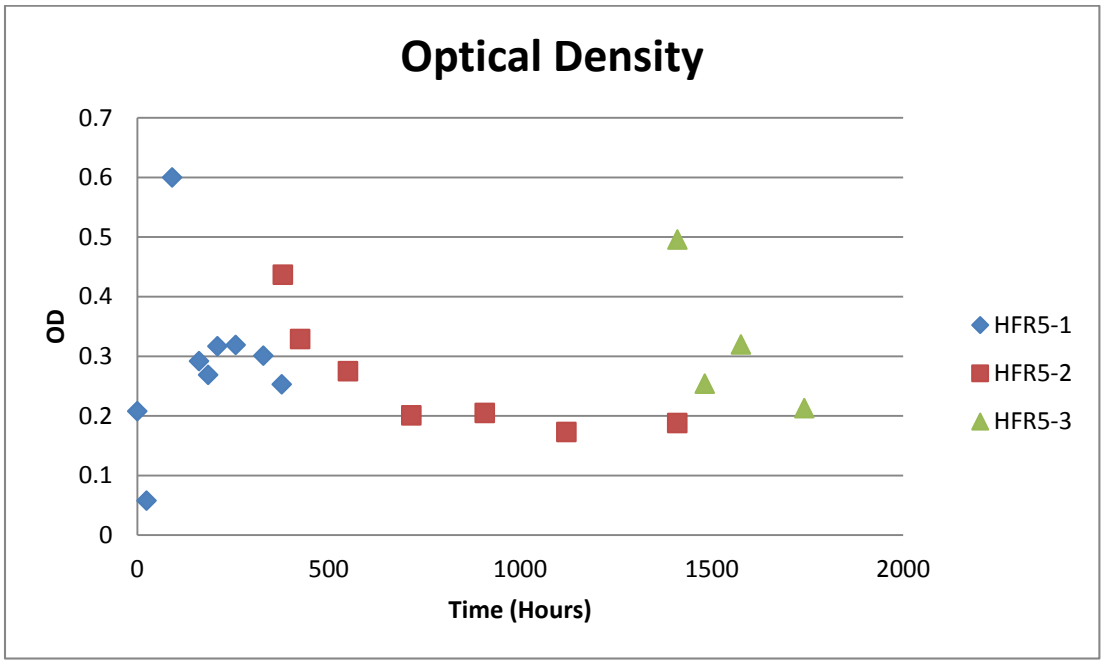

Figure 5-36. Optical density for the free floating cells over time for HFR5. Each media replacement data set is labeled as HFR5-1, 2, and 3 respectively.

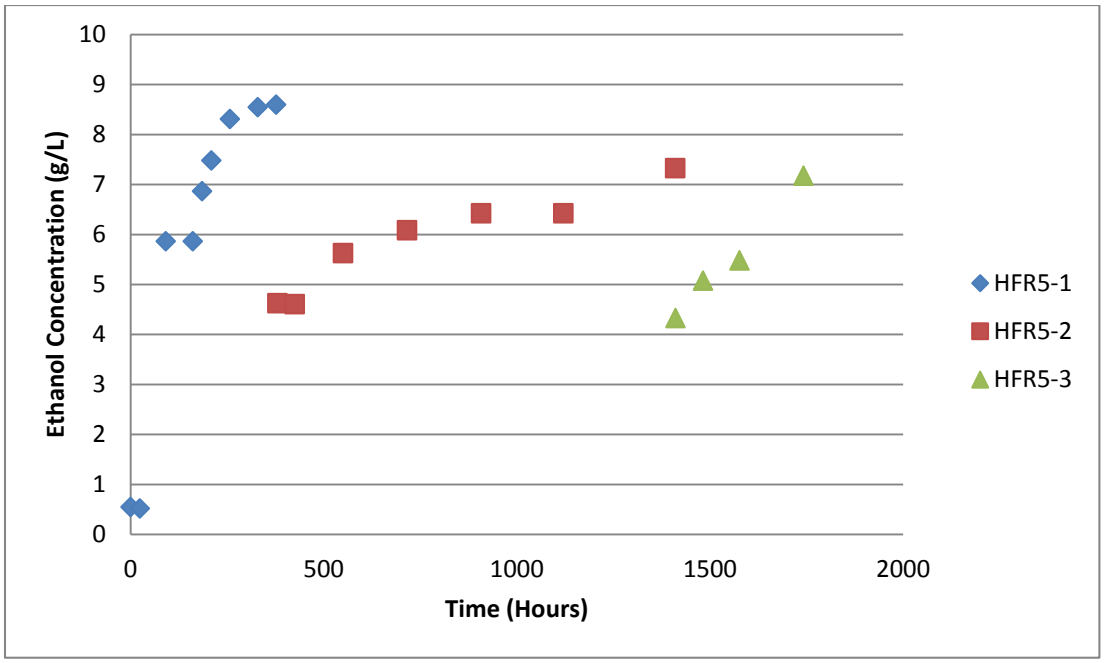

Figure 5-37. Liquid ethanol concentration over time for HFR5. Each media replacement data set is labeled as HFR5-1, 2, and 3 respectively.

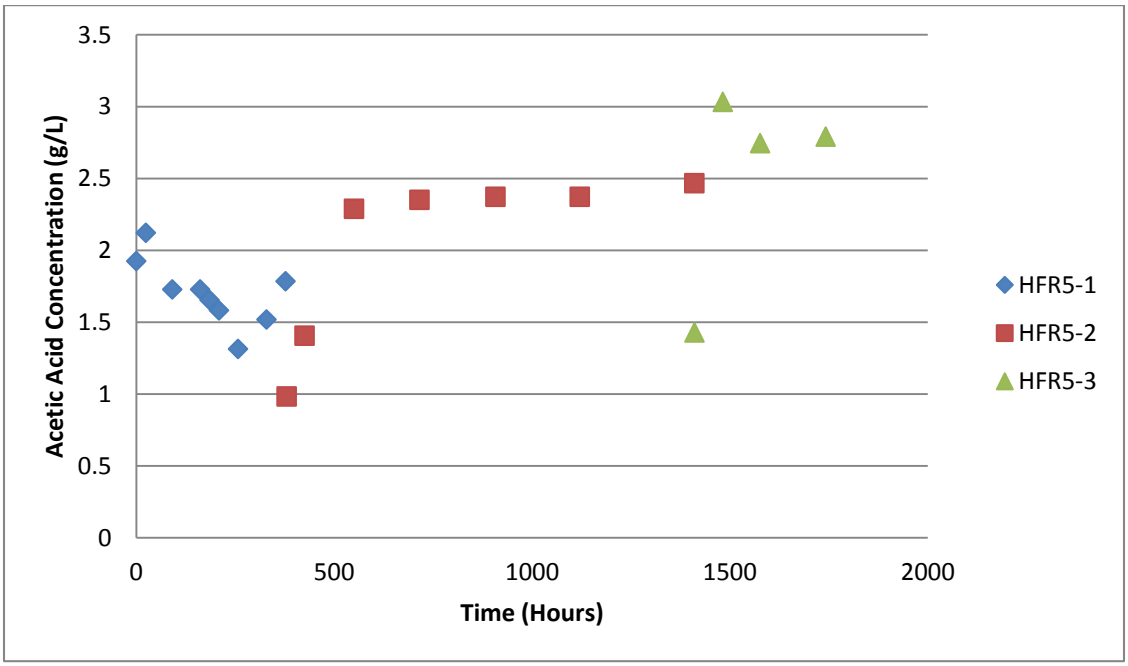

Figure 5-38. Liquid acetic acid concentration over time for HFR5. Each media replacement data set is labeled as HFR5-1, 2, and 3 respectively.

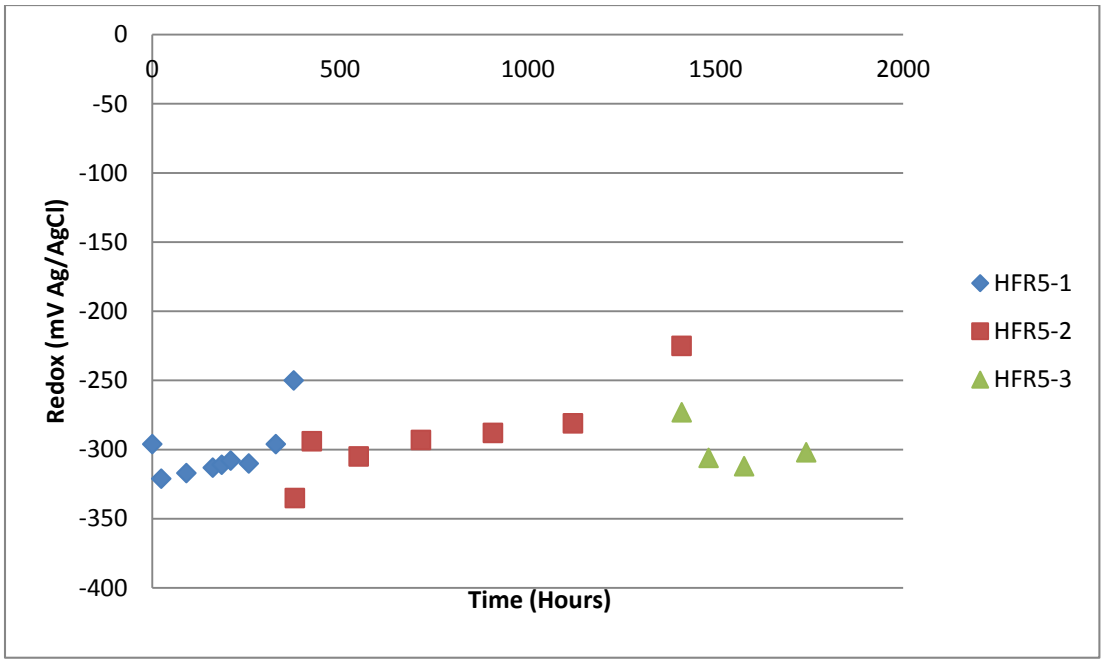

Figure 5-39. Redox potential over time for HFR5. Each media replacement data set is labeled as HFR5-1, 2, and 3 respectively.

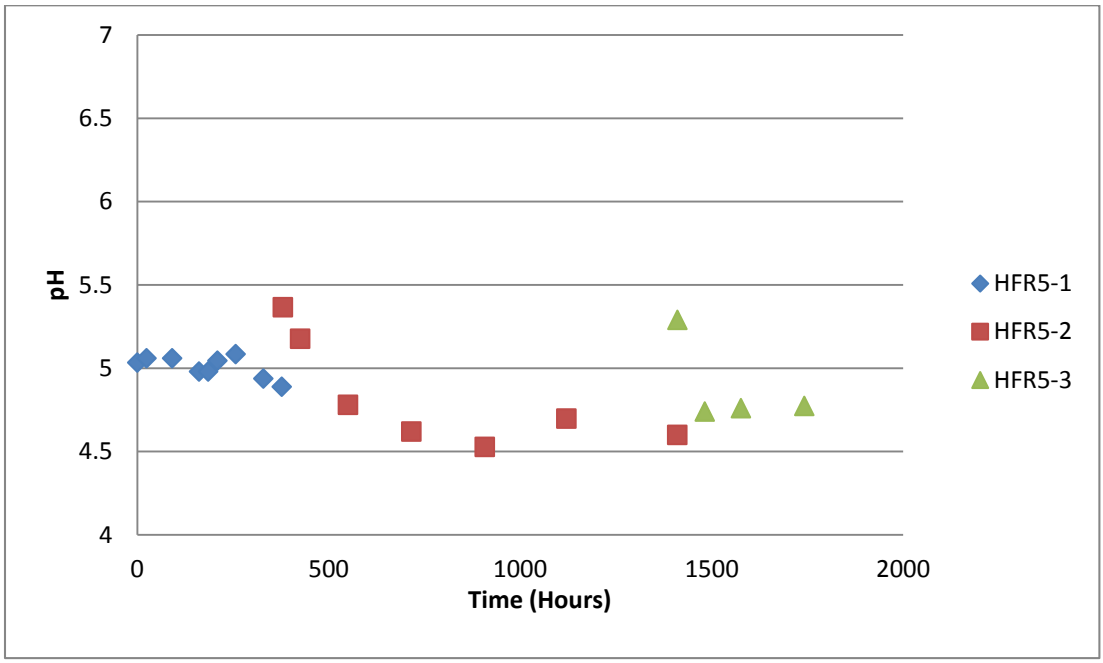

Figure 5-40. pH with time for HFR5.

HFR5 was different from the previous runs because the flow rate was changed in one of the runs. The flow rate can affect the mass transfer rates and also the amount of loosely attached cells on the fibers. The OD for HFR5-1 increased and then decreased as was typical in the previous runs. However, the OD in HFR5-2 only decreased throughout the whole experiment. This may be due to the fact that HFR5-2 had only half the flow rate of HFR5-1. Thus, there are less shear forces around the fibers in the HFR. This could have allowed for more cells to aggregate in the interstitial spaces of the fibers or on the fiber surface than at the higher flow rate. When the flow rate was set back to the initial rate in HFR5-3, the OD increased and then decreased as in previous runs. Acetic acid levels shown in Figure 5-38 never showed a decrease even though the pH dropped down to levels that triggered acetic acid conversion in HFR1 and HFR2. As in HFR3, this implies that the NAD_{red}/NAD_{ox} ratio in the cells was probably lower than in HFR1 and HFR2. The redox for HFR5-2 rose to the highest value which is consistent with the possibility. This corresponded to an OD that was decreasing. It may be that cells in solution can lower redox levels more than cells aggregated on the fibers. Thus, as the number of cells on the fibers increase, the redox levels also increase.

Figure 5-41 shows the total cumulative carbon concentration as liquid product with time. The slope of a linear regression on these data gives the rate of formation of liquid carbon-containing products (ethanol and acetic acid), R_{Lc} (mM_{Lc}/hr). The shading below the data shows the amount of carbon from ethanol and the amount of carbon from acetic acid. Decreasing the flow rate by half should decrease the mass transfer coefficient by 37% and thus the production rates by 37%. Though there is a drop in production rates, the results were not statistically different enough to say that the flow rate had an effect on the production rates. This is discussed in detail in Section 5.3.2.6.

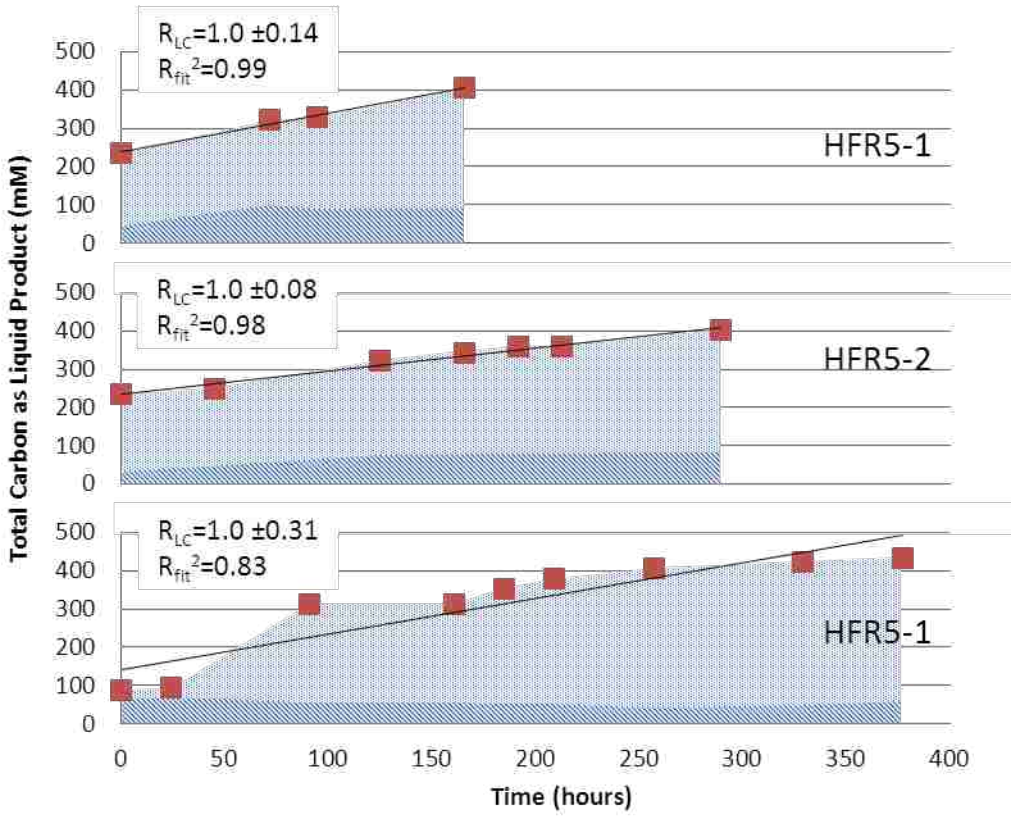

Figure 5-41. Cumulative carbon concentration as liquid product with time for HFR4. The slope of a linear regression on these data gives the rate of formation of moles of carbon in the liquid products (ethanol and acetic acid) per total liquid volume, R_{Lc} (mM_{Lc}/hr). The lighter hashed area ( ) area represents the amount of carbon from ethanol and the darker area ( ) represents the amount of carbon from acetic acid with the total amount equal to the square data points.

5.3.2.6 Liquid Production Rate Discussion

The rate of carbon consumed in a syngas fermentation system is shown in Equation 5-1.

$$R_{Cc} = R'_{xc} \cdot X_{cells} + R_{Lc} \quad \textbf{(5-1)}$$

where R_{Cc} is the volumetric consumption of carbon (units of mM_c/hr), R'_{xc} is the rate of carbon used for cell anabolism per gram of cells (units of $mmol_c/g_c$/hr), R_{Lc} is the rate of formation of mmoles of carbon in the liquid products (ethanol and acetic acid) per total liquid volume (units

of M_c/hr), and X_{cells} is the grams of cells per total liquid volume (units of g_c/L). R_{Lc} is equal to $(\alpha\mu_g+\beta)\bullet X_{cells}$ (Shuler and Kargi 2002a), where μ_g is the specific growth rate of cells (units of hr^{-1}), and α (units of $mmol_c/g_c$) is a coefficient for product formation associated with cell growth and β (units of $mmol_c/g_c$/hr) is a coefficient for product formation associated with non-growth (Shuler and Kargi 2002a). The volumetric formation rate of carbon in products, $(\alpha\mu_g+\beta)X_{cells}$, is referred to from here on as R_{Lc} (mM_c/hr). This equation assumes that the rate of formation of bicarbonate from the CO_2 is very small due to the near saturated state of the solution.

Assuming a well-mixed reactor, the rate of carbon in the gas transferred to a HFR is shown in Equation 5-2.

$$R_{Tc} = \left(\frac{V_{L\,tot}}{V_s}\right)\left[\left(\frac{K_{tot}A_T}{V_L}_{co} \cdot \left(C_{sat,co} - C_{Liquid,co}\right)\frac{mmol_c}{mmol_{co}}\right) + \left(\frac{K_{tot}A_T}{V_L}_{co2} \cdot \left(C_{sat,co2} - C_{Liquid,co2}\right)\frac{mmol_c}{mmol_{co2}}\right)\right] \quad \textbf{(5-2)}$$

where R_{Tc} is the volumetric transfer rate of carbon into the system (mM_c/hr), $C_{sat,co}$ and $C_{sat,co2}$ are the well-mixed saturated mmolar concentrations of CO and CO_2 in the system, and $C_{Liquid,co}$ and $C_{Liquid,co2}$ are the well-mixed mmolar concentrations of CO and CO_2 in the liquid, and $K_{tot}A/V_{L,co}$ and $K_{tot}A/V_{L,co2}$ are the mass transfer coefficients of CO and CO_2, respectively. This equation assumes that the hollow fiber inlet and outlet concentration changes are small during the fermentation, and thus, ΔC_{lm} approaches (C_{sat}-C_{liquid}). In a real HFR fermentation system there needs to be circulating liquid and ports for removing product etc., thus, there is also an additional term that accounts for liquid that is not in the HFRs by multiplying by a V_{Ltot}/V_s ratio. V_{Ltot} (m^3) is the total volume of liquid in the HFR reactors (i.e. $V_{Ltot} = 3 \cdot V_L$ if three reactors of equal volumes were used), V_S is the total liquid volume of the reactor system (m^3) which includes the reactor, recycle loop, sump and other sampling ports.

At steady state, the rate of carbon consumed in the HFR system must equal the rate of carbon transferred, and thus R_{Cc} and R_{Tc} must be equal. If we assume that R'_{xc} is negligible, then the rate of gaseous carbon consumption is equal to the rate of formation of carbon-containing liquid products, $R_{Tc} = R_{Lc}$. This is a reasonable assumption because the cellular concentrations achieved in this work (OD of 0.4-1.2) correspond to only about 2-5% of the total amount of carbon accumulated in the system from ethanol and acetic acid. Though there are other liquid products produced in syngas fermentation, almost all of the liquid products are ethanol and acetic acid (Frankman 2009). Thus, for this study, R_{Lc} was estimated from the ethanol and acetic acid production rates.

In Equation 5-2, for a given HFR, the variables that can be directly controlled are V_S, $K_{tot}A/V_L$, V_{Ltot} , and the saturated concentrations. This work used a set partial pressure for each gas, so the saturated concentrations were not changed. V_S is changed by simply increasing the total volume of the fermentation system, $K_{tot}A/V_L$ is changed by changing the circulation flow rate and V_{Ltot} can be changed by increasing the number of HFRs in the fermentation system. Therefore, when high mass transfer rates are desired in a fermentation system, it is important to have a system with a large ($K_{tot}A/V_L$) and a large (V_{Ltot}/V_S). Thus, if a system is mass transfer limited ($C_{liquid} \approx 0$), with a decrease in V_{Ltot}/V_S, R_{Lc} would decrease. Also, as $K_{tot}A/V_L$ decreases, R_{Lc} would also decrease. However, if the system is not mass transfer limited, there should be no change in R_{Lc} when $K_{tot}A/V_L$ or V_{Ltot}/V_S is changed.

In order to determine if the system was in a mass transfer limiting regime, R_{Lc} from HFR1-HFR5 were determined by performing a linear regression on the accumulated carbon in the system as shown in Figures 5-17, 5-23, 5-29, 5-35, and 5-41. The slopes from these data

represent R_{Lc}. The rates from all runs along with the 95% confidence intervals from the linear regression are shown in Figure 5-42.

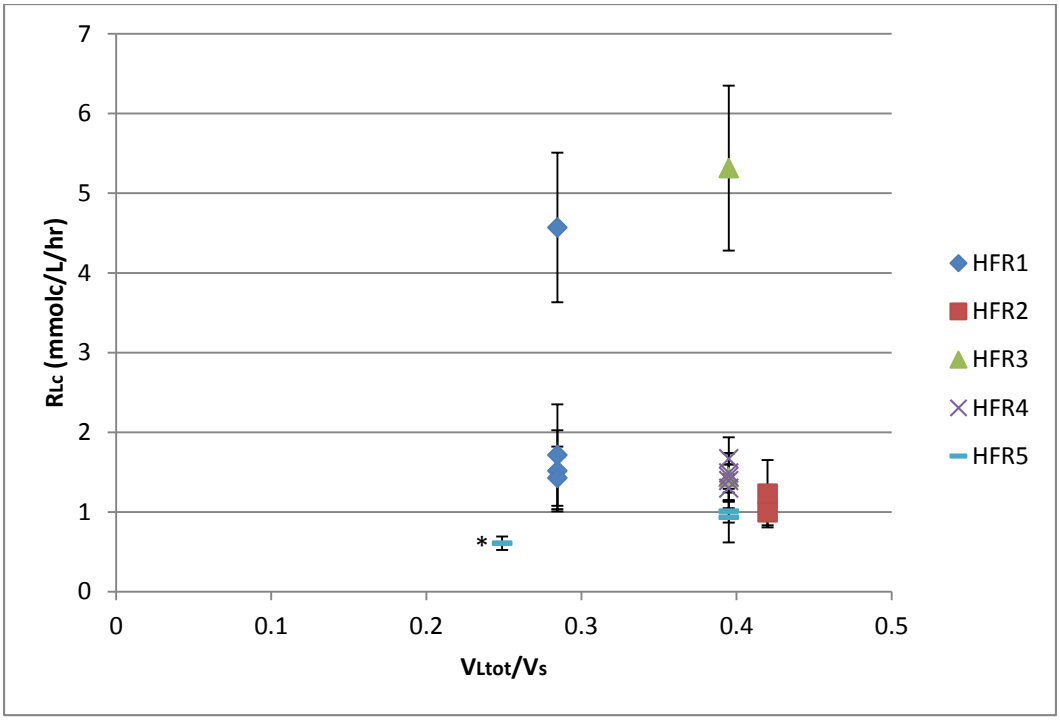

Figure 5-42. R_{Lc} as a function of V_{Ltot}/V_S. The data point with an asterisk indicates that the decrease on the x-axis was due to a decrease in the mass transfer coefficient and not a change in V_{Ltot}/V_S. Error bars indicate the 95% confidence intervals for the linear regression.

In this work three different V_{Ltot}/V_S ratios were used, 0.28 and 0.4, and 0.42. In addition to changing V_{Ltot}/V_S ratios, $K_{tot}A/V_L$ was also changed in one run. In experiment HFR5, the liquid flow rate was first set at 170 ml/min for a full fermentation run (HFR5-1), and then in the next run (HFR5-2), the liquid flow rate was decreased by half, thus decreasing the mass transfer coefficient. According to the mass transfer coefficient Equation 4-14, decreasing the flow rate by half should decrease the mass transfer coefficients of CO and CO_2 by 37% (this is assuming a γ of 0.10 and δ of 0.67 as attained in Chapter 4). Thus, this is equivalent to reducing the V_{Ltot}/V_S ratio by 37% since the overall mass transfer coefficient is a product of $K_{tot}A/V_L$ and V_{Ltot}/V_S. This

data point is shown with a star next to it indicating that the decrease on the x-axis was due to a decrease in the mass transfer coefficient and not a change in V_{Ltot}/V_S.

In order to test whether these data are in a mass transfer limiting regime, we performed a statistical analysis on all of the data points in order to determine if a change in the effective mass transfer coefficient (V_{Ltot}/V_S or $K_{tot}A/V_L$) produced a statistically significant effect on the rate of product formation (α=0.5). The results from this statistical analysis show that there is no statistical difference between the data at the several different V_{Ltot}/V_S ratios or the run with the decreased $K_{tot}A/V_L$. This shows that none of the HFR fermentations in this work were mass transfer limited because despite changes in R_{Tc}, R_{Lc} stayed essentially the same.

Within HFR1 and HFR4, there is a noticeable shift in the carbon production rates for at least one of the runs in the series. This shift in production rates shown in Figure 5-37 again indicates that the HFR fermentations performed in this work were not mass transfer limited. For example, in a mass transfer limiting case, C_{Liquid} in Equation 5-2 would be zero. Thus, the remaining variables would be fixed such that the rate of production would be dependent only upon those fixed variables. However, since we saw a shift in liquid production rates during runs where there were no changes in mass transfer parameters, this indicates that the system is not mass transfer limited.

In this regime, it is apparent the kinetic limitations were occurring since product formation rates were independent of V_{Ltot}/V_S or $K_{tot}A/V_L$. Intrinsic limitations are subject to change depending on the cellular activity and thus allows for discontinuous jumps when enzymes or other factors are up-regulated due to perturbations in the system. However, the mass transfer limited range is only dependent on the system setup.

The overall near linearity of the liquid production rates shown for all of the experiments indicate that there may be an intrinsic kinetic limitation that is present. For example, Equation 5-3 shows the reaction rate of an enzyme following Michaelis–Menten kinetics

$$v = \frac{k_{cat} \cdot E \cdot [S]}{K_m + [S]} \quad \textbf{(5-3)}$$

In this equation, v is the production rate of product, k_{cat} is the turnover number representing the maximum product formation rate, E is the enzyme concentration, and $[S]$ is the substrate concentration used to make the product. If [S]>> K_m, then a reaction rate would be intrinsically limited by the amount of enzyme and the associated turnover number. For HFR1-3 and HFR3-2, the production rates more than doubled suddenly with no change in reactor settings. As shown in Equation 5-3 this could be due to an increase in an enzyme level E. Perturbations to microbiological systems are known to affect enzyme levels (Chubukov, et al. 2013). Thus, during media replacement in between experiments, a trigger could increase a specific limiting enzyme level. The relatively linear production rates also shows that product rates are independent of redox potential and even pH. In the above experiments the pH ranged from around 6.0 to 4.8 in between each media replacement and the redox ranged from as much as -250 mV to -400 mV in between media replacements.

The production rates in this work were fairly linear indicating that $(\alpha\mu_g+\beta)X_{cells}$ was a constant. For many of the studies in which ethanol production was much greater than acetic acid production, $\beta >> \alpha\mu_g$ since β represents product formation associated with non-growth (i.e. ethanol) and $\alpha\mu_g$ represents product formation associated with growth (i.e. acetic acid). For this case, a constant β signifies a constant X_{cells}.

It should be noted that there is a period in some runs where the rates follow an exponential-type growth and then turn linear. This is most apparent in runs HFR1-3, HFR2-2, HFR3-2, HFR4-4 and HFR5-3. This could be due to an increase in X_{cells} or it could be due to an increase in an enzyme level causing α or β to increase. This exponential type increase in production rates could indicate that initially the cells are not intrinsically limited, but become limited after a certain enzyme level is reached. It is also interesting to note that for 15 of the 17 runs, the R_{Lc} stayed within 1-2 mM_c/hr. This may be the optimal production range for the cells. However, this range could possibly be manipulated to achieve the higher rates achieved in this work.

5.3.2.7 HFR Fermentation Gas Usage

In order to measure the total gas consumption rates, 5% N_2 was added to the inlet syngas. Based on a material balance of N_2 using the inlet and outlet N_2 concentrations and inlet volumetric flow rate (v_{in}), the total outlet volumetric flow rate (v_{out}) could be calculated. Afterwards, using v_{in}, v_{out} and the inlet and outlet concentrations of CO, CO_2 and H_2, the gas utilization of each gas could be calculated. However, when a carbon balance was performed in which carbon consumption via ethanol, acetic acid, and cell production was compared to carbon utilization via CO and CO_2 gas utilization, the carbon from gas utilization over-predicted the carbon from product formation by about 80%. It is possible that there were carbon species in the liquid that were not accounted for, but products such as isobutanol and propanol are usually much less than acetic acid and ethanol (Frankman 2009). One possible reason for the discrepancy could be that small amounts of N_2 from the atmosphere were introduced into the reactor or sample although this is unlikely due to the positive gas pressure relative to the atmosphere. A more likely scenario is that gas losses may have occurred because of the

pressurization of the vessel. This would result in an underestimation of v_{out} and an associated overestimation of the amount of carbon used by the gas. Thus, the value of v_{out} was difficult to determine from GC data and was also difficult to measure via other methods because of the very low gas flow rates utilized in the study. However useful information can still be gleaned from the gas GC concentration data. For example, one ratio that is of particular interest is the ratio of the flow rate of CO exiting relative to entering the reactor divided by the ratio of the flow rate of H_2 exiting the reactor relative to entering the reactor according to:

$$R = \frac{\left(v_{out} C_{CO,out} / v_{in}\, C_{CO,in}\right)}{\left(v_{out} C_{H_2,out} / v_{in}\, C_{H_2,in}\right)} = \frac{\left(C_{CO,out} / C_{CO,in}\right)}{\left(C_{H_2,out} / C_{H_2,in}\right)} \quad \textbf{(5-4)}$$

here C_{COout} is the concentration of CO measured at the outlet of the HFR, C_{COin} is the concentration of CO measured at the inlet of the reactor system, C_{H2out} is the concentration of H_2 measured at the outlet of the reactor system, C_{H2in} is the concentration of H_2 measured at the inlet of the reactor system. An advantage of this ratio is that the values of v_{out} and v_{in} are not needed. More importantly, R can be used to address relative increases and decreases in CO and H_2, which both can be used as electron donors. For example, as *R* increases, this means that the ratio of CO consumption to H_2 consumption is decreasing. As *R* decreases, the ratio of CO consumption to H_2 consumption is increasing. The electrons used to reduce the electron carriers in the methyl and carbonyl branch of the Wood-Ljungdahl pathway can be provided by H_2 or CO. The most carbon efficient method is to use H_2 for electrons so that all CO can be converted into product as opposed to CO_2. The gas usage data is shown in Figures 5-43 through 5-47 for HFR1-HFR5 respectively.

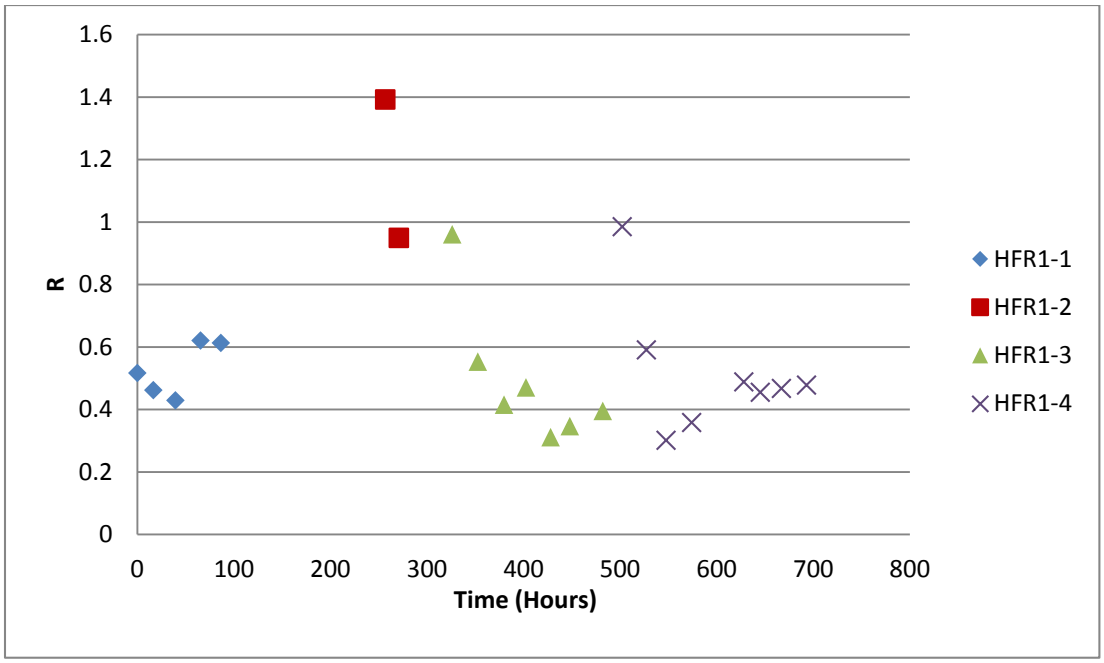

Figure 5-43. The ratio "R" as shown in equation 5-4 for HFR1.

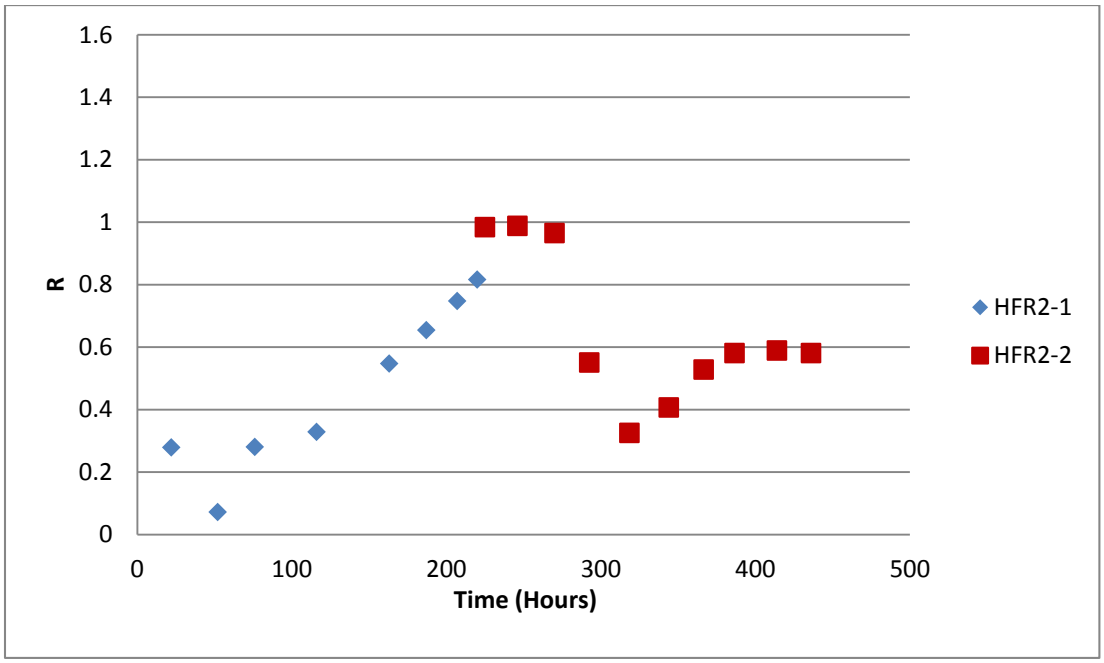

Figure 5-44. The ratio "R" as shown in equation 5-4 for HFR2.

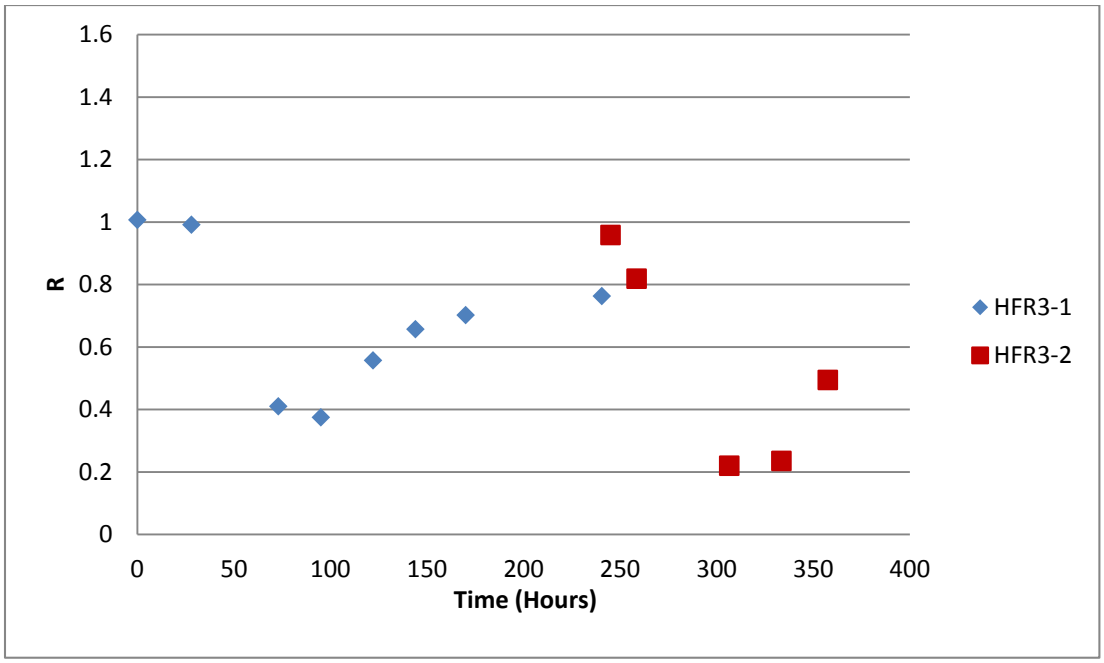

Figure 5-45. The ratio "R" as shown in equation 5-4 for HFR3.

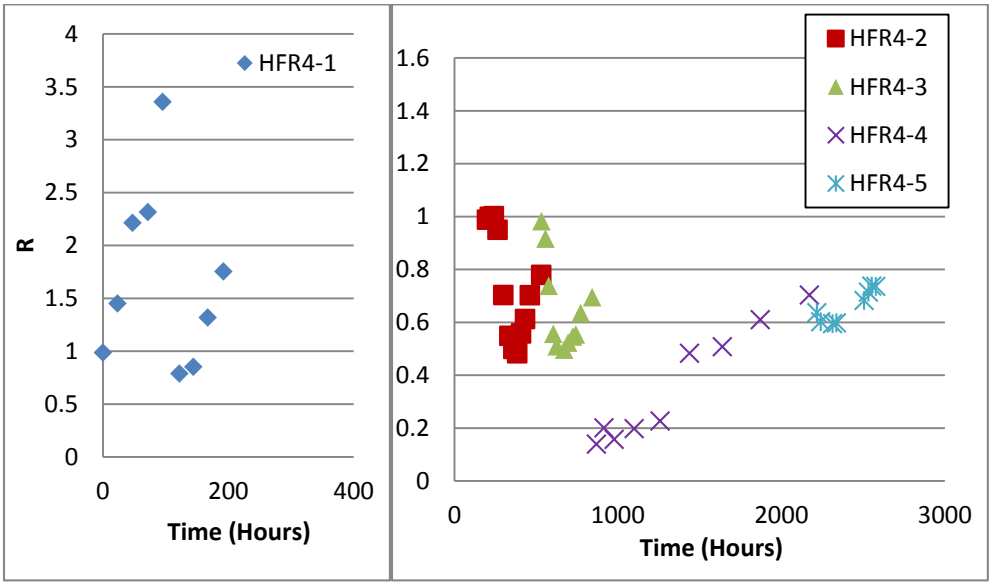

Figure 5-46. The ratio "R" as shown in equation 5-4 for HFR4. HFR4-1 is shown on a larger scale because of the larger ratios attained in this run.

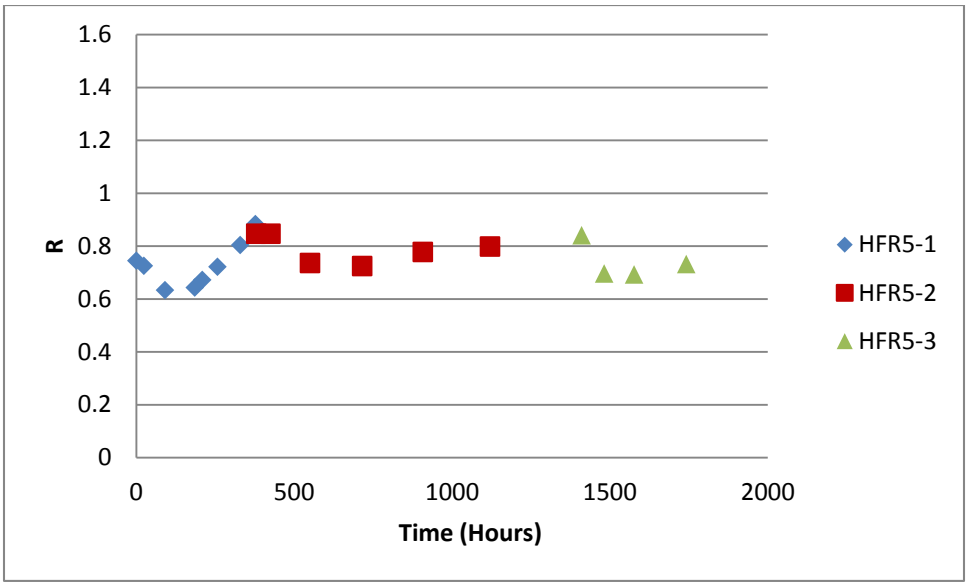

Figure 5-47. The ratio "R" as shown in equation 5-4 for HFR5.

In most of these graphs, after the initial inoculation, CO usage compared to H_2 increases with time (*R* decreases) and then decreases (R increases). This could be due to the fact that the hydrogenase enzyme initially is at low levels, and then increases with time. After there is enough hydrogenase, the cells can start to use more H_2 and CO_2 thus reducing the relative amount of CO usage. This is supported by Deshun Xu's dissertation work that shows an increase in hydrogenase activity with time due to both amount of enzyme and lower inhibition (Xu 2011). Peng Hu, in his dissertation, showed that reduction by CO at standard conditions is much more favored than H_2. However, as redox, pH, cellular activity, and NAD_{red}/NAD_{ox} ratios change the electron usage via H_2 does become thermodynamically favorable. In Figure 5-43 showing HFR1 gas usage data, HFR1-3 and HFR1-4 show very similar gas usage ratios indicating very similar CO and H_2 usage. However, the production rate R_{Lc}, for HFR1-3 is 3 times larger than HFR1-4. This tells us that that the CO consumption compared to H_2 consumption increased at almost the same rate in order to produce more product. Thus, the jump in production rates seen in this work cannot necessarily be attributed to an increase in hydrogenase production or H_2 usage. In Figure

5-44, HFR2-1 achieved the lowest R ratio indicating that this run used the most CO relative to H_2 than any other run. However, the production rate for this run was very similar to HFR2-2. This is also true of the gas usage data in Figure 5-46 which shows the largest R ratio, indicating that this run used the least CO relative to H_2 than any other run. Again, the production rate for this run was very similar to all other runs. This shows that the cells are capable of keeping production rates fairly constant by switching between CO and H_2 as electron donors.

5.3.2.8 HFR Fermentation Overview and Comparison

There were a total of 5 semi-batch HFR fermentations performed, each containing multiple media replacements. The ending ratio of ethanol to acetic acid along with the maximum R_{Lc} achieved for HFR1-HFR5 are shown in Table 5-1. Data from other syngas fermentation studies in several different bioreactors are also shown in Table 5-1 for comparison. The ethanol and acetic acid data were acquired by a literature review and also from a review of syngas fermentation by Abubackar (Abubackar, et al. 2011). The rates for Table 5-1 were calculated by assuming a linear production rate by dividing the total moles of carbon from ethanol and acetic acid by the total culture run time reported. Though the rates might not have been linear, the results from this work indicate that a linear production rate is a reasonable assumption.

The highest reported ethanol to acetic acid ratio was 21, the next highest ratio achieved was 13 in in HFR4-4. The other HFR runs ranged from 3.4 to 8.5. These ratios are much higher than almost all of the reported values in Table 5-1. The ratios shown in Table 5-1 indicate that the HFR may provide better ethanol to acetic acid ratios than other reactors. This could be due to the high mass transfer rates achieved in an HFR and the possibility that the HFR leads to high cell concentrations of predominantly non-growing cells around the fibers.

Table 5-1. Comparison of the ethanol and acetic acid ratios and product rates achieved in this work and other work.

Reactor	Microbe	Ethanol/ Acid (mol/mol)	R_{Lc} (mM_c/hr)	Reference
This Work				
HFR1-3	*Clostridium ragsdalei (P11)*	7.4	4.6	-
HFR2-1	*Clostridium ragsdalei (P11)*	6.4	1.2	-
HFR3-2	*Clostridium ragsdalei (P11)*	8.5	5.3	-
HFR4-4	*Clostridium ragsdalei (P11)*	13	1.7	-
HFR5-3	*Clostridium ragsdalei (P11)*	3.4	1.0	-
Other Work				
STR	*Clostridium ljungdahlii*	21	0.98	(Phillips, et al. 1993)
STR	*Clostridium ljungdahlii*	1.5	3.4	(Klasson, et al. 1990)
Bottle	*Butyribacterium methylotrophicum*	0.02	0.09	(Heiskanen, et al. 2007)
Flasks	*Clostridium carboxidivorans (P7)*	0.40	2.0	(Ahmed and Lewis 2007)
STR	*Clostridium autoethanogenum*	0.06	0.17	(Cotter, et al. 2009)
Bottle	*Moorella* sp. HUC22–11	0.03	0.19	(Sakai, et al. 2004)
Fermenter	*Moorella* sp. HUC22–11	0.02	0.36	(Sakai, et al. 2005)
50 mL Bottles	*Clostridium ragsdalei (P11)*	6.0	0.23	(Frankman 2009)
100 mL Bottles	*Clostridium ragsdalei (P11)*	4.0	0.16	(Frankman 2009)

Research has shown that an increase in electron donors can cause the onset of solventogenesis (Frankman 2009). Thus, if the HFR is able to provide electron donors such as CO and H_2 at higher rates, this could push the ratio of ethanol to acetic acid ratios higher than in

work with lower mass transfer rates. More evidence of this is shown in Table 5-1 by the work of Frankman with 50 mL and 100 mL bottles. In her thesis, Frankman studied the effects of mass transfer on bottles by comparing 50 mL bottles with 100 mL bottles with the gas-liquid contact surface area. It was assumed that the 50 mL bottles had higher mass transfer rates because of the larger gas-liquid contact surface area to volume ratio than the 100 mL bottles. As a result, the 50 mL bottles showed larger ethanol to acetic acid ratios than the 100 mL bottles. Also, the 50 mL bottles showed a larger production rate. This shows that both bottle studies are likely in the mass transfer limiting regime since a change in the mass transfer rate led to a change in the product formation rate. This is in contrast to the HFR which showed no change in the product formation rate when changing the mass transfer rate—signifying operation in a kinetic limiting regime.

The largest production rate (R_{Lc}) achieved in Table 5-1 was 5.3 mM_c/hr in HFR3-2. This is nearly double the next closest rate achieved in any other work. The next highest rate was 4.6 mM_c/hr again achieved in this work (HFR1-3). The rates achieved in this work shown in Table 5-1 ranged from 1.0 to 5.3 mM_c/hr. Only two other production rates achieved in other studies fell within this range. The rates shown in Table 5-1 are volumetric rates, meaning that it is not on a per cell basis. Thus, the differences in rates could be due to higher cell masses. However, it is more likely that the increase is again due to the higher mass transfer rates in the HFR because the HFR rates are, in some cases, 30 times higher than the rates in other work. One other important aspect of the HFR fermentations is that most runs had an R_{Lc} of 1-2 mM_c/h. However, in two runs this rate suddenly increased by more than two-fold. This indicates that there is some intrinsic factor that can be triggered allowing for much higher production rates. Finding this trigger and utilizing it to improve production rates could be an important aspect of future research.

5.3.2.9 HFR Fermentation Challenges

The fermentations performed in this work presented many challenges. Since HFRs are a newer possibility for syngas fermentation, traditional reactor systems are not available. Therefore, the fermentation systems had to be made from scratch. This presented a challenge as to making the system anaerobic. All connections, tubing, sampling ports, and measurement ports need have very good seals in order to prevent oxygen from entering the system. Also, when using a porous HFR the lumen and shell pressures have to be equal in order to prevent flooding of the fibers (water in the fibers blocking the gas flow). This is the reason that the syngas was piped to run through the HFR and then back into the sump, in order to equalize the pressures on both sides of the fiber. If any tubing becomes slightly pinched on the shell side it would cause a slight pressure rise and cause the fibers to flood. Flooding could be rectified by pressurizing the fibers by pinching the gas tubing until the liquid was visually cleared from the fibers. Though this problem could be rectified, it was undesirable because of the potential changes in mass transfer rates because some fibers become blocked by liquid and thus reduce the apparent gas liquid contact area of the HFR. In order to avoid flooding of the HFR when autoclaving because of the pressure changes in the autoclaving procedure, sterile media had to be added to the system afterword.

Because mass transfer rates are higher in the HFR than other bioreactors, initial startup was more difficult. Because CO is a known inhibitor of hydrogenase, too much CO initially in the system can cause stunted growth. Thus, in order to avoid exposing the cells to large amounts of CO during inoculation, large inoculation volumes were needed. This work used a 20-50% inoculation volume as compared to the standard 10% used in bottle fermentations. Because of these difficulties, there were many instances where the cells simply did not grow, or died.

However, once the method described in this work was determined then the success rate was much higher. However, even with a better procedure, there were cases when the HFR fermentations failed. Thus, because HFRs as applied to syngas fermentation is a relatively new idea, it could take more effort initially for successful fermentation as opposed to more traditional bioreactors.

5.4 Short Chain Alcohol Effects on Fermentation

5.4.1.1 Isopropanol Study

In one preliminary HFR fermentation study, not shown above, the HFR module was reused. In order to sterilize the HFR, a 70% isopropanol water mixture was injected into the HFR and circulated. The HFR was then flushed with sterilized DI water. The fermentation was then run for 473 hours and liquid samples were taken. The liquid GC analysis yielded an extra peak that is not normally present in these fermentations. It was hypothesized that it was left over isopropanol from the sterilization. In order test this, a standard isopropanol sample was analyzed on the GC and determined that the extra peak was indeed isopropanol. Based on the standard isopropanol sample, the HFR fermentation in question had 1.9 g/L of isopropanol in the system. In order to determine the effect of the isopropanol on the cells, a bottle study was organized in which a control without isopropanol was compared to bottles containing varying amounts of isopropanol. The “control” bottles contained no isopropanol, the “low” bottles contained 1 g/L of isopropanol, the “medium” bottles contained 2 g/L of isopropanol, the “high” bottles contained 4 g/L of isopropanol.

The bottle media was the same as described in Section 5.2.1. The bottles were inoculated with 10% inoculum of active cells as outlined in Section 5.2.1. The bottle studies were done in

duplicate. The bottles were regassed daily with syngas. A liquid sample was taken daily and analyzed on the liquid GC in order to measure product formation and cell mass. The OD, ethanol and acetic acid concentrations of these bottle fermentations are shown in Figure 5-48 through 5-50.

The growth of the cells shows a typical cell growth curve with a short lag phase followed by an exponential phase, then a stationary stage and finally a slight decline phase. The OD for all runs were statistically the same, showing that this range of isopropanol has no effect on cell growth. However, the ethanol results show that with increasing isopropanol concentrations, the end ethanol concentration increases. The increase is not due to conversion of isopropanol because the levels of isopropanol stayed the same through the experiment.

Also, with increasing isopropanol concentrations, the end acetic acid concentration decreases. Typically, during the non-growth stage, acetic acid is converted back into acetyl CoA via the CoA Transferase enzyme, and then the acetyl CoA can be converted into ethanol as shown in Figure 2-1. The end acetic acid and ethanol concentrations for the control bottles were 4.4 and 2.1 g/L respectively. For the highest concentration of isopropanol, the end acetic acid and ethanol concentrations were 2.3 and 4.8 g/L respectively. The difference in ethanol molar concentrations between the control and high isopropanol bottles was 0.06 mol/L. However, the difference between acetic acid molar concentrations between the control and high isopropanol bottles was 0.03 mol/L. This shows that since one mole of acetic acid can convert to one mole of ethanol, the additional ethanol comes from acetic acid conversion in addition to increased basic ethanol conversion.

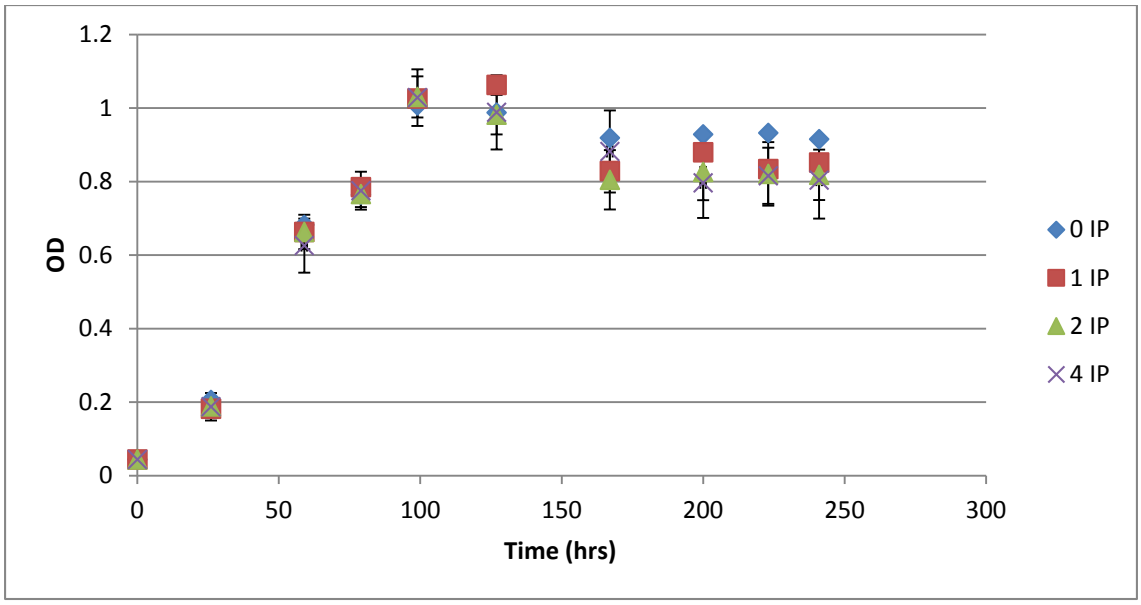

Figure 5-48. Cell growth for bottle fermentations in isopropanol study. 0 IP, 1 IP, 2 IP, and 4 IP represent the "control" bottles containing no isopropanol, the "low" bottles containing 1 g/L of isopropanol, the "medium" bottles containing 2 g/L of isopropanol, the "high" bottles containing 4 g/L of isopropanol, respectively.

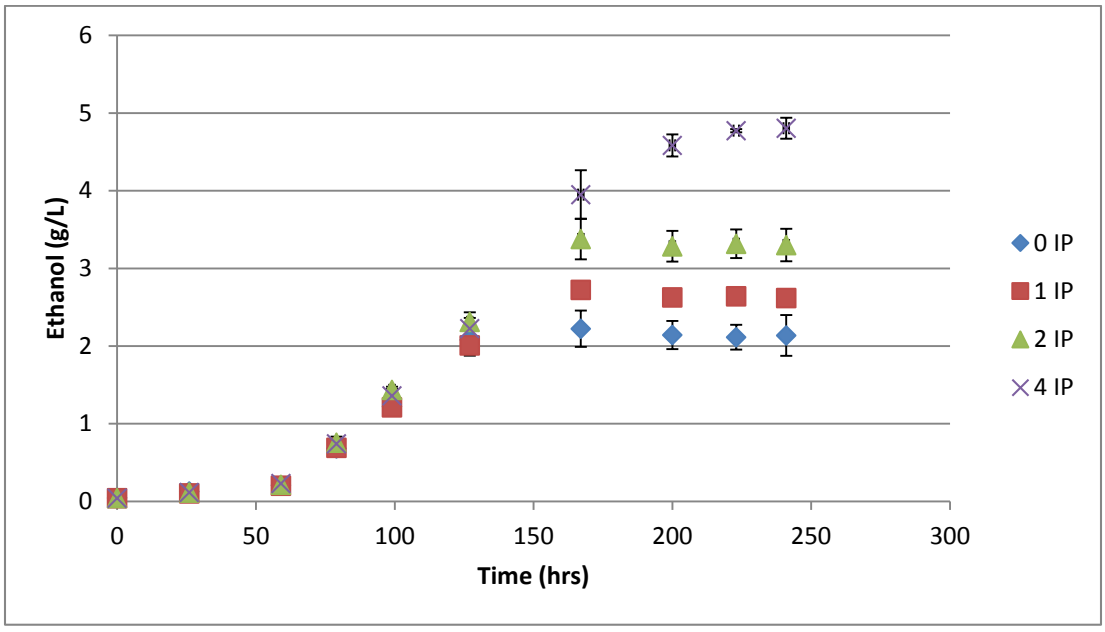

Figure 5-49. Ethanol concentrations for bottle fermentations in isopropanol study. 0 IP, 1 IP, 2 IP, and 4 IP represent the "control" bottles containing no isopropanol, the "low" bottles containing 1 g/L of isopropanol, the "medium" bottles containing 2 g/L of isopropanol, the "high" bottles containing 4 g/L of isopropanol, respectively.

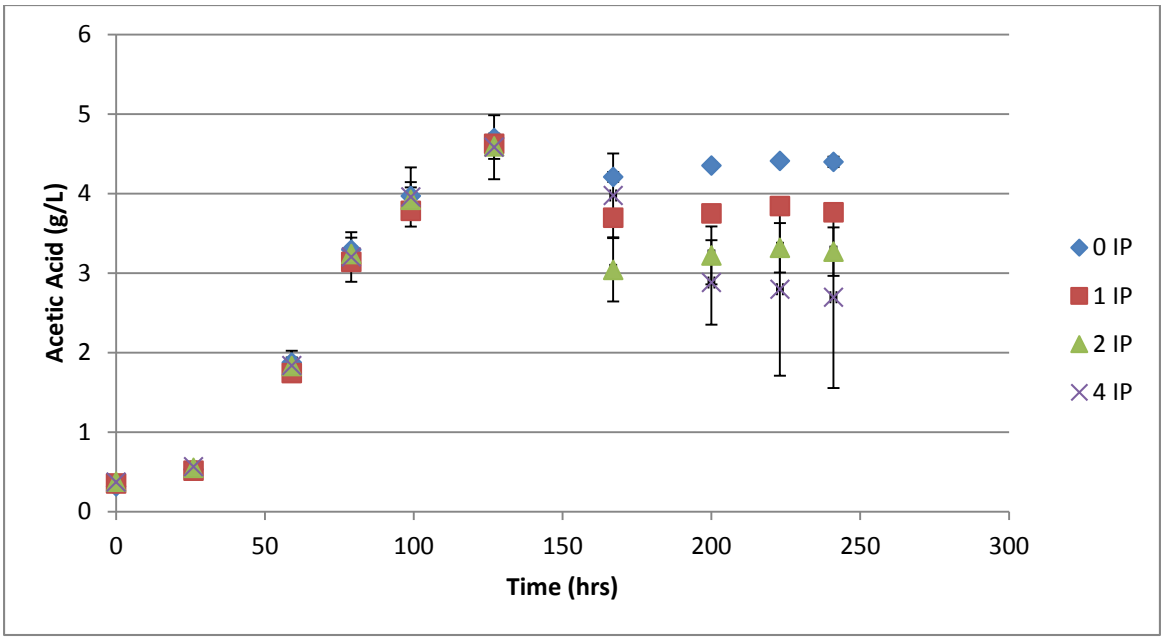

Figure 5-50. Acetic acid concentrations for bottle fermentations in isopropanol study. 0 IP, 1 IP, 2 IP, and 4 IP represent the "control" bottles containing no isopropanol, the "low" bottles containing 1 g/L of isopropanol, the "medium" bottles containing 2 g/L of isopropanol, the "high" bottles containing 4 g/L of isopropanol, respectively.

It was hypothesized that this increase in ethanol to acetic acid ratios seen with increased concentrations of isopropanol was caused by the production of heat shock proteins in response to the isopropanol. Stress from short chain alcohols parallel the stresses caused by heat shock (Dunlop 2011). These proteins assist with prevention of protein aggregation and in protein refolding, thus reducing the effects of solvents on the cell. Another possibility is that the isopropanol acts as an enzyme inductor in the production of ethanol and conversion of acetic acid to ethanol. Isopropanol enhances the toxicity of CCl_4 in the liver due to enzyme induction (Calabrese 1991) . Also, studies have shown that isopropanol induces activating and deactivating enzymes in rat kidneys and livers (Tu, et al. 1983; Zahlsen, et al. 1985). Thus, it is very plausible that the isopropanol is inducing enzymes in the Wood-Ljungdahl pathway. In order to test this hypothesis another short chain alcohol, isobutanol, was used in the bottle fermentations instead of isopropanol.

5.4.1.2 Isobutanol Study

In order to determine the effect of the isobutanol on the cells, a bottle study was organized in which a control was compared to bottles containing varying amounts of isobutanol. The "control" bottles contained no isobutanol, the "low" bottles contained 1 g/L of isobutanol, the "medium" bottles contained 2 g/L of isobutanol, the "high" bottles contained 4 g/L of isobutanol. The bottle media was the same as described in Section 5.2.1. The bottles were inoculated with 10% inoculum of active cells as outlined in Section 5.2.1. The bottle studies were done in triplicate. The bottles were regassed daily with syngas. A liquid sample was taken daily and analyzed on the liquid GC in order to measure product formation and cell mass. The OD, ethanol and acetic acid concentrations of these bottle fermentations are shown in Figures 5-51 through 5-53.

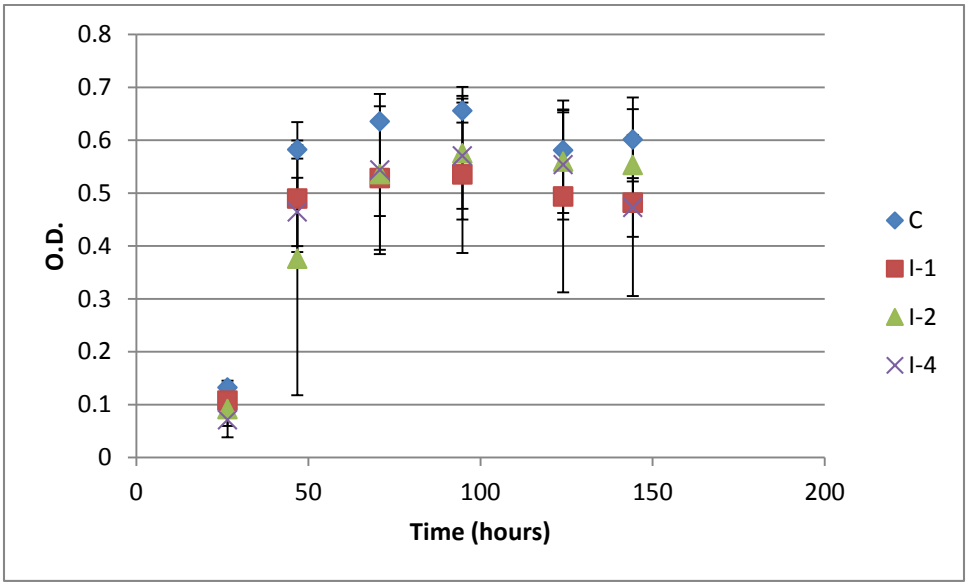

Figure 5-51. Cell growth for bottle fermentations in isopropanol study. C, I-1, I-2, and I-4 represent the "control" bottles containing no isobutanol, the "low" bottles containing 1 g/L of isobutanol, the "medium" bottles containing 2 g/L of isobutanol, the "high" bottles containing 4 g/L of isobutanol, respectively.

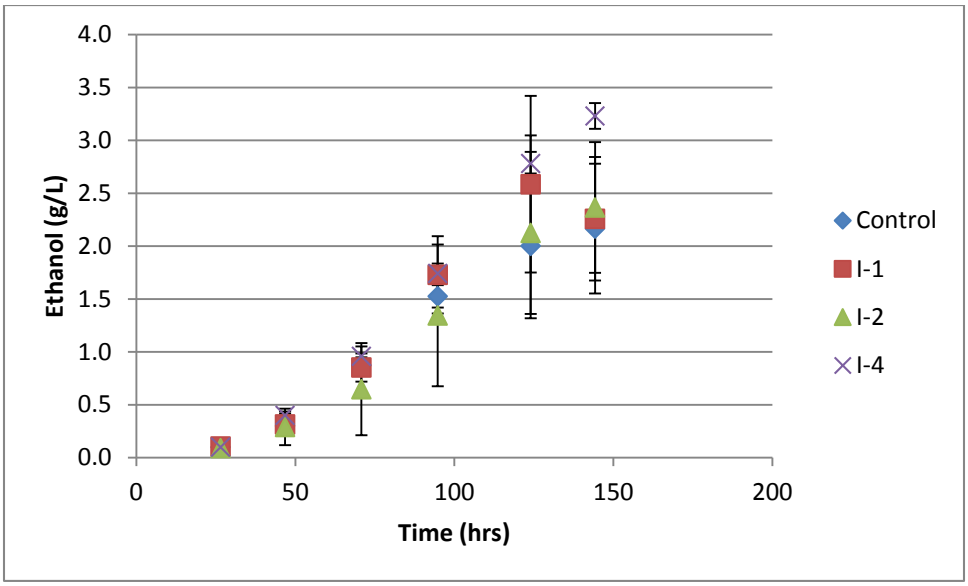

Figure 5-52. Ethanol Concentration for bottle fermentations in isopropanol study. C, I-1, I-2, and I-4 represent the "control" bottles containing no isobutanol, the "low" bottles containing 1 g/L of isobutanol, the "medium" bottles containing 2 g/L of isobutanol, the "high" bottles containing 4 g/L of isobutanol, respectively.

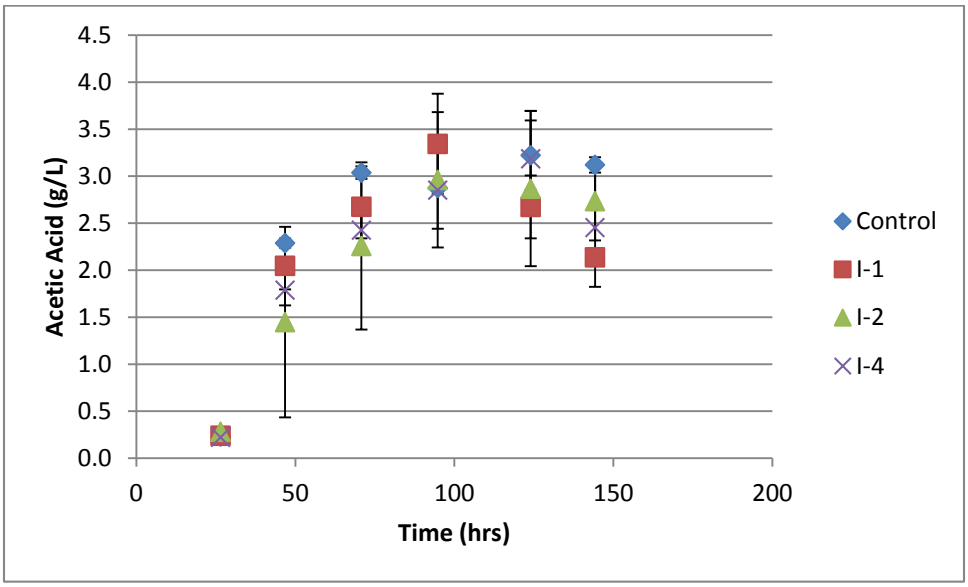

Figure 5-53. Acetic acid Concentration for bottle fermentations in isopropanol study. C, I-1, I-2, and I-4 represent the "control" bottles containing no isobutanol, the "low" bottles containing 1 g/L of isobutanol, the "medium" bottles containing 2 g/L of isobutanol, the "high" bottles containing 4 g/L of isobutanol, respectively.

In this study, the cells were slightly affected by the addition of isobutanol with the control cell growth curve being above all the others. Though the effects are not as pronounced, the ethanol production results for the isobutanol study are similar to the isopropanol study. The end acetic acid and ethanol concentrations for the control bottles were 3.1 and 2.2 g/L respectively. For the highest concentration of isopropanol, the end acetic acid and ethanol concentrations were 2.5 and 3.2 g/L respectively. This study showed that the effect of adding another short chain alcohol was not nearly as pronounced as with the isopropanol study. This indicates that the ability to induce ethanol production may be more unique to isopropanol.

5.4.1.3 Alcohol Study Conclusion

These bottle fermentation studies show that isopropanol affects ethanol production capabilities and ethanol to acetic acid ratios. This could be due to an increase in heat shock proteins caused by the addition of solvents from the beginning of the fermentation. However, it is more likely that isopropanol is acting as an enzyme inductor. Isopropanol has been shown to cause enzyme induction on proteins in the range of 50-52 kDa (Tu, et al. 1983). The CoA transferase enzyme in *C. carboxidivorans,* a related species, is about 43 kDa (Paul, et al. 2010). Thus, it is likely that CoA transferase may be induced by isopropanol. This would cause an increase in the conversion of acetic acid to ethanol as was shown in the isopropanol study. Because this does not fall under the work outlined in this thesis, no further work was performed on this hypothesis. However this could be an important finding that could help achieve greater ethanol to acetic acid ratios in syngas fermentation.

5.5 Conclusions

This work showed that the HFR was able to outperform other traditional bioreactors. For example, the HFR fermentations were able to achieve high production rates (5.3 mM_c/hr). Also, the ethanol to acetic acid ratios achieved in this work were higher than all but one other study. Since research has shown that an increase in electron donors can cause the onset of solventogenesis, the HFRs ability to provide electron donors such as CO and H_2 at higher rates could push the ratio of ethanol to acetic acid ratios higher than in reactors with lower mass transfer rates. In addition to high mass transfer rates, the cells are able to aggregate on the fibers very near the high gas concentrations again allowing for exposure to more electron equivalents needed for the reduction of CO and CO_2 to ethanol. The gas usage data in this work showed evidence that the ratio of CO consumed to H_2 consumed can vary greatly, even in very similar reactor setups. This may highlight the cells ability to keep production rates fairly constant even though intracellular aspects, such as hydrogenase levels ,may not be high enough to consume all of the H_2 present. This worked also showed evidence that there is no formation of a biolayer that contains bacteria enclosed in a protective extracellular polymeric matrix in the HFRs. However, there is abundant evidence of a loosely attached aggregates cells. Thus, the total amount of cells in an HFR system is difficult to know until after the experiment is stopped and the HFR can be washed.

This work also showed evidence that the HFR was not mass transfer limited. When V_{Ltot}/V_S increased or decreased there was no significant change in product formation rates. Also, when $K_{tot}A/V_L$ was decreased there was no significant decrease in production rates. These results are consistent with Equation 5-2, but also show that the fermentation system used in this work is not mass transfer limited. Also, gas usage ratios showed evidence that cells prefer CO as opposed to

H_2 as an electron donor. Though HFR fermentation can be initially difficult to perform reliable fermentations, once an appropriate procedure is determined it has a very good chance to being just as reliable as other traditional bioreactors.

Finally, isopropanol was shown to increase ethanol to acetic acid ratios and overall ethanol production. This effect could be due to the up-regulation of heat shock proteins that improve the cell's tolerance to ethanol. However, it is more likely due to the induction of CoA transferase or some other enzyme in the Wood-Ljungdahl pathway by isopropanol.

6 CO and H_2 as Electron Donors and Effects on Ethanol Production

6.1 Introduction

There are many different types of bioreactors used in the fermentation of syngas. However, the fundamental aspects of the reactors are the same. In order for the microbes to metabolize the syngas, they have to be exposed to the gas dissolved in the liquid media, or in the gas phase. The concentrations of CO, H_2 and CO_2 at the inlet of the reactor will not be the same at the outlet. In a well-designed reactor, there will be little to no wasted CO and H_2. Several different organisms can be used in the conversion of syngas to ethanol. These organisms include the Clostridiums; *C. ljungdahlii, C. carboxidivorans, C. autoethanogenum,C. ragsdalei.* Different genera can also be used in syngas fermentation, however Clostridium have generally shown the highest ethanol yields (Abubackar, et al. 2011).

The Clostridium listed above follow the Wood-Ljungdahl pathway to convert syngas to ethanol and acetic acid, simplified in Figure 6-1 (Wood, et al. 1986). In this pathway CO and CO_2 are used as carbon sources to form acetyl-CoA which can then be used to make ethanol and acetic acid. In the methyl branch of the Wood-Ljungdahl pathway, six electrons and one ATP are used to convert CO_2 into a methyl moiety that combines with a CO and coenzyme A to form acetyl-CoA. In the carbonyl branch, CO_2 is reduced by two electrons to form CO. The electrons used to reduce the electron carriers in the methyl and carbonyl branch can be provided by H_2 or CO as shown in Equations 6-

1 and 6-2 where X_c represents an electron carrier. Figure 6-1 shows the number of electrons necessary for each step in the Wood-Ljungdahl pathway.

$$H_2 + X_c \leftrightarrow 2H^+ + X_c^{2-} \quad \textbf{(6-1)}$$

$$CO + H_2O + X_c \leftrightarrow CO_2 + 2H^+ + X_c^{2-} \quad \textbf{(6-2)}$$

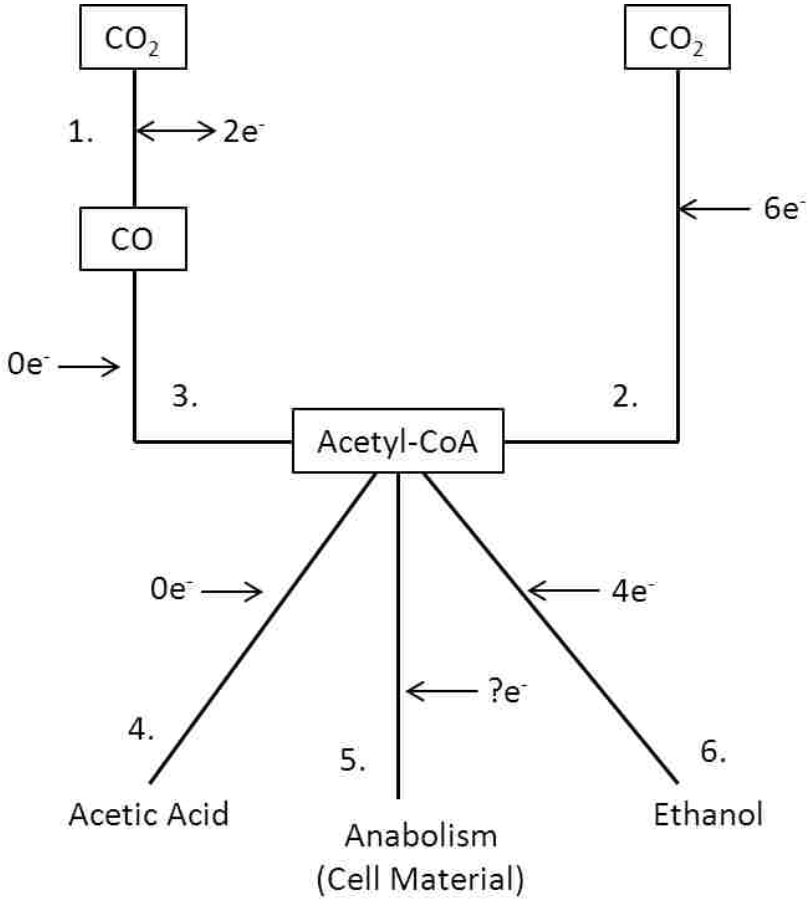

Figure 6-1. Wood-Ljungdahl pathway showing electrons necessary for each path.

Step 1 is reversible and can accept or give two electrons depending on whether CO_2 is being converted to CO or vice versa. Step 2 requires 6 electrons, steps 3 and 4 do not require any electrons, step 5 requires an unknown amount of electrons, and step 6 requires 4 electrons.

Because CO can be used as a carbon source, the most efficient use of syngas would be when H_2 is used as the electron source and both CO and CO_2 are used as carbon sources. A summary of the net reactions that can occur and also how many electrons come from CO and H_2 in each case are shown in in Equations 6-3 through 6-6:

	Electrons Provided		
	CO	H_2	
When all three gasses are present:	0	10	$CO + CO_2 + 5\ H_2 \leftrightarrow C_2H_6O + 2\ H_2O$ **(6-3)**
When there is only CO_2 and H_2:	0	12	$2\ CO_2 + 6\ H_2 \leftrightarrow C_2H_6O + 3\ H_2O$ **(6-4)**
When there is only CO and H_2:	2	8	$2\ CO + 4\ H_2 \leftrightarrow C_2H_6O + H_2O$ **(6-5)**
When there is only CO	10	0	$6\ CO + 3\ H_2O \leftrightarrow C_2H_6O + 4\ CO_2$ **(6-6)**

In Equation 6-3, all of the CO and CO_2 are used to make ethanol with no net production of CO_2. This is the most efficient process possible in syngas fermentation resulting in 100% efficiency. However, this situation is highly unlikely. In his dissertation, Peng Hu performed an in-depth thermo analysis in order to address the question of electron production between CO and H_2 during typical syngas fermentation conditions (Hu 2011). In this analysis he used transformed Gibbs free energies to compare CO and H_2 as electron donors. Hu's results showed that reduction by CO at standard conditions is much more favored than H_2. At different reactor conditions H_2 electron production does become thermodynamically favorable. However, CO electron production is always more thermodynamically favorable than H_2 production despite any changes in pH, ionic strength, gas partial pressure, and electron carrier pairs.

If only CO is used in syngas fermentation as shown in Equation 6-6, the reaction produces CO_2 which is not incorporated into ethanol or acetic acid. The efficiency of this

reaction is only 33%. However, as mentioned above, the most likely reaction scenario is one that uses both CO and H_2 as electron sources. This means that the carbon conversion efficiency for syngas fermentation could range anywhere from 33% to 100% depending on reactor conditions and cellular enzyme regulation.

In addition to ethanol, another product of the Wood-Ljungdahl pathway is acetic acid. For acetic acid production the net reactions would be:

	Electrons Provided			
	CO	H_2		
When all three gasses are present:	0	6	$CO + CO_2 + 3\ H_2 \leftrightarrow C_2H_4O_2 + H_2O$	**(6-7)**
When there is only CO_2 and H_2:	0	8	$2\ CO_2 + 4\ H_2 \leftrightarrow C_2H_4O_2 + 2\ H_2O$	**(6-8)**
When there is only CO and H_2:	2	4	$2\ CO + 2\ H_2 \leftrightarrow C_2H_4O_2$	**(6-9)**
When there is only CO	6	0	$4\ CO + 2\ H_2O \leftrightarrow C_2H_4O_2 + 2CO_2$	**(6-10)**

For acetic acid production the carbon efficiency could range from 50% to 100%. In order to assess the viability of ethanol produced from syngas fermentation, appropriate bounds need to be set for the theoretical yield of ethanol. These bounds include the syngas compositions that can be produced from current gasification technologies, theoretical maximum and minimum ethanol production, and carbon lost to acetic acid.

Acetic acid, or acetate, is produced at different rates depending on many different factors, including cell growth stage, partial pressure of CO, and pH (Hu 2011; Hurst and Lewis 2010). During the growth stage of the cells, it is likely that only acetic acid is produced and ethanol production is a result of acetic acid depletion (Hurst and Lewis 2010). However, during the stationary stage of the cell growth the cells begin to produce ethanol while also depleting acetic

acid. Using data from Hurst and Lewis, the ethanol to acetic acid ratio in the stationary phase ranged from about 1.6 (P_{CO}=2 atm) to essentially 0 (P_{CO}=0.35 atm) depending on the partial pressure of CO (Hurst and Lewis 2010). This could mean that in the absolute worst case scenario, there is essentially no ethanol production, only acetic acid. In Hu's dissertation while studying the effects of pH on ethanol production, the ethanol to acetic acid ratio ranged from about 13 to 1.3 (Hu 2011). While acetic acid is valuable, one important goal of syngas fermentation is to produce a renewable liquid fuel that can be used in combustion engines.

6.2 Ethanol Production Scenarios

There has been much optimism in the use of anaerobic bacteria to convert biomass derived syngas to ethanol. The Biomass R&D Technical Advisory Committee found in their study that there is enough biomass produced annually to meet more than one third of the transportation energy costs (Perlack 2005). Several biofuel companies have made predictions for syngas derived ethanol production. These predictions range from 85 to 100 gallons of ethanol per ton of dry biomass, 55 gallons of ethanol per ton of municipal waste, and up to 150 gallons of ethanol for hydrocarbon rich fuels (Brienergy 2011; Coskata 2011; Mackaluso 2007). This work analyzed the maximum amount of ethanol that can be produced from gasification of biomass and the best predictions based on current research in ethanol fermentation. The difficulty with these predictions in that the predictions were not based on typical gas compositions observed with biomass gasification but rather the biomass composition.

Using Equations 6-3 through 6-10, tables were constructed showing the range of possible ethanol production rates per ton of biomass from different gasifiers and types of biomass. Alauddin et al. provided an in depth review of gasification of biomass in fluidized bed reactors (Alauddin, et al. 2010). In this review several different biomass types were compared along with

different types of fluidized bed reactors. Based on this reactor data and Equations 6-3 to 6-10, Table 6-1 was constructed. The last rows in the table give predictions based on the assumption that all H_2 was used, or no H_2 was used. In the predictions where all H_2 was used, Equations 6-3 through 6-10 were used. Equation 6-3 and 6-7 were used until any one of the three gasses ran out. After that, if CO ran out then Equations 6-4 and 6-8 were. If CO_2 ran out then Equations 6-5 and 6-9 were used. If H_2 ran out then Equations 6-6 and 6-10 were used. Once there was no H_2 or CO then the reaction stopped. In the predictions where no H_2 was used, then only Equations 6-6 and 6-10 were used. The volume of gas given in Table 6-1 was converted to moles by using the volume fractions from the table and the ideal gas law. The moles of liquid product were converted to liquid volumes by using the molecular weight and density of ethanol and acetic acid.

Table 6-1 shows the several different theoretical yields of ethanol if no acetic acid were produced. The largest theoretical yield of ethanol per ton that could be produced would be when there is no acetic acid produced. Table 6-1 shows that the most ethanol that could be produced would be 80.5 gallons of ethanol per ton of biomass (Almond Shell) when all H_2 is used, and 40.1 gallons of ethanol per ton of biomass (Sawdust) when no H_2 is used. The range of ethanol shown in Table 6-1 is 11.4 to 80.5 gallons per ton of biomass. These predictions based on syngas composition are lower than predictions based on biomass composition. It should be noted that some of the biomass sources in Table 6-1 may not be as abundant as others and thus are less realistic than others for large scale analysis. For example, almond shells as biomass are not likely as abundant as wood chips or sawdust. The advantage of looking at ranges with complete H_2

utilization and no H_2 utilization is that H_2 use can vary depending on the activity of hydrogenase. Table 6-1 assumed that no acetic acid was produced, however during the growth phase, acetic acid is produced in a much higher ratio to ethanol (Hurst and Lewis 2010).

Table 6-1. Theoretical ethanol production with no acetic acid production. [1](Cao, et al. 2006), [2](Turn, et al. 1998), [3](Pan, et al. 2000), [4](Weerachanchai, et al. 2009), [5](Rapagna, et al. 2000), [6](Mansaray, et al. 1999), [7](Miccio, et al. 2009), [8](Bingyan X. 1994), [9](Li, et al. 2004).

Reference	1	2	3	4	5	6	7	8	9
Fluidized bed type	Bubble	Bubble	Bubbling	Bubbling	Bubbling	Bubbling	Bubbling	Circulating	Circulating
Biomass type	Sawdust	Cedar Wood	Pine Chips / Coal	Larch Wood	Almond Shell	Rice Husk	Spruce Wood Pellet	Wood Powder	Sawdust
Gas yield (Nm^3gas/kg biomass)	2.99	1.90	2.46	1.55	1.10	1.05	1.20	1.93	2.35
Syngas composition									
vol% CO	9	16	17	8	33	20	18	17	18
vol% CO_2	13	16	8	29	12	14	14	16	16
vol% Cn compounds	6	6	2	7	12	5	1	0	3
vol% H_2	9	11	13	56	44	4	30	16	7
vol% N_2 + other	62	51	59	0	0	57	0	43	55
Uses all H_2									
Gal AA/ton	0.0	0.0	0.0	0.0	0.0	0.0	0.0	0.0	0.0
Gal EtOH/ton	52.7	48.5	70.0	76.8	80.5	23.9	54.8	60.6	56.4
Uses no H_2									
Gal AA/ton	0.0	0.0	0.0	0.0	0.0	0.0	0.0	0.0	0.0
Gal EtOH/ton	26.3	29.0	39.4	11.4	34.8	19.9	20.1	30.7	40.1

With time, this ratio decreases as a result of the decreased acetic acid production and acetic acid conversion to ethanol. Previous studies have shown a steady state ethanol to acetic ratio of about 6.0 (Rajagopalan, et al. 2002). Table 6-2 shows the several different theoretical yields of ethanol and acetic acid if the ethanol to acetic acid ratio is 6.0. Table 6-2 shows that the most ethanol that could be produced with this ratio would be 74.6 gallons of ethanol per ton of biomass (Larch Wood) when all H_2 is used, and 36.1 gallons of ethanol per ton of biomass (Wood Powder) when no H_2 is used. The range of ethanol shown in Table 6-1 is 10.2 to 74.6 gallons per ton of

biomass. It is obvious that the high ethanol/acetic acid ratio assumed for Table 6-2 gives a similar ethanol range as to that shown in Table 6-1.

Table 6-2. Theoretical ethanol production with ethanol/acetic acid =6.0. Refer to Table 2-1 for references.

Reference	**1**	**2**	**3**	**4**	**5**	**6**	**7**	**8**	**9**
Fluidized bed type	Bubble	Bubble	Bubbling	Bubbling	Bubbling	Bubbling	Bubbling	Circulating	Circulating
Biomass type	Sawdust	Cedar Wood	Pine Chips / Coal	Larch Wood	Almond Shell	Rice Husk	Spruce Wood Pellet	Wood Powder	Sawdust
Gas yield (Nm^3gas/kg biomass)	2.99	1.90	2.46	1.55	1.10	1.05	1.20	1.93	2.35
Syngas composition									
vol% CO	9	16	17	8	33	20	18	17	18
vol% CO_2	13	16	8	29	12	14	14	16	16
vol% Cn compounds	6	6	2	7	12	5	1	0	3
vol% H_2	9	11	13	56	44	4	30	16	7
vol% N_2 + other	62	51	59	0	0	57	0	43	55
Uses all H_2									
Gal AA/ton	7.8	7.1	10.3	12.2	11.8	3.5	8.0	8.3	7.8
Gal EtOH/ton	47.5	43.7	63.0	74.6	72.4	21.5	49.3	50.8	47.5
Uses no H_2									
Gal AA/ton	3.9	4.3	5.8	1.7	5.1	2.9	3.0	5.9	3.9
Gal EtOH/ton	23.7	26.1	35.5	10.2	31.3	17.9	18.1	36.1	23.7

Tables 6-1 and 6-2 show theoretical yields of ethanol and acetic acid assuming that all of the syngas is used by the microbes. However, under real reactor conditions, all of the syngas cannot be used. Furthermore, as shown by Hurst et al., the production of ethanol depends on the partial pressure of CO (Hurst and Lewis 2010). High partial pressures result in higher ethanol production. In a syngas fermentation reactor as CO is used, partial pressure decreases along with ethanol production. Thus, the previous results could even be lower than predicted depending on the type of reactor used and how the partial pressures of each component of the syngas change. For example, in one study

using only CO, CO_2, N_2 and *C. Carboxydivorian* as the microbial catalysis the CO utilization was only 60% (Rajagopalan, et al. 2002).

As shown above, the range of ethanol production can be quite broad, from 10.2-80.5 gallons of ethanol per ton biomass. This range depends on gasification material, electron usage, acetic acid conversion, and partial pressure effects of syngas components. As gasification procedures are enhanced to produce more usable producer gas from the biomass, the amount of ethanol can potentially increase to the projected 85-100 gallons per ton of biomass based on the biomass composition. However, it is obvious from the above analysis that syngas variability can lead to high variability of ethanol predictions which would be a better predictive method than based solely on biomass composition. If ethanol produced from syngas fermentation is going to be synthesized on a large scale, these issues need to be addressed.

6.3 H_2 and CO Bottle Studies

The theoretical ethanol production situations discussed above gave the scenario of all H_2 and no H_2 consumed to provide a range of ethanol production since H_2 utilization depends on the state of the cell and its surroundings. There is not yet a full understanding as to the effects of H_2 and CO on growth and product formation, especially when both gasses are used together. The effects of CO and H_2 on *C. ragsdalei* were analyzed in order to analyze electron usage as a function of gas composition. This study will enable future researchers to make more accurate predictions about liquid production yields from biomass.

6.3.1 Materials and Methods

The media solution was made by adding 10 ml metals stock solution, 30 ml mineral stock solution, 10 ml vitamin stock solution, 1 g yeast extract, and 10 g MES buffer to 950 ml distilled

water. The trace metals stock solution contained (per liter) 0.2 g cobalt chloride, 0.02 g cupric chloride, 0.8 g ferrous ammonium sulfate, 1 g manganese sulfate, 0.2 g nickel chloride, 2 g nitrilotriacetic acid, 0.02 g sodium molybdate, 0.1 g sodium selenate, 0.2 g sodium tungstate, and 1 g zinc sulfate. The mineral stock solution contained (per liter) 4 g calcium chloride, 20 g hydrated magnesium sulfate, 10 g potassium chloride, 10 g potassium phosphate monobasic, and 80 g sodium chloride. The vitamin stock solution contained (per liter) 0.005 g aminobenzoic acid, 0.002 g d-Biotin, 0.005 g pantothenic acid, 0.002 g folic acid, 0.01 g MESNA, 0.005 g nicotinic acid, 0.01 g pyridoxin, 0.005 g riboflavin, 0.005 g thiamine, 0.005 g thioctic acid, and 0.005 g vitamin B12 (Rajagopalan, et al. 2002). After adding the initial ingredients, the media was titrated to pH 6.0 using 5N KOH (EMD Chemicals, Gibbstown, New Jersey). After titration, the solution was made anaerobic by boiling and purging with nitrogen. Then, 1% vol/vol of a Na_2S solution, containing 4 g of $Na_2S \cdot 9H_20$ (EMD Chemicals, Gibbstown, New Jersey) in 100 mL water and 4 g of L-cysteine (Sigma-Aldrich, St. Louis, Missouri) in 100 mL water, was added to each bottle to act as an oxygen scavenger.

In order to analyze the effects of H_2 electron equivalents, cells were grown on three different initial partial pressures of H_2, while keeping the initial partial pressure of CO and CO_2 constant. N_2 was used as an inert gas to achieve the correct partial pressures of the syngas components. The bottles contained 50 mL of media and about 230 mL of headspace. The syngas ratio traditionally used with *C. ragsdalei* is a 40:30:30 mixture of $CO:CO_2:H_2$ resulting in a 4:3:3 ratio of $CO:CO_2:H_2$. The ratio of CO to CO_2 was held constant at a 4:3 ratio. The high partial pressure bottles were at a 4:3:13 ratio of $CO:CO_2:H_2$, medium partial pressures were at a 4:3:7 ratio of $CO:CO_2:H_2$, low partial pressures were a 4:3:0 ratio of $CO:CO_2:H_2$, and a control with a 4:3:3 ratio of $CO:CO_2:H_2$. This is summarized in Table 6-3.

Table 6-3. H_2 bottle study syngas variation.

H_2 Levels	Ratio $CO/CO_2/H_2$	Gas Percentage	Partial Pressure
High	4:3:13	20% CO, 15% CO_2, 65% H_2, 0% N_2	4 psig CO, 3 psig CO_2, 13 psig H_2, 0 psig N_2
Medium	4:3:7	20% CO, 15% CO_2, 35% H_2, 30% N_2	4 psig CO, 3 psig CO_2, 7 psig H_2, 6 psig N_2
Low	4:3:0	20% CO, 15% CO_2, 0% H_2, 65% N_2	4 psig CO, 3 psig CO_2, 0 psig H_2, 13 psig N_2
Control	4:3:3	20% CO, 15% CO_2, 15% H_2, 50% N_2	4 psig CO, 3 psig CO_2, 3 psig H_2, 10 psig N_2

The bottle studies were done in triplicate. The bottles were regassed every 12 hours with the appropriate syngas mixture as stated in Table 6-3. Every 24 hours, the headspace pressure was measured and a gas sample was taken and analyzed on a gas GC in order to measure the amount of CO, CO_2, and H_2 consumed or generated. A liquid sample was also taken every 24 hours in order to measure product formation, pH, and cell mass.

In order to analyze the effects of CO electron equivalents, cells were grown on three different initial partial pressures of CO, while keeping the initial partial pressure of H_2 and CO_2 constant. The ratio of H_2 to CO_2 was held constant at a 1:1 ratio. The high partial pressure bottles were at a 14:3:3 ratio of $CO:CO_2:H_2$, medium partial pressures were at a 8:3:3 ratio of $CO:CO_2:H_2$, low partial pressures were a 1:3:3 ratio of $CO:CO_2:H_2$, and a control was at 4:3:3 ratio of $CO:CO_2:H_2$. N_2 was used as an inert gas to achieve the correct partial pressures of the syngas components. This is summarized in Table 6-4.

Table 6-4. CO bottle study syngas variation.

CO Levels	Ratio $CO/CO_2/H_2$	Gas Percentage	Partial Pressure
High	14:3:3	70% CO, 15% CO_2, 15% H_2, 0% N_2	14 psig CO, 3 psig CO_2, 3 psig H_2, 0 psig N_2
Medium	8:3:3	40% CO, 15% CO_2, 15% H_2, 30% N_2	8 psig CO, 3 psig CO_2, 3 psig H_2, 6 psig N_2
Low	1:3:3	5% CO, 15% CO_2, 15% H_2, 65% N_2	1 psig CO, 3 psig CO_2, 3 psig H_2, 13 psig N_2
Control	4:3:3	20% CO, 15% CO_2, 15% H_2, 50% N_2	4 psig CO, 3 psig CO_2, 3 psig H_2, 10 psig N_2

These bottle studies were done in triplicate. These bottles were regassed every 24 hours as opposed to every 12 hours because the ratios of gas were did not significantly change in 12 vs. 24 hours. The bottles were regassed with the appropriate syngas mixture as stated in Table 6-4 and the headspace pressure was measured and a gas sample was taken and analyzed on a gas GC in order to measure the amount of CO, CO_2, and H_2 consumed or generated. A liquid sample was taken every 24 hours in order to measure product formation, pH, and cell mass.

6.3.2 H_2 Variation Results and Discussion

The results for cell growth for the varying H_2 bottle studies are shown in Figure 6-2. The growth of the cells shows a typical cell growth curve with a short lag phase followed by an exponential phase, then a stationary stage and finally a decline phase. It is interesting to note that although the total electron equivalents for each of the 4 groups ranged from 57-242% compared to the control, the cell growth showed very similar results. Since the lowest amount of H_2 moles used was zero, this confirms that cell anabolism does not necessarily require H_2. This fits in well with what would be expected, since the cells use the Wood-Ljungdahl pathway shown in Figure 6-1. In step 5, the cell mass must come from either CO or CO_2. Since H_2 is not necessary for

anabolism, this means that step 5 likely prefers electrons from CO. This is made apparent in the growth curves shown in the CO variation study shown in Section 6.3.3 that shows lower growth with low CO. In addition to the data in this study, the hypothesis that cell anabolism is dependent on CO and not H_2 is supported even more by comparing growth data from a study done by Chris Hoeger in his thesis (Hoeger 2012). In this study, cells were grown in bottles on only H_2 and CO_2. This growth curve is shown in Figure 6-2. The cells that did not have CO in the headspace had very little growth compared to the control. Thus, even though there was CO_2 providing enough carbon for step 5, the cells did not grow well, indicating that the electrons for step 5 could not readily be supplied by H_2.

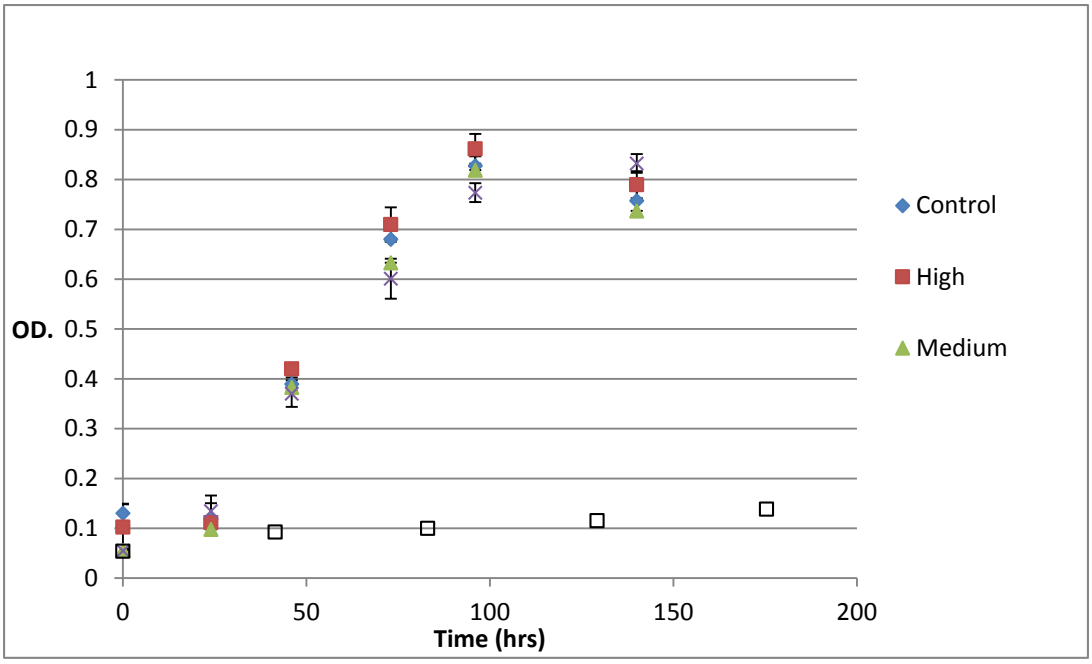

Figure 6-2. OD of bottle fermentations in H_2 variation study.

The reason that CO can provide electrons to step 5 for anabolism but not H_2 may be associated with the transfer of electrons from H_2 as compared with CO. The difference could be due to the type of electron carrier associated with the hydrogenase and CO dehydrogenase

enzyme (CODH). Currently, the electron carriers for *C. ragsdalei* have not been identified. One electron carrier that is likely used by *C. ragsdalei* is NAD(P)H/NAD(P)$^+$, since these electron carrier pairs are very common in physiological systems (Ljungdahl 1986). However, it is likely that ferredoxin is also used as an electron carrier in *C. ragsdalei* (Ragsdale 2008). NADPH is predominantly used in anabolic reactions as opposed to NADH (Alberts, et al. 2002). Whereas, the acetaldehyde dehydrogenase enzyme and alcohol dehydrogenase enzymes used in in step 6 to make ethanol can both use NADH as an electron carrier. Thus, if the hydrogenase enzyme used by *C. ragsdalei* used NADH as opposed to NADPH as an electron carrier, then this could be the reason why electrons from H_2 cannot be used for cell anabolism but can be used for ethanol production. Thus, CO is the preferred electron source for cell growth (step 5). Though CO is preferred for cell growth it is not necessarily preferred for ethanol production (step 6). This is evident by again looking at the cells in Hoeger's study shown in Figure 6-2. These cells showed very little cell growth, but they produced about the same amount of ethanol per cell (~160 $g/L/g_{cell}$) as the cells grown on the high levels of H_2 in this work (Hoeger 2012). This indicates that having no CO caused low cell growth, but did not affect the levels of ethanol production per cell.

The cumulative gas consumption with time is shown in Figures 6-3 through 6-5. Based on the slopes in Figure 6-3, as H_2 availablity increased, the rate of H_2 consumption also increased. According to the Wood-Ljungdahl pathway, when H_2 consumption increases, we would also expect an increase in carbon consumption. This is because the electrons from H_2 can be used to reduce CO_2 in step 1 and also to reduce acetyl-CoA to ethanol in step 6 (see Figure 2-1). As H_2 consumption increased there was a large increase in the amount of CO_2 consumed as shown in

Figure 6-5. Also, as H_2 consumption increased there was also a small increase in the rate of CO consumed as shown in Figure 6-4.

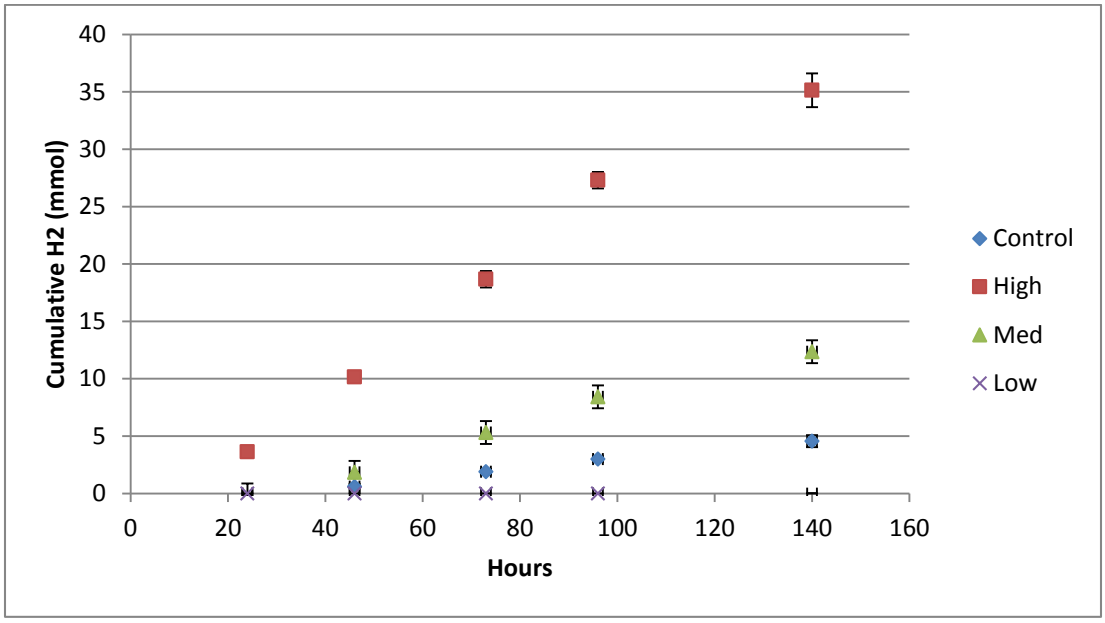

Figure 6-3. Cumulative H_2 consumed in the H_2 variation study. Error bars represent ± 1 standard deviation.

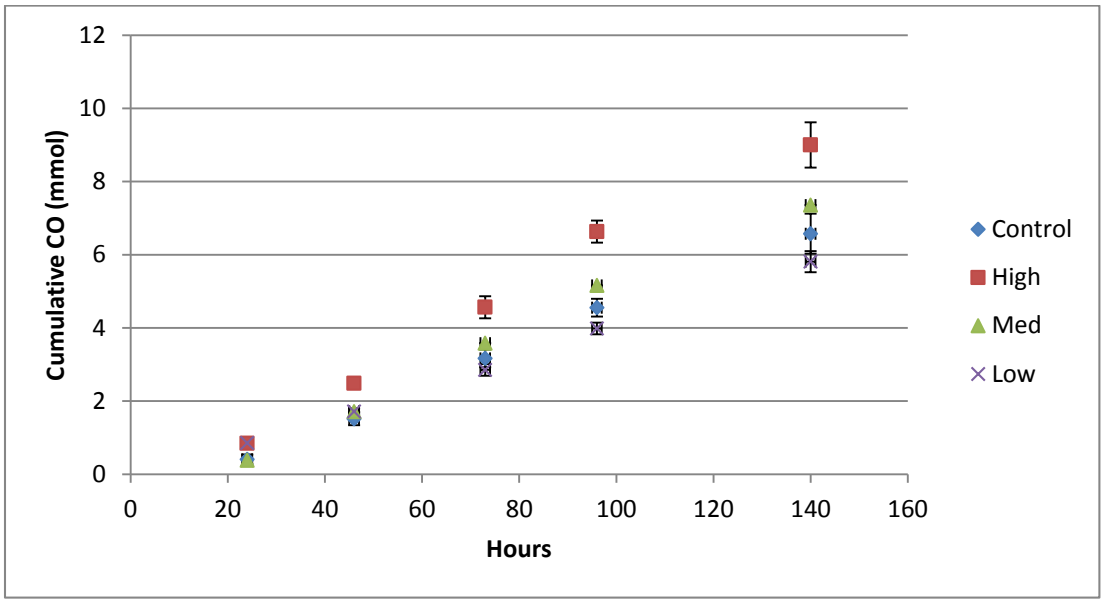

Figure 6-4. Cumulative CO consumed in the H_2 variation study. Error bars represent ± 1 standard deviation.

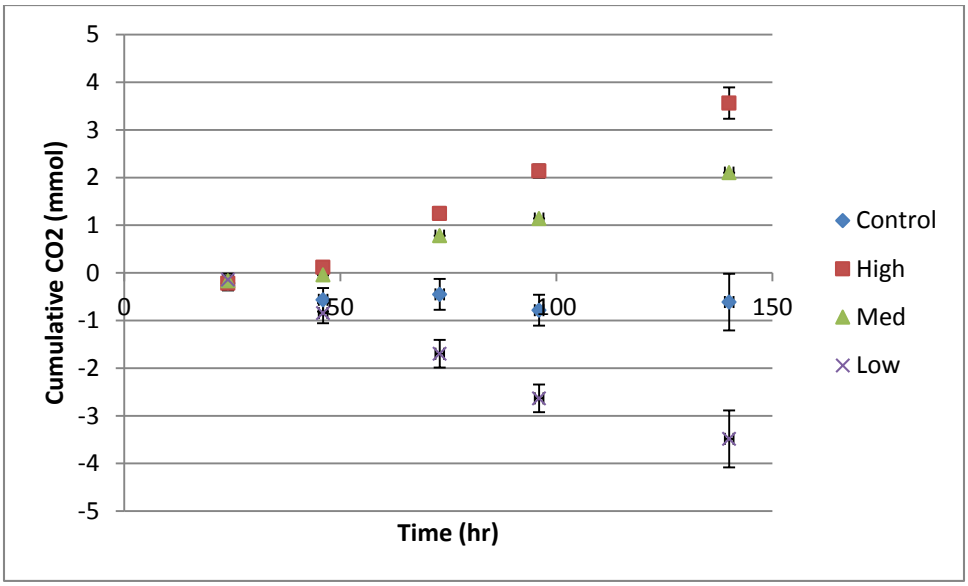

Figure 6-5. Cumulative CO_2 consumed in the H_2 variation study. Negative values indicate production of CO_2. Error bars represent ± 1 standard deviation.

The average consumption rates per gram of cell for CO, CO_2 and H_2 were attained by performing a linear regression on the data from Figures 6-3 through 6-5 and dividing by the peak amount of cells (g_{cell}). These rates are shown in Table 6-5.

Table 6-5. Table of consumption rates for H_2 variation studies. ± values are the 95% confidence intervals.

	R_{CO} *(mmol/hr/g_{cell})*	R_{CO2} *(mmol/hr/g_{cell})*	R_{H2} *(mmol/hr/g_{cell})*	*The % increase in R_{H2} as compared with the control divided by the % increase in partial pressure as compared with the control*
High (65% H_2)	3.38 ±0.18	1.73 ±0.09	13.13 ±0.95	1.89
Medium (35% H_2)	2.89 ±0.24	1.04 ±0.15	5.21 ±0.49	1.42
Low (0% H_2)	2.16 ±0.06	-1.43 ±0.14	0.00 ±0.00	-
Control (15% H_2)	2.43 ±0.12	-0.05 ±0.13	1.80 ±0.12	NA

Table 6-5 shows that as the partial pressure of H_2 in the gas increases while all other partial pressures stay constant, the rate of H_2 and CO consumption per cell increases. A rise in H_2 consumption is expected because the increased partial pressure would result in more dissolved hydrogen to be catalyzed by hydrogenase. However, the rise in H_2 is higher than would be expected just from an increase in partial pressure. For example, the partial pressure of H_2 increased by 3.3 times between the control and high level bottles, but the rate of H_2 consumption per gram of cell increased by 6.4 times between the control and high level bottles. The fourth column shows the percent increase in R_{H2} divided by the percent increase in partial pressure as compared with the control group. If this ratio is unity then it means that the R_{H2} increased linearly with an increase in partial pressure. However, if it is greater than unity then R_{H2} increases more than linearly with an increase in partial pressure. This extra increase in H_2 consumption is most likely due to the up-regulation of hydrogenase in response to the increase in hydrogen partial pressures. The rise in CO consumption could be due to the increase in electron availability and thus step 3 is up-regulated in order to provide the carbonyl moiety for acetyl-CoA. It should be noted that the increase in carbon usage (both CO and CO_2) with an increase of H_2 did not result in more carbon going to cells, rather more carbon went to product as shown below.

Figures 6-6 through 6-8 show the pH, and ethanol and acetic acid concentrations. The pH shown in Figure 6-6 follows the acetic acid trend in Figure 6-8 as is expected with an acid. Figure 6-7 shows the ethanol concentrations. As electron equivalents available from H_2 increase, the ethanol concentrations increase. Based on these results, even though H_2 electron equivalents do not increase cell anabolism (step 5) to any significant degree, they directly affect the amount of ethanol produced (step 6). The reason for this could be because even though the cell growth is

dependent on electrons from CO, the product formation is not. Thus, as electron equivalents from H_2 increase, so does ethanol production

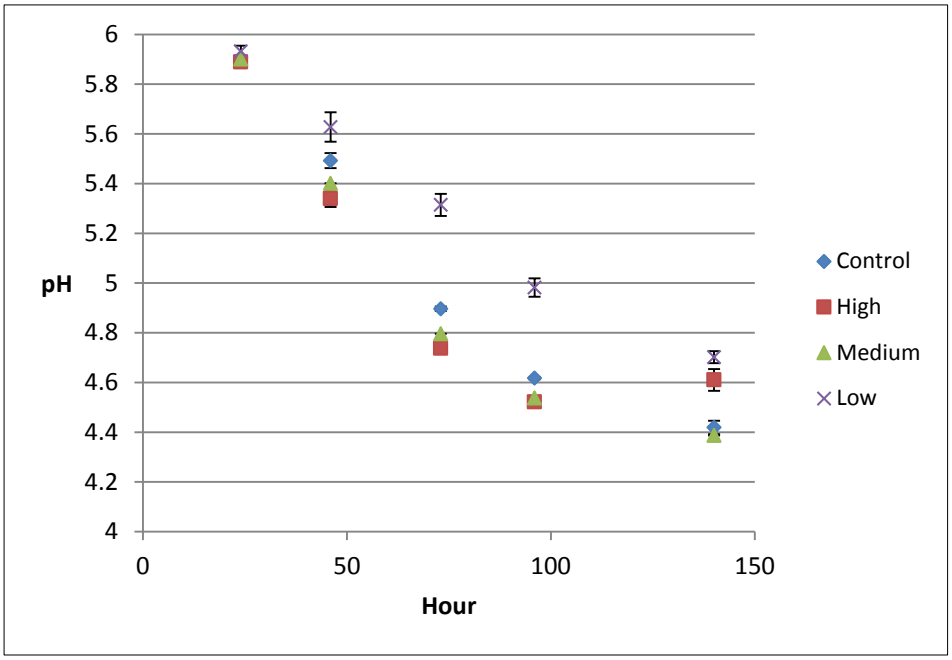

Figure 6-6. pH in H_2 variation study.

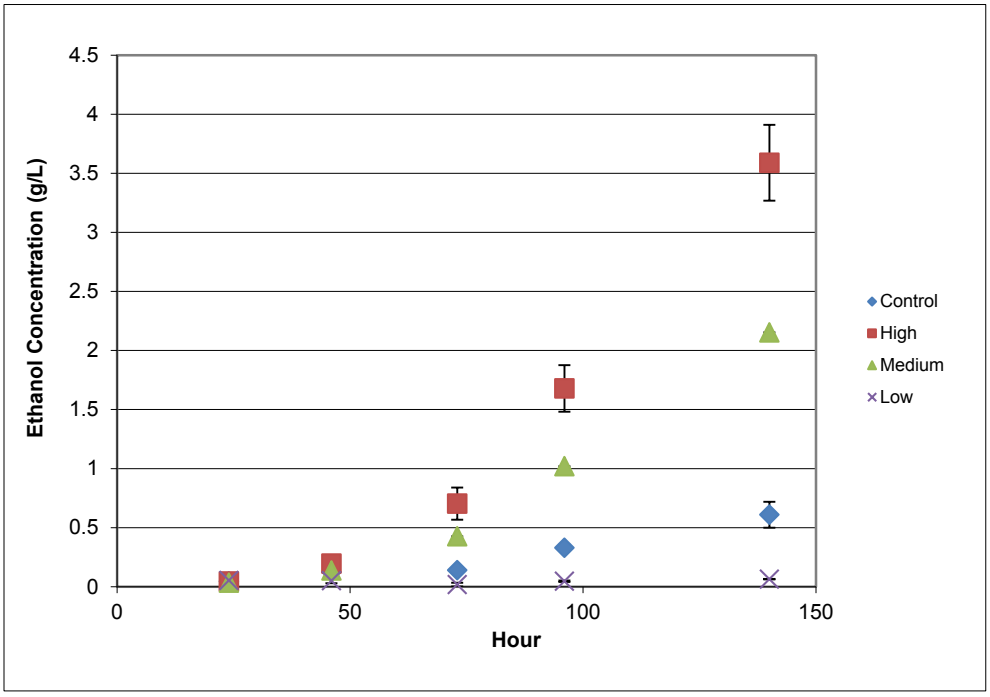

Figure 6-7. Ethanol concentrations in H_2 variation study.

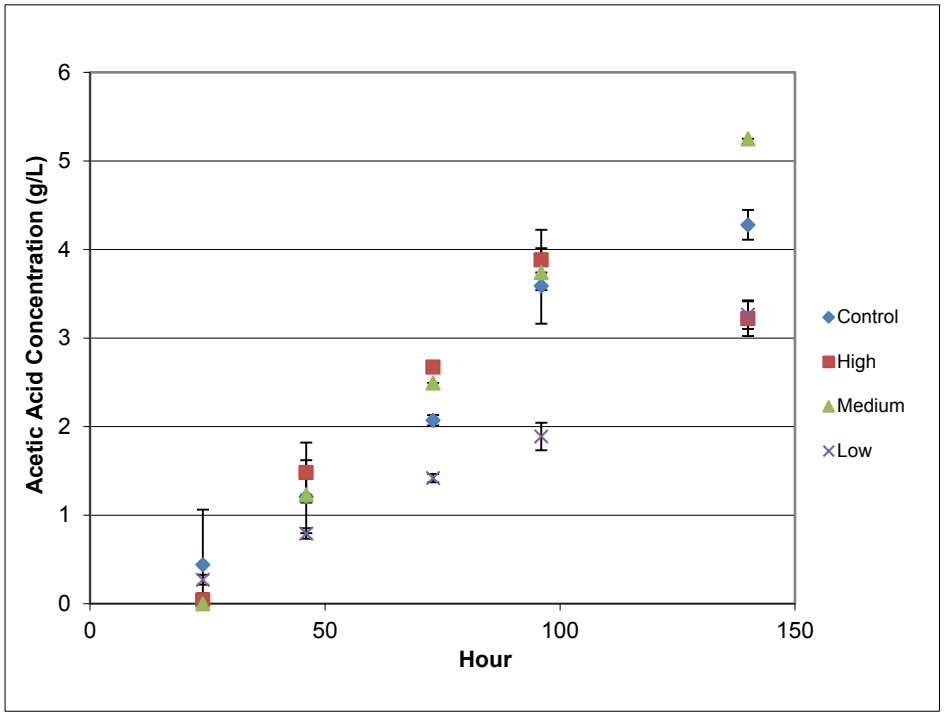

Figure 6-8. Acetic acid concentrations in H_2 variation study.

Acetic acid production shows a slight increase in slope as electron equivalents from H_2 increase. However, since acetic acid production in step 4 is not directly dependent on electrons, there is almost no increase in slopes between the medium, control, and high bottles. Thus, it may be that once a minimum amount of electron equivalents are available, the acetic acid production does not increase with increasing electron equivalents. Another interesting point is that for the high levels of H_2 bottles, the acetic acid levels dropped at the last data point indicating that acetic acid to ethanol conversion was happening. However for the other bottles, there was no apparent conversion of acetic acid to ethanol. Overall the H_2 variation studies showed very good repeatability between bottles indicating that all of the bottles reacted similar to the varying levels of H_2.

6.3.3 CO Variation Results and Discussion

The results for the cell growth for the varying CO bottle studies are shown in Figure 6-9.

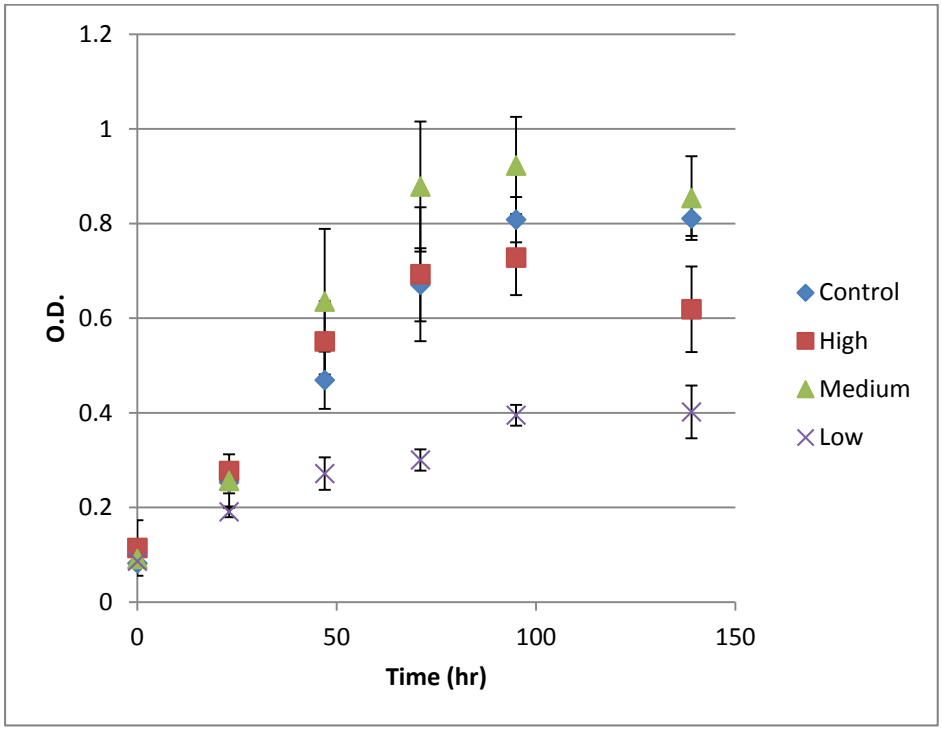

Figure 6-9. OD of bottle fermentations in CO variation study.

The cell growth for all levels of CO are similar except for the lowest level of CO. It is most likely that in the "low" case, the cells were limited by the amount of CO available since the electron equivalents from H_2 were not used for cell anabolism as described above. In contrast, Figure 6-2 does not show any growth inhibition even though the same electron equivalents were used. The only difference between the two is that, in one case H_2 was reduced, in the other case CO was reduced. For the other bottle results shown in Figure 6-9, the cells become limited by some other reagent as long as CO is above a certain level. Thus, this convincingly shows that CO is necessary for strong cell growth and H_2 is not used.

The cumulative gas consumption with time is shown in Figures 6-10 through 6-12.

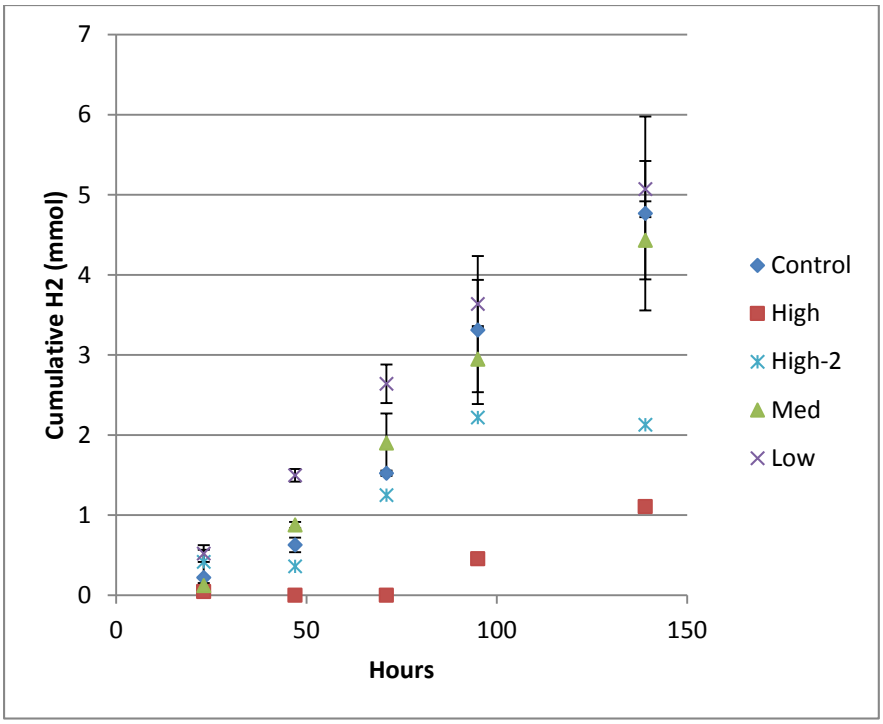

Figure 6-10. Cumulative H_2 consumed in the CO variation study. Error bars represent ± 1 standard deviation. The "high" bottles were shown as individual data points because of the lag time in one bottle labeled as High-2. The third "high" bottle did not grow.

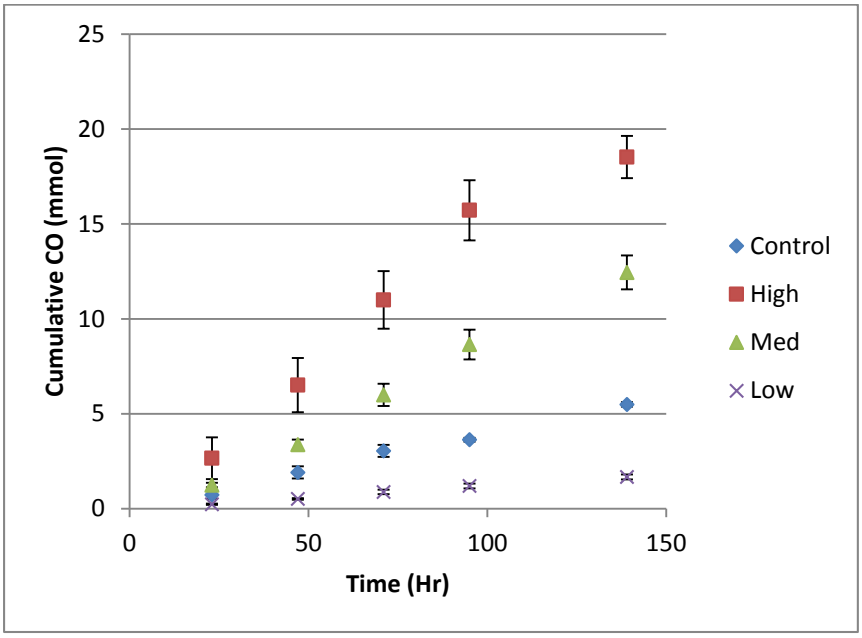

Figure 6-11. Cumulative CO consumed in the CO variation study. Error bars represent ± 1 standard deviation.

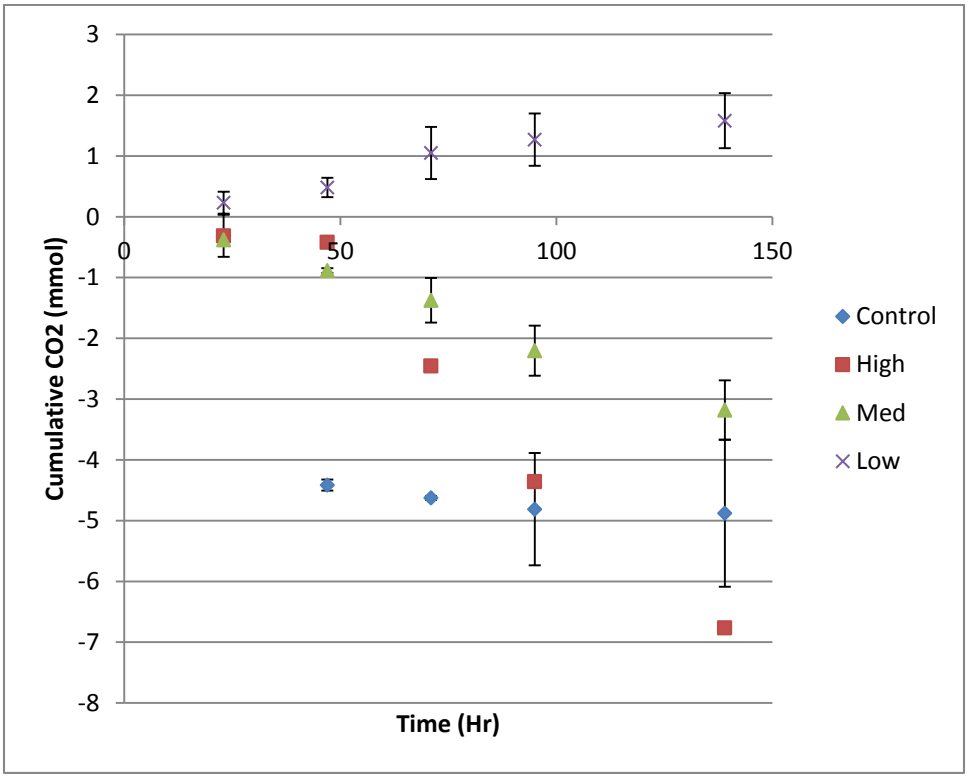

Figure 6-12. Cumulative CO_2 consumed in the CO variation study. Negative values indicate production of CO_2. Error bars represent ± 1 standard deviation.

Based on the slopes in Figure 6-11, as CO availability increases, the rate of CO consumption also increases. As CO consumption increases there is decrease in the amount of CO_2 consumed as shown in Figure 6-12. This is because when CO gives up electrons in step 1 it is oxidized to become CO_2. As CO availability increases there is a slight decrease in the slopes of H_2 consumption shown in Figure 6-10. This is due to the fact that CO is a known inhibitor of hydrogenase. The average consumption rates per gram of cell for CO, CO_2 and H_2 were attained by performing a linear regression on the data from Figures 6-10 through 6-12 and dividing by the peak amount of cells (g_{cell}). These rates are shown in Table 6-6.

Table 6-6. Table of consumption rates for CO variation studies.
± values are the 95% confidence intervals

	R_{CO} *(mmol/hr/g_{cell})*	R_{CO2} *(mmol/hr/g_{cell})*	R_{H2} *(mmol/hr/g_{cell})*	*The % increase in R_{CO} as compared with control divided by the % increase in partial pressure as compared with control*	*The % decrease in R_{H2} as compared with control (negative value indicate increase)*
High (70% CO)	7.56 ±1.43	-3.21 ±0.71	1.40 ±0.75	1.17	30
Medium (40% CO)	4.13 ±0.30	-1.04 ±0.16	1.60 ±0.16	1.15	20
Low (5% CO)	1.22 ±0.12	1.17 ±0.41	3.83 ±0.30	0.46	-91
Control (20% CO)	1.92 ±0.18	-0.23 ±1.10	2.01 ±0.31	NA	NA

The control group from this study shows statistically the same rates as in the H_2 variation study above. Table 6-6 also shows that as the partial pressure of CO in the gas increases the rate of H_2 consumption per cell decreases. For example, there is a 91% increase when the CO is at the low level of 5% compared to the control group. As discussed above, this decrease in H_2 consumption with rising CO levels is evidence of the inhibitory effects of CO on hydrogenase in the cells. There does not appear to be a large increase in the rates of CO used compared to the increase in partial pressure as shown in the fourth column. If this ratio is unity then it means that

the R_{CO} increased linearly with an increase in partial pressure. However, if it is greater than unity then R_{CO} increases more than linearly with an increase in partial pressure. The low CO group had a decrease in partial pressure compared to control so in this case a value of less than unity indicates that the R_{CO} decreased less than linearly with a decrease in partial pressure. For the high and medium CO bottles, this ratio is very near unity so it appears that CO dehydrogenase is not up-regulated as readily as hydrogenase in the H_2 study above. As CO levels increase, CO_2 production also increases, as discussed above this is due to the conversion of CO to CO_2 when CO donates electrons.

Figures 6-13 through 6-15 show the pH, and ethanol and acetic acid concentrations.

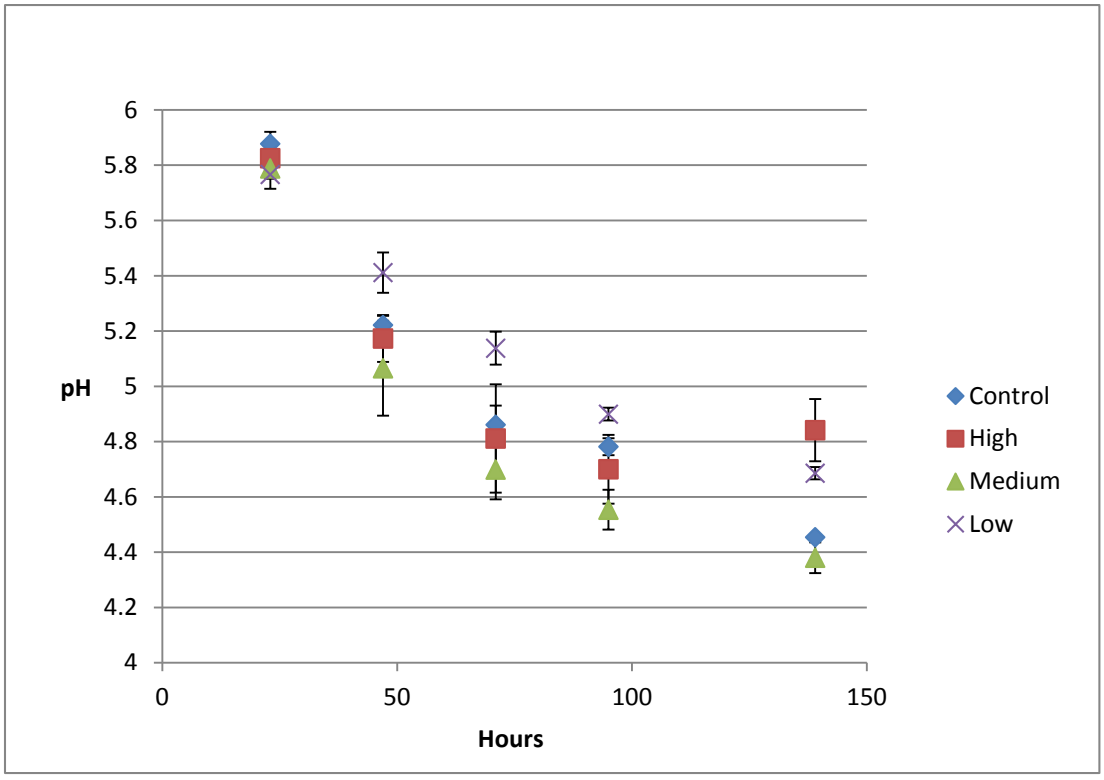

Figure 6-13. pH in CO study.

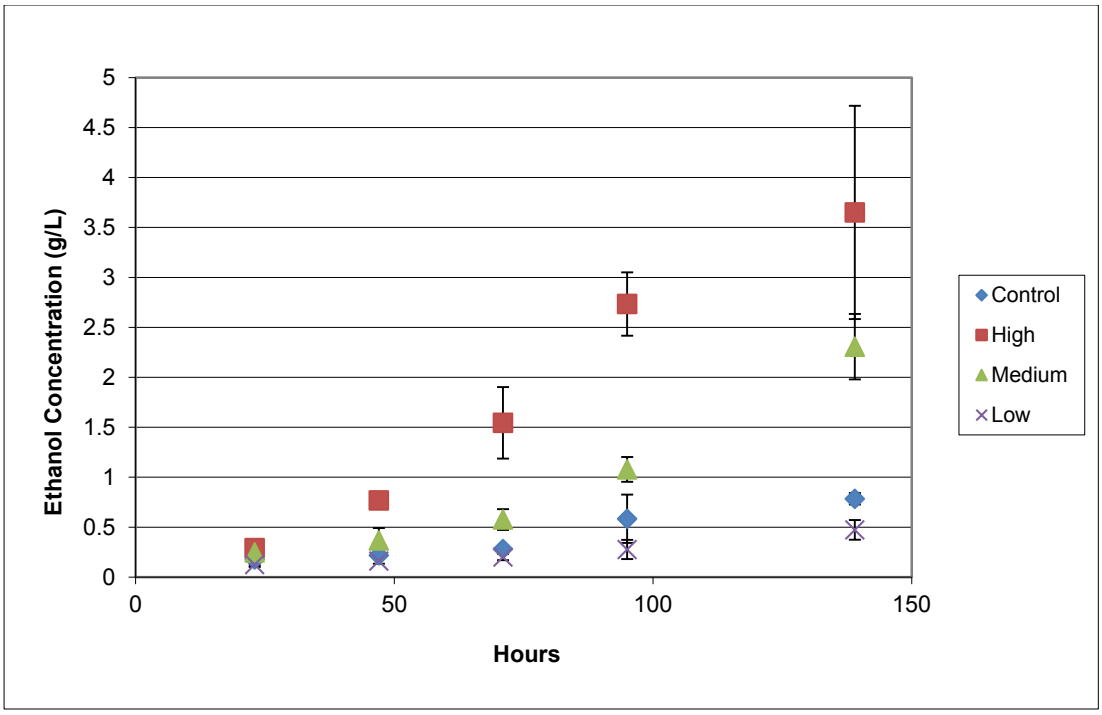

Figure 6-14. Ethanol concentrations in CO study.

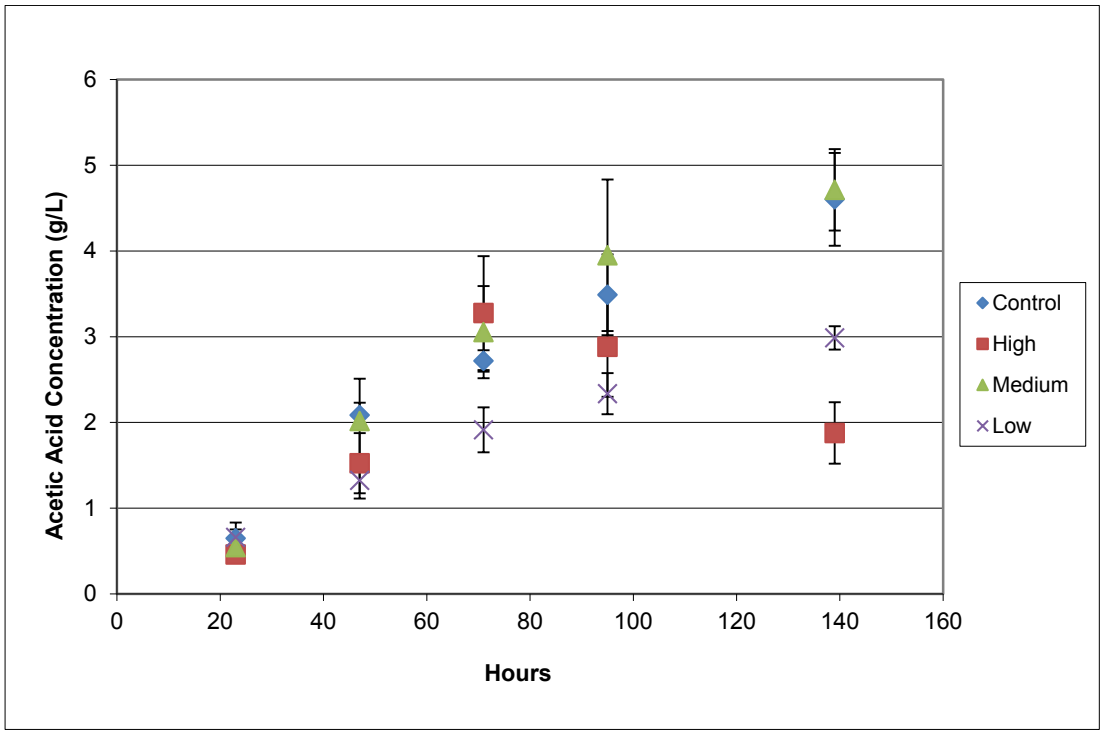

Figure 6-15. Acetic acid concentrations in CO study.

The pH shown in Figure 6-13 follows the acetic acid trend in Figure in 6-15 as expected. Figure 6-14 shows the ethanol concentrations. As electron equivalents available from CO increase, the ethanol concentrations increase very similar to the H_2 variation study. These product results are expected based on the earlier hypothesis that even though the cell growth may be limited by electron carrier type or availability, the product formation is only limited by lack of electron equivalents. This means that step 6 can likely accept electrons from either CO or H_2. Thus, as electron equivalents increase, so does ethanol production. Again, since acetic acid is not directly dependent on electrons, there is almost no increase seen in Figure 6-15 with increasing CO electron equivalents. As with the hydrogen variation study, ethanol to acetic acid ratio increases along with ethanol production as CO electron equivalents increase.

6.3.4 CO and H_2 Variation Study Comparisons

This study was designed to compare the high, medium and low levels of electron equivalents from H_2 and CO. The "high" bottles in both bottle studies had 92% moles of electron equivalents per total moles of gas. The "medium" bottles in both bottle studies had 71% moles of electron equivalents per total moles of gas. The "low" bottles in both bottle studies had 35% moles of electron equivalents per total moles of gas. The "control" bottles in both bottle studies had 52% moles of electron equivalents per total moles of gas. Table 6-7 shows a comparison of the rates of moles of carbon produced as product (ethanol and acetic acid) per gram of cell for each bottle study. These product data are shown in Figures 6-16 and 6-17. The slopes of these product formation lines are very near linear like the HFR fermentation production rates discussed in Chapter 5. The grams of cells used in these rates was a constant calculated at the maximum OD of each bottle set.

The two control bottles had the same amount of electron equivalents and gas ratios. As expected they both had the same rate of product formation, ~3.15 $mmol_c/hr/g_{cell}$. The fact that the two control rates are the same validates the assumption that the differences seen between the two studies are a result of the changing gas ratios and not an effect caused by cell culture differences or some other effect. The highest rate of product formation was attained in the bottles with the "high" and "medium" levels of H_2 and CO. The lowest rate of product formation was attained in the bottles with the "low" levels of H_2. Thus, increasing electron equivalents in both cases resulted in higher production rates. Of the two electron equivalents, the highest production rates were achieved when H_2 was the main electron source as opposed to CO. This could be due to the hydrogenase inhibition caused by high CO rates. Thus, CO is the preferred electron source for cell growth and H_2 is the preferred electron source for product formation. Since cell growth and product formation are both needed for efficient fermentation these gas ratios can be optimized by growing cells on high H_2 levels while still providing enough CO to provide the electrons for cell growth.

Table 6-7. Comparison table for H_2 and CO variation studies. ± values are the 95% confidence intervals.

	H_2 Variation Study	***CO Variation Study***
	Rate of Carbon Produced as Product ($mmol_c/hr/gcell$)	*Rate of Carbon Produced as Product ($mmol_c/hr/gcell$)*
Control	3.11 ±0.61	3.20 ±0.47
High	5.45 ±0.93	4.64 ±2.33
Medium	5.55 ±0.33	4.12 ±0.20
Low	2.15 ±0.23	3.82 ±0.37

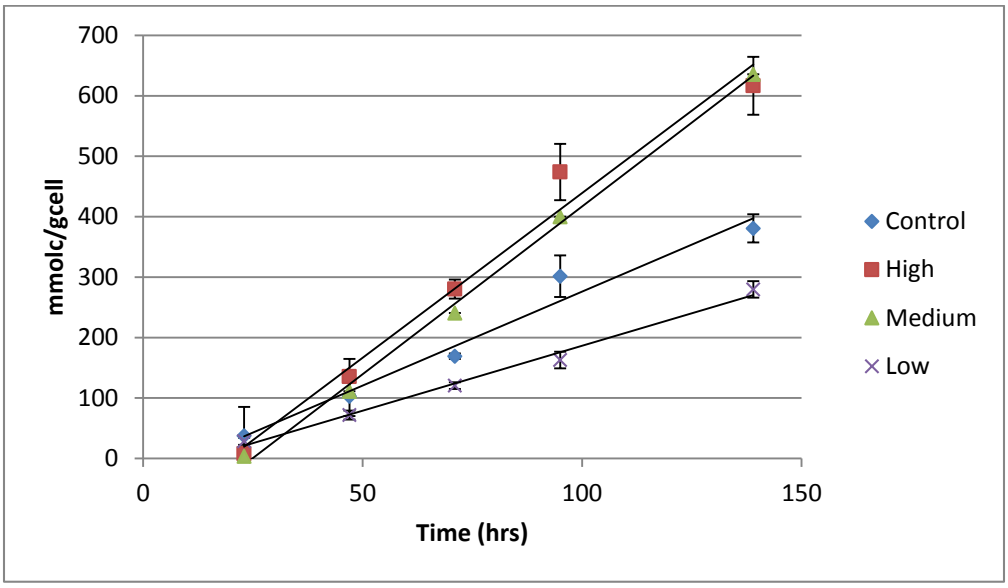

Figure 6-16. Carbon produced as product (ethanol and acetic acid) per gram of cell for H_2 variation study.

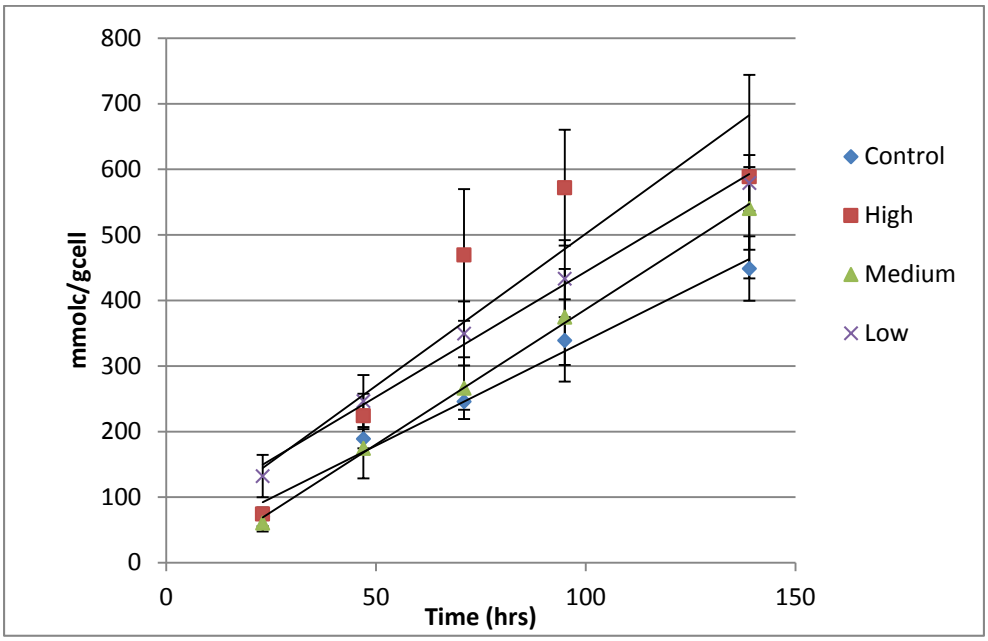

Figure 6-17. Carbon produced as product (ethanol and acetic acid) per gram of cell for CO variation study.

6.4 Conclusion

There have been many predictions about the amount of ethanol that can be produced from syngas fermentation. We have shown that the accuracy of these predictions is largely dependent on the type of biomass used and even the gasifier used to produce the syngas. Predictions showed that the range of ethanol production can be quite broad, from 10.2-80.5 gallons of ethanol per ton biomass. The bottle studies performed in this work showed that cell growth in the cellular media is not largely affected by syngas composition as long as there is at least some minimum amount of CO present (about 5%) and another electron equivalent such as H_2. This study showed that as the partial pressure of H_2 in the gas increases the rate of H_2 and CO consumption per cell increases. This extra increase in H_2 consumption is most likely due to the up-regulation of hydrogenase in response to the increase in hydrogen partial pressures. The rise in CO consumption could be due to the increase in electron availability and thus the carbonyl branch is up-regulated in order to provide the carbonyl moiety. This study also showed that cell anabolism is largely independent of the H_2 partial pressure when CO is present. However, when CO is removed there is very little cell growth. This is most likely because the hydrogenase enzyme in *C. ragsdalei* uses an electron carrier that is not used or has a lower abundance in the redox reactions in cell anabolism than the CODH enzyme. Thus, CO is the required electron equivalent for cell growth. This gives insight to optimal gas ratios to use for syngas fermentation. For example, cells should be exposed to high H_2 levels while still providing enough CO to provide the electrons for cell anabolism. However, after cell growth stops, the cells could be exposed to even higher H_2 levels.

This study also showed that as the partial pressure of CO in the gas increases the rate of H_2 consumption per cell decreases. This decrease in H_2 consumption with rising CO levels is

evidence of the inhibitory effects of CO on hydrogenase in the cells. The highest rate of product formation was achieved in the bottles with the "medium" and "high" levels of CO and H_2 in both bottle studies, respectively. This means that even though the cell growth may be limited by electron carrier type or availability, the product formation is only limited by lack of electron equivalents. Thus, as electron equivalents increase, so does ethanol production and the ethanol to acetic acid ratio. This could be the reason that there were large production rates seen in the HFR fermentations in Chapter 5. The HFR had large mass transfer rates and thus could provide a greater amount of electron equivalents thus increasing product formation.

These predictions and bottle studies show that the fuel production efficiency of syngas fermentations depends on the biomass input, gasifier, and syngas ratios. Since realistically, the only input factors that can be easily changed are the biomass input and gasifier type these should be chosen so as to maximize the electron equivalents while still providing enough CO for cell anabolism.

7 Methyl Viologen as an Electron Carrier

7.1 Introduction

In addition to providing electrons from CO and H_2, electrodes can also be used to augment the supply of electrons or provide the only source of electrons for syngas fermentation (Aulenta, et al. 2007; Lymar and Hurst 1994; Marshall and May 2009; Park and Zeikus 1999; Wang, et al. 2011). While some cells can directly accept electrons from an electrode, most cannot (Nevin, et al. 2010; Nevin, et al. 2011b). Therefore, in order to transfer electrons to the cells, external electron mediators must be used.

Methyl viologen (MV), N,N′-dimethyl-4,4′-bipyridinium dichloride, or Paraquat is a low-potential redox indicator that is widely used as an artificial electron carrier to help optimize biological processes (Bird and Kuhn 1981; Panneerselvam, et al. 2010; Peguin, et al. 1994). The reducing equivalents supplied to oxidized viologens can be provided by reduced species such as glucose and H_2 (Lan and Liao 2011; Llobell, et al. 1986; Rao and Mutharasan 1986). More recently, there has been a focus on using electrodes to supply reducing equivalents (Aulenta, et al. 2007; Kim, et al. 1999; Nevin, et al. 2011a; Wang, et al. 2011). MV has been shown to be an effective extracellular electron carrier to promote redox reactions involving bio-catalysis (Aulenta, et al. 2007; Erbes and Burris 1978; Kim, et al. 1999; Lymar and Hurst 1994). Rao and Mutharasan (Rao and Mutharasan 1986) reported that MV can act as an electron mediator and increase the ethanol yield from 0.001 g/ g glucose to 0.134 g/g glucose. Aulenta et al. (Aulenta, et al. 2007) also presented an application of MV as an artificial electron mediator for cell

fermentation with an efficiency of 20%-60%. Yukihiro Tashiro (Tashiro, et al. 2007) demonstrated that with MV as the electron mediator, the yield of butanol increased by 16%. Further, there are many more reports, with little information of the material or energy efficiency, that simply illustrate the positive effects of MV on electron transport and product formation (Asada, et al. 1990; Erbes and Burris 1978; Kim, et al. 2001; Llobell, et al. 1986; Lymar and Hurst 1994; McLachlan and Crumbliss 1990; Mills, et al. 1990; Park, et al. 1995).

Although there have been many reports of the positive effects of MV in biological systems, some adverse effects of MV on cell growth have been reported (Bus and Gibson 1984; Bus, et al. 1974; Panneerselvam, et al. 2010; Peguin, et al. 1994). This is not surprising since MV is also used as an herbicide and is a known toxin to many organisms (Bus and Gibson 1984). The toxicity of MV is largely related to the redox state of MV in biological systems. Depending on the redox state of MV, toxicity can develop because of the generation of activated oxygen species (superoxide anions, hydrogen peroxide, and hydroxyl radicals) and/or the depletion of NADPH/NADH used in normal cellular function (Bus and Gibson 1984; Bus, et al. 1974). Thus, predicting and controlling the actual state of MV in the biological system is of great importance when using MV as an electron carrier in biological systems.

For many of the above studies, it is unclear as to the state of MV during the study since MV can exist in three redox states MV^{2+}, MV^{+}, or MV^{0} (neutral), as non-dissociated $MVCl_2$, as the dimer MV_2^{2+}, the MV radical proton complex (MVH^{2+}), and even as crystalline films when electrodes are used (Bauer and Werner 1992; Bird and Kuhn 1981; Monk and Hodgkinson 1998; Thorneley 1974). Because MV is commonly sold as $MVCl_2$, MV^{2+} is possibly the species initially used in many of the reports. However, in electrode systems with varying potentials, MV could be in one or more of the forms listed above. Even in biological systems where the potential

is not directly controlled, MV can react with electron carriers inside the cells forming any redox state (Kim and Yun 2004). In order to measure and/or predict the forms of MV to help understand the impact of MV on systems, many experimental parameters are needed. These parameters include the extinction coefficients of MV species for photometric measurements, standard redox potentials for the two reductions of MV^{2+}, and equilibrium constants for the dimer and radical proton complex. The literature values reported for these parameters vary greatly. Thus, it can be difficult to accurately predict the form of MV in a given system. This work will review the relevant parameters that have been reported in the literature with the goal of narrowing down the most accurate values that should be used in thermodynamic modeling and measurements. Using these values, a thermodynamic model is presented in order to illustrate the most likely redox state of MV depending on the system setup. The model is then validated by experimental data. Assessing the state of MV can help provide additional insights into the role of MV when interpreting experimental data.

7.2 Materials and Methods

7.2.1 Bioelectric Reactor

A Bio-electric Reactor (BER) for anaerobic systems was used for all experiments (Figure 7-1). The BER is made of Pyrex glass and contains two 50-mm ID jacketed glass chambers. The two chambers are connected with a 30-mm diameter pinch clamp but the solutions are separated with a cation-selective membrane (Nafion, Fuel Cell Store, San Diego, CA) with a thickness of 25.4 μm. The Nafion membrane is designed to allow protons to cross the membrane easily.

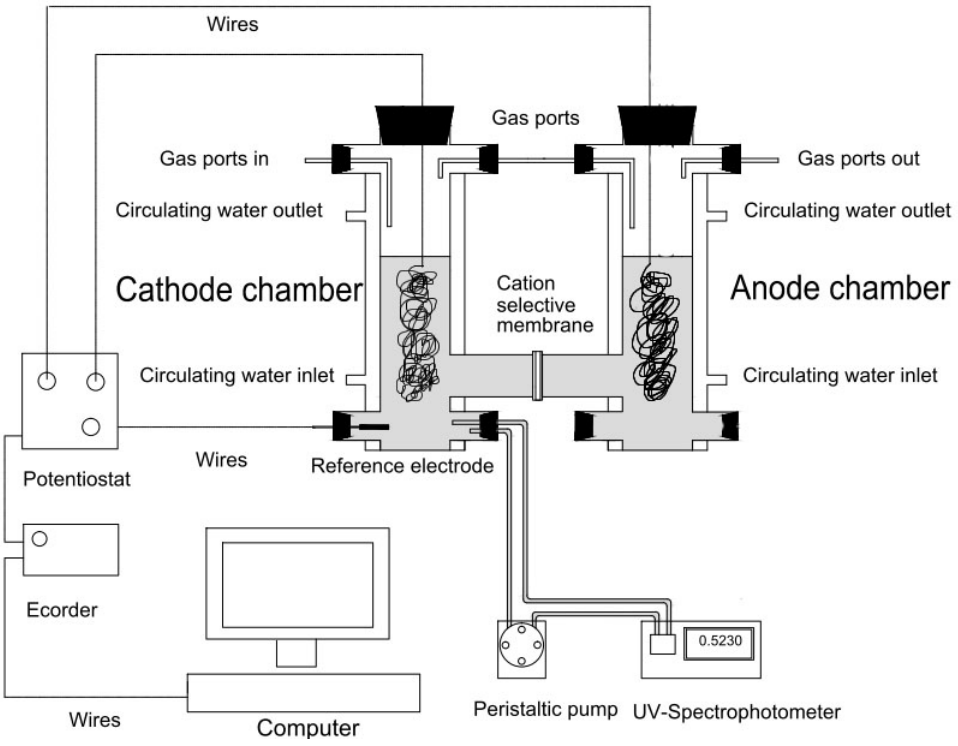

Figure 7-1. Bio-electric reactor (BER). The reactor is a three-electrode electrochemical system controlled by a potentiostat. Absorbance in the solution is continuously measured by a UV-spectrophotometer. The reactor is maintained anaerobic by purging N_2 throughout the experiment.

The anode and cathode electrodes, each one placed in one of the chambers, were made from graphite initially, and then replaced with 12-foot silver wire (0.016 in diameter). The wires were threaded through butyl rubber stoppers in the top of each chamber and were connected to a potentiostat. The potentiostat (Potentiostat EZ161, eDAQ, Colorado Springs, CO) was connected to an Ecorder (Ecorder ED821, eDAQ, Colorado Springs, CO) and interfaced with Chart® (version 5.0, eDAQ, Colorado Springs, CO). A reference electrode was also connected to the potentiostat (non-leaking 3M Ag/AgCl reference electrode, Warner Instruments, Hamden, CT) and placed close (~1 cm) to the cathode electrode using one of the ports at the bottom of the chamber to maintain an applied voltage potential of the cathode relative to an Ag/AgCl reference electrode.

Each chamber was constructed with two gas ports on the upper part of the chamber in which gas tubing with inner diameter of 0.25 inches (Masterflex Tubing Puri-Flex, L/S® 17,Cole-Parmer, Vernon Hills, IL) was inserted for gas to flow in and out of the gas headspace of each chamber. Throughout the experiment, the chambers were maintained anaerobic by continuously purging N_2 gas through the cathode chamber and then the anode chamber since O_2 is a byproduct of the reaction in the anode chamber. Ports at the bottom of each chamber were also designed for liquid analysis. For this study, liquid analysis of MV^+ was assessed in the cathode chamber. In the BER, the applied voltage potential drives the electrochemical reaction in the system. In the anode chamber, water electrolysis occurs and donates electrons to the anode during the formation of H^+ and O_2. O_2 is purged out of the system with N_2. In the cathode chamber, MV^{2+} and MV^+ reduction occur on the cathode. The pH for all experiments was between 10 and 10.5 in the cathode chamber and between 4.4 and 6 in the anode chamber. The pH difference is a result of OH^- formation on the cathode side and H^+ formation on the anode side during electrolysis.

7.2.2 Experimental Procedure

Experimental MV reductions were performed at applied potentials near -600 mV, -650 mV, -700 mV, -800 mV, -900 mV, -950 mV, -1000 mV, and -1100 mV (relative to Ag/AgCl). Each experiment was performed between 4 and 6 times. $MVCl_2$ (0.0051g, Sigma Aldrich) was added to the cathode chamber to obtain an initial concentration of 0.1 mM. The cathode chamber also contained 30 mL dimethylformamide (DMF, Mallinckrodt Baker Inc.) combined with a balance of deionized water to obtain a 200 mL solution to minimize side reactions. To assess the effects of side reactions, additional studies at -800 mV were performed using 0, 10, 20, or 40 mL DMF. The anode chamber contained 200 mL of deionized water. Both chambers contained 200 mM KCl (EMD Chemicals Inc.). All experiments were maintained at 37 °C by flowing heated

water through the outer jacket of each reaction chamber during the experiments. Following the addition of MV^{2+}, MV reduction was allowed to proceed for 10 hours for applied voltages of -600 mV through -900 mV and 24 hours for applied voltages of -950 mV through -1100 mV. After each experiment, the BER was disassembled and cleaned. The silver electrodes were soaked in pure sulfuric acid and then rinsed with DI water. The reference electrode was washed with soap and stored in DI water.

Continuous spectrophotometric analysis at 600 nm was performed by flowing the cathodic solution through a UV-spectrophotometer (1700 UV-spectrophotometer, Shimadzu, Columbia, MD). The flow-through system consisted of Viton® pump tubing with an inner diameter tubing of 0.06 inches (Cole Parmer, Vernon Hills, IL) connected to a pump (Cole Parmer, Vernon Hills, IL) and sealed to a flow-through cuvette (585.3-SOG, Starna Cells, Atascadero, CA). It is critical to have low-O_2 permeable tubing since MV reduction is highly susceptible to residual O_2. The UV spectrophotometer was blanked with the initial solution containing MV^{2+}. Following each experiment, the tube between the chambers and the UV-spectrophotometer was cleansed by flowing 500 mL of clean DI water through the tube. Of the six forms of MV mentioned in the introduction, only MV^{+} and MV_2^{2+} absorb light at 600 nm. In order to convert from absorbance to concentrations, the extinction coefficients of 13,570 $M^{-1}cm^{-1}$ and 1,260 $M^{-1}cm^{-1}$ were used for MV^{+} and MV_2^{2+}, respectively. The discrepancies in literature values of the extinction coefficients and the procedure for conversion from absorbance to concentration are discussed in detail in the results and discussion section.

7.3 Thermodynamic Modeling

In order to predict the bulk concentration of each MV species in an experimental system (e.g. the bulk solution of the cathode chamber for this study), which could help provide insights into the role of MV, Equations 7-1 through 7-5 are used.

$$F \cdot U_{ex} = F \cdot E_1^0 - \mathrm{R} \cdot \mathrm{T} \ln \frac{[MV^+]}{[MV^{2+}]} \tag{7-1}$$

$$F \cdot U_{ex} = F \cdot E_2^0 - \mathrm{R} \cdot \mathrm{T} \ln \frac{[MV^0]}{[MV^+]} \tag{7-2}$$

$$K_{salt} = \frac{[MV^{2+}][Cl^-_{soln}]^2}{[MVCl_2]} \tag{7-3}$$

$$K_d = \frac{[MV^+]^2}{[\mathrm{MV_2}^{2+}]} \tag{7-4}$$

$$[MV_T] = [MV^{2+}] + [MV^+] + [MV^0] + 2[\mathrm{MV_2}^{2+}] + [MVCl_2] + [MV_{other}] \tag{7-5}$$

Equations 7-1 and 7-2 are based on the Nernst Equation. Equations 7-3 and 7-4 are equilibrium constraints with Cl^- and the dimerized form, respectively. Equation 7-5 is the material balance for MV. In these equations U_{ex} is the redox potential of the solution, MV_T is the total amount of methyl viologen added to the experiment, F is Faraday's constant (9.65×10^4 C/mol), R is the gas constant (8.314 J/mol/K), T is the experimental temperature, and E^0_1 and E^0_2 are the standard potentials for the reduction of MV^{2+} to MV^+ and MV^+ to MV^0, respectively. K_d is the equilibrium constant for the formation of MV dimer and K_{salt} is the dissociation constant for $MVCl_2$ which is equal to 0.663 M^2 as calculated from Monk and Hodgkinson (Monk and Hodgkinson 1998). Cl^-_{soln} is the concentration of Cl^- in the bulk solution.

As discussed later in Section 7.5.3, if the pH is neutral or higher, then the concentration of MVH^{2+} is negligible and does not need to be included in Equation 7-5. If it is not negligible, MVH^{2+} must be included in Equation 7-5 and an additional equilibrium relationship between MV^{+} and MVH^{2+} must also be included. If there are large amounts of Cl^{-} compared to $MVCl_2$ added to the system, then Cl^{-}_{soln} will not change appreciably due to any $MVCl_2$ dissociation and can be assumed to be a constant. $[MV_{other}]$ is any other form(s) of MV not accounted for in the system material balance, such as MV film formation on the electrode and MV transported to the anodic chamber. When $[MV_{other}]$ is negligible or known, Equations 7-1 through 7-5 can be solved simultaneously to predict the concentrations of MV^{2+}, MV^{+}, MV^{0}, MV_2^{2+}, and $MVCl_2$ at various values of U_{ex}, MV_T, and temperature.

7.4 Standard Redox Potential

To predict the state of MV using the thermodynamic model described above, standard redox potentials, E^0_1 and E^0_2 for the two reduction reactions shown in Equation 7-6 and 7-7 are needed.

$$E^0_1: MV^{2+} + e^- \leftrightarrow MV^{+} \quad (7\text{-}1)$$

$$E^0_2: MV^{+} + e^- \leftrightarrow MV^{0} \quad (7\text{-}2)$$

There is a wide range of reported values in the literature for E^0_1 and E^0_2. Table 7-1 summarizes reported E^0_1 and E^0_2 values for MV in aqueous media.

Table 7-1. Summary of reported E^0_1 and E^0_2 for methyl viologen in aqueous media. [a] Referencing original 1933 Michaelis and Hill work. These values were only used once to calculate the average and standard deviation. [b] Values that were determined to be statistical outliers.

E^0_1 (mV vs. NHE)	E^0_2 (mV vs. NHE)	Reference
-656		(Michaelis and Hill 1933a)
-656[a]		(Michaelis and Hill 1933b)
-644	-1002	(Elofson and Edsberg 1957)
-656[a]	-1090[b]	(Bird and Kuhn 1981)
-570[b]	-910	‘‘’’
-640		(Prince, et al. 1981)
-665		‘‘’’
-866[b]		(Osa and Kuwana 1969)
-664		‘‘’’
-646		‘‘’’
-664		‘‘’’
-644	-966	‘‘’’

The values in Table 7-1 and in the current work are reported in reference to a 3M Ag/AgCl electrode, which has a value of 210 mV vs. NHE (Friis, et al. 1998). As noted, there is a wide variation among the results. There may be several reasons for the discrepancy among reported values including the use of different anions and electrolytes used in the analysis. Prince et al. (Prince, et al. 1981) also shows some variation in the first reduction potential simply by using different electrodes. These variations in experimental protocols can lead to side reactions, differing equilibriums, and film formation that can affect the measured potentials. However, Bird suggests that there is not enough information in literature to make a correlation between anion effects and redox potential (Bird and Kuhn 1981). Bird also states that the electrolyte used in experiments is rarely quoted and this is also a serious omission because of the interactions between electrolytes and MV. Another reason for the variation may be the non-reversibility of the second reduction in aqueous media (Bird and

Kuhn 1981; Kim, et al. 2001; Osa and Kuwana 1969). Using the data reported in Table 7-1, excluding outliers and repeated values, average values of E^0_1 = -653 ±11 mV and E^0_2 = -959 ±46 mV vs. 3M Ag/AgCl (error is ±1 standard deviation) are obtained. The average E^0_1 and E^0_2 values were used in the thermodynamic model in this work although sensitivity to these values on model predictions is shown.

7.5 Results and Discussion

7.5.1 Electrode Issues

The experiments done with MV in this work were initially intended to be a continuation of the work of Chang Chen performed on the thermodynamics and kinetics of MV (Chen 2012). In the reported work, Chen used graphite electrodes. Initially in this work, graphite electrodes were also used. However, the experiments performed did not replicate the Chen's work. After several experiments, we could not even replicate our own work. One hypothesis was that the electrodes were absorbing the MV. Since the same electrodes were used in each experiment, the electrodes could either supply MV or absorb MV^+ or MV^{2+} depending on the amount of MV absorbed in the electrode on the previous run. In between each experiment the electrodes were allowed to soak for 24 hours. However, depending on the potential used in the previous experiment, the required soak time could be longer than 24 hours. To test this hypothesis, three runs were performed in which the graphite electrodes were only rinsed and not soaked in between experiments. Figure 7-2 shows the absorbance change (proportional to MV^+) in the cathode chamber at 600 nm at -900 mV vs. 3M Ag/AgCl for each of these runs.

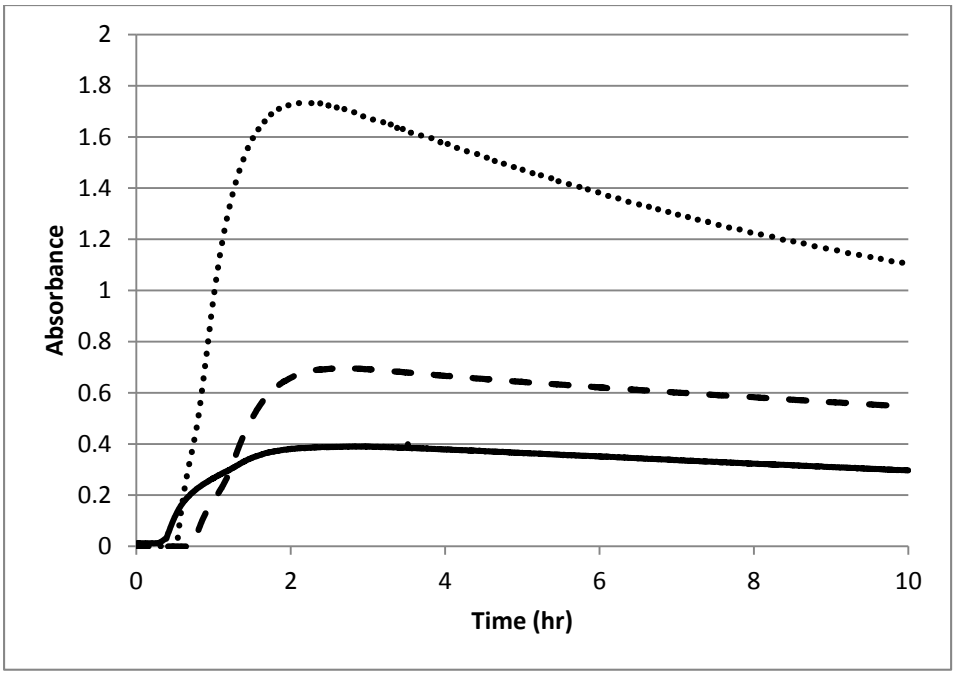

Figure 7-2. The absorbance change (proportional to MV^+) in the cathode chamber at 600 nm at -900 mV vs. 3M Ag/AgCl for three runs showing the non-repeatability.

The maximum absorbance of 1.7 correlated with a concentration of 0.1mM which is twice the amount of total MV initially put into the system. Thus, the electrode was apparently releasing MV into the bulk solution, perhaps using absorbed MV from a previous run. Since the effect that the graphite electrodes had on the MV^+ bulk concentration was unknown and could not be properly characterized, new experiments were performed with non-porous silver electrodes in order to avoid any issues with the porosity of the graphite electrodes.

7.5.2 Absorbance with Varying Potential

Using the non-porous silver electrodes, a representative example of the absorbance change in the cathode chamber at 600 nm (related to the MV^+ concentration) at each applied potential (U_{ex}) is shown in Figure 7-3 as a function of time.

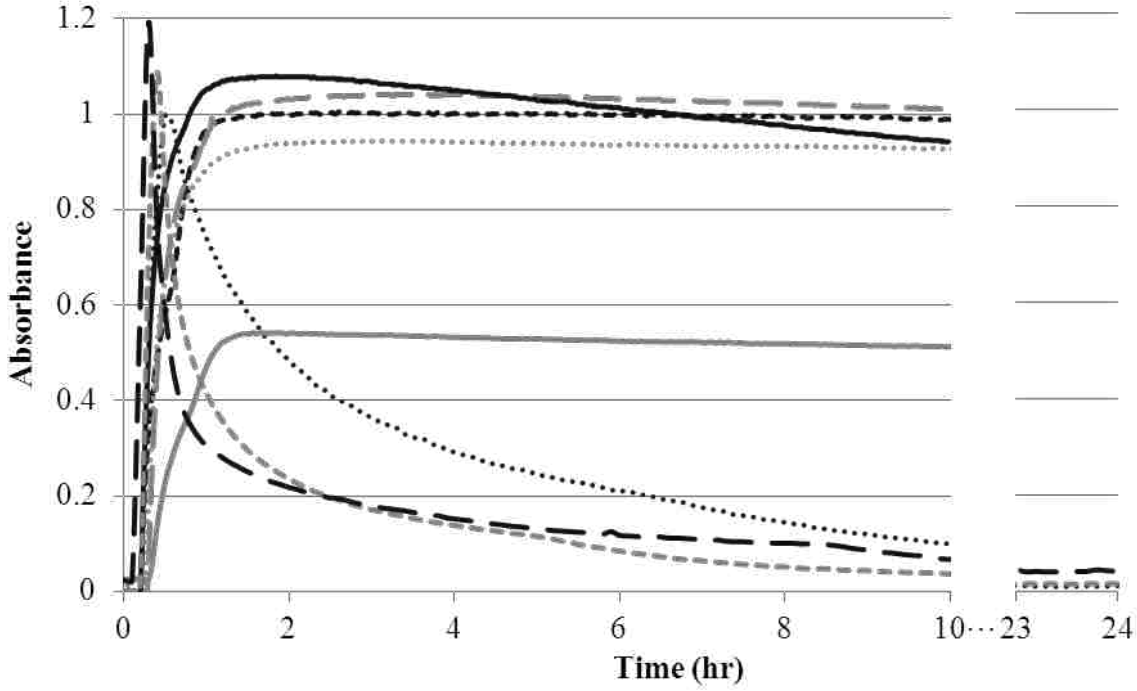

Figure 7-3. Absorbance data at varying potentials. -600 mV, -650 mV, -700 mV, -800 mV, -900 mV, -950 mV, -1000 mV, -1100 mV. All potentials are relative to a 3M Ag/AgCl electrode.

Initial absorbance changes are similar for most runs, indicative of initial kinetic rates that are independent of the applied voltage. For runs between -600 mV and -800 mV, an initial increase of the absorbance occurs followed by the equilibration of the absorbance. This is indicative of MV^+ not undergoing a second reduction step. For runs between -900 mV and -1100 mV, the potential is low enough for MV^+ to be converted to MV^0, and thus a significant drop in the absorbance is observed after the initial increase until the absorbance equilibrates. The equilibrium absorbance was assumed to be 10 hours for -600 mV through -900 mV and 24 hours for -950 mV through -1100 mV. However, it should be noted that in reality a pseudo-equilibrium is achieved because of minor losses of MV. Small amounts of MV can be lost by diffusion into

the anode chamber. The Nafion membrane allows for some diffusion of positively charged MV species into the anodic chamber due to the MV concentration difference between the anode and the cathode chamber. However, because these losses are minor (about 5% in 8 hours), a pseudo-equilibrium value could be used to approximate the true equilibrium value for the absorbance.

7.5.3 Extinction Coefficient

In order to convert the absorbance in Figure 7-3 to a MV^+ concentration to assess the validity of a thermodynamic model, appropriate extinction coefficients are needed. Most authors assume that MV^+ is the only absorbing species such that Beer's law can be used along with a reported extinction coefficient for MV^+ (ε_m). However, oftentimes there are other absorbing species present, such as the dimer of MV, which can affect the experimental value of ε_m. Thus, the accuracy of the conversion from absorbance to MV^+ depends on the accuracy of ε_m. Though ε_m = 13,000 $M^{-1}cm^{-1}$ at 600 nm is often cited as the most reliable value to use to predict the MV^+ concentration (Bird and Kuhn 1981; Thorneley 1974), literature values of ε_m range from 4,000 to 18,800 $M^{-1}cm^{-1}$ at ~600 nm (Asada 1967; Bauer and Werner 1992; Kok, et al. 1965; Kosower and Cotter 1964; Steckhan and Kuwana 1974; Trudinger 1970; Watanabe and Honda 1982; Yuen, et al. 1967). Thorneley's value of 13,000 $M^{-1}cm^{-1}$ has been cited as the most accurate value to use because he accounts for the dimerization of MV^+, and thus gives an observed extinction coefficient that is dependent on the mole fraction of MV^+ (Bird and Kuhn 1981).

The precise amount of absorbing species (such as MV^+ or the dimer) in the experimental system must be known to obtain an accurate value for ε_m. In his work, Thorneley assumes that all MV added to the experimental system exists as either MV^+ or the dimer MV_2^{2+}. If any of the added MV were actually in the $MVCl_2$, MV^{2+}, MV^0, or MVH^{2+} state, then this would give a lower extinction coefficient than not having these species present. Bauer presents the idea that

the reason for the discrepancy in reported ε_m values is because there may be a significant amount of MVH^{2+} present in some of the experiments (Bauer and Werner 1992). Thus, this work will present a modified Thorneley model for the observed extinction coefficient that combines the model presented by Thorneley and the potential presence of MV species beyond MV^+ and the dimer MV_2^{2+}. The modified model is used to address reasons for possible discrepancies in ε_m and to provide guidance for predicting MV^+ concentrations in solution using the thermodynamic model described above.

To predict ε_m at 600 nm, Thorneley uses a form of Beer's law for two absorbing species as shown in Equation 8 (Thorneley 1974).

$$\varepsilon_o = \frac{abs_o}{MV_T \cdot l} = \varepsilon_m \cdot X_{MV^+} + \varepsilon_d \cdot X_{MV_2^{2+}} \tag{7-1}$$

In this equation, MV_T is the total amount of MV added to the system, l is the cell path length, and ε_o is the observed extinction coefficient calculated from the observed absorbance (abs_0) and MV_T. ε_m is the extinction coefficient of MV^+, ε_d is the extinction coefficient of the dimer, X_{MV^+} is the fraction of MV^+ relative to MV_T, and $X_{MV_2^{2+}}$ is the fraction of dimer relative to MV_T. In Thorneley's model, $X_{MV_2^{2+}}$ is replaced with ½ (1- X_{MV^+}), based on Equation 7-5 where only MV^+ and the dimer exist, such that the observed absorbance is only a function of the MV^+ fraction. However, in reality other MV species as noted in Equation 7-5 can also exist depending upon the solution potential U_{ex}. Thus, a more appropriate model would replace $X_{MV_2^{2+}}$ with $1/2\ (1 - X_{MV^+} - \sum_i X_{MV,i})$. Here, $\sum_i X_{MV,i}$ is the sum of additional mole fractions of MV^0, MV^{2+}, $MVCl_2$, MVH^{2+} and other MV species. In work besides Thorneley, authors reporting values of ε_m assume

X_{MV+} is unity such that $X_{MV_2^{2+}}$ is zero and ε_0 is equivalent to ε_m. Depending upon U_{ex} and MV_T, which are generally not reported, this assumption may or may not be valid and can lead to varying values of ε_m. This is a likely explanation of the wide variation in reported values.

As an example, Equation 7-9 shows the effect of adding MVH^{2+}, which is in equilibrium with MV^+, to Thorneley's model.

$$\varepsilon_o = \frac{abs_o}{MV_T \cdot l} = \varepsilon_m \cdot X_{MV^+} + \frac{\varepsilon_d}{2} \cdot (1 - X_{MV^+} - K_H \cdot X_{MV^+} \cdot [H^+]) \tag{7-2}$$

Here, K_H is the equilibrium value for the proton complex and $[H^+]$ is the concentration of H^+ ions. In Thorneley's work, they performed their experiments at a pH of 7.5. Thus, $[H^+]$ in Equation 1 is $10^{-7.5}$ M. When this value is used, the term $K_H \cdot X_{MV^+} \cdot [H^+]$ is much smaller than unity and can be neglected. Consequently, at a pH of 7.5 the model used by Thorneley is still accurate even without accounting for MVH^{2+} as long as other MV species are not present. Thus, neither Thorneley's nor any of the other reported values for ε_m are effected by any significant loss to MVH^{2+} because all experiments were performed above pH=6. This is in contrast to Bauer & Werner (Bauer and Werner 1992) who suggested that pH could be a reason for the discrepancies of ε_m.

Besides MVH^{2+}, there could also be amounts of MV^{2+} and MV^0 present in the reported experiments depending upon U_{ex}. Since these species both have an extinction coefficient of 0 at 600 nm, any amount of these species present would give a lower predicted ε_m if they were not appropriately accounted for. Trudinger reported that when using Na_2SO_4 or alkaline glucose to reduce MV^{2+} to MV^+, the solutions were distinctly yellow, indicating that there was significant reduction to MV^0. If we exclude the experiments that used Na_2SO_4 or alkaline glucose to reduce

MV^{2+} to MV^{+}, then the lowest value reported for ε_m is 10,006 $M^{-1}cm^{-1}$ (Kosower and Cotter 1964). Yuen et al. predicted the highest ε_m value of 18,800 (Trudinger 1970; Yuen, et al. 1967). However, they are the only researchers who did not use $MVCl_2$; they used a mixture of $MVCl_2$ and $MV(CH_3SO_4)_2$. Asada (Asada 1967) predicted the next highest value of 14,000 $M^{-1}cm^{-1}$ followed by 13,700 $M^{-1}cm^{-1}$ by Watanabe et al. Theoretically, the largest ε_m predicted should be the most correct because that means there were minimal losses to MV^{2+} and MV^{0}. Thus, excluding the value given by Yuen at al., the highest literature values for ε_m are 13,000 $M^{-1}cm^{-1}$, 13,700 $M^{-1}cm^{-1}$, 14,000 $M^{-1}cm^{-1}$ reported by Thorneley, Watanabe, and Asada respectively. Therefore, even though the reported range of literature values for ε_m is quite large, the most likely is between 13,000 and 14,000 $M^{-1}cm^{-1}$ with an average value of 13,570 $M^{-1}cm^{-1}$. This average value was used in this work.

Since in some cases there may be a significant amount of dimer present, the extinction coefficient for the dimer (ε_d) at 600 nm must also be known in order to accurately convert absorbance into an MV^{+} concentration. An ε_d of 6,000 $M^{-1}cm^{-1}$ is reported by Thorneley. However, the ε_d value was obtained by extrapolating the ε_o data to infinite MV_T although experiments were only conducted up to MV_T of 20.6 M. Fitting the data showed that extrapolation never converged at infinity to a constant value.

To obtain a better approximation for ε_d, Equations 7-4 (with concentrations rather than mole fractions) and 7-8 were combined to give Equation 7-10. Using the last three abs_0 data points at three different MV_T values from Thorneley's dimerization data, the K_d value of 2.6×10^{-3} M reported by Kosower (Kosower and Cotter 1964), and the material balance with only dimer and MV^{+} present (Equation 5), an average ε_d of 1,260 ±88 $M^{-1}cm^{-1}$ was obtained. Since this value does not rely on extrapolation, this may be a more correct value for ε_d. It is important to note that

all MV species need to be predicted or measured for the determination of ε_m and ε_d as a result of the material balance.

$$\frac{abs_o}{MV_T \cdot l} = \varepsilon_m \cdot \frac{[MV^+]}{MV_T} + \varepsilon_d \cdot \frac{[MV^+]^2}{K_d \cdot MV_T} \tag{7-3}$$

In Thorneley's work it should be noted that U_{ex} was at -760 mV vs. a 3M Ag/AgCl which, as shown later, suggests that the added MV_T did not convert to MV^{2+} or MV^0. This is consistent with the assumed material balance for the ε_d prediction.

7.6 MV^+ Redox Potential

Now, with more accurate values for ε_m and ε_d of 13570 $M^{-1}cm^{-1}$ and 1260 $M^{-1}cm^{-1}$, respectively, Equation 7-11 was used to convert the experimental equilibrium absorbance data into MV^+ concentration data to assess the validity of the thermodynamic model. Figure 7-4 shows the measured MV^+ equilibrium concentration plotted as a function of U_{ex}. The bell-shaped curve shows that MV^+ is highest at -800 mV. Of interest is the precipitous drop of the MV^+ concentration in the -600 to -650 mV range and the -900 to -950 mV range. Thus, over the wide range of -650 and -900 mV, MV^+ is a dominant species. It should be noted that the highest MV^+ concentration (at -800 mV) is 76% of the original amount of MV (0.1 mM) added to the system such that some of the MV is converted to other MV forms.

Several irreversible reactions of MV are known to occur that can contribute to other MV forms or losses. When electrodes are used, MV can form a solid crystalline film on the electrode surface depending on the electrode surface, solutes, and analytes (Bird and Kuhn 1981). There is also evidence that suggests that MV^+ reacts irreversibly with oxygen because of the formation of

H_2O_2 (Bird and Kuhn 1981; Thorneley 1974). Thorneley shows a 15% loss of MV^+ after oxidation with H_2O_2 and re-reduction. Since complete O_2 removal is difficult in many experimental systems, there is some expected MV loss due to this phenomenon. There are also numerous other side reactions possible with the viologen family.

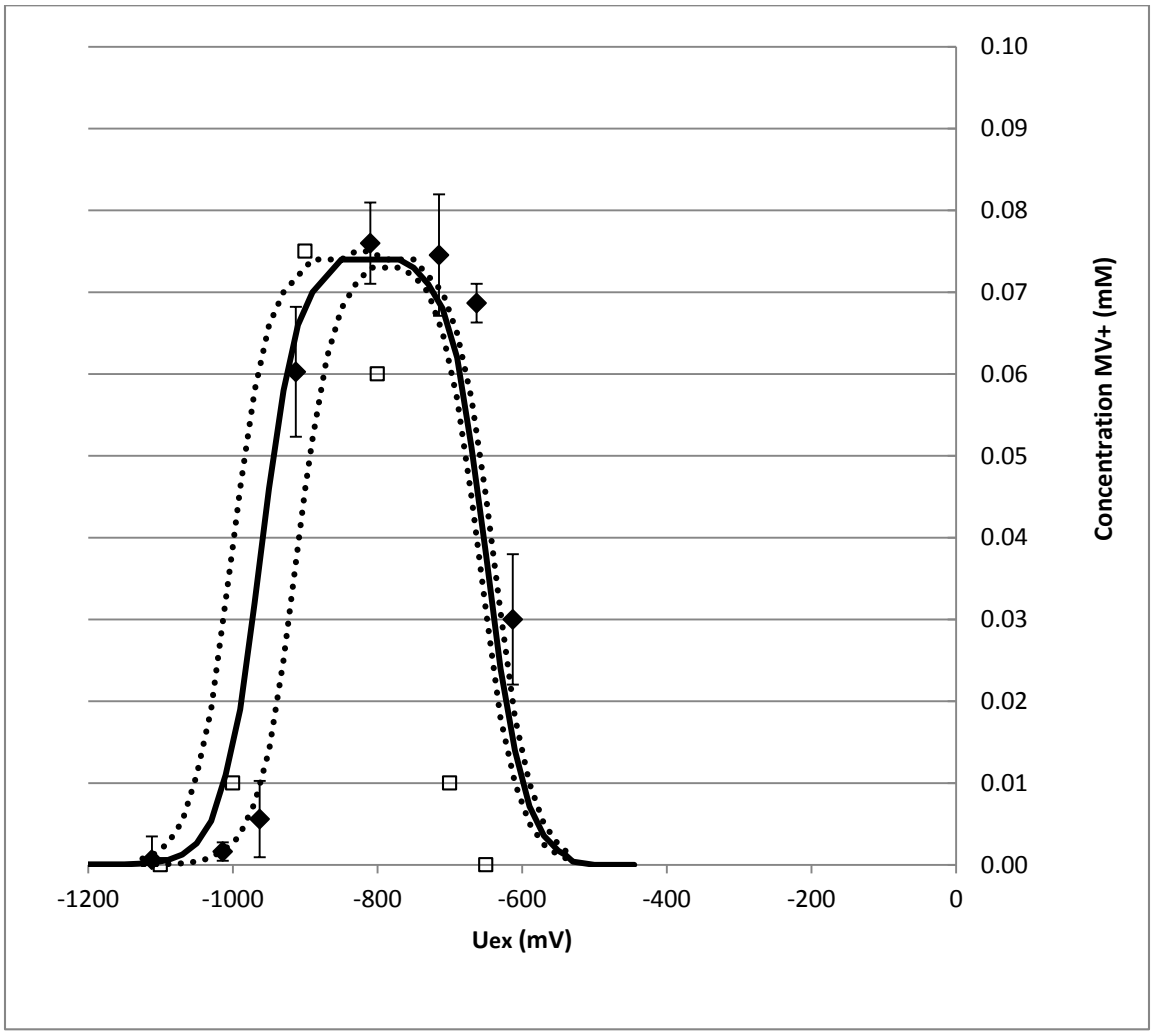

Figure 7-4. Experimental data (this work=filled diamonds, Chang Chen's work=open squares) and thermodynamic model (solid line) of equilibrium concentration of MV^+ versus potential. The model used values for E^0_1 and E^0_2 of -0.653 mV and -0.959 mV, respectively, vs. a 3M Ag/AgCl electrode, K_d of 2.6×10^{-3} M, and K_{salt} of 0.663 M^2. MV^+ concentration data was obtained using ε_m of 13,570 $M^{-1}cm^{-1}$ and ε_d of 1,260 $M^{-1}cm^{-1}$ according to Equation 7-11. The model sensitivity was calculated using ±11 mV for E^0_1 and ±46 mV for E^0_2 and is shown as dotted lines.

As part of this work, some experiments were performed at U_{ex} of -810 mV (vs. 3M Ag/AgCl) with varying amounts of DMF because DMF has been shown to minimize film formation and other side reactions (Bird and Kuhn 1981; Heli, et al. 2004; Kim, et al. 2001). This U_{ex} value was chosen since MV^+ is the dominant species with little MV^0 or MV^{2+} formation as noted below. Using the measure abs_0 at varying DMF amounts and $[MV_T] = 0.1$ mM, Equation 11 was used to predict $[MV^+]$ and then Equation 5 was used to estimate $[MV_{other}]$. The ratio of $[MV_{other}]$ to $[MV_T]$ was 52%, 26%, 33%, 21%, and 26% with 0%, 5%, 10%, 15%, and 20% of DMF in water respectively. The lowest $[MV_{other}]$ occurred when the percentage of DMF was 15% which is equivalent to 30 mL of DMF and 170 mL water. This is why the data shown in Figure 7-4 was obtained using 30 mL DMF. At 30 mL DMF, $[MV_{other}] = 0.21[MV_T] = 0.021$ mM although $[MV_{other}]$ will depend upon the experimental system and associated conditions.

Figure 7-4 also shows the predicted MV^+ concentrations based on simultaneously solving Equations 7-1 through 7-5 of the thermodynamic model with $E^0_1 = -653$ mV, $E^0_2 = -959$ mV, $[MV_T] = 0.1$ mM, and $[MV_{other}] = 0.021$ mM. It should be noted that model predictions used no experimental data except for the prediction of $[MV_{other}]$ such that the model was an *a prior* prediction. $[MV_{other}]$ affects only the magnitude of the curve but not the shape of the curve. The parameter sensitivity of the model, also shown in Figure 7-4 as dotted lines, was calculated using one standard deviation for E^0_1 and E^0_2 (±11 mV and ±46 mV vs. 3M Ag/AgCl respectively).

As shown, the experimental data follows the thermodynamic model reasonably well. The larger uncertainty in the value of E^0_2 as compared to E^0_1 provides a wider range of model uncertainty in the -800 to -1000 mV region. The uncertainty basically changes the width of the bell-shaped curve which affects the range in which MV^+ is the dominant species. However, it is clear that there are still regions of sharp transition between significant and insignificant MV^+

concentrations. This could be a potential reason for experimental variations between positive and negative effects of MV on biological systems. As for the slight discrepancies between experimental data and the model, effects not accounted for in the model such as the variable nature of the second reduction of MV because of its slight irreversibility (Bird and Kuhn 1981) can have an impact. In general, the model agreement with the experimental data provides an opportunity to predict other MV species to ascertain the types of MV species that would be present under various solution potentials.

Figure 7-4 also shows the MV^+ experimental data from Chang Chen's thesis using the graphite electrodes. Chen's data show a deviation from thermodynamic predictions at potentials more positive than -900 mV. As discussed in Section 7.5.1, this could be due to the absorption of MV^+ into the carbon electrodes used in Chen's work which would reduce the measured MV^+ concentration compared to non-adsorbing electrodes. Originally, Chen's thermodynamic predictions were based on an online source that predicted K_{salt} to be very close to zero, which would shift the thermodynamic curve to fit Chen's data more closely. However, further in depth research showed the value for K_{salt} has been measured and is equal to 0.663 M^2 as calculated from Monk and Hodgkinson (Monk and Hodgkinson 1998). This is the value used in Figure 7-4.

Figure 7-5 shows the thermodynamic model predictions of all MV species at a pH of 6 or higher for this study. At lower pH, MVH^{2+} could be present in significant amounts depending on the kinetics, mass transfer, and amount of H_2 present as discussed earlier. pH effects could be assessed in the model by including the equilibrium constraint for the proton complex which was discussed in Section 3.2. Figure 7-5 shows that many MV forms can be present depending on the potential. At voltages more positive than -500 mV, only $MVCl_2$ and MV^{2+} are present. Between

-600 and -1000 mV there are significant amounts of MV^+ and some dimer present. Below -1000, the dominant species is MV^0.

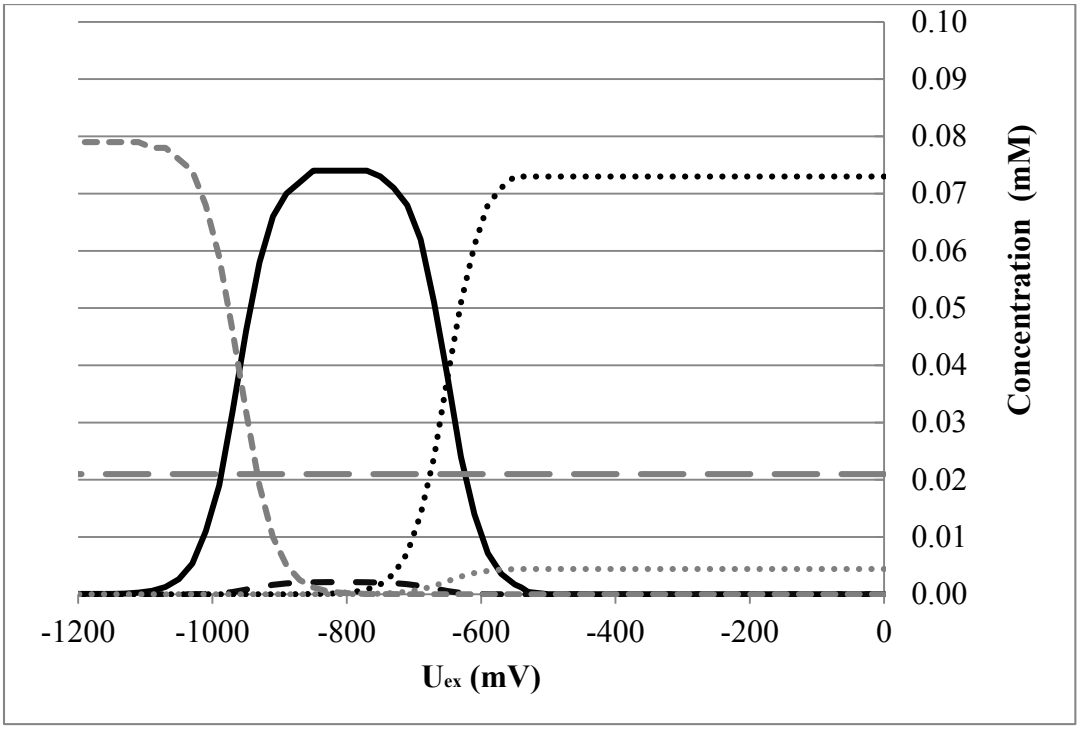

Figure 7-5. Thermodynamic model predictions of all MV species at varying potentials vs. a 3M Ag/AgCl electrode. MV^+, MV_2^{2+}, MV^{2+}, MV^0, $MVCl_2$, MV_{other}.

As previously mentioned, some studies have shown that MV is toxic to cells while other studies have shown positive effects. The reason for this discrepancy may be the fact that MV can exist in many different forms depending on factors such as redox potential, initial MV concentration, pH, electrolyte solution, anions, and type of electrode (in electrode systems). The redox range for natural microbial growth can range from positive to more negative than -610 mV (vs. Ag/AgCl) for strict anaerobic bacteria (Sigma-Aldrich 2013; Zajic 1969). For instance, if an experiment was initiated at a redox potential -600 mV, primarily MV^{2+} would exist. However, if the redox potential slightly changes during the experiment to -650 mV, then MV^+ (which has

reducing potential) becomes a significant species. Thus, having an awareness of the redox potential is important when seeking to interpret experimental results using MV.

If electrodes are used, even more negative redox potentials can easily be applied to biological systems. This can be a useful tool if one wants to study the toxic effects of MV^{2+}, MV^{+}, and MV^{0}. Thus, in non-anaerobic systems, the state of MV is most likely MV^{2+} and $MVCl_2$. The toxicity of these two species could vary greatly. MV^{2+} can accept electrons and could interfere with the natural electron cascade in the cell. Since $MVCl_2$ is not dissociated and electrically neutral, it will not accept electrons as readily. In anaerobic systems with a redox potential between -600 and -1000 mV, MV^{+} and the dimer dominate. This is the species that is most likely to impact cell processes because of its ability to accept electrons and also create activated oxygen species that are toxic to cells. When redox potentials are below -1000 mV, MV^{0} is the dominant species and can be a significant donor of electrons. However, there are few biological systems that grow naturally to this redox potential, thus an electrode system would need to be used to reach this state.

7.7 Conclusions

This work presented a thermodynamic model capable of predicting important MV species at differing experimental conditions, with a particular emphasis on the redox potential. Standard redox potentials and extinction coefficients for validating model predictions were discussed with identification of appropriate values to use. The experimental data fell within the error for the thermodynamic model. Because the toxicity of MV may be different in different redox states, an electrode system may prove useful for controlling the redox potential to study MV effects. Researchers should use caution when applying MV to a biological system without accounting for redox effects on MV.

This study showed that the concentrations of MV species can be predicted accurately in order to aid future research in the use of electrodes to augment the supply of electrons in syngas fermentation. Bioelectric reactors may be of great use for syngas fermentation. The ultimate goal of using BERs in syngas fermentation is to provide electrons to the cells via an electrode as opposed to providing electrons via H_2 or CO. This additional supply of electrons could potentially increase the carbon conversion efficiency through reducing the amount of electrons provided by CO and/or enabling unused CO_2 to be further converted to products through the Wood-Ljungdahl pathway. However, in order for this to be accomplished much more work needs to be performed with BERs and electron mediators.

8 Conclusions and Future Work

8.1 Conclusions

8.1.1 Mass Transfer

8.1.1.1 A Comparison of Hollow Fiber Membrane Reactors

- In mass transfer studies, the HFR (non-porous PDMS) provided the highest mass transfer coefficient, $K_{tot}A/V_L$, of 1062 h^{-1}, followed by the TBR with 6 mm beads (421 h^{-1}), and then the STR (114 h^{-1}).
- The HFR and TBR can transfer O_2, a sparingly soluble gas similar to the fermentation substrates CO and H_2, into water at rates much higher than achieved in the STR.
- Higher mass transfer in the HFR and TBR suggest a more efficient process design might be attained for syngas fermentation.
- Caution should be used when simply comparing the $K_{tot}A/V_L$ values between reactors because of volume and driving force effects.

8.1.1.2 H_2 and CO Mass Transfer Coefficients in a Hollow Fiber Reactor

- A new technique was developed to measure the mass transfer coefficients for H_2 and CO using gas GC and gas flow rate measurements.

- This new technique was validated by comparing O_2 data to an established traditional technique using a dissolved oxygen probe and the two techniques were found to be in agreement.
- A mass transfer coefficient model was presented for mass transfer through a non-porous HFR. The model parameters were determined using oxygen data. The mass transfer model was found to be in very good agreement with the experimental data for CO and H_2. The mass transfer coefficient for H_2 was about twice that of CO and CO_2.
- HFRs can support high cell densities without mass transfer limitations if the proper experimental configuration is achieved.

8.1.1.3 Hollow Fiber Membrane Fermentation

- This work showed that the HFR fermentations were able to outperform other traditional bioreactors. For example, the HFR fermentations were able to achieve high production rates (5.3 mM_c/hr). Also, the ethanol to acetic acid ratios achieved in this work were higher than all but one other study.
- This worked also showed evidence that there is no formation of a biolayer that contains bacteria enclosed in a protective extracellular polymeric matrix in the HFRs. However, there is abundant evidence of a loosely attached aggregates cells on the fibers allowing for exposure to more electron equivalents needed for the reduction of CO and CO_2 to ethanol.
- The gas usage data in this work showed evidence that the ratio of CO consumed to H_2 consumed can vary greatly, even in very similar reactor setups. This may highlight the cells ability to keep production rates fairly constant even though intracellular

aspects, such as hydrogenase levels ,may vary. Also, gas usage ratios showed evidence that cells prefer CO as opposed to H_2 as an electron donor

- This work also showed evidence that the HFR fermentations performed were not mass transfer limited during by showing that there was no significant change in product formation rates when V_{Ltot}/V_S or $K_{tot}A/V_L$ increased or decreased. Also, when was decreased there was no significant decrease in production rates.
- Though HFR fermentation can be initially difficult to perform reliable fermentations, once an appropriate procedure is determined it has a very good chance to being just as reliable as other traditional bioreactors.

8.1.1.4 Fermentation with Isopropanol Effects

- Isopropanol was shown to increase ethanol to acetic acid ratios and overall ethanol production. This effect could be due to the up-regulation of heat shock proteins that improve the cell's tolerance to ethanol. However, it is more likely due to the induction of CoA transferase or some other enzyme in the Wood-Ljungdahl pathway by isopropanol.

8.1.2 Electron Usage

8.1.2.1 CO and H_2 as Electron Donors and Effects on Ethanol Production

- Predictions using syngas production from different biomass types showed that the range of ethanol production can be quite broad, from 5.1-80.5 gallons of ethanol per ton biomass.

- The bottle studies performed in this work showed that cell growth in the cellular media used is not largely effected by syngas composition as long as there is at least some minimum amount of CO present (about 5%) and another electron equivalent such as H_2.
- As the partial pressure of H_2 in the gas increases the rate of H_2 and CO consumption per cell increases.
- Anabolism is largely independent of the H_2 partial pressure when CO is present. However, when CO is removed there is very little cell growth. This is most likely because the hydrogenase enzyme in *C. ragsdalei* uses an electron carrier that is not used or has a lower abundance in the redox reactions in cell anabolism than the CODH enzyme.
- Cells should be exposed to high CO partial pressures during cell growth because CO is the preferred electron source for cell anabolism. However, after cell growth stops, the cells should be exposed to higher H_2 levels to provide electrons for the methyl branch of the Wood-Ljungdahl pathway and for product formation.

8.1.2.2 Methyl Viologen as an Electron Carrier

- Electrode systems may be used for fermentations in which the electrodes provide electron equivalents.
- In the case that cells cannot directly accept electrons, an electron mediator such as methyl viologen may be used.

- This work presented a thermodynamic model capable of predicting important MV species at differing experimental conditions, with a particular emphasis on the redox potential.
- Standard redox potentials and extinction coefficients for validating model predictions were discussed with identification of appropriate values to use. The experimental data fell within the error for the thermodynamic model.
- Because the toxicity of MV may be different in different redox states, an electrode system may prove useful for controlling the redox potential to study MV effects.
- Researchers should use caution when applying MV to a biological system without accounting for redox effects on MV.

8.2 Future Work

The syngas-fermentation platform may have a future in the production of ethanol and other biofuels (e.g. butanol). However, there is still a need for more research in order to improve the current process. One major issue is still mass transfer limitations of syngas in the bacterial media. Future research needs to be performed in order to increase mass transfer rates while still keeping production costs feasible. One possible reactor in the future of syngas fermentation is the HFR. This work showed that, depending on the experimental setup, the HFR can have much greater mass transfer rates than other common bioreactors. This work performed fermentations using one specific HFR, however, much more fermentation work needs to be performed with various other types of HFRs in order to validate the assumption that the HFR is a superior bioreactor for syngas fermentation. This work showed evidence of loosely attached biolayers in HFR syngas fermentation, however these cell aggregates were not intensely studied in this work.

If HFR fermentation is going to be fully understood and predictable, the cell growth and attachment in the HFR needs to be more fully studied with different HFR materials and flow patterns. This work showed evidence that isopropanol may induce enzymes in the Wood-Ljungdahl pathway that leads to larger ethanol to acetic acid ratios and overall ethanol production. Future research would include a better understanding of the effects of isopropanol on cells in syngas fermentation.

Still another issue besides mass transfer in syngas fermentation is electron usage. This work showed that cells grow well on CO and form products well on CO and H_2. Future research needs to focus on improving syngas fermentation efficiency by understanding and collecting more data on H_2 and CO as electron sources so that methods can be developed to provide greater carbon conversion to ethanol. There may be optimal ratios for growth and product formation that need to be explored and validated. One method of implementing a different source of electrons into the syngas fermentation platform is by using an electrode system to provide the electrons. This work showed that methyl viologen could possibly be used as an electron carrier. However, future work should include cellular fermentation studies in an electrode system using methyl viologen as an electron carrier in order to assess its toxicity. Also, other electron carriers could be assessed for use in syngas fermentation with electrodes that may not be as toxic to cells. In addition to electron carriers, future research could explore the use of electrode systems with acetogenic microbes in which electrons are transferred directly to the cells attached to the electrode.

REFERENCES

1992 The Energy Policy Act of 1992. House of Representatives.

2005 Energy Policy Act of 2005. House of Representatives.

2007 Energy Independence and Security Act of 2007.

Abubackar H., Veiga M., and Kennes C.
2011 Biological conversion of carbon monoxide: rich syngas or waste gases to bioethanol. Biofuels, Bioproducts and Biorefining 5(1):93-114.

Ahmed A., and Lewis R. S.
2007 Fermentation of biomass-generated synthesis gas: Effects of nitric oxide. Biotechnology and Bioengineering 97(5):1080-1086.

Alauddin Z., et al.
2010 Gasification of lignocellulosic biomass in fluidized beds for renewable energy development: A review. Renewable and Sustainable Energy Reviews 14(9):2852-2862.

Alberts B., Johnson A., Lewis J., et al.
2002 Molecular Biology of the Cell. 4th edition. New York: Garland Science. Pp 110-111.

Asada K.
1967 Purification and properties of a sulfite reductase from leaf tissue. J Biol Chem 242(16):3646-54.

Asada K., et al.
1990 Methyl Viologen-Dependent Cyclic Electron Transport in Spinach Chloroplasts in the Absence of Oxygen. Plant and Cell Physiology 31(4):557-564.

Atchariyawut S., Jiraratananon R., and Wang R.
2008 Mass transfer study and modeling of gas-liquid membrane contacting process by multistage cascade model for CO2 absorption. Separation and Purification Technology 63(1):15-22.

Aulenta F., et al.
2007 Electron transfer from a solid-state electrode assisted by methyl viologen sustains efficient microbial reductive dechlorination of TCE. Environmental Science & Technology 41(7):2554-2559.

Babu S. P.
2005 Biomass gasification for hydrogen production-process description and research needs. Task 33: thermal gasification of biomass (IEA bioenergy technology report) ExCo56, Dublin, Ireland, www.ieatask33.org.

Bauer R., and Werner H.
1992 New mechanism for electron transfer between methyl viologen radicals and water. Journal of molecular catalysis 72(Compendex):67-74.

BEC
2011 What is Biomass?, Vol. 2011: Biomass Energy Centre.

Bingyan X., Zengfan L., Chungzhi W., Haitao H., Xiguang Z.
1994 Circulating Fluidized Bed Gasifier for Biomass. Integrated energy systems in China-The Cold Northeastern Region Experience Food and Agriculture Organization of the United Nations.

Bird C. L., and A. T. Kuhn
1981 Electrochemistry of the viologens. Chemical Society Reviews 10(1):49-82.

Bird R.B., Stewart W.E., and Lightfoot E.N.
2007 Transport Phenomena: Wiley.

Bond D. R., et al.
2002 Electrode-Reducing Microorganisms That Harvest Energy from Marine Sediments. Science 295(5554):483-485.

Bredwell M. D., Srivastava P., and Worden R. M.
1999 Reactor Design Issues for Synthesis-Gas Fermentations. Biotechnology Progress 15(5):834-844.

Brienergy
2011, Vol. 2011.

Brotherton J. D., Chau P. C.
1996 Modeling of Axial- Flow Hollow Fiber cell culture bioreactors. Biotechnology progress 12:575-590.

Bus J. S., and Gibson J. E.
1984 Paraquat - Model for Oxidant-Initiated Toxicity. Environmental Health Perspectives 55(Apr):37-46.

Bus J. S., Gibson J. E., and Aust S. D.
1974 Superoxide-Catalyzed and Singlet Oxygen-Catalyzed Lipid Peroxidation as a Possible Mechanism for Paraquat (Methyl Viologen) Toxicity. Biochemical and Biophysical Research Communications 58(3):749-755.

Calabrese E. J.
1991 Alcohol Interactions with Drugs and Chemicals. Michigan: CRC Press.

Cao Y., et al.
2006 A novel biomass air gasification process for producing tar-free higher heating value fuel gas. Fuel Processing Technology 87(4):343-353.

Chen C.
2012 Thermodynamic, Kinetic and Efficiency Analysis of Methyl Viologen, Chemical Engineering, Brigham Young University.

Cheng H., Abo M., and Okubo A.
2003 Development of dimethyl sulfoxide biosensor using a mediator immobilized enzyme electrode. Analyst 128(6):724-727.

Chubukov V., et al.
2013 Transcriptional regulation is insufficient to explain substrate-induced flux changes in Bacillus subtilis. Molecular Systems Biology 9(1).

Coskata
2012 Technology Advantages, www.coskata.com Accessed on 11/09/2012.

Cotter J. L., Chinn M. S., and Grunden A. M.
2009 Influence of process parameters on growth of Clostridium ljungdahlii and Clostridium autoethanogenum on synthesis gas. Enzyme and Microbial Technology 44(5):281-288.

Damian A.
2007 Direct electrochemical regeneration of NADH on Au, Cu and Pt-Au electrodes. CHEMICAL AND BIOCHEMICAL ENGINEERING QUARTERLY 21(1):21-32.

Datar R. P., et al.
2004 Fermentation of biomass-generated producer gas to ethanol. Biotechnology and Bioengineering 86(5):587-594.

Davis B., Dulbecco R., Eisen H., Ginsberg H.
1973 Bacterial physiology: microbiology. Maryland.

Dayton D. C, and Spath P. L.
2003 Preliminary screening--technical and economic assessment of synthesis gas to fuels and chemicals with emphasis on the potential for biomass-derived syngas [electronic resource] / P.L. Spath and D.C. Dayton. Golden, Colo. :: National Renewable Energy Laboratory.

Dunlop M. J.
2011 Engineering microbes for tolerance to next-generation biofuels. Biotechnology for Biofuels 4.

DuPont
2011 Biobutanol fact sheet. DuPont.

Ebrahimi S., et al.
2005 Biofilm growth pattern in honeycomb monolith packings: Effect of shear rate and substrate transport limitations. Catalysis Today 105(3-4):448-454.

Elofson R. M. , and Edsberg R. L.
1957 Polarographic Behavior of the Viologen Indicators. Canadian Journal of Chemistry 35(7):646-650.

Erbes D. L., and Burris R. H.
1978 The kinetics of methyl viologen oxidation and reduction by the hydrogenase from Clostridium pasteurianium. Biochimica et Biophysica Acta (BBA) - Enzymology 525(1):45-54.

Ezeji T., Qureshi N., and Blaschek H.P.
2007 Bioproduction of butanol from biomass: from genes to bioreactors. Current Opinion in Biotechnology 18(3):220-227.

Fang Y., et al.
2002 Passive dissolution of hydrogen gas into groundwater using hollow-fiber membranes. Water Research 36(14):3533-3542.

Frankman A. W.
2009 Redox, Pressure and Mass Transfer Effects on Syngas Fermentation, Chemical Engineering, Brigham Young University.

Friis E. P., et al.
1998 Dynamics of Pseudomonas aeruginosa azurin and its Cys3Ser mutant at single-crystal gold surfaces investigated by cyclic voltammetry and atomic force microscopy. Electrochimica Acta 43(9):1114-1122.

Gassanova L. G., et al.
2006 Fuel gases from organic wastes using membrane bioreactors. Desalination 198(1-3):56-66.

GTC
2011 Gasification: An Investment In Our Energy Future. Gasification Technologies Council G.T. Council.

Hall-Stoodley L., Costerton J. W., and Stoodley P.
2004 Bacterial biofilms: From the natural environment to infectious diseases. Nature Reviews Microbiology 2(2):95-108.

Hamper M. J.
2006 Manufactured gas history and processes. Environmental Forensics 7(1):55-64.

Heiskanen H., Virkajarvi I., and Viikari L.
2007 The effect of syngas composition on the growth and product formation of Butyribacterium methylotrophicum. Enzyme and Microbial Technology 41(3):362-367.

Heli H., S. Z. Bathaie, and M. F. Mousavi
2004 Electrochemical investigation of neutral red binding to DNA at the surface. Electrochemistry Communications 6(Compendex):1114-1118.

Hickey R.
2009 Moving bed biofilm reactor (mbbr) system for conversion of syngas components to liquid products, Vol. US 20090035848. United States.

Hickey R., et al.
2010 Method of conversion of syngas using microorganism on hydrophilic membrane, Vol. US 20100047886. United States.

Hickey Robert F., et al.
2009 Submerged membrane supported bioreactor for conversion of syngas components to liquid products, Vol. US 20090286296. United States.

Higman C., and Van der Burgt M.
2003 Gasification. Amsterdam, Boston: Gulf Professional Publishing.

Hoeger C.
2012 Foundational Work in Bioelectrochemical Anaerobic Reactor Design, Chemical Engineering, Brigham Young University.

Hsieh W., et al.
2002 Engine performance and pollutant emission of an SI engine using ethanol-gasoline blended fuels. Atmospheric Environment 36(3):403-410.

Hu P.
2011 Thermodynamic, Sulfide, Redox Potential, and pH Effects on Syngas Fermentation, Chemical Engineering, Brigham Young University.

Hurst K. M., and Lewis R. S.
2010 Carbon monoxide partial pressure effects on the metabolic process of syngas fermentation. Biochemical Engineering Journal 48(2):159-165.

Incropera F.P., et al.
2011 Fundamentals of Heat and Mass Transfer: Wiley.

Incropera F.P., et al.
2006 Fundamentals of Heat and Mass Transfer: John Wiley & Sons.

Kadar Z., Szengyel Z., and Reczey K.
2004 Simultaneous saccharification and fermentation (SSF) of industrial wastes for the production of ethanol. Industrial Crops and Products 20(1):103-110.

Kim I. W., et al.
2008 A statistically robust Wilson-plot methodology for calculating membrane mass transfer coefficients. Journal of Industrial and Engineering Chemistry 14(5):584-588.

Kim J.Y., Lee C., and Park J.W.
2001 The kinetics of neutral methyl viologen in acidic H2O+DMF mixed solutions studied by cyclic voltammetry. Journal of Electroanalytical Chemistry 504(1):104-110.

Kim M., and Yun S.
2004 Construction of an electro-enzymatic bioreactor for the production of -mandelate from benzoylformate. Biotechnology Letters 26(1):21-26.

Kim S., Yun S., and Kang C.
1999 Electrochemical evaluation of the reaction rate between methyl viologen mediator and diaphorase enzyme for the electrocatalytic reduction of NAD+ and digital simulation for its voltammetric responses. Journal of Electroanalytical Chemistry 465(Compendex):153-159.

Klasson K. T., et al.
1990 Biological Production of Liquid and Gaseous Fuels from Synthesis Gas. Applied Biochemistry and Biotechnology 24-5:857-873.

Kleinstreuer C., and Agarwal S. S.
1986 Analysis and Simulation of Hollow-Fiber Bioreactor Dynamics. Biotechnology and Bioengineering 28(8):1233-1240.

Kok B., Rurainski H.J., and Owens O.
1965 The reducing power generated in photoact I of photosynthesis. Biochimica et Biophysica Acta 109(2):347-356.

Korikov A. P., and Sirkar K. K.
2005 Membrane gas permeance in gas-liquid membrane contactor systems for solutions containing a highly reactive absorbent. Journal of Membrane Science 246(1):27-37.

Kosower E.M., and Cotter J.L.
1964 Stable Free Radicals. II. The Reduction of 1-Methyl-4-cyanopyridinium Ion to Methylviologen Cation Radical. Journal of the American Chemical Society 86(24):5524-5527.

Kundiyana D.K., Huhnke R.L., and Wilkins M.R.
2010 Syngas fermentation in a 100-L pilot scale fermentor: Design and process considerations. Journal of Bioscience and Bioengineering 110(6):724-724.

Lan E.I., and Liao J.C.
2011 Metabolic engineering of cyanobacteria for 1-butanol production from carbon dioxide. Metabolic Engineering 13(4):353-363.

Lee P. H., et al.
2012 Enhancement of carbon monoxide mass transfer using an innovative external hollow fiber membrane (HFM) diffuser for syngas fermentation: Experimental studies and model development. Chemical Engineering Journal 184:268-277.

Li X. T., et al.
2004 Biomass gasification in a circulating fluidized bed. Biomass & Bioenergy 26(2):171-193.

Lide D. R.
1995 Handbook of Chemistry and Physics, 76th edition. CRC Press, Inc.

Liu K., et al.
2012 Fermentative production of ethanol from syngas using novel moderately alkaliphilic strains of Alkalibaculum bacchi. Bioresource Technology 104:336-341.

Liu K., et al.
2011 Fermentative production of ethanol from syngas using novel moderately alkaliphilic strains of *Alkalibaculum bacchi*. Bioresource Technology 104:336-341.

Ljungdahl L. G.
1986 The Autotrophic Pathway of Acetate Synthesis in Acetogenic Bacteria. Annual Review of Microbiology 40:415-450.

Llobell A., Fernandez V.M., and López-Barea J.
1986 Electron transfer between reduced methyl viologen and oxidized glutathione: A new assay of Saccharomyces cerevisiae glutathione reductase. Archives of Biochemistry and Biophysics 250(2):373-381.

Lymar S. V., and Hurst J. K.
1994 Electrogenic and electroneutral pathways for methyl viologen-mediated transmembrane oxidation-reduction across dihexadecylphosphate vesicular membranes. Journal of physical chemistry 98(Compendex):989-996.

Lynd Lee R.
1996 Overview and evaluation of fuel ethanol from cellulosic biomass: Technology, economics, the environment, and policy. Annual Review of Energy and the Environment 21:403-465.

Mackaluso J.D.
2007 The use of syngas derived from biomass and waste products to produce ethanol and hydrogen. MMG445 Basic Biotechnology eJournal.

Mansaray K. G., et al.
1999 Air gasification of rice husk in a dual distributor type fluidized bed gasifier. Biomass & Bioenergy 17(4):315-332.

Marshall C.W., and May H.D.
2009 Electrochemical evidence of direct electrode reduction by a thermophilic Gram-positive bacterium, Thermincola ferriacetica. Energy & Environmental Science 2(6):699-705.

McIlveen-Wright D. R., et al.
2006 A comparison of circulating fluidised bed combustion and gasification power plant technologies for processing mixtures of coal, biomass and plastic waste. Fuel Processing Technology 87(Compendex):793~801.

McKendry P.
2002a Energy production from biomass (Part 1): Overview of biomass. Bioresource Technology 83(1):37-46.

—
2002b Energy production from biomass (Part 3): Gasification technologies. Bioresour Technol 83(1):55-63.

McLachlan K. L., and Crumbliss A. L.
1990 The use of the methyl viologen neutral species as a mediator. Journal of electroanalytical chemistry and interfacial electrochemistry 295(1-2):113-122.

MedArray
2011 Membrane Basics.

Meyer C. L., Mclaughlin J. K., and Papoutsakis E. T.
1985 The Effect of CO on growth and product formation in batch cultures of *Clostridium acetobutylicum*. Biotechnology Letters 7(1):37-42.

Miccio F., et al.
2009 Biomass gasification in a catalytic fluidized reactor with beds of different materials. Chemical Engineering Journal 154(1-3):369-374.

Michaelis L., and Hill E. S.
1933a The Viologen Indicators. J Gen Physiol 16(6):859-73.

Michaelis L., and Hill E.S.
1933b Potentiometric Studies on Semiquinones. Journal of the American Chemical Society 55:1481-1494.

Mills A., Douglas P., and Russel T.
1990 Kinetic Study of the Reduction of Water to Hufrogen by Reduced Methyl viologen mediated by Platinised Alumina. J. Chem. Soc 86(9):7.

Monk P, and Hodgkinson N.
1998 Charge-transfer complexes of the viologens: effects of complexation and the rate of electron transfer to methyl viologen. Electrochimica Acta 43(Compendex):245-255.

Monk P., Turner C., and Akhtar S.P.
1999 Electrochemical behaviour of methyl viologen in a matrix of paper. Electrochimica Acta 44(Compendex):4817-4826.

Munasinghe P. C., and Khanal S. K.
2010a Biomass-derived syngas fermentation into biofuels: Opportunities and challenges. Bioresource Technology 101(13):5013-5022.

—
2010b Syngas Fermentation to Biofuel: Evaluation of Carbon Monoxide Mass Transfer Coefficient (k(L)a) in Different Reactor Configurations. Biotechnology Progress 26(6):1616-1621.

—
2010c Syngas fermentation to biofuel: Evaluation of carbon monoxide mass transfer coefficient (k_La) in different reactor configurations. Biotechnology Progress 26(6):1616-1621.

Nejadnik M. R., et al.
2008 Determination of the shear force at the balance between bacterial attachment and detachment in weak-adherence systems, using a flow displacement chamber. Applied and Environmental Microbiology 74(3):916-919.

Nerenberg R., and Rittmann B. E.
2004 Hydrogen-based, hollow-fiber membrane biofilm reactor for reduction of perchlorate and other oxidized contaminants. Water Science and Technology 49(11-12):223-230.

Nevin K. P., et al.
2011a Electrosynthesis of organic compounds from carbon dioxide is catalyzed by a diversity of acetogenic microorganisms. Appl Environ Microbiol 77(9):2882-6.

Nevin K. P., et al.
2010 Microbial electrosynthesis: feeding microbes electricity to convert carbon dioxide and water to multicarbon extracellular organic compounds. MBio 1(2).

Nevin Kelly P., et al.
2011b Electrosynthesis of Organic Compounds from Carbon Dioxide Catalyzed by a Diversity of Acetogenic Microorganisms. Appl. Environ. Microbiol.:AEM.02642-10.

Orgill J. J., et al.
2013 A comparison of mass transfer coefficients between trickle-bed, hollow fiber membrane and stirred tank reactors. Bioresource Technology 133:340-346.

Osa T., and Kuwana T.
1969 Non-aqueous electrochemistry using optically transparent electrodes. Journal of Electroanalytical Chemistry and Interfacial Electrochemistry 22(3):389-406.

Pan Y. G., et al.
2000 Fluidized-bed co-gasification of residual biomass/poor coal blends for fuel gas production. Fuel 79(11):1317-1326.

Panneerselvam A., et al.
2010 Effects of various reducing agents on syngas fermentation by clostridium ragsdalei. Biological Engineering 2(Compendex):135-144.

Park D. H., and Zeikus J. G.
1999 Utilization of electrically reduced neutral red by Actinobacillus succinogenes: Physiological function of neutral red in membrane-driven fumarate reduction and energy conservation. Journal of Bacteriology 181(8):2403-2410.

Park J. W., Choi M. H., and Park K. K.
1995 Electrocatalytic reduction of benzoylformic acid mediated by methyl viologen. Tetrahedron Letters 36(Compendex):2637-2637.

Paul D., et al.
2010 Genome sequence of the solvent-producing bacterium Clostridium carboxidivorans strain P7T. J Bacteriol 192(20):5554-5.

Peguin S., et al.
1994 Enhanced alcohol yields in batch cultures of Clostridium acetobutylicum using a three-electrode potentiometric system with methyl viologen as electron carrier. Biotechnology Letters 16(3):269-274.

Perlack R.D. et al.
2005 Biomass as Feedstock for A Bioenergy and Bioproducts Industry: The Technical Feasibility of a Billion-Ton Annual Supply.

Pessani N. K., et al.
2011 Simultaneous saccharification and fermentation of Kanlow switchgrass by thermotolerant Kluyveromyces marxianus IMB3: The effect of enzyme loading, temperature and higher solid loadings. Bioresource Technology 102(22):10618-10624.

Phillips J. R., et al.
1993 Biological Production of Ethanol from Coal Synthesis Gas - Medium Development Studies. Applied Biochemistry and Biotechnology 39:559-571.

Prince R. C., Linkletter S. J., and Dutton P. L.
1981 The Thermodynamic Properties of Some Commonly Used Oxidation-reduction Mediators, Inhibitors and Dyes, as Determined by Polarography. Biochim Biophys Acta 635(1):132-48.

Ragauskas A.J., et al.
2006 The Path Forward for Biofuels and Biomaterials. Science 311(5760):484-489.

Ragsdale S.
2008 Enzymology of the Wood-Ljundahl Pathway of Acetogenesis. Annals of the New York Academy of Science 1125:8.

Rajagopalan S., Datar R. P., and Lewis R. S.
2002 Formation of ethanol from carbon monoxide via a new microbial catalyst. Biomass & Bioenergy 23(6):487-493.

Ranade V.V., Chaudhari R., and Gunjal P.R.
2011 Trickle Bed Reactors: Reactor Engineering & Applications. UK: Elsevier.

Rao G., and Mutharasan R.
1986 Alcohol production by clostridium-acetobutylicum induced by methyl viologen. Biotechnology Letters 8(12):893-896.

Rao G., Mutharasan R.
1986 Alcohol Production by Clostridium acetobutylicum induced by methyl viologen. Biotechnology Letters 8(12):893-896.

Rapagna S., et al.
2000 Steam-gasification of biomass in a fluidised-bed of olivine particles. Biomass & Bioenergy 19(3):187-197.

RFA
2011 2011 Ethanol Industry Outlook. RFA, R.F. Association.

Rickard A. H., et al.
2004 Shear rate moderates community diversity in freshwater biofilms. Applied and Environmental Microbiology 70(12):7426-7435.

Sakai S., et al.
2005 Acetate and ethanol production from H-2 and CO2 by Moorella sp using a repeated batch culture. Journal of Bioscience and Bioengineering 99(3):252-258.

Sakai S., et al.
2004 Ethanol production from H-2 and CO2 by a newly isolated thermophilic bacterium, Moorella sp HUC22-1. Biotechnology Letters 26(20):1607-1612.

Schroder U.
2007 Anodic electron transfer mechanisms in microbial fuel cells and their energy efficiency. Physical Chemistry Chemical Physics 9(21):2619-2629.

Shuler M.L., and Kargi F.
2002a Bioprocess Engineering: Basic Concepts: Prentice Hall.
—
2002b Bioprocess Engineering: Basic Concepts: Prentice Hall.

Sierra R., et al.
2008 Producing fuels and chemicals from lignocellulosic biomass. Chemical Engineering Progress 104(8):S10-S18.

Sigma-Aldrich
2013 Microbiology Introduction.

Smith F. L., and Harvey A. H.
2007 Avoid common pitfalls when using Henry's law. Chemical Engineering Progress 103(9):33-39.

Spath P.L., and Dayton D.C.
2003 Preliminary screening--technical and economic assessment of synthesis gas to fuels and chemicals with emphasis on the potential for biomass-derived syngas. *In* NREL/TP ; 510-34929. D.C. Dayton and L. National Renewable Energy, eds. Golden, CO.: National Renewable Energy Laboratory.

Srinivasan S.
2009 The food v. fuel debate: A nuanced view of incentive structures. Renewable Energy 34(4):950-954.

Steckhan E., and Kuwana T.
1974 Spectroelectrochemical Study of Mediators I. Bipyridylium Salts and Their Electron Transfer Rates to Cytochrome c. Berichte der Bunsengesellschaft für physikalische Chemie 78(3):253-259.

Strehlitz B., et al.
1994 Artificial electron donors for nitrate and nitrite reductases usable as mediators in amperometric biosensors. Fresenius' Journal of Analytical Chemistry 349(8):676-678.

Sund C., et al.
2007 Effect of electron mediators on current generation and fermentation in a microbial fuel cell. Applied Microbiology and Biotechnology 76(3):561-568.

Tamimi A., Rinker E. B., and Sandall O. C.
1994a Diffusion coefficients for hydrogen sulfide, carbon dioxide, and nitrous oxide in water over the temperature range 293-368 K. Journal of Chemical and Engineering Data 39(2):330-332.

Tamimi A., Rinker E.B., and Sandall O.C.
1994b Diffusion Coefficients for Hydrogen Sulfide, Carbon Dioxide, and Nitrous Oxide in Water over the Temperature Range 293-368 K. Journal of Chemical & Engineering Data 39(2):330-332.

Tashiro Y., et al.
2007 Novel high-efficient butanol production from butyrate by non-growing Clostridium saccharoperbutylacetonicum N1-4 (ATCC 13564) with methyl viologen. Journal of Bioscience and Bioengineering 104(3):238-240.

Thorneley R.N. F.
1974 A convenient electrochemical preparation of reduced methyl viologen and a kinetic study of the reaction with oxygen using an anaerobic stopped-flow apparatus. Biochimica et Biophysica Acta (BBA) - Bioenergetics 333(3):487-496.

Trudinger P. A.
1970 On the absorbancy of reduced methyl viologen. Anal Biochem 36(1):222-5.

Tsai S., et al.
2009a Horizontal array bioreactor for conversion of syngas components to liquid products, Vol. US 20090215142. United States.

—
2009b Stacked array bioreactor for conversion of syngas components to liquid products, Vol. US 20090215153. United States.

Tsai S., et al.
2009c Modular membrane supported bioreactor for conversion of syngas components to liquid products, Vol. US 20090029434. United States.

Tsai S., et al.
2009d Syngas conversion system using asymmetric membrane and anaerobic microorganism, Vol. US 20090215163. United States.

Tu Y. Y., et al.
1983 Induction of a high affinity nitrosamine demethylase in rat liver microsomes by acetone and isopropanol. Chem Biol Interact 44(3):247-60.

Turn S. Q., et al.
1998 The fate of inorganic constituents of biomass in fluidized bed gasification. Fuel 77(3):135-146.

Ukpong M. N., et al.
2012a Physiological response of Clostridium carboxidivorans during conversion of synthesis gas to solvents in a gas-fed bioreactor. Biotechnology and Bioengineering 109(11):2720-2728.

Ukpong M.N., et al.
2012b Physiological response of *Clostridium carboxidivorans* during conversion of synthesis gas to solvents in a gas-fed bioreactor. Biotechnology and Bioengineering 109(11):2720-2728.

Ungerman A. J., and Heindel T. J.
2007 Carbon monoxide mass transfer for syngas fermentation in a stirred tank reactor with dual impeller configurations. Biotechnol Prog 23(3):613-20.

Verhallen P., et al.
1984a The Diffusion-Coefficients of Helium, Hydrogen, Oxygen and Nitrogen in Water Determined from the Permeability of a Stagnant Liquid Layer in the Quasi-Steady State. Chemical Engineering Science 39(11):1535-1541.

—
1984b The diffusion coefficients of helium, hydrogen, oxygen and nitrogen in water determined from the permeability of a stagnant liquid layer in the quasi-steady state. Chemical Engineering Science 39(11):1535-1541.

Wang K., Liu Y., and Chen S.
2011 Improved microbial electrocatalysis with neutral red immobilized electrode. Journal of Power Sources 196(1):164-168.

Watanabe T., and Honda K.
1982 Measurement of the extinction coefficient of the methyl viologen cation radical and the efficiency of its formation by semiconductor photocatalysis. The Journal of Physical Chemistry 86(14):2617-2619.

Weerachanchai P., Horio M., and Tangsathitkulchai C.
2009 Effects of gasifying conditions and bed materials on fluidized bed steam gasification of wood biomass. Bioresource Technology 100(3):1419-1427.

Whims J.
2002 Pipeline Considerations for Ethanol. Kansas State University.

Wilkins M. R., and Atiyeh H. K.
2011 Microbial production of ethanol from carbon monoxide. Current Opinion in Biotechnology 22(3):326-330.

Wise D. L., and Houghton G.
1968 Diffusion coefficients of neon, krypton, xenon, carbon monoxide and nitric oxide in water at 10-60°C. Chemical Engineering Science 23(10):1211-1216.

Wood H.G., Ragsdale S.W., and Pezacka E.
1986 The Acetly CoA pathway for autotrophic growth. FEMS Microb Rev 39:345-362.

Xu D.
2011 Syngas Impurity Effects on Cell Growth, Enzymatic Activities and Ethanol Production via Fermentation, Chemical Engineering, Brigham Young University.

Younesi H., Najafpour G., and Mohamed A.
2005 Ethanol and acetate production from synthesis gas via fermentation processes using anaerobic bacterium, Clostridium ljungdahlii. Biochemical Engineering Journal 27(Compendex):110-119.

Yuen S. H., Bagness J. E., and Myles D.
1967 Spectrophotometric determination of diquat and paraquat in aqueous herbicide formulations. Analyst 92(1095):375-381.

Yun C.H., et al.
1993 Hollow fiber solvent extraction removal of toxic heavy metals from aqueous waste streams. Industrial & Engineering Chemistry Research 32(6):1186-1195.

Zahlsen K., Aarstad K., and Nilsen O. G.
1985 Inhalation of isopropanol: induction of activating and deactivating enzymes in rat kidney and liver. Increased microsomal metabolism of n-hexane. Toxicology 34(1):57-66.

Zajic J.E.
1969 Microbial Biogeochemistry: Academic Press Inc.

Zheng J. M., Xu Y. Y., and Xu Z. K.
2003 Shell side mass transfer characteristics in a parallel flow hollow fiber membrane module. Separation Science and Technology 38(6):1247-1267.